THERMOELECTRIC PROPERTIES OF V-VI SEMICONDUCTOR ALLOYS AND NANOCOMPOSITES

Submitted by OVGU CEYDA YELGEL to the University of Exeter

as a thesis for the degree of Doctor of Philosophy in Physics.

August 2013

Abstract

Thermoelectric materials are materials which are capable of converting heat directly into electricity and vice versa. They have long been used in electric power generation and solid-state cooling. The performance of a thermoelectric device determined by the dimensionless figure of merit (ZT) of the material, defined as $ZT = (S^2\sigma/\kappa)T$, where S is the Seebeck coefficient, σ is the electrical conductivity, κ is the total thermal conductivity, and T is the absolute temperature. The total thermal conductivity consists of contribution from electrons, electron-hole pairs and phonons. Since the 1960s, the best thermoelectric material has been Bi_2Te_3 alloys, with a ZT of 1.0 at room temperature. In recent years, the idea of using nanotechnology has opened up the possibility of engineering materials at nanoscale dimensions to achieve higher values of ZT in other words to have more efficient thermoelectric devices.

This thesis starts with a broad introduction to thermoelectricity including various thermoelectric effects and their applications. The state-of-the-art thermoelectric materials and the optimisation methods to enhance the value of ZT have also been reviewed.

A systematic theoretical modelling of the thermoelectric properties of three dimensional bulk semiconductors has been presented in Chapter 2. Electronic properties (Fermi level, Seebeck coefficient, and electrical resistivity) and thermal conductivity contribution from carriers (donor electrons or acceptor holes) have been derived by using the nearly-free electron approximation and the Fermi-Dirac statistics. Other thermal conductivity contributions originated from electron-hole pairs and phonons have also been described in detail. In Chapter 3, this theoretical study is extended to two dimensional semiconducting quantum well structures bearing in mind that the Fermi level should change with the temperature as well as the quantum well width and additional interface scattering mechanisms

(interface mass-mixing and interface dislocation scatterings) should be included for the definition of anharmonic scattering rate.

Thermoelectric properties of n-type $(Bi_2Te_3)_{0.85}(Bi_2Se_3)_{0.15}$ single crystals doped with 0.1 wt.% CuBr and 0.2 wt.% SbI_3 and p-type $(Bi_2Te_3)_x(Sb_2Te_3)_{1-x}$ single crystals doped with 3 wt.% Te ($0.18 \leq x \leq 0.26$) have been explored in Chapter 4 and 5, respectively. It has been found that p-type Bi_2Te_3 based alloys showed higher values of ZT due to their larger power factor ($S^2\sigma$) and smaller thermal conductivity values. These calculations have concluded that the influence of the composition range of semiconductor alloys together with its type and amount of dopant plays an important role in enhancing the ZT. In Chapter 6, a detailed theoretical investigation and comparision of the thermal conductivities of these single crystals have been reported including frequency dependence of the phonon thermal conductivity for different temperatures. In Chapter 7, based on temperature and well width dependent Fermi level, a full theory of thermoelectric properties has been investigated for n-type 0.1 wt.% CuBr doped $Bi_2Se_3/Bi_2Te_3/Bi_2Se_3$ and p-type 3 wt.% Te doped $Sb_2Te_3/Bi_2Te_3/Sb_2Te_3$ quantum well systems. Different values of well thicknesses have been considered for both types of quantum well systems to study the effect of confinement on all thermoelectric transport coefficients. It has been found that reducing the well thickness has a pronounced effect on enhancing the ZT. Compared to bulk single crystals studied in Chapter 4 and 5, significantly higher thermoelectric figure of merits have been estimated theoretically for both n- and p-type semiconducting quantum well systems. For the n-type $Bi_2Se_3/Bi_2Te_3/Bi_2Se_3$ quantum well system with taking 7 nm well width the maximum value of ZT has been estimated to be 0.97 at 350 K and for the p-type $Sb_2Te_3/Bi_2Te_3/Sb_2Te_3$ quantum well with well width 10 nm the highest value of the ZT has been found to be 1.945 at 440 K.

Chapter 8 briefly recapitulates the results presented in this thesis and outlines possibilities for future work.

for my husband...

Acknowledgments

First of all, I would like to express my deepest gratitude and appreciation to my supervisor, Professor Gyaneshwar P. Srivastava, for all his suggestions, guidance, encouragement and unlimited support throughout my PhD. Without his advice, this thesis would not have come into being. I will forever be thankful to my dear supervisor.

I gratefully acknowledge the financial support by the Recep Tayyip Erdoğan University through the award of the PhD studentship received from The Republic of Turkey Ministry of National Education.

I would like to extend my sincerest thanks and appreciation to my father Mustafa Haluk Güven and my mother Nesrin Güven for their emotional support, unconditional love and care. I owe so much thanks to their personal sacrifices made for bringing me up. I love them so much and very grateful for having such wonderful parents.

My only sibling, my sister Duygu Güven is so special to me. She has been my best friend all my life and I love her dearly. I would like to thank her for all her advice, encouragement and support.

Last but not least, I would like express my heartfelt thanks to my dear husband, Celal Yelgel, for his continued and unfailing love, sincere moral support and remarkable patience. There are no words to convey how much I love him and I married the best person out there for me. Without him I simply would not have finished my PhD. This is why I dedicate this thesis to my husband with all my love.

List of Publications

Ö. Ceyda YELGEL and G. P. SRIVASTAVA, Thermoelectric Properties of n-type $Bi_2(Te_{0.85}Se_{0.15})_3$ Single Crystals Doped with CuBr and SbI_3, Phys. Rev. B **85**, 125207 (2012).

Ö. Ceyda YELGEL and G. P. SRIVASTAVA, A Detailed Theoretical Study of the Thermal Conductivity of $Bi_2(Te_{0.85}Se_{0.15})_3$ Single Crystals, Mater. Res. Soc. Symp. Proc. **1404**, mrsf11-1404-w03-02 (2012).

Ö. Ceyda YELGEL and G. P. SRIVASTAVA, Thermoelectric Properties of p-type $(Bi_2Te_3)_x(Sb_2Te_3)_{(1-x)}$ Single Crystals Doped with 3wt.% Te, J. Appl. Phys. **113**, 073709 (2013).

Ö. Ceyda YELGEL and G. P. SRIVASTAVA, Detailed Theoretical Investigation and Comparison of the Thermal Conductivities of n- and p-type Bi_2Te_3 Based Alloys, Mater. Res. Soc. Symp. Proc. **1543**, mrss13-1543-h03-24 (2013).

Ö. Ceyda YELGEL and G. P. SRIVASTAVA, Thermoelectric Properties of Bi_2Se_3 /Bi_2Te_3/Bi_2Se_3 and Sb_2Te_3/Bi_2Te_3/Sb_2Te_3 Quantum Well Systems, Phil. Mag., *review process* (2013).

Attended Conferences

- VII International Workshop on Semiconductor Surface Passivation, 11-15 September 2011, Kraków, Poland, (*Attendee*).

- 2011 Materials Research Society Fall Meeting and Exhibit, 28 November - 2 December 2011, Boston, USA, (*Oral presentation*).

- 2013 Materials Research Society Spring Meeting and Exhibit, 1-5 April 2013, San Francisco, USA, (*Poster presentation*).

Contents

List of Figures

List of Tables

Chapter 1

Introduction to Thermoelectricity

1.1 A Brief History

One of the most critical current issues of our time is to find alternative energy sources which are environmentally friendly. Research to discover energy sources other than fossil fuels has been sparked by different energy conversion technologies. Thermoelectric energy conversion is one of the types of energy conversion technology that has received great attention because of their fascinating properties which can be listed [1]:

- they are extremely reliable and silent in operation since they have no mechanical moving parts and require considerably less maintenance,
- they are simple, compact and safe,
- they are in a very small size and virtually weightless,
- they are capable of operating at elevated temperatures,

- they are environmentally friendly,
- they are not position-dependent, and
- they are suited for small-scale and remote applications typical of rural power supply where there is limited or no electricity.

Thermoelectricity was first discovered by the German physicist T. J. Seebeck in 1821 [2]. He found that electromotive force could be generated by heating the junction between two dissimilar electrical conductors. Thirteen years after Seebeck's discovery, J. C. Peltier, a French watchmaker, found that the passage of an electric current through a thermocouple[1] produces a small heating or cooling effect depending on its direction [3]. After a long time, in 1855, W. Thomson (known as Lord Kelvin) recognised that by applying the theory of thermodynamics he could establish a relationship between the Seebeck and Peltier effects. Thomson's work showed that a thermocouple is a type of heat engine and that it can be used as a device for generating electricity from heat or, alternatively, as a heat pump or refrigerator [4].

In 1911, the problem of energy conversion using thermocouples was studied in detail by E. Altenkirch [5, 6]. He pointed out that the performance of a thermocouple could be improved by increasing the magnitude of the differential Seebeck coefficient and the electrical conductivities and reducing their thermal conductivities. At that time, unfortunately, there were no thermocouples available in which the combination of properties was good enough for reasonably efficient energy conversion.

By introducing the idea of semiconductors as thermoelectric materials, modern

[1] it is a device consisting of two dissimilar metals and when it is heated, it develops an emf output.

research in thermoelectricity first started with Ioffe's observation. He suggested that doped semiconductors should be the best thermoelectric materials among others [7]. After his suggestion, there was a very active research period for thermoelectricity from 1957 to 1965 and the best refrigeration materials were found as Bi_2Te_3, PbTe, and bismuth antimony alloys. After a while, $Si_{1-x}Ge_x$ alloys were studied as thermoelectric materials and successfully used to build power sources for spacecraft and space stations. Despite these encouraging investigations thermoelectric materials still have not been in common use which is because they have not high enough efficiency comparing with mechanical cycle. Therefore, the goal is to search for novel thermoelectric materials with high thermoelectric efficiency. In this manner thermoelectric devices can be broadly used in everyday applications and compete with other energy conversion technologies.

During the past few years, a large number of materials systems have been investigated for their potential as thermoelectrics and several new ideas have been put forward to improve the performance of thermoelectric conversion efficiency. The most exciting and promising suggestion to have a high efficient thermoelectric device is using nanostructured thermoelectric materials such as quantum wells, quantum wires or quantum dots [8, 9]. These nanostructured thermoelectric materials use nanotechnology to modify material properties (both electronic and thermal) in ways that are not possible in bulk materials.

In this thesis, systematic theoretical works are provided for the thermoelectric transport properties of bulk and quantum well systems. Significant improvements on thermoelectric efficiencies are presented by doping bulk materials and using quantum well structures.

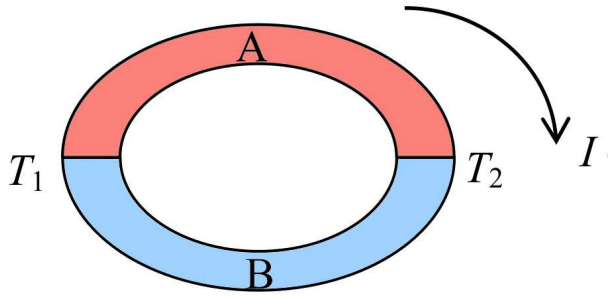

Figure 1.1: Seebeck effect in a closed circuit where A and B are two different materials and T_1 and T_2 are the temperatures at the junctions ($T_1 > T_2$). When differential Seebeck coefficient (S_{AB}) is positive, the current (I) flows clockwise direction through the material A.

1.2 Thermoelectric Phenomena

1.2.1 Seebeck Effect

In 1821, T. J. Seebeck reported the results of experiments in which a compass needle was detected when it was placed in the vicinity of a closed loop built by two different metals with a temperature difference between the junctions. This observation clearly provides evidence that a current flows along the closed circuit driven by the temperature difference which is called the Seebeck effect and presented in Fig. 1.1. In this closed circuit charge carriers (electrons or holes) diffuse from the hot side to the cold side due to a temperature difference. Mobile charge carriers move to the cold side and leave behind their oppositely charged and immobile nuclei at the hot side therefore giving rise to a thermoelectric voltage. Increase in charge carriers on the cold side finally starts to decrease when there exists an equal amount of charge carriers drifting back to the hot side as a result of the electric field created by charge separation. At this point, the material reaches

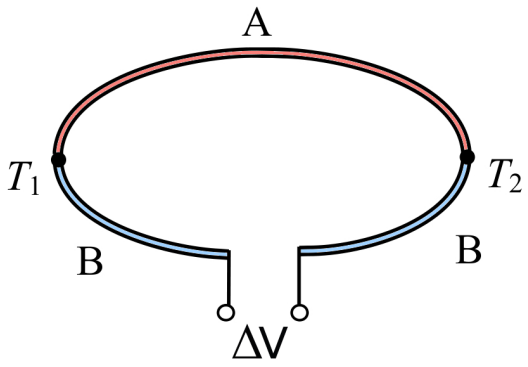

Figure 1.2: Seebeck effect in an open circuit where voltage (ΔV) is obtained between the two open ends of the circuit.

the steady state. An increase in the thermoelectric voltage can only be achieved by a rise in the temperature difference which causes a buildup of more charge carriers on the cold side of a material. The voltage, called the thermoelectric *emf* is generated by a temperature difference between two dissimilar materials that causes a continuous current flowing along the conductors if their junctions are kept at different temperatures.

In the case of an open circuit situation, as represented in Fig. 1.2, the junctions 1 and 2 are maintained at different temperatures T_1 and T_2 where $T_1 > T_2$, ΔV is developed between the two ends of the thermocouple and given by [1]

$$\Delta \mathrm{V} = \mathrm{V_a} - \mathrm{V_b} = \int_{T_1}^{T_2} (S_\mathrm{A} - S_\mathrm{B}) dT, \tag{1.1}$$

where S_A and S_B are the absolute Seebeck coefficients of material A and B, respectively. The absolute Seebeck coefficient S (also called thermopower) measures the magnitude of an induced thermoelectric voltage in response to a temperature difference across that material and is conventionally given in units of μV/K.

1.2.2 Peltier Effect

The Peltier effect was first discovered by Jean Peltier in 1834. This effect is the conversion of electricity into heat transfer which can be regarded as the reverse of the Seebeck effect. If an electric current is driven through two dissimilar materials, heat will be generated at one junction and absorbed at the other junction. If the reverse situation is considered in Fig. 1.2 with an external *emf* source applied across two ends of an open circuit, and a current I flows through the circuit then heat is absorbed at one junction and liberated at the other junction. Eventually, one junction cools off while other heats up, depending on the direction of the current. The Peltier heat (Q) absorbed by the cold junction per unit time is given by [1]

$$\frac{dQ}{dt} = \Pi_{\mathrm{AB}} I = (\Pi_{\mathrm{A}} - \Pi_{\mathrm{B}}) I, \tag{1.2}$$

where Π_{A} and Π_{B} are the Peltier coefficients of material A and B, respectively.

1.2.3 Thomson Effect

The last of the thermoelectric effects, the Thomson effect is expressed as the rate of heat absorbed or emitted in a current-carrying conductor subjected to a temperature gradient. When a current density J flows through a homogeneous conductor, heat is produced in a unit volume q due to the Thomson effect which is defined as [1]

$$q = \rho J^2 - \mu J \frac{dT}{dx}, \tag{1.3}$$

where ρ is the resistivity of the material, μ is the Thomson coefficient and dT/dx is the temperature gradient along the conductor. The first term in Eq. (1.3) defines the Joule heat per unit volume which is not reversible and the second term represents the Thomson heat which changes with the sign of the J.

1.2.4 The Kelvin Relationships

The three thermoelectric coefficients, the Seebeck coefficient, S, the Peltier coefficient, Π, and the Thomson coefficient, μ, are related to each other by the application of the theory of irreversible thermodynamics [1]:

$$S_{\mathrm{AB}} = \frac{\Pi_{\mathrm{AB}}}{T}, \tag{1.4}$$

and

$$\frac{dS_{\mathrm{AB}}}{dT} = \frac{\mu_{\mathrm{AB}}}{T}. \tag{1.5}$$

The validity of these relationships has been shown for many thermoelectric materials and it is assumed that they are acceptable for all materials used in thermoelectric applications.

1.3 Thermoelectric Figure of Merit

The concept of thermoelectric figure of merit was first introduced by E. Altenkirch in the early 1900s [5, 6]. It was found that good thermoelectric materials should have high electrical conductivity to minimise Joule heating, large Seebeck coefficients for maximum conversion of heat to electrical power (or electrical power to cooling performance), and low thermal conductivity to retain heat at the junctions and maintain a large temperature gradient. These three thermoelectric properties were later combined mathematically into one formula and written as

$$Z = \frac{S^2\sigma}{\kappa}, \tag{1.6}$$

where S is the Seebeck coefficient, σ is the electrical conductivity, and κ is the total thermal conductivity with the contributions of carriers (electrons or holes) (κ_{c}), electron-hole pairs (bipolar) (κ_{bp}) and phonons (κ_{ph}) and defined as $\kappa_{\mathrm{total}} =$

$\kappa_{\mathrm{c}} + \kappa_{\mathrm{bp}} + \kappa_{\mathrm{ph}}$. Due to Z is in a unit of K^{-1}, one often uses dimensionless figure of merit given as ZT. The standard measure of a single material's thermoelectric performance is determined by the figure of merit (ZT). The larger the figure of merit, the better the efficiency of the thermoelectric cooler or power generator. Therefore, there is significant interest in improving ZT in thermoelectric materials.

1.4 Applications of Thermoelectric Effects

Recent developments in both theoretical and experimental studies on thermoelectric properties of materials provide new opportunities for wide range of applications. Most of the thermoelectric devices have many thermoelectric couples consisting of n- (electrons as mobile charge carriers) and p- (holes as mobile charge carriers) type materials which are connected thermally in parallel and electrically in series. The top electrode, generally known as the thermoelectric bond, connects the n- and p-type thermoelectric materials. When a temperature gradient is applied on the thermoelectric device, the mobile charge carriers diffuse along the gradient direction and result in an electric current for the application of thermoelectric power generation or *vice versa* for the application of thermoelectric refrigeration.

The working principle of a thermoelectric generator is presented in Fig. 1.3. When a temperature gradient is applied to the device, the charge carriers diffuse from the hot side to the cold side and result in an electric voltage (or current) in the device. Having many of the p-n junctions in series improves the conversion efficiency of the thermoelectric device.

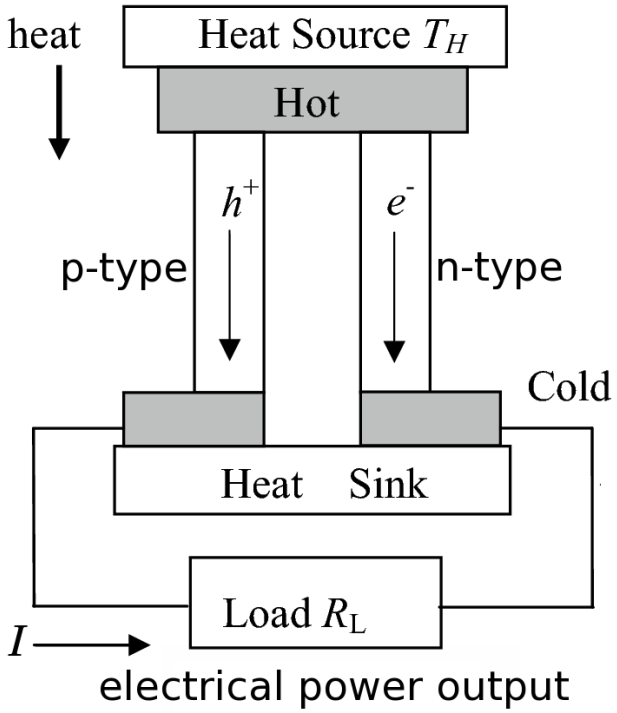

Figure 1.3: Illustration of thermoelectric power generator module.

The efficiency of a thermoelectric power generation η is defined as

$$\eta = \frac{\text{energy supplied to the load}}{\text{heat energy absorbed at hot junction}}. \tag{1.7}$$

By considering that the Seebeck coefficients, electrical and thermal conductivities of n- and p-type legs are constant and the contact resistances at the hot and cold junctions are negligible compared to total arm resistance, the efficiency has been derived to be [10, 11, 12]

$$\eta = \frac{I^2 R}{S_{pn} I T_{\mathrm{H}} + \kappa(T_{\mathrm{H}} - T_{\mathrm{C}}) - I^2 R/2}, \tag{1.8}$$

where I is the electrical current, $S_{pn} = S_p - S_n$ with S_n and S_p are the Seebeck coefficients of n- and p-type leg, respectively. In Eq. (1.8), R is the series resistance of n- and p-type legs, κ is the total thermal conductance of n- and p-type

material in parallel, T_{H} and T_{C} are the temperatures of the hot and cold sides of the generator.

The thermoelectric figure of merit for a thermocouple is directly related to the maximum efficiency of thermoelectric power generator $\eta_{\max}$. As shown in Fig. 1.3 the thermocouple is connected to an electrical load of resistance and if it is chosen to maximise the efficiency η, the maximum efficiency is then given by [10, 11, 12]

$$\eta_{\max} = \frac{T_{\mathrm{H}} - T_{\mathrm{C}}}{T_{\mathrm{H}}} \frac{\sqrt{1 + Z_c \overline{\overline{T}}} - 1}{\sqrt{1 + Z_c \overline{\overline{T}}} + \frac{T_{\mathrm{C}}}{T_{\mathrm{H}}}}, \tag{1.9}$$

where the average temperature is

$$\overline{T} = \frac{T_{\mathrm{H}} + T_{\mathrm{C}}}{2}, \tag{1.10}$$

and the figure of merit of thermocouple is

$$Z_c = \frac{S_{pn}^2}{R\kappa}. \tag{1.11}$$

In practice, the two legs of the thermoelectric junction have similar material constants, in which case the concept of a figure of merit for a material is employed and written by

$$Z = \frac{S^2 \sigma}{\kappa}, \tag{1.12}$$

where $S^2\sigma$ is referred to as the electrical power factor.

In Fig. 1.4, the power generating efficiency is represented as a function of the dimensionless figure of merit of the thermocouple for different T_{H} temperatures with choosing T_{C} as 300 K. From this calculation it is found that a thermocouple with having ZT=2.0 would have an efficiency of nearly 13%, 20%, 24%, when the temperatures are taken as T_{H}=500 K, 700 K, and 900 K, respectively.

The working mechanism of a thermoelectric refrigerator is shown in Fig. 1.5. When a voltage is applied on the bottom electrode, the free charge carriers move

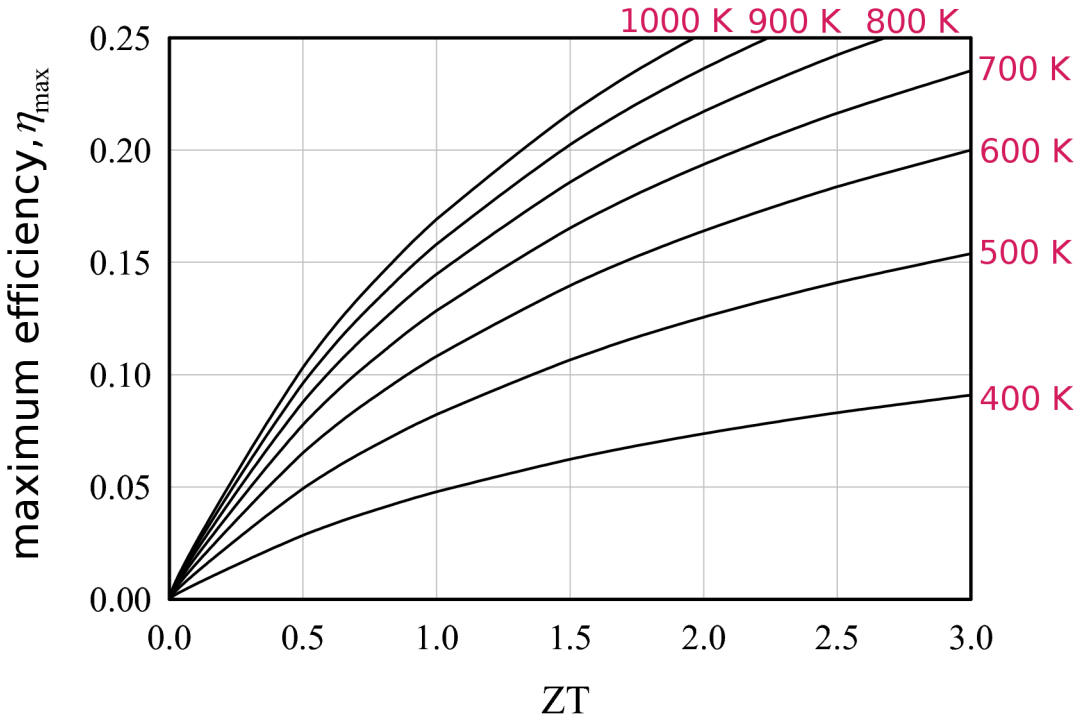

Figure 1.4: Generating efficiency as a function of the dimensionless figure of merit of the thermocouple for different T_{H} and T_{C} =300 K [13].

from the thermoelectric bond to the bottom electrode. As a result, a temperature gradient which varies according to the magnitude of current applied, is generated owing to the diffusion of charge carriers that bring heat from one side to the other. Eventually, the top thermoelectric bond becomes cooler which can be used in refrigeration mechanism.

The energy efficiency of a thermoelectric refrigerator is quantified by its coefficient of performance (COP) defined as [10, 11, 12]

$$\mathrm{COP} = \phi = \frac{\text{heat absorbed}}{\text{electrical power input}} = \frac{S_{pn} I T_{\mathrm{C}} - I^2 R/2 - \kappa \Delta T}{I(S_{pn}\Delta T + IR)} \tag{1.13}$$

where R is the electrical resistance of the thermoelements in series and κ is the thermal conductance of the thermoelements in parallel. Evidently, the coefficient of performance for a given temperature difference is dependent on the current I.

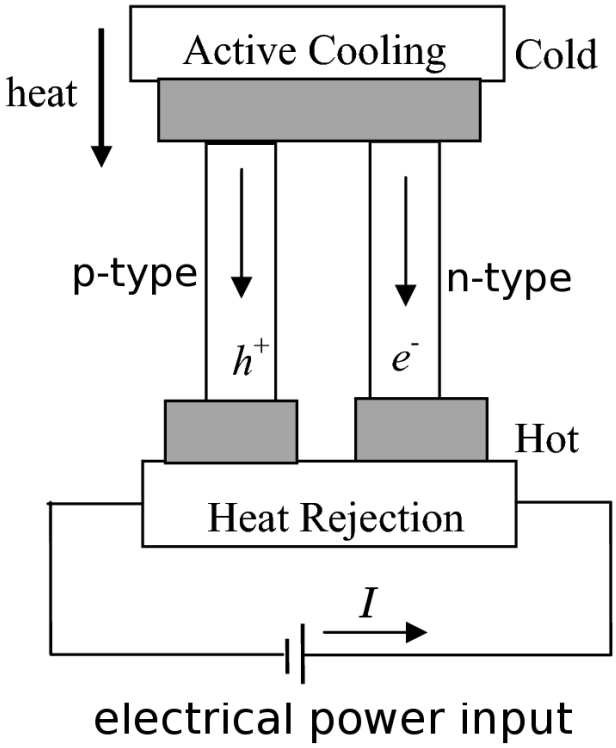

Figure 1.5: Illustration of thermoelectric refrigerator.

The maximum coefficient of performance is then given by [10, 11, 12]

$$\phi_{\max} = \frac{T_{\rm C}\left[\sqrt{1+ZT_{\rm C}} - \frac{T_{\rm H}}{T_{\rm C}}\right]}{(T_{\rm H}-T_{\rm C})\left[\sqrt{1+ZT_{\rm C}}+1\right]}, \tag{1.14}$$

where the current for maximum coefficient of performance and the maximum temperature difference is written as

$$I_{\max} = \frac{S_{pn}T_{\rm C}}{R} \quad , \quad \Delta T_{\max} = (T_{\rm H}-T_{\rm C})_{\max} = \frac{1}{2}ZT_{\rm C}^2. \tag{1.15}$$

1.5 Good Thermoelectrics

Good thermoelectric materials have a high figure of merit (ZT) and as follows from Eq. (1.6) they should have large power factor and low thermal conductivity. There are limited choices for finding materials in nature that exhibit a high figure

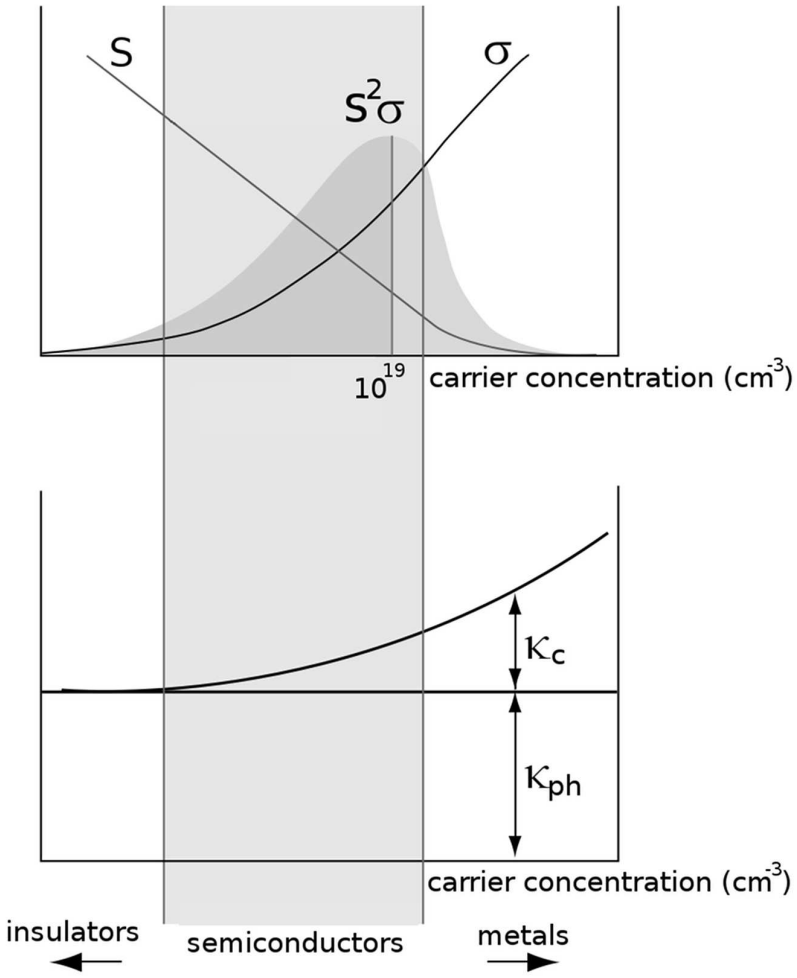

Figure 1.6: Schematic dependence of Seebeck coefficient, electrical conductivity, power factor, and thermal conductivity on carrier concentration [12].

of merit (i.e., with ZT $>$ 1) because all the three thermoelectric properties (S, σ, κ) are inter-related with each other. The difficulties of improving ZT relate to the following reasons: increasing S for simple materials leads to a simultaneous decrease in σ, and an increase in σ results in a comparable increase in κ_c due to the Wiedemann-Franz law. Figure 1.6 illustrates each of the three thermoelectric properties (S, σ, κ) as a function of carrier concentration. The horizontal scale is the carrier concentration which is divided into three regions as insulators, semiconductors, and metals, from the left to the right. Insulators have high values

Table 1.1: Comparison of thermoelectric properties (S, σ, ZT) of insulators, semiconductors, and metals at 300 K.

Property	Insulators	Semiconductors	Metals
S (μV K^{-1})	~ 1000	~ 200	~ 5
σ (Ω^{-1} cm^{-1})	$\sim 10^{-12}$	$\sim 10^{3}$	$\sim 10^{6}$
ZT	$\sim 1.5\times10^{-14}$	~ 0.6	$\sim 9\times10^{-4}$

of S and low values of κ but the properties are countered by low values of σ. Metals have high σ values but also have high κ and S values. The maximum electrical power factor ($S^2\sigma$) is gained at a carrier concentration of around 10^{19} cm^{-3} which is in the semiconductor materials region. The carrier contribution to the thermal conductivity (κ_c) for thermoelectric materials is generally 1/3 of the total thermal conductivity. Eventually, the best thermoelectric materials which produce the highest values of ZT are semiconductors. Additionally, in Tab. 1.1, the comparison of S, σ, and ZT values for insulators, semiconductors, and metals is given at 300 K. It is clearly seen that the optimal ZT with a large value of power factor is located in the semiconductors region. It should be noted that the discussion presented in this section is made by assuming that the lattice thermal conductivity is similar for all three types of materials.

1.6 Optimisation of Thermoelectric Figure of Merit

An effective way to maximise the ZT is to manipulate the phonon thermal conductivity which is the only coefficient not determined by the electronic structure. All other materials parameters (S, σ and κ_c) are inter-correlated with the elec-

tronic structure of the materials hence, in most cases, can not be optimised independently. There are three general strategies to reduce phonon thermal conductivity that have been successfully used. The first and traditional way is to modify an already promising compound by introducing point defects via alloying. In this manner, atomic mass fluctuation throughout the crystal lattice induces strong phonon scattering and leads to significantly lower thermal conductivity. As a result of this method, the best room temperature thermoelectric materials are based on compounds such as Bi_2Te_3 and $Si_{1-x}Ge_x$ [12, 14].

The second strategy to achieve maximum ZT is using phonon-glass electron-crystal (PGEC) concept. Here the goal is to be able to achieve a phonon glass without disrupting the crystallinity of the electron-transport region. By using this approach significant increases in ZT are reported for several compounds such as the clathrates which are composed of tetrahedrally coordinated Al, Ga, Si, Ge, or Sn [12].

A third and highly successful strategy to improve ZT is using nanostructured thermoelectric materials introduced by Hicks and Dresselhaus [8, 9] in the 1990s. They showed that by using two-, one- or even zero-dimensional structures one could obtain significant increases in ZT, far beyond what was believed possible in bulk materials. In particular, using lower dimensional structures decreases the phonon thermal conductivity by scattering phonons with the numerous boundaries or interfaces throughout the thermoelectric materials and even possibly enhances the electronic properties (S and/or σ). This approach led to an increased study of superlattices (2D structures), nanowires (1D structures), and quantum dots (0D structures) in the thermoelectric research area. By the same group in M.I.T, it was also experimentally shown that superlattices can significantly reduce the phonon thermal conductivity [15]. Soon after, the extraordinarily large value of ZT was achieved as 2.4 for p-type Bi_2Te_3/Sb_2Te_3 superlattices at room

temperature [16] and $ZT \simeq 3.5$ was reported for Bi-doped n-type PbSeTe/PbTe quantum dot superlattice at 550 K [17].

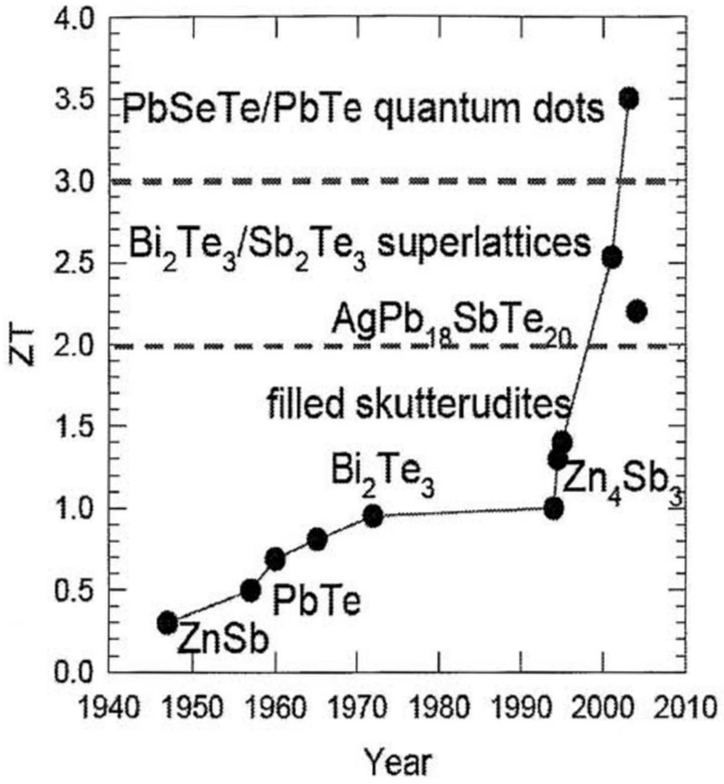

Figure 1.7: Timeline of ZT for many typical thermoelectric materials [18].

The history of thermoelectric materials characterised by the progress of increasing ZT with applying these three methods is represented in Fig. 1.7. It is seen that the most effective method for getting higher values of ZT is using low-dimensional thermoelectric materials.

What is the upper limit for ZT ?

While thermodynamics does not place any upper limit on the ZT, for many years it was impossible to find ZT values significantly greater than unity. After a while, it was empirically predicted that by combining the best electronic properties of any known crystalline material with a phonon conductivity that is characteristic

of a glass, the upper limit of ZT could be found to be about four [19]. Recently, however, it has been demonstrated that certain low-dimensional structures can have values of ZT that notably exceed those found in bulk materials [8, 9]. This shows that ZT=4 is no longer a theoretical barrier and upgrades our predicted limit for ZT to, perhaps, 20 [20]. If this value were eventually achieved, thermoelectric energy converters would have no less than about 50% of the efficiency of a Carnot cycle and would be comparable with the best known converters based on the vacuum diode [1, 20].

1.7 State-of-the-art Thermoelectric Materials

1.7.1 Bismuth Telluride and Its Alloys

Bismuth Telluride (Bi_2Te_3) based materials have been studied as near room temperature thermoelectric materials since 1950s [21]. Bi_2Te_3 dominates the market of thermoelectric refrigerator with its alloys with isomorphous compounds, Bi_2Se_3 and Sb_2Te_3. Additionally, the potential application in solid state solar thermoelectric power generator initiates another utilisation for this material.

Bi_2Te_3 is a typical member of group V chalcogenides and one of the best thermoelectric material at room temperature with $ZT \approx 1$. It is a narrow-gap semiconductor ($\sim$ 160 meV) having rhombohedral crystal structure with a layer structure shown in Fig. 1.8, along the c axis. The atomic planes follow the sequence Te_1-Bi-Te_2-Bi-Te_1 which is then repeated. The subscripts 1 and 2 denote differently bonded tellurium atoms. The Te_1-Te_1 layers are held together by weak van der Walls forces. Other remaining atoms (Te_1-Bi and Bi-Te_2) are linked by strong ionic-covalent bonds.

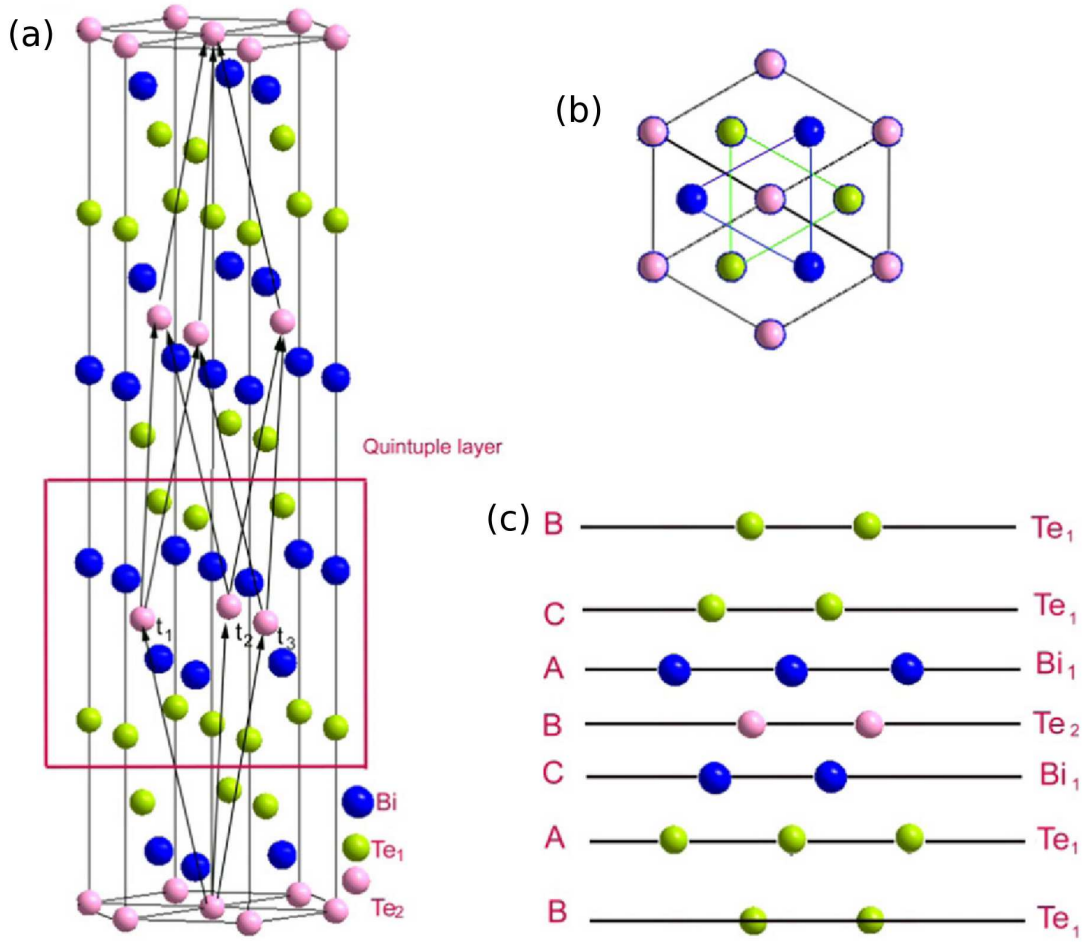

Figure 1.8: (a) Crystal structure of rhombohedral Bi_2Te_3 with three primitive lattice vectors labelled as t_1, t_2 and t_3. (b) Top view along z direction. (c) Side view of the quintuple layer [25].

Using Bi_2Te_3 based bulk materials significant improvements in thermoelectric figure of merit have been reported [12, 22, 23, 24]. Peak values of ZT are typically in the range of 0.8 to 1.1 with p-type materials having larger ZT values. By adjusting the carrier concentration of Bi_2Te_3 based materials it is possible to optimise ZT and push the peak value at different temperatures which enables the tuning of the materials for specific applications such as cooling or power generation. Also, superlattice systems with low dimensionality have been proposed to greatly enhance the ZT value of Bi_2Te_3 based materials. The highest ZT of about 2.4 at 300 K

was claimed for the p-type Bi_2Te_3/Sb_2Te_3 superlattices by Venkatasubramanian *et al.* [16]. It was claimed that this extraordinarily high ZT value dominantly originates from its exceedingly low lattice thermal conductivity resulting from the quantum confinement effect.

1.7.2 Silicon, Germanium, and SiGe Alloys

The crystal structures of Si, Ge, and SiGe alloys are cubic diamond and have been the primary thermoelectric materials in power generation devices operating in the temperature range of 600 °C - 1000 °C. These materials have been used in radio-isotope thermoelectric generators for deep-space missions to convert radio-isotope heat into electricity. Both Si and Ge have high thermal conductivities, though they can yield reasonably large values for the power factor since both elements have high carrier mobilities. Therefore, if their lattice thermal conductivities can be reduced, their ZT values will rise to a worthwhile value. Since the 1960s, many efforts have been made to improve the ZT of Si, Ge based materials. Dramatic decrease in the lattice thermal conductivity of Ge can be attained when it is alloyed with Si. The SiGe alloys can not compete with other thermoelectric materials at ordinary temperatures but they are very effective at high temperatures. The peak value of the ZT was found to be 1 at 900 °C - 950 °C for its n-type alloy and 0.65 for its p-type alloy [26, 27, 28, 29]. The energy gaps for Si and Ge are 1.15 eV and 0.65 eV, respectively. This suggests that Si rich alloys, when heavily doped, remain effectively free of minority carriers up to high temperatures. Recently, a peak value of ZT was also achieved as 1.3 at 900 °C for n-type SiGe nanocomposites [30]. Additionally, Bux *et al.* [31] reported that in nanostructured bulk Si the grain boundaries with very high density do not strongly affect electron mobility, but they significantly reduce the lattice thermal conductivity.

Therefore, the combined transport coefficients produce an increase in the ZT of nanostructured bulk Si by a factor of nearly 3.5.

1.7.3 Lead Telluride and Related Compounds

In the 1950s, Ioffe *et al.* [32] realised that semiconductors of high mean atomic weight were likely to be good thermoelectric materials and studied on lead telluride (PbTe) and isomorphous compounds. PbTe has the cubic rock salt structure and its band gap is 0.32 eV. It can be doped either n- or p-type with appropriate dopants (Zn, Cd, In, Bi, Cl for n-type and Na, Au, Ti, O for p-type). The maximum value of ZT for PbTe was found to be 0.8-1.0 at nearly 650 K [12]. When PbTe is compared with Bi_2Te_3, it has a higher melting point temperature at 923 °C. This means that, although ZT of PbTe is lower than for Bi_2Te_3, it can be used up to higher temperatures without chemical stability problems or unwanted contributions from the minority charge carriers. PbTe, then, has been considered more as a material for thermoelectric generation at mid-range temperature (450 K - 800 K) rather than for refrigeration at room temperature and below. In the past decade, significant recent works have focused on enhancing the thermoelectric figure of merit of PbTe by nanostructuring method. A very high ZT of about 2.2 was obtained in complex nanostructured PbTe-based alloy $Ag_{1-x}Pb_{18}SbTe_{20}$ at 800 K [34]. Furthermore, by Harman *et al.* [17] the highest value of ZT was reported for Bi-doped n-type PbSeTe/PbTe quantum dot superlattice as 3.5 at 550 K.

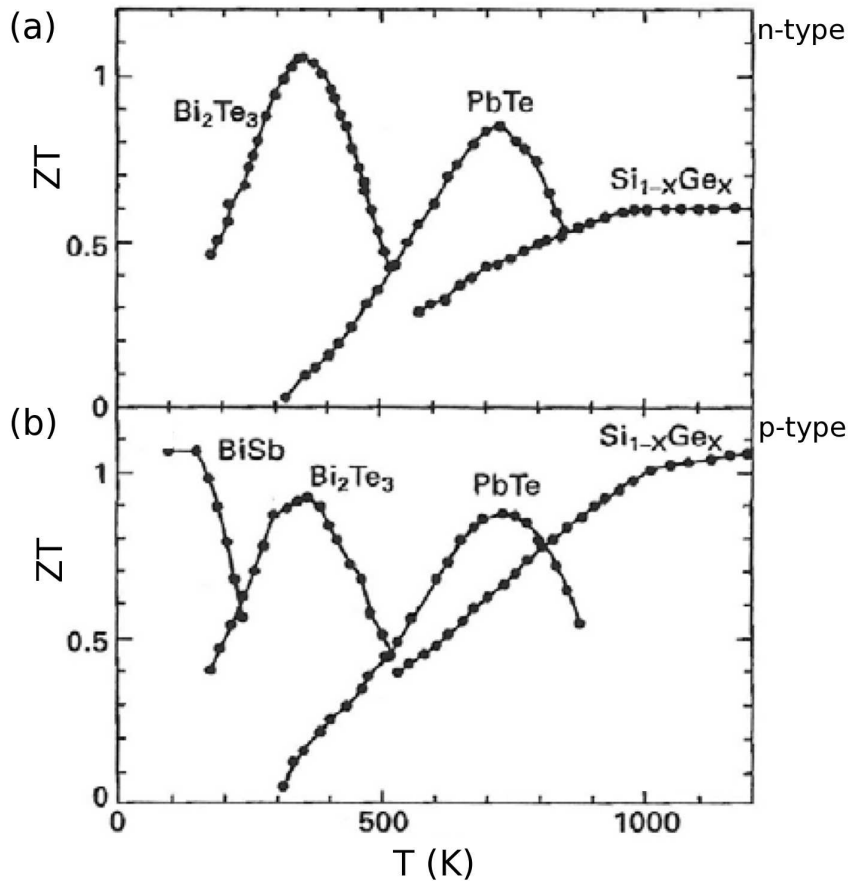

Figure 1.9: Thermoelectric figure of merit (a) n-type and (b) p-type Bi_2Te_3, PbTe, and $Si_{1-x}Ge_x$ systems [33].

Figure 1.9 summarises the temperature dependence of ZT for Bi_2Te_3, PbTe, and $Si_{1-x}Ge_x$ materials [33].

1.7.4 Skutterudites

The name of skutterudite was first given to the mineral $CoAs_3$ and extended to other compounds in the same family, such as $CoSb_3$. The general chemical formula for binary skutterudites can be written as MX_3, where atom M can be Co, Ir, or Rh, and atom X can be P, As, or Sb. The original thermoelectric skutterudite

$CoSb_3$ has very high power factor but its phonon thermal conductivity is too high to get larger values of ZT. One successful approach to reduce its lattice thermal conductivity is void-filling in the structure with many different elements including lanthanide, actinide, alkaline-earth, alkali, thallium, and Group IV elements. Skutterudite antimonides possess the largest voids thus they are of particular interest for thermoelectric applications. Particularly, ZT values of $Ce_{0.9}Fe_3CoSb_{12}$ and $La_{0.9}Fe_3CoSb_{12}$ compositions were observed to be about unity at 700 K and predicted to be 1.4 at 1000 K [35].

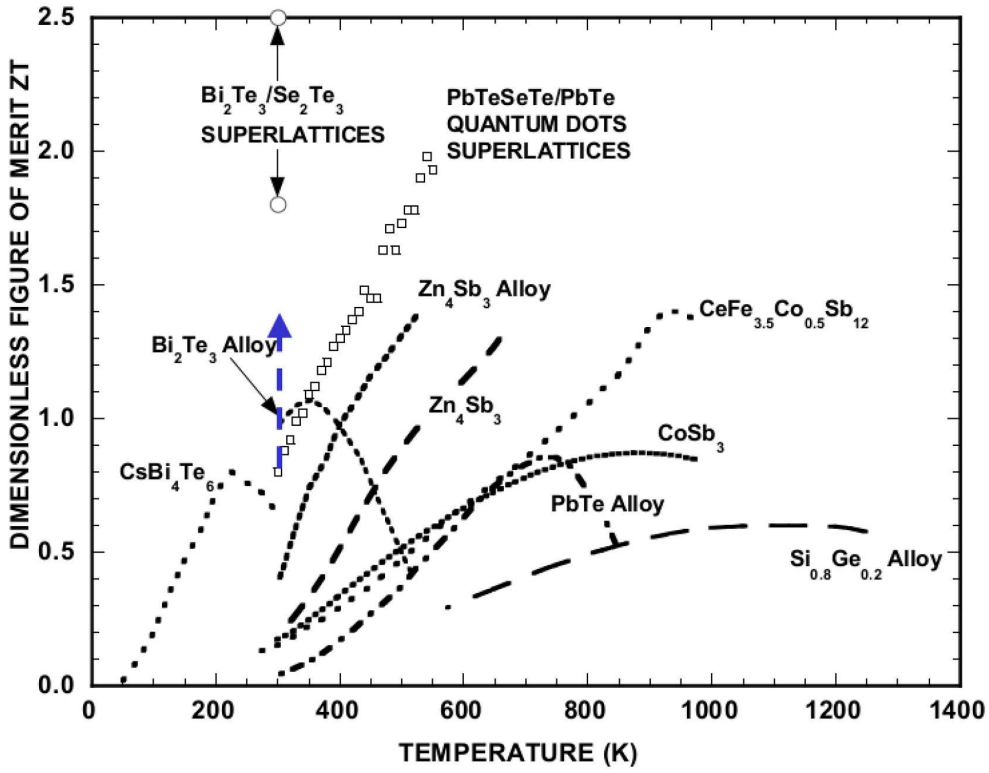

Figure 1.10: Temperature dependence of ZT for different material systems [36].

In Fig. 1.10, temperature variation of ZT is represented for state-of-the-art thermoelectric materials. Zinc antimonide (Zn_4Sb_3) is also presented due to its higher ZT values in the temperature range 263 K - 765 K which originate from its lower lattice thermal conductivity via its disordered crystal structure.

1.8 Scope and Organisation of This Thesis

In this chapter, a broad introduction to thermoelectricity has been presented including various thermoelectric effects and their applications. Additionally, the-state-of-the-art thermoelectric materials have been described in detail.

The thesis is organised as following:

- In Chapter 2, a full theory of thermoelectric properties is developed for 3D bulk materials.

- Our bulk theory is extented to 2D quantum well structures and presented in Chapter 3.

- In Chapter 4 and 5, theoretical calculations of thermoelectric properties are discussed for $(Bi_2Te_3)_x$ $(Bi_2Se_3)_{1-x}$ and $(Bi_2Te_3)_x$ $(Sb_2Te_3)_{1-x}$ single crystals. In Chapter 6, a detailed theoretical investigation and comparision of thermal conductivity is presented for both n- and p-type Bi_2Te_3 based alloys.

- In Chapter 7, thermoelectric properties of $Bi_2Se_3/Bi_2Te_3/Bi_2Se_3$ and $Sb_2Te_3/Bi_2Te_3/Sb_2Te_3$ quantum well systems are investigated.

- Finally, the summary of the thesis and a plan for future studies are briefly presented in Chapter 8.

Bibliography

[1] H. J. Goldsmid, Introduction to Thermoelectricity (Springer, London, 2010).

[2] T. J. Seebeck, Abhandlungen der Deutschen Akademie der Wissenschaften zu Berlin, 265 (1822-1823).

[3] J. C. Peltier, Ann. Phys. Chim. **56**, 371 (1834).

[4] D. D. Pollock, Thermoelectricity: Theory, Thermometry, Tool (American Society for Testing and Materials, New York, 1985).

[5] E. Altenkirsch, E. Phys. Z. **10**, 560 (1909).

[6] E. Altenkirsch, E. Phys. Z. **12**, 920 (1911).

[7] A. F. Ioffe, Semiconductor Thermoelements and Thermoelectric Cooling (Infosearch, London, 1957).

[8] L. D. Hicks and M. S. Dresselhaus, Phys. Rev. B **47**, 12727 (1993).

[9] L. D. Hicks and M. S. Dresselhaus, Phys. Rev. B **47**, 16631 (1993).

[10] D. M. Rowe and C. M. Bhandari, Modern Thermoelectrics (Reston Publishing Company, Virginia, 1983).

[11] G. S. Nolas, J. Sharp, and H. J. Golsmid, Thermoelectrics Basic Principles and New Materials Developments (Springer, Germany, 2001).

[12] D. M. Rowe, Thermoelectrics Handbook Macro to Nano (Taylor and Francis Group, London, 2006).

[13] H. Kong, Thermoelectric Property Studies on Lead Chalcogenides, Double-filled Cobalt Tri-Antimonide and Rare Earth- Ruthenium-Germanium, Ph.D. Thesis, University of Michigan (2008).

[14] T. M. Tritt and M. A. Subramanian, MRS Bulletin **31**, 188 (2006).

[15] T. Koga, S. B. Cronin, M. S. Dresselhaus, J. L. Liu, and K. L. Wang, Appl. Phys. Lett. **77**, 1490 (2000).

[16] R. Venkatasubramanian, E. Siivola, T. Colpitts, and B. O'Quinn, Nature **413**, 597 (2001).

[17] T. C. Harman, M. P. Walsh, B. E. LaForge, and G. W. Turner, J. Elect. Mat. **34**, L19 (2005).

[18] J. Zheng, Front. Phys. China **3**, 269 (2008).

[19] H. J. Goldsmid, British J. App. Phys. **11**, 209 (1960).

[20] H. J. Goldsmid, J. Thermoelec. **4**, 14 (2005).

[21] R. R. Heikes and R. W. Ure, Thermoelectricity: Science and Engineering (Interscience, New York, 1961).

[22] X. B. Zhao, X. H. Ji, Y. H. Zhang, T. J. Zhu, J. P. Tu, and X. B. Zhang, Appl. Phys. Lett. **86**, 062111 (2005).

[23] X. Tang, W. Xie, H. Li, W. Zhao, and Q. Zhang, Appl. Phys. Lett. **90**, 012102 (2007).

[24] B. Poudel, Q. Hao, Y. Ma, Y. Lan, A. Minnich, B. Yu, X. Yan, D. Wang, A. Muto, D. Vashaee, X. Chen, J. Liu, M. S. Dresselhaus, G. Chen, and Z. Ren, Science **320**, 634 (2008).

[25] Z-G. Chen, G. Han, L. Yang, L. Cheng, and J. Zou, Mat. Int. **22**, 535 (2012).

[26] D. M. Rowe, V. S. Shukla, and N. Savvides, Nature **290**, 765 (1981).

[27] C. B. Vining, J. Appl. Phys. **69**, 331 (2009).

[28] C. B. Vining, W. Laskow, J. O. Hanson, R. R. V. der Beck, and P. D. Gorsuch, J. Appl. Phys. **69**, 4333 (1991).

[29] D. M. Rowe, L .W. Fu, and S. G. K. Williams, J. Appl. Phys. **73**, 4683 (1993).

[30] X. W. Wang, H. Lee, Y. C. Lan, G. H. Zhu, G. Joshi, D. Z. Wang, J. Yang, A. J. Muto, M. Y. Tang, J. Klatsky, S. Song, M. S. Dresselhaus, G. Chen, and Z. F. Ren, Appl. Phys. Lett. **93**, 193121 (2008).

[31] S. K. Bux, R. G. Blair, P. K. Gogna, H. Lee, G. Chen, M. S. Dresselhaus, R. B. Kaner, and J. P. Fleurial, Adv. Funct. Mater. **19**, 2445 (2009).

[32] A. F. Ioffe, A. V. Airapetyants, A. V. Ioffe, N. V. Kolomoets, and L. S. Stil'bans, Dokl. Akad. Nauk SSSR **106**, 981 (1956).

[33] C. C. Sorrell, S. Sugihara, and J. Nowotny, Introduction to Thermoelectricity: Materials for Energy Conversion Devices (Woodhead Publishing in Materials, Cambridge, 2005).

[34] K. F. Hsu, S. Loo, F. Guo, W. Chen, J. S. Dyck, C. Uher, T. Hogan, E. K. Polychroniadis, and M. G. Kanatzidis, Science **303**, 818 (2004).

[35] B. C. Sales, D. Mandrus, B. C. Chakoumakos, V. Keppens, and J. R. Thompson, Phys. Rev. B **56**, 15081 (1997).

[36] G. Chen, M. S. Dresselhaus, G. Dresselhaus, J. -P. Fleurial, and T. Caillat, Int. Mat. Rev. **48**, 45 (2003).

Chapter 2

Thermoelectric Transport Theory in 3D Bulk Materials

When an electric field, a concentration gradient, or temperature gradient exists in a semiconductor we observe charge transport (electric current), mass transport (diffusion of carriers), or energy transport (heat conduction). The theory of transport processes deals with the relation between these currents and the forces which produce them. The formulations used for the calculation of thermoelectric transport properties are essentially based on a semiclassical treatment[1]. Although there are other approaches describing the semiclassical transport equation, the Boltzmann equation is always used due to it is being reasonably easy to track. Additionally, it yields a form of the expressions for the transport parameters that are intuitive and that can be readily compared with the experimental measure-

[1] In this treatment one regards electrons and holes as particles with well-defined position and crystal momenta except for the duration of a collision which is assumed negligible compared to the time between collisions. Therefore this system is completely analogous to an ideal classical gas. However, the collision process itself requires quantum mechanics and in this sense the treatment is called semiclassical.

ments. In this chapter, a detailed derivation of thermoelectric transport properties (S, σ, and κ_{c}) in 3D bulk systems will be presented with using Boltzmann equation and relaxation time approximation. Moreover, other thermal conductivity contributions from electron-hole pairs (κ_{bp}) and phonons (κ_{ph}) will be described in detail including several scattering mechanisms.

2.1 Electronic Transport Properties

2.1.1 Fermi Level

To make a quantitative assessment of the thermoelectric figure of merit (ZT) for semiconductor materials the electronic transport properties (S, σ, and κ_{c}) are strongly required the temperature dependent Fermi level. The temperature variation of the Fermi level (E_{f}) for n- and p-type bulk semiconductors in the extrinsic regime is expressed by McKelvey [6] as

for n-type;

$$E_{\mathrm{f}}^{\mathrm{ext}} = \frac{1}{2}(E_{\mathrm{c}} + E_{\mathrm{d}}) + \frac{k_{\mathrm{B}}T}{2}\ln\frac{N_{\mathrm{d}}}{2U_{\mathrm{c}}} - k_{\mathrm{B}}T\sinh^{-1}\Big[\sqrt{\frac{U_{\mathrm{c}}}{8N_{\mathrm{d}}}}\exp\Big(\frac{-\Delta E_{\mathrm{i}}}{2k_{\mathrm{B}}T}\Big)\Big],$$

for p-type; (2.1)

$$E_{\mathrm{f}}^{\mathrm{ext}} = \frac{1}{2}(E_{\mathrm{a}} + E_{\mathrm{v}}) + \frac{k_{\mathrm{B}}T}{2}\ln\frac{N_{\mathrm{a}}}{2U_{\mathrm{v}}} - k_{\mathrm{B}}T\sinh^{-1}\Big[\sqrt{\frac{U_{\mathrm{v}}}{8N_{\mathrm{a}}}}\exp\Big(\frac{-\Delta E_{\mathrm{i}}}{2k_{\mathrm{B}}T}\Big)\Big],$$

where E_{c} is the conduction band edge, E_{v} is the valence band edge, E_{d} is the donor energy level and E_{a} is the acceptor energy level. ΔE_{i} is determined as $(E_{\mathrm{c}} - E_{\mathrm{d}})$ for the donor ionisation and $(E_{\mathrm{a}} - E_{\mathrm{v}})$ for the acceptor ionisation energies. N_{d} and N_{a} are the concentrations of donor impurity and acceptor impurity atoms, respectively. Parameters U_{c} and U_{v} are given as U_{c}=$2((m_{\mathrm{n}}^{*}k_{\mathrm{B}}T)/(2\pi\hbar^{2}))^{3/2}$

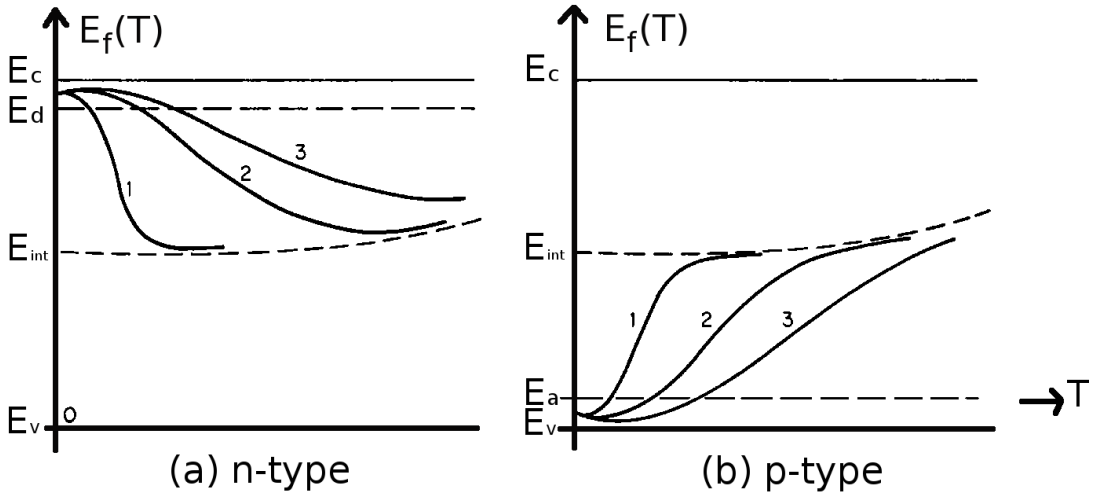

Figure 2.1: Temperature dependence of Fermi level for (a) n-type and (b) p-type semiconductor materials. The curves marked "1, 2, and 3" correspond to low, intermediate and high impurity densities, respectively [6].

and $U_{\rm v}$=$2((m_{\rm p}^* k_{\rm B} T)/(2\pi\hbar^2))^{3/2}$ with $k_{\rm B}$ is the Boltzmann constant and $\hbar$ is the reduced Planck's constant [6]. The effective masses are represented by $m_{\rm n}^*$ for the electron mass and $m_{\rm p}^*$ for the hole mass. For both types of semiconductors beyond a sufficiently high temperature donors at the $E_{\rm d}$ level (or acceptors at the $E_{\rm a}$) become fully ionized and the materials behave like intrinsic semiconductors. In this regime the temperature dependences of $E_{\rm f}$ for both n- and p-type doped semiconductors is written as [6]

$$E_{\rm f}^{\rm int} = \frac{E_{\rm v} + E_{\rm c}}{2} + \frac{3}{4} k_{\rm B} T \ln\Big(\frac{m_{\rm p}^*}{m_{\rm n}^*}\Big). \tag{2.2}$$

In Fig. 2.1, the temperature dependence of Fermi level is presented for both n- and p-type semiconductors. For n-type materials, at absolute zero temperature, Eq. (2.1) gives $E_{\rm f}$=$\frac{1}{2}(E_{\rm c} + E_{\rm d})$, which means that the Fermi level is midway between the donor levels and the conduction band. When the temperature increases, $E_{\rm f}$ goes up slightly (remaining nevertheless below $E_{\rm c}$) and then goes

down through the donor levels toward the centre of the gap. For temperatures such that E_{f} is several $k_{\mathrm{B}}T$ units below the donor energy level E_{d} at which point the donors are almost completely ionized and E_{f} approaches the intrinsic value $E_{\mathrm{f}}^{\mathrm{int}}$ as given in Eq. (2.2). Similarly for p-type semiconductor materials, at absolute zero temperature the Fermi level lies midway between the acceptor levels and the valence band. Following Eq. (2.1), as the temperatures increases E_{f} first decreases a bit, then rises continuously approaching the $E_{\mathrm{f}}^{\mathrm{int}}$ value given in Eq. (2.2) when the acceptor levels become fully ionized.

2.1.2 The Boltzmann Equation

In the thermoelectric transport theory, the fundamental issue concerns the distribution function of carriers about how the occupation number of carriers changes as a result of an electric field, thermal gradient, and the effect of various scattering mechanisms that the carriers undergo. The distribution function $f_k(\mathbf{r})$ of a carrier is defined as the probability that a band state with energy E_k will be occupied by this carrier at a carrier temperature T. The equilibrium distribution of carriers is governed by the Fermi-Dirac distribution function written as [1, 2, 3, 4, 5]

$$f_k^0 = \frac{1}{\exp\left[(E_k - \zeta^*)/(k_{\mathrm{B}}T)\right] + 1} \tag{2.3}$$

where ζ^* is the chemical potential. Equation (2.3) is independent of the spatial coordinate $\mathbf{r}$ because it is assumed that in equilibrium the temperature is the same everywhere (homogeneity). Away from equilibrium, the distribution may vary with the $\mathbf{r}$ therefore it is assumed that local equilibrium spreads over the region larger than the atomic dimensions on the time t. Additionally, owing to the wave vector dependence of E the distribution function depends on $\mathbf{k}$ and therefore it is considered explicitly $f(\mathbf{r}, \mathbf{k}, t)$. Changes in $f(\mathbf{r}, \mathbf{k}, t)$ arise from [1, 2, 3, 4, 5]:

- As a result of diffusion, carriers can move in or out in the region in the vicinity of point $\mathbf{r}$.

- Carriers are acted upon by driving forces (electric field or thermal gradient).

- Carriers are scattered by lattice vibrations or crystal imperfections therefore they are deflected into and out of the region near point $\mathbf{r}$. This is called the scattering effect on the distribution function and the respective partial derivative is named the collision term.

The Liouville theorem is related with the first two effects on $f(\mathbf{r}, \mathbf{k}, t)$ concerning the invariance of the volume occupied in phase space [1, 2, 3, 4, 5]. Therefore, the number of carriers in the neighborhood of point $\mathbf{r}$ at time t must equal the number of carriers in $r - \mathbf{v}(\mathbf{k})dt$ at time $t - dt$ where $\mathbf{v}(\mathbf{k})$ is the carrier velocity. Due to the applied external electric field ($\mathcal{E}$) carriers accelerate and their momentum is expressed by $(d\mathbf{k}/dt) = -q\mathcal{E}dt/h$ (assuming that there is no magnetic field and q is the carrier charge which equals to $-e$ for electrons and e for holes) [1, 2, 3, 4, 5]. Similar to the Liouville theorem we now consider the same volume invariance for k-space. The carriers are at point $\mathbf{k}$ at time t must be at a location $\mathbf{k} - q\mathcal{E}dt/h$. It is therefore can be written [4]

$$f(\mathbf{r}, \mathbf{k}, t) = f\Big[\mathbf{r} - \mathbf{v}(\mathbf{k})dt, \mathbf{k} - q\mathcal{E}\frac{dt}{\hbar}, t - dt\Big], \tag{2.4}$$

in the absence of any kind of collisions. However, collisions cannot be neglected because they significantly change the population of carriers. In time dt a change of population due to scattering is expressed by $(\partial f/\partial t)_{\text{coll}}dt$ [1, 2, 3, 4, 5]. By putting it all together, it can be found that [4]

$$f(\mathbf{r}, \mathbf{k}, t) = f\Big[\mathbf{r} - \mathbf{v}(\mathbf{k})dt, \mathbf{k} - q\mathcal{E}\frac{dt}{\hbar}, t - dt\Big] + \Big(\frac{\partial f}{\partial t}\Big)_{\text{coll}}dt. \tag{2.5}$$

When Eq. (2.5) is expanded to terms linear in dt, the Boltzmann equation is ex-

pressed as [1, 2, 3, 4, 5]

$$\frac{\partial f}{\partial t} + \mathbf{v} \cdot \nabla_r f + \frac{q\mathcal{E}}{\hbar} \cdot \nabla_k f = \Big(\frac{\partial f}{\partial t}\Big)_{\text{coll}}. \tag{2.6}$$

The terms on the left and right hand side are called the streaming terms and the collision term, respectively. The collision term contains all the information about the nature of the scattering processes.

One of the most successful approaches for solving the Boltzmann equation is based on the **relaxation time approximation** [1, 2, 3, 4, 5]. In this approach it is assumed that scattering processes can be described by a relaxation time $\tau(\mathbf{k})$ which specifies how the system returns to equilibrium, i.e., how the distribution function $f(\mathbf{r}, \mathbf{k}, t)$ approaches its equilibrium value $f^0(\mathbf{k})$ [1, 2, 3, 4, 5]. Therefore, the collision term is written as [1, 2, 3, 4, 5]

$$\Big[\frac{\partial f}{\partial t}\Big]_{\text{coll}} = -\frac{f(\mathbf{k}) - f^0(\mathbf{k})}{\tau(\mathbf{k})} = -\frac{g(\mathbf{k})}{\tau(\mathbf{k})}, \tag{2.7}$$

where $g(\mathbf{k})$ is the deviation of the distribution function $f(\mathbf{k})$ from its equilibrium value $f^0(\mathbf{k})$. Further considerable simplification of the transport problem is achieved by **linearized Boltzmann equation** which is done simply by replacing the steady-state carrier distribution in the gradient $\nabla_r f(\mathbf{r}, \mathbf{k}, t)$ and $\nabla_k f(\mathbf{r}, \mathbf{k}, t)$ to the equilibrium distribution function as $\nabla_r f^0(\mathbf{r}, \mathbf{k})$ and $\nabla_k f^0(\mathbf{r}, \mathbf{k})$ [4]. We can now easily express the linearized Boltzmann equation rewriting Eq. (2.6) by evaluating these two respective gradients as [4]

$$\Big(-\frac{\partial f^0}{\partial E}\Big)\mathbf{v}(\mathbf{k})\Big[\frac{E-\zeta^*}{T}\nabla_r\zeta^* + q\Big(\mathcal{E} + \frac{1}{q}\nabla_r\zeta^*\Big)\Big] = \Big(\frac{\partial f}{\partial t}\Big)_{\text{coll}}. \tag{2.8}$$

A general form of the distribution function describing carrier population perturbed by a weak electric field and a small temperature gradient is given the perturbed distribution function $f(\mathbf{r}, \mathbf{k}, t)$ and can be found after some algebra as [4]

$$f(\mathbf{k}) = f^0(\mathbf{k}) + \Big(-\frac{\partial f^0}{\partial E}\Big)\mathbf{v}(\mathbf{k})\tau(\mathbf{k})\Big[-q\Big(\mathcal{E} + \frac{1}{q}\nabla_r\zeta^*\Big) + \frac{E-\zeta^*}{T}(-\nabla_r T)\Big]. \tag{2.9}$$

2.1.3 Seebeck Coefficient

Themoelectric transport coefficients (S, σ, and $\kappa_{\rm c}$) of 3D bulk systems are derived when an electric field and a temperature gradient is applied. We have taken conditions appropriate to an isotropic solid with the diagonal components of all transport coefficients are equal and the non-diagonal components zero. Additionally, it is assumed that electrons (or holes) can move almost freely and they are in a band that is strictly parabolic (nearly free electron/hole model) and all flows (flow of charge and heat current) are in the x direction. In such 3D bulk systems, the dispersion relation for a single carrier pocket is assumed to be

$$E_{\rm 3D}(k_x, k_y, k_z) = \frac{\hbar^2 k_x}{2m_x^*} + \frac{\hbar^2 k_y}{2m_y^*} + \frac{\hbar^2 k_z}{2m_z^*}, \tag{2.10}$$

where the propagation vectors are k_x, k_y, and k_z along the three principal axes x, y, and z of the crystal. The effective mass tensor is diagonal and consists of components m_x^*, m_y^*, and m_z^*. The density of states for 3D bulk systems, presented in Fig. 2.2, is written as

$$g_{\rm 3D}(E) = \frac{\sqrt{2}}{\hbar^3 \pi^2} \sqrt{m_x^* m_y^* m_z^*} E^{1/2}. \tag{2.11}$$

By solving the linearized Boltzmann equation the electric current is given by [4],

$$i = \mp \int_0^\infty ev f(E) g(E) dE, \tag{2.12}$$

where $-$ sign refers to electrons and $+$ sign to holes, $-e$ is the electronic charge, v is the velocity of charge carriers in the x direction and $f(E)$ is the Fermi distribution [4, 5, 7]. The rate of flow of heat per unit cross-sectional area is defined as [4, 5, 7]

$$w = \int_0^\infty v(E - E_{\rm f}) f(E) g(E) dE, \tag{2.13}$$

where $E - E_{\rm f}$ represents the total energy transported by a carrier.

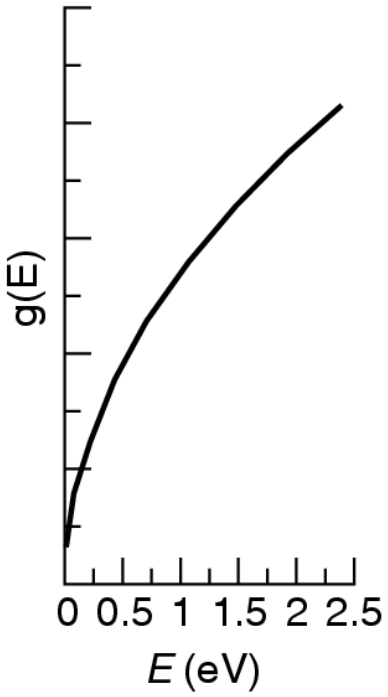

Figure 2.2: Electronic density of states $g(E)$ as a function of carrier energy E for 3D bulk crystal.

The preceding Eqs. (2.12) and (2.13) can be re-written by replacing f with $f - f_0$ (since there is no transport when $f = f_0$) as [4]

$$i = \mp \int_0^\infty ev^2 \tau g(E) \frac{\partial f_0}{\partial E} \Big(\frac{\partial E_\mathrm{f}}{\partial x} + \frac{E - E_\mathrm{f}}{T} \frac{\partial T}{\partial x} \Big) dE, \tag{2.14}$$

and

$$w = \pm \frac{E_\mathrm{f}}{e} i + \int_0^\infty v^2 E g(E) \tau \frac{\partial f_0}{\partial E} \Big(\frac{\partial E_\mathrm{f}}{\partial x} + \frac{E - E_\mathrm{f}}{T} \frac{\partial T}{\partial x} \Big) dE. \tag{2.15}$$

The condition $i = 0$ is that for the definition of the Seebeck coefficient and it can be found that [4]

$$\int_0^\infty eV^2 \tau g(E) \frac{\partial f_0}{\partial E} \frac{\partial E_\mathrm{f}/\partial x}{\partial T/\partial x} dE + \int_0^\infty ev^2 \tau g(E) \frac{\partial f_0}{\partial E} \frac{E - E_\mathrm{f}}{T} \frac{\partial T/\partial x}{\partial T/\partial x} dE = 0. \tag{2.16}$$

As discussed in Chapter 1, Seebeck coefficient is defined by [4]

$$S = -\frac{\Delta V}{\Delta T} = \frac{\mathcal{E}}{\nabla T} = \frac{1}{e} \frac{\partial E_\mathrm{f}/\partial x}{\partial T/\partial x}. \tag{2.17}$$

Therefore, from Eqs. (2.16) and (2.17) it is found that

$$S = -\frac{1}{e}\frac{\int_0^\infty v^2\tau g(E)\frac{\partial f_0}{\partial E}\frac{E-E_\mathrm{f}}{T}dE}{\int_0^\infty v^2\tau g(E)\frac{\partial f_0}{\partial E}dE}, \tag{2.18}$$

where the assumptions are made as $\tau = \frac{\mu_x m^*}{e}$ with μ_x is the carrier mobility in the x direction and $v^2 = \frac{2E}{3m^*}$. Eventually, the final expression of the Seebeck coefficient is then given by [4, 7, 8]

$$S = \pm\frac{k_\mathrm{B}}{e}\Big[\frac{E_\mathrm{f}}{k_\mathrm{B}T} - \frac{5}{3}\frac{F_{3/2}}{F_{1/2}}\Big], \tag{2.19}$$

where the plus is sign for the p-type semiconductors, the minus sign is for the n-type semiconductors and Fermi integral F_i is defined as [4, 7, 8]

$$F_i = \int_0^\infty \frac{x^i dx}{e^{(x-\zeta^*)}+1}. \tag{2.20}$$

2.1.4 Electrical Conductivity

Similarly, the electrical conductivity of a semiconductor in the extrinsic regime can be found by setting the temperature gradient equal to zero ($\partial T/\partial x = 0$) [4]. The electric field is given by [4]

$$\mathcal{E} = \pm\frac{1}{e}\frac{\partial E_\mathrm{f}}{\partial x}, \tag{2.21}$$

so that electrical conductivity can be written as

$$\sigma = \frac{i}{\mathcal{E}} = -\int_0^\infty e^2 v^2 \tau g(E)\frac{\partial f_0}{\partial E}dE. \tag{2.22}$$

By substituding the expressions of v^2, τ, and $g(E)$ as written in previous section it can be found that

$$\sigma = -\frac{2}{3}e\mu_x\frac{1}{2\pi^2}\Big(\frac{2}{\hbar^2}\Big)^{1/2}(m_x^* m_y^* m_z^*)^{1/2}\int_0^\infty E^{3/2}\frac{\partial f_0}{\partial E}dE. \tag{2.23}$$

By integrating by parts the final form of the electrical conductivity in the extrinsic regime can be found in terms of the Fermi integral as [4, 7, 8]

$$\sigma_\mathrm{extrinsic} = \frac{1}{2\pi^2}\Big(\frac{2k_\mathrm{B}T}{\hbar^2}\Big)^{3/2}(m_x^* m_y^* m_z^*)^{1/2}F_{1/2}e\mu_x. \tag{2.24}$$

In the intrinsic regime, the electrical conductivity of semiconductors is expressed as [6, 10]

$$\sigma_{\text{intrinsic}} = eN_i(\mu_n + \mu_p) = A^{'}e^{-E_g/2k_bT}, \tag{2.25}$$

where N_i is the equilibrium carrier density, μ_n, μ_p are the electron and hole mobilities, $A^{'}$ as a parameter that does not strongly depend on temperature, and E_{g} is the band gap of a material.

2.2 Thermal Transport Properties

2.2.1 Electronic Thermal Conductivity

Same condition as for the Seebeck coefficient ($i = 0$) is used to determine the electronic thermal conductivity which is described as [4]

$$\kappa_{\text{c}} = -\frac{w}{\partial T/\partial x}. \tag{2.26}$$

By substituding the expression of w in the above equation it can be found that

$$\begin{aligned}\kappa_{\text{c}} = &-\int_0^\infty v^2 E g(E)\tau\frac{\partial f_0}{\partial E}\underbrace{\frac{\partial E_{\text{f}}/\partial x}{\partial T/\partial x}}_{=eS}dE - \int_0^\infty v^2\frac{E^2}{T}g(E)\tau\frac{\partial f_0}{\partial E}dE \\ &+\int_0^\infty \frac{E_{\text{f}}}{T}v^2 E g(E)\tau\frac{\partial f_0}{\partial E}dE.\end{aligned} \tag{2.27}$$

Following the same procedure as for S and σ the final expression of the electronic thermal conductivity can be written in terms of the Fermi integrals as [4, 7, 8]

$$\kappa_{\text{c}} = \frac{\tau\hbar^2}{6\pi^2}\Big(\frac{2k_{\text{B}}T}{\hbar^2}\Big)^{5/2}\Big(\frac{m_y^* m_z^*}{m_x^*}\Big)^{1/2}k_{\text{B}}\Big[\frac{7}{2}F_{5/2} - \frac{25F_{3/2}^2}{6F_{1/2}}\Big]. \tag{2.28}$$

2.2.2 Bipolar Thermal Conductivity

In the above section, it has been assumed that one type of charge carrier (electrons or holes) is present in the conductor (called an extrinsic semiconductor). If

an extrinsic semiconductor is taken up to a high enough temperature a certain number of electron-hole pairs are created by excitation across the forbidden gap. When there are appreciable numbers of both electrons and holes, but their concentrations are unequal, the semiconductor is said to show mixed conduction. If the impurity level is very low or the semiconductor is taken up to a sufficiently high temperature that the concentrations of electrons and holes are essentially equal, then the semiconductor is called to be intrinsic.

When carriers of both signs are present simultaneously, a continuous stream of charges can flow in the direction of the temperature gradient without a corresponding electric current. This leads to a clear increment to the thermal conductivity. In this bipolar diffusion process, electron-hole pairs are created at the hot end of the specimen and absorb energy from the heat sources. They move down to the cold end of the specimen under the influence of the temperature gradient and recombine there at the cold end, giving up the ionization energy (equal to the forbidden energy gap) to the surroundings. Therefore, there is transport of ionization energy in addition to the normal direct transport of kinetic energy by carriers.

In small-band gap semiconductors such as Bi_2Te_3, PbTe, PbSe the bipolar thermal conductivity becomes the dominant contribution above room temperature. For a very idealised semiconductor which possesses simple parabolic valence and conduction bands and in which the charge carriers only undergo acoustic mode lattice scattering, the bipolar thermal conductivity is expressed by Glassbrenner and Slack [9] as

$$\kappa_{\mathrm{bp}} = \frac{b}{(1+b)^2}\left[\frac{E_{\mathrm{g}}}{k_{\mathrm{B}}T} + 4\right]^2\left[\frac{k_{\mathrm{B}}}{e}\right]^2 \sigma_{\mathrm{intrinsic}} T, \tag{2.29}$$

where b is the ratio of electron to hole mobility. With Eqs. (2.25) and (2.29) we can

simply write the bipolar part of thermal conductivity as

$$\kappa_{\mathrm{bp}} = F_{\mathrm{bp}} T^{p} \exp(-E_{\mathrm{g}}/2k_{\mathrm{B}}T), \tag{2.30}$$

with regarding F_{bp} and p as adjustable parameters, changing with doping type.

2.2.3 Phonon Thermal Conductivity

In solids atoms are not quite stationary but oscillate around their equilibrium positions (crystal lattice) as a result of thermal energy. The vibrations of atoms are not independent of each other and in fact, the motion of one atom anywhere in the solid affects all other atoms present. The crystal lattice vibration is characterised by the normal modes or standing waves. The quanta of the crystal vibrational field are referred to as *phonons*. In the presence of a temperature gradient, the thermal energy is considered as propagating through wave packets consisting of various normal modes, or phonons. The relationship between phonon frequency ω and wave vector q ($q = 2\pi/\lambda$, where λ is the wavelength) is known as *dispersion relation*. Figure 2.3 (a) shows a schematic phonon dispersion curve for one particular direction of propagation in a crystal with monoatomic lattice (one atom per unit cell). For a given value of q, there are three independent modes, one longitudinal and two transverse. When there is more than one atom per unit cell in the crystal the dispersion curves become more complicated. For instance, in Fig. 2.3 (b) the phonon dispersion curve is presented for a diatomic lattice (two atoms per unit cell). The low-frequency acoustic branches correspond to atoms in a unit cell moving in same phase whereas high-frequency optical branches represent atoms in unit cell moving in opposite phases. In general, optical phonons are not effective in transporting heat energy due to their small group velocity ($\partial\omega/\partial q$). However, they can affect the heat conduction by interacting with the acoustic phonons which are the main heat conductors.

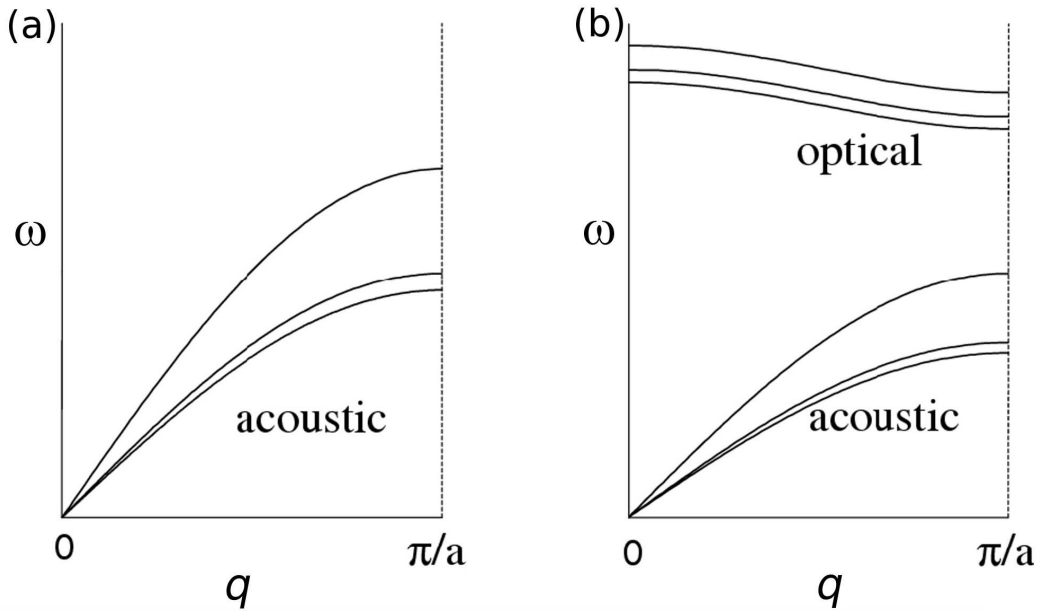

Figure 2.3: Schematic phonon dispersion curves for lattice vibrations where there is (a) one atom in a unit cell, and (b) two atoms in a unit cell. The lattice parameter is denoted a.

Phonons in a crystal are in thermal equilibrium with each other. The average number of phonons in the $\mathbf{q}$th mode in thermal equlibrium at temperature T is given by Bose-Einstein distribution function as [11]

$$\bar{n}_{\mathbf{q}} = \frac{1}{\exp\left(\hbar\omega_{\mathbf{q}}/k_{\mathrm{B}}T\right) - 1}. \tag{2.31}$$

From above expression it is clearly seen that at absolute zero temperature there are no phonons in a crystal. At low temperatures $\hbar\omega \gg k_{\mathrm{B}}T$, $\bar{n} \backsimeq \exp\left(-\hbar\omega/k_{\mathrm{B}}T\right)$ and there is an exponentially small probability for a phonon to be present. At high temperatures $k_{\mathrm{B}}T \gg \hbar\omega$, $\bar{n} \backsimeq k_{\mathrm{B}}T/\hbar\omega$ and the number of phonons increases linearly with temperature.

2.2.3.1 The Phonon Boltzmann Equation

The fundamental assumption in deriving the phonon Boltzmann equation is that there exists a distribution function $n_{\mathbf{q},s}(\mathbf{r},t)$ which measures the occupation number of phonons $(\mathbf{q},s)$ for their different modes s in the neighbourhood of $\mathbf{r}$ at time t. When a temperature gradient ∇T is applied across a dielectric, the rate of charge of this distribution function is controlled by two mechanisms.

(*i*) *Diffusion*: A spatial dependence of temperature ($T = T(\mathbf{r})$) is involved when a temperature gradient ∇T is applied. This leads $n_{\mathbf{q},s}(\mathbf{r},t)$ to diffuse (vary from one point to another) at the rate [11]

$$\frac{\partial n_{\mathbf{q}s}}{\partial t}\Big|_{\text{diff}} = -\mathbf{c}_s(\mathbf{q}) \cdot \nabla T \frac{\partial n_{\mathbf{q}s}}{\partial T}, \tag{2.32}$$

where $\mathbf{c}_s$ is the velocity of phonons in mode s.

(*ii*) *Scattering*: Various scattering processes also contribute to a rate of change $\frac{\partial n_{\mathbf{q}s}}{\partial t}|_{\text{diff}}$. In the steady state of heat flow through the solid, the total rate of $n_{\mathbf{q}s}$ must vanish and thus [11]

$$-\mathbf{c}_s(\mathbf{q}) \cdot \nabla T \frac{\partial n_{\mathbf{q}s}}{\partial T} + \frac{\partial n_{\mathbf{q}s}}{\partial t}\Big|_{\text{scatt}} = 0. \tag{2.33}$$

This is the general form of the Boltzmann equation for phonons. A solution of this equation is required for a calculation of phonon conductivity. However, this very complicated integro-differential equation requires a knowledge of the distribution function $n_{\mathbf{q}'s'}$ for all possible states $\mathbf{q}'s'$ together with transition rates from $\mathbf{q}'s'$ to $\mathbf{q}s$, thus, in general cannot be solved. Having said that, a simplification (linearisation) of this equation is possible. In equilibrium the phonon distribution does not change with time [11],

$$\frac{\partial \bar{n}_{\mathbf{q}s}}{\partial t} = 0. \tag{2.34}$$

Then $n_{\mathbf{q}s}$ in the second term of Eq. (2.33) can be replaced with the linear term $(n_{\mathbf{q}s} - \bar{n}_{\mathbf{q}s})$ in a Taylor expansion of $n_{\mathbf{q}s}$ about the equilibrium distribution $\bar{n}_{\mathbf{q}s}$.

Another assumption which can be made is that in the steady state the deviation from equilibrium due to the presence of a temperature gradient is small so that $n_{\mathbf{q}s}$ can be replaced with $\bar{n}_{\mathbf{q}s}$ in the first term of Eq. (2.33). For conciseness, it has been derived in detail that [11]

$$\frac{\partial n_{\mathbf{q}s}}{\partial t}\Big|_{\text{scatt}} = -\frac{(n_{\mathbf{q}s} - \bar{n}_{\mathbf{q}s})}{\tau_{\mathbf{q}s}}, \tag{2.35}$$

where $\tau_{\mathbf{q}s}$ is the relaxation time for the phonon $\mathbf{q}s$. Therefore, the linearised phonon Boltzmann equation can be expressed as [11]

$$-\mathbf{c}_s(\mathbf{q}) \cdot \nabla T \frac{\partial \bar{n}_{\mathbf{q}s}}{\partial T} = \frac{(n_{\mathbf{q}s} - \bar{n}_{\mathbf{q}s})}{\tau_{\mathbf{q}s}}. \tag{2.36}$$

2.2.3.2 Single-Mode Relaxation-Time Theory

(Debye Theory)

When a finite temperature gradient ∇T is established across a solid, in the steady state the rate of heat energy flow per unit area normal to the gradient is given by the macroscopic expression [11]

$$\dot{\mathbf{Q}} = -\kappa_{\text{ph}} \nabla T \tag{2.37}$$

where κ_{ph} is the lattice thermal conductivity. The heat current Q can be microscopically expressed by adding contributions from phonons in all possible modes as [11]

$$\begin{aligned} \dot{\mathbf{Q}} &= \frac{1}{N_0 \Omega} \sum_{\mathbf{q}s} \hbar\omega(\mathbf{q}s) n_{\mathbf{q}s} \mathbf{c}_s(\mathbf{q}) \\ &= \frac{1}{N_0 \Omega} \sum_{\mathbf{q}s} \hbar\omega(\mathbf{q}s) \psi_{\mathbf{q}s} \bar{n}_{\mathbf{q}s} (\bar{n}_{\mathbf{q}s} + 1) \mathbf{c}_s(\mathbf{q}), \end{aligned} \tag{2.38}$$

where we have considered a crystal with N_0 unit cells, each of volume Ω, $\mathbf{c}_s(\mathbf{q})$ is the group velocity for phonon $\mathbf{q}s$, and $\psi_{\mathbf{q}s}$ represents a deviation from the equilibrium system. The second equality in Eq. (2.38) is written by noting that it is

the deviation of the phonon distribution from equilibrium ($n_{\mathbf{q}s} - \bar{n}_{\mathbf{q}s}$) which contributes to the heat current. From Eqs. (2.37) and (2.38) the following expression for the lattice thermal conductivity tensor can be obtained as [11]

$$\begin{aligned}\kappa_{\rm ph}(ij) &= -\frac{\dot{\mathbf{Q}}_{\mathbf{i}} \cdot \nabla T_j}{|\nabla T|^2} \\ &= -\frac{1}{N_0 \Omega |\nabla T|^2} \sum_{\mathbf{q}s} \hbar\omega(\mathbf{q}s)\psi_{\mathbf{q}s}\bar{n}_{\mathbf{q}s}(\bar{n}_{\mathbf{q}s}+1)\mathbf{c}_i(\mathbf{q}s)\cdot\nabla T_j.\end{aligned} \tag{2.39}$$

For cubic crystals and an isotopic medium $\mathbf{c}$ is parallel to ∇T. Thus the lattice thermal conductivity is a scalar quantity and can be simplified as $\kappa_{\rm ph}(ij) = \kappa_{\rm ph}\delta(ij)$ and hence the above equation can be written as [11]

$$\kappa_{\rm ph} = -\frac{1}{N_0 \Omega |\nabla T|^2} \sum_{\mathbf{q}s} \hbar\omega(\mathbf{q}s)\psi_{\mathbf{q}s}\bar{n}_{\mathbf{q}s}(\bar{n}_{\mathbf{q}s}+1)\mathbf{c}_s(\mathbf{q})\cdot\nabla T. \tag{2.40}$$

However, from Eq. (2.36) it can be shown that [11]

$$\psi_{\mathbf{q}s} = -\mathbf{c}_s(\mathbf{q})\cdot\nabla T \tau_{\mathbf{q}s}\frac{\hbar\omega(\mathbf{q}s)}{k_{\rm B}T^2}. \tag{2.41}$$

Substituting Eq. (2.41) into Eq. (2.40) it can be found that [11]

$$\begin{aligned}\kappa_{\rm ph} =& \frac{1}{N_0\Omega k_{\rm B}T^2}\sum_{\mathbf{q}s}\frac{(\mathbf{c}_s(\mathbf{q})\cdot\nabla T)^2}{|\nabla T|^2}\hbar^2\omega^2(\mathbf{q}s)\bar{n}_{\mathbf{q}s}(\bar{n}_{\mathbf{q}s}+1)\tau_{\mathbf{q}s} \\ =& \frac{\hbar}{N_0\Omega k_{\rm B}T^2}\sum_{\mathbf{q}s}\omega^2_{\mathbf{q}s}c_s\tau_{\mathbf{q}s}\bar{n}_{\mathbf{q}s}(\bar{n}_{\mathbf{q}s}+1)\cos^2\theta,\end{aligned} \tag{2.42}$$

where $\cos\theta = \hat{\mathbf{c}}_s(\mathbf{q})\cdot\hat{\nabla}T$. In isotropic three dimensional systems $< \cos^2 > \theta = 1/3$, hence the lattice thermal conductivity in the single-mode relaxation-time ($smrt$) approach becomes [11]

$$\kappa_{\rm ph}(smrt) = \frac{\hbar^2}{3N_0\Omega k_{\rm B}T^2}\sum_{\mathbf{q}s}\omega^2_{\mathbf{q}s}c^2_s(\mathbf{q})\tau_{\mathbf{q}s}\bar{n}_{\mathbf{q}s}(\bar{n}_{\mathbf{q}s}+1). \tag{2.43}$$

This $smrt$ result for the lattice thermal conductivity is also be referred to as the Debye result since it is equivalent to the formula derived by Debye $\kappa_{\rm ph}(smrt) \equiv \kappa_{\rm ph}(D)$ [12].

Specific heat at constant volume is a fundamental quantity for thermal properties of solids. The specific heat is defined as [11]

$$C_v = \Big(\frac{\partial E}{\partial T}\Big)|_{N_0\Omega}, \tag{2.44}$$

where E is the thermal energy of the crystal described as [11]

$$E = \sum_s \int g_s(\omega)\hbar\omega_s(\mathbf{q})\bar{n}_s(\mathbf{q})d\omega. \tag{2.45}$$

with $g_s(\omega)$ represents the phonon density of states. The specific heat then can be expressed as [11]

$$C_v = \frac{\hbar^2}{k_{\rm B}T^2}\sum_s \int g_s(\omega)\omega_s^2(\mathbf{q})\frac{\exp\left(\hbar\omega/k_{\rm B}T\right)}{[\exp\left(\hbar\omega/k_{\rm B}T\right)-1]^2}, \tag{2.46}$$

since

$$\bar{n}_{\mathbf{q}s}(\bar{n}_{\mathbf{q}s}+1) = \frac{\exp\left(\hbar\omega/k_{\rm B}T\right)}{[\exp\left(\hbar\omega/k_{\rm B}T\right)-1]^2}. \tag{2.47}$$

Then Eq. (2.46) can be written as [11]

$$C_v = \frac{\hbar^2}{k_{\rm B}T^2}\sum_s \int g_s(\omega)\omega_s^2(\mathbf{q})\bar{n}_{\mathbf{q}s}(\bar{n}_{\mathbf{q}s}+1)d\omega. \tag{2.48}$$

In Debye's model, it is considered that in practice the crystal volume is very large and the $\mathbf{q}$ values are densely spaced, thus $\sum_{\mathbf{q}}$ can be replaced by an integral as $d\mathbf{q} \equiv \int g(\omega)d\omega$. The $smrt$ or Debye result for the lattice thermal conductivity then can be written as [11]

$$\kappa_{\rm ph}(D) = \frac{\hbar^2}{3N_0k_{\rm B}T^2}\sum_s c_s^2\int_0^{\omega_D} g(\omega)\omega^2(\mathbf{q}s)\tau_{\mathbf{q}s}\bar{n}_{\mathbf{q}s}(\bar{n}_{\mathbf{q}s}+1)d\omega, \tag{2.49}$$

where ω_D is an energy cut-off (called the Debye frequency). In the Debye model only acoustic phonon branches are considered and the phonon density of states is given by [11]

$$g(\omega) = \frac{N_0\omega}{2\pi^2}\sum_s \frac{1}{c_s^3}\int_0^{\omega_D}\omega d\omega. \tag{2.50}$$

Therefore, by substituting Eq. (2.50) into Eq. (2.49) we can write [11]

$$\kappa_{\rm ph}(D) = \frac{\hbar^2}{6\pi^2k_{\rm B}T^2}\sum_s c_s^2\int_0^{\omega_D}\frac{\omega^4(\mathbf{q}s)}{c_s^3}\tau_{\mathbf{q}s}\bar{n}_{\mathbf{q}s}(\bar{n}_{\mathbf{q}s}+1)d\omega. \tag{2.51}$$

Using linear dispersion relations required in the Debye scheme (*i.e.* $\omega = c_s q \Rightarrow d\omega = c_s dq$), the above equation can be re-expressed as [11]

$$\kappa_{\rm ph}(D) = \frac{\hbar^2}{6\pi^2 k_{\rm B} T^2} \sum_s c_s^4 \int_0^{q_D} q_D^4 \tau_{\mathbf{q}s} \bar{n}_{\mathbf{q}s}(\bar{n}_{\mathbf{q}s} + 1) dq, \tag{2.52}$$

where q_D is the Debye radius. By introducing a reduced wave number x as $x = q/q_D$, the $smrt$ or Debye result can be expressed finally within the Debye scheme as [11]

$$\kappa_{\rm ph}(D) = \frac{\hbar^2 q_D^5}{6\pi^2 k_{\rm B} T^2} \sum_s c_s^4 \int_0^1 x^4 \tau_{\mathbf{q}s} \bar{n}_{\mathbf{q}s}(\bar{n}_{\mathbf{q}s} + 1) dx. \tag{2.53}$$

2.2.3.3 Phonon Scattering Rates

Now that we have derived the formula for the lattice thermal conductivity and the problem is to calculate the relaxation times. The phonon relaxation time τ in Eq. (2.53) is governed by various scattering mechanisms. Within Matthiessen's rule the total phonon scattering rate is obtained as [11]

$$\tau^{-1} = \sum_i \tau_i^{-1}, \tag{2.54}$$

where τ_i^{-1} represents contributions from ith scattering mechanism.

Boundary Scattering:

Phonons are scattered by boundaries of a real crystal. The problem of boundary scattering of phonons was discussed by Casimir [13], Berman *et al.* [14, 15], Ziman [1], and Carruthers [16]. The importance for studying boundary scattering mechanism emerges from the fact that the strength of most of the phonon scattering processes is negligible for long wavelength phonons. Therefore, at low enough temperatures for the phonon mean free path to be as large as crystal dimensions, boundary scattering has significant effect. Although the scattering perturbation

Hamiltonian can be used for other different phonon scattering processes, it is not defined for phonon boundary scattering process. Detailed calculations made by Casimir [13] show that the phonon boundary scattering is not due to any transitions by phonon boundary scattering hence its transition matrix can be neglected. In this theory, a long cylindrical rod is considered to be the specimen, the temperature is assumed to be low enough that the only collision made by the phonons are with the boundary and it is supposed that the collision is completely diffuse. This means that the incident phonons are absorbed and then re-emitted with the equilibrium distribution corresponding to the local temperature. Assuming that a constant fraction of the phonons is speculary reflected, Berman, Simon, and Ziman have managed to generalise Casimiri's theory to account for multiple reflection and end effect. A simple conclusion from all that is that a constant relaxation time (independent of phonon frequency and temperature) for a phonon with speed c_s in the polarisation mode s can be defined as [11]

$$\tau_{\mathbf{q}s}^{-1}(\mathrm{bs}) = \frac{c_s}{L}, \tag{2.55}$$

where L is the phonon mean free path determined by the crystal size in single crystals and by average grain size in polycrstalline materials.

Mass Difference Scattering:

In 1941, it was for the first time pointed out that isotopes occuring in a crystal will disturb the periodicity of the lattice and hence cause thermal resisitivity by Pomeranchuk [17]. Later, in 1955, Klemens [18, 19] studied the scattering of phonons by mass difference and derived an expression for the relaxation time as [11]

$$\tau_{\mathbf{q}s}^{-1}(md) = \frac{\Gamma_{md}\Omega}{4\pi\bar{c}^3}\omega^4(qs), \tag{2.56}$$

where $\bar{c}$ is the average phonon speed, ω=cq, and Γ_{md} is the mass-defect parameter.

For a single-species crystal, the isotopic mass-defect parameter takes the form [11, 20]

$$\Gamma_{\text{isotopes}} = \sum_i f_i \Big(\frac{\Delta M_i}{\bar{M}}\Big)^2, \tag{2.57}$$

where f_i is the percentage of i^{th} isotope present in the crystal and ΔM_i=$M_i - \bar{M}$, with M is the average atomic mass.

In a composite material, such as an alloy, phonons also suffer scattering from the mass difference caused by alloying. In such materials with molecular formula $\text{A}_x\text{B}_y\text{C}_z$... mass-difference scattering of phonons are calculated with the formula given in Eq. (2.56) where the mass-defect parameter is given by [20]

$$\begin{aligned}\Gamma_{\text{alloy}}(\text{A}_x\text{B}_y\text{C}_z...) =& \frac{x}{(x+y+z+...)}\Big(\frac{M_{\text{A}}}{\bar{M}}\Big)^2\Gamma(\text{A}) \\ &+\frac{y}{(x+y+z+...)}\Big(\frac{M_{\text{B}}}{\bar{M}}\Big)^2\Gamma(\text{B}) \\ &+\frac{z}{(x+y+z+...)}\Big(\frac{M_{\text{C}}}{\bar{M}}\Big)^2\Gamma(\text{C}) \\ &+...,\end{aligned} \tag{2.58}$$

where

$$\Gamma(\text{A}) = \sum_i f_i \Big(\frac{\Delta M_i(A)}{\bar{M}_A}\Big)^2, \tag{2.59}$$

and represents the defect parameter for atomic species A, and the average atomic mass is expressed as $\bar{M} = (xM_A + yM_B + zM_C + ...)/(x+y+z+...)$.

Phonon-Donor Electron (-Acceptor Hole) Scattering:

In doped insulators and semiconductors, phonons relaxation is also subject to their interaction with donor electrons (or acceptor holes). The expression for phonon relaxation rate due to such interaction takes different forms depending on donor (or acceptor) concentration level (above or below 10^{17}cm^{-3}). In this work, the application of the phonon scattering theory is needed for Bi_2Te_3 based

alloys which have impurity levels exceed 10^{17}cm^{-3} and, thus Ziman's theory [1] can be applied which has a simplified form as following expression [21]

$$\tau_{\mathbf{q}}^{-1}(\text{ep},\text{hp}) = \frac{N_{d,a}E_D^2\omega}{\rho c_L^2 k_\text{B}T}\sqrt{\frac{\pi m_{n,p}^* c_L^2}{2k_\text{B}T}}\exp\Big(\frac{-m_{n,p}^* c_L^2}{2k_\text{B}T}\Big). \tag{2.60}$$

where N_d (N_a) is the concentration of donor electrons (acceptor holes), E_D is the deformation potential, and c_L is the longitudinal acoustic phonon speed.

Anharmonic Scattering:

When a phonon encounters another phonon in a crystal, the two scatter from each other because of the anharmonic interaction between them. At temperature above the absolute zero anharmonic lattice forces exist in real crystals. Additionally, at high enough temperatures, where the atomic displacements are large, these phonon-phonon interactions become particularly important.

While it is reasonably straightforward to derive relaxation time expressions for above scattering mechanisms, the same is not true for the anharmonic relaxation time for two reasons: (i) while other scattering mechanisms are elastic in nature, anharmonic interactions are inelastic in nature, and (ii) to derive an acceptable form of the anharmonic interaction Hamiltonian is much more diffucult compared to others. Deriving a workable expression for anharmonic crystal potential and hence for anharmonic relaxation time is one of the most difficult objectives in phonon physics.

The theory of lattice thermal conductivity, including the inelastic nature of anharmonic phonon interactions, has been developed using relaxation time and variational approaches at different levels of sophistication. In 1954, Herring [22] was the among the first to use a relaxation time approach to understand and explore these interactions in bulk materials. He showed that the relaxation rate of phonon modes undergoing three phonon processes was directly proportional to the tem-

perature. However, this approach relies on the condition that the temperature is higher than the Debye temperature [11] and uses a simplified form for the potential cubic anharmonic term. This relaxation time approach was adopted by Liebfried and Schlömann [23] who had previously developed an anharmonic potential [24] as part of their specific heat calculations in 1952. This anharmonic potential was calculated using a Debye-like continuum approach to modelling the potential. Using their potential, Leibfried et al. [23] were able to calculate the lifetime of the acoustic phonon modes undergoing three phonon interactions for bulk semiconductors. This potential was advantageous in that it had only one adjustable parameter, but was disadvantageous in that it required linear dispersion relations. This theory was then applied to several semiconductors and showed good agreement with experiment [1], though in their results it was a necessity to vary at least one adjustable parameter with temperature to match high and low temperature experimental results. Klemens, in 1958, proposed a second form for the anharmonic potential in bulk [33], which also only applied in the long wavelength limit to acoustic phonons, by applying symmetry arguments. The advantage of Klemens potential was that it applied to non-linear dispersion curves, which is the case in most real systems. The disadvantage of this potential was that it required one to have knowledge of the average velocity of the phonon modes (with no clear definition of how to calculate this) and had two scalable parameters. Also, Klemens' expression, like Leibfried's, had an arbitrary coupling between the interacting phonon modes. However, Klemens and Liebfrieds models did not agree on the low temperature relaxation rates. Later, in 1966 Klemens [25, 26] improved and generalised this potential and the resultant expression for the relaxation rate of phonon modes by including the effects of optical modes, but still the two theories could not agree. Hamilton and Parrott [27], in 1968, re-adapted and improved the form of the Leibfried's potential by expanding the potential in terms of the isotropic continuum model based upon the relations de-

rived by Landau and Lifschitz [28]. By applying this approach, they showed that these scattering processes could explain the thermal conductance of Ge as a function of temperature using the variational principle. Later, on this basis, Parrott applied this potential using the knowledge gained from the variational approach to a relaxation time approach [29, 30].

In 1974, Srivastava [31] presented a detailed description of the relaxation rate of phonon modes. Previous arbitrary parameters and coupling constants were replaced with measurable quantities and a clear description of the difference between Class 1 and Class 2 events was presented. Also, by removing arbitrary coupling parameters, Srivastava was able to show that at high temperatures, Umklapp processes would dominate in bulk materials and at low temperatures Normal processes would dominate. In his approach, he was able to discuss the exact contributions from different phonon modes, and only applied one semi-adjustable parameter, the Grüneisen constant, which did not need to change with temperature. Later, in 1976, Srivastava [32] improved upon the potential which Parrott had applied [30] by removing the necessity to use linear dispersion relations and correcting the potential to show a similar form to that of Klemens [33], but with only one semi-adjustable parameter (the Grüneisen constant) and no arbitrary coupling factor. Later, by applying this relaxation time approach to Ge, Srivastava [34] showed excellent agreement with experiment and explained the thermal conductivity in all regimes. This included the high temperature regime which is dominated completely by three phonon events.

In this thesis, for the anharmonic phonon scattering rate we restrict ourselves to only three-phonon interaction and follow the Srivastava's scheme. In his scheme,

the anharmonic scattering mechanism is expressed as [11]

$$\tau_{\mathbf{q}s}^{-1}(\text{anh}) = \frac{\hbar q_D^5 \gamma^2}{4\pi\rho\bar{c}^2} \sum_{s's''\varepsilon} \Bigg[\int dx' x'^2 x''_+ [(1-\varepsilon+\varepsilon(Cx+Dx')] \frac{\bar{n}_{\mathbf{q}'s'}(\bar{n}''_+ + 1)}{(\bar{n}_{\mathbf{q}s}+1)} + \frac{1}{2} \int dx' x'^2 x''_- [1-\varepsilon+\varepsilon(Cx-Dx')] \frac{\bar{n}_{\mathbf{q}'s'}\bar{n}''_-}{\bar{n}_{\mathbf{q}s}} \Bigg]. \tag{2.61}$$

Here γ is the Grüneisen constant, $x' = q'/q_D$, $x''_{\pm}$=$Cx \pm Dx'$, $\bar{n}''_{\pm} = \bar{n}(x''_{\pm})$, $C = c_s/c_{s''}$, $D = c_{s'}/c_{s''}$. The processes described by the first and second terms in Eq. (2.61) may be referred to as Class 1 and Class 2 events, governed by the momentum and energy conservation conditions:

$$\begin{aligned} &\text{Class 1 events:} \quad \mathbf{q}+\mathbf{q}' = \mathbf{q}'' + \mathbf{G} \quad ; \quad \omega+\omega' = \omega'', \\ &\text{Class 2 events:} \quad \mathbf{q}+\mathbf{G} = \mathbf{q}' + \mathbf{q}'' \quad ; \quad \omega = \omega' + \omega''. \end{aligned} \tag{2.62}$$

For each class, an event is called *Normal process* if it involves wave-vectors of all participating phonons within the central Brillouin zone. If a reciprocal lattice vector G is required to meet the momentum conservation condition, the event is called *Umklapp process*. These processes are schematically illustrated for a Class 1 event in panels (a) and (b) of Fig. 2.4.

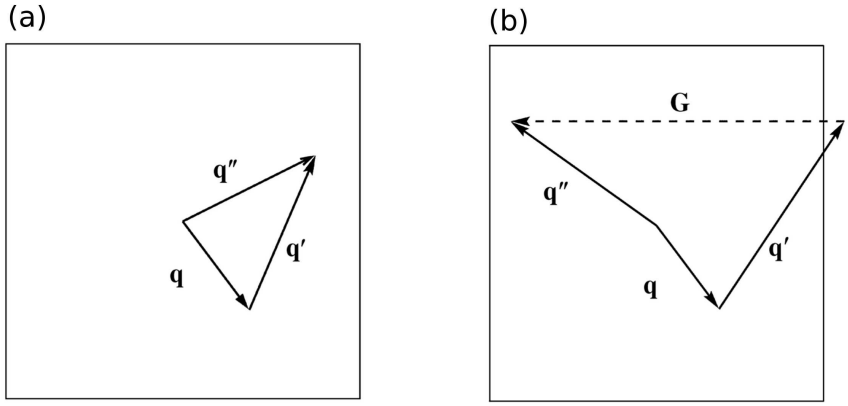

Figure 2.4: Schematic illustration of a Class 1 three-phonon scattering process in a single crystal solid: (a) an Normal process and (b) an Umklapp process.

In Eq. (2.61), $\varepsilon = 1$ for momentum-conserving Normal processes, and ε=-1 for

momentum-nonconserving Umklapp processes. The integration limits on the variables x and $x^{'}$ in Eq. (2.61), derived from a detailed consideration of the energy and momentum conservation requirements, have been given as [11]

Class 1 events:

$$0 \leqslant x \leqslant 1$$

$$\text{N processes: } 0, \frac{(1-C)x}{(1+D)} \leqslant x^{'} \leqslant \frac{(1+C)x}{(1-D)}, \frac{(1-Cx)}{D}, 1$$

$$\text{U processes: } 0, \frac{(2-(1+C)x)}{(1+D)} \leqslant x^{'} \leqslant \frac{(1-Cx)}{D}, 1$$

Class 2 events:

$$\text{N processes: } (0 \leqslant x \leqslant 1)$$

$$0, \frac{(C-1)x}{(D+1)}, \frac{(Cx-1)}{D} \leqslant x^{'} \leqslant \frac{(C+1)x}{(D+1)}, \frac{(C-1)x}{D-1}, 1$$

$$\text{U processes: } \left(\frac{2}{1+C} \leqslant x \leqslant 1\right)$$

$$0, \frac{(2-(1+C)x)}{(1-D)}, \frac{Cx-1}{D}, \frac{(C+1)x-2}{D+1} \leqslant x^{'} \leqslant \frac{(C+1)x-2}{D-1}, 1.$$

In thermoelectric research area, although detailed full-scale expressions for anharmonic relaxation rates due to three phonon Normal and Umklapp processes are available as described above, these have not been widely employed in calculations of lattice thermal conductivity. Most researchers have ignored the contribution from three phonon Normal (momentum conserving) processes and have employed grossly oversimplified expressions, containing adjustable parameters, for Umklapp (momentum nonconserving) scattering rate (e.g., Ref. [35]).

Bibliography

[1] J. M. Ziman, Electrons and Phonons: The Theory of Transport Phenomena in Solids (Oxford University Press, London, 1960).

[2] F. Seitz and D. Turnbull, Solid State Physics: Advances in Research and Applications (Academic Press Inc., New York, 1957).

[3] M. Balkanski and R. F. Wallis, Semiconductor Physics and Applications (Oxford University Press, New York, 2000).

[4] T. M. Tritt, Thermal Conductivity: Theory, Properties, and Applications (Kluwer Academic/Plenum Publishers, New York, 2004).

[5] P. Y. Yu, Fundamentals of Semiconductors: Physics and Materials Properties (Springer, London, 2010).

[6] J. P. McKelvey, Solid State and Semiconductor Physics (Harper and Row Publishers, New York, 1966).

[7] Y. Gogotsi, Nanomaterials Handbook: Chapter 27 (Low Dimensional Thermoelectricity) by J. P. Heremans and M. S. Dresselhaus (Taylor and Francis Group, London, 2006).

[8] L. D. Hicks and M. S. Dresselhaus, Phys. Rev. B **47**, 12727 (1993).

[9] C. J. Glassbrenner and G. A. Slack, Phys. Rev. **134**, A1058 (1964).

[10] A. H. Wilson, The Theory of Metals (Cambridge University Press, London, 1953).

[11] G. P. Srivastava, The Physics of Phonons (Taylor and Francis Group, New York, 1990).

[12] P. Debye, Vortraege Über Die Kinetische Theorie Der Materie Und Der Elektrizitaet (Teubrer, Berlin, 1914).

[13] H. B. G. Casimir, Physica **5**, 92 (1938).

[14] R. Berman, F. E. Simon, and J. M. Ziman, Proc. R. Soc. A **220**, 171 (1953).

[15] R. Berman, E. L. Foster, and J. M. Ziman, Proc. R. Soc. A **231**, 130 (1955).

[16] P. Carruthers, Rev. Mod. Phys. **32**, 92 (1961).

[17] I. Pomeranchuk, J. Phys. (USSR) **4**, 259 (1941).

[18] P. G. Klemens, Proc. Phys. Soc. A **68**, 1113 (1955).

[19] F. Seitz and D. Turnbull, Solid State Physics: Chapter by P. G. Klemens (Academic Press, New York, 1955).

[20] M. G. Holland, Phys. Rev. **134**, A471 (1964).

[21] J. E. Parrott, Rev. Int. Hautes Temp. Refract **16**, 393 (1979).

[22] C. Herring, Phys. Rev. **95**, 954 (1954).

[23] G. Leibfried and G. Schlömann, Math. Phys. K1 II(a) **4**, 71 (1954).

[24] G. Leibfried and W. Brenig, Zeitschrift für Physik **134**, 451 (1952).

[25] P. G. Klemens, Phys. Rev. **148**, 845 (1966).

[26] P. G. Klemens, J. Appl. Phys. **38**, 4573 (1967).

[27] R. A. H. Hamilton and J. E. Parrott, Phys. Rev. **178**, 1284 (1969).

[28] L. D. Landau and E. M. Lifschitz, Theory of Elasticity, (Pergamon Press, Inc., New York, 1959).

[29] J. E. Parrott, Phys. Stat. B **48**, K159 (1971).

[30] J. E. Parrott, Proc. Int. Cong. on Phonon Scattering in Solids (Paris), 27 (1972).

[31] G. P. Srivastava, Pramäna **3**, 209 (1974).

[32] G. P. Srivastava, Pramäna **6**, 1 (1976).

[33] P. G. Klemens, Solid State Phys. **7**, 1 (1958).

[34] G. P. Srivastava, Phil. Mag. **34**, 795 (1976).

[35] W. Fon, K. C. Schwab, J. M. Worlock, and M. L. Roukes, Phys. Rev. B **66**, 045302 (2002); D. T. Morelli, J. P. Heremans, and G. A. Slack, Phys. Rev. B **66**, 195304 (2002); W. Liu and A. Balandin, J. Appl. Phys. **97**, 073710 (2005).

Chapter 3

Thermoelectric Transport Theory in 2D Quantum Well Materials

As discussed in Chapter 1, the progress since the 1960s in improving thermoelectric figure of merit (ZT) had been very slow before the 1990s. The maximum value of ZT, which was found only for heavily doped semiconductors, had essentially remained around unity and research had been dwindled significantly [1]. In the 1990s, the idea of selectively modifying material properties using lower dimensional structures was introduced by Hicks and Dresselhaus [2, 3]. They theoretically showed that by using low-dimensional structures (two-, one-, or even zero-dimensional systems) one could obtain significant enhancement in ZT value, far beyond what was believed possible in bulk materials [2, 3].

Hicks and Dresselhaus focused on general theoretical models using the simplest kind of calculations, such as for a quantum confined low dimensional electron gas [2]. The results of these simple calculations implied that significant enhancement in ZT could indeed be attained within the quantum well of a superlattice when the quantum well was made of a good bulk thermoelectric material, the quan-

tum well width was sufficiently small, and the optimum carrier concentration was present. Even greater enhancement in ZT was predicted for a good thermoelectric material when prepared as a 1D quantum wire [3, 4]. This enhancement in the ZT for the low-dimensional thermoelectric materials comes from a combination of two mechanisms:

(*i*) There is a reduction in lattice thermal conductivity due to the scattering [5, 6], or to the refraction [7] of phonons at the physical boundaries of the nanoscale structure.

(*ii*) There is an increase in power factor (PF=$S^2\sigma$), or at least the avoidance of a decrease in PF through size quantization [2, 3] or through energy filtering of the electrons [8, 9].

Moreover, low dimensionality enables some materials that do not exhibit a high ZT in three dimensional cases to show high ZT value in lower dimensions [2, 3, 10]. For example, bulk Bi is a semimetal for which the contributions from electrons and holes to the Seebeck coefficient are of opposite sign and almost cancel each other, so that the net S is very small, although the contributions to S from electrons and holes are large, individually [11]. Low dimensional systems form subbands for the direction where quantum confinement occurs, and the resulting lowest quantized subband in the conduction band lies above the 3D (bulk) conduction extremum, and correspondingly the highest quantum subband in the valence band lies below the 3D valence band extremum [11]. Furthermore, as the size of the quantum well (2D), quantum wire (1D), or quantum dot (0D) decreases, the lowest conduction subband increases in the energy, and the highest valence subband decreases in the energy [11]. Therefore, the band overlap between the valence and conduction bands, which is responsible for the semimetallic behaviour of materials such as Bi, will vanish at some critical confinement size

where the semimetal-semiconductor transition occurs [11]. In the semiconducting regime, single carrier transport can be achieved, thereby enabling effective use of these materials for thermoelectric applications [11].

Stimulated by these theoretical predictions, researchers were able to fabricate nanostructures such as superlattices, nanowires, and quantum dots, forming thin-film materials for which thermoelectric properties could be measured. Soon thereafter, significantly high ZT values were reported in thin-film superlattices [5], quantum dot superlattices [12], and Silicon nanowires [13, 14]. All of these materials exhibited a decrease in lattice thermal conductivity thereby enhanced values of ZT were gained. Some researchers have also tried to use nanoparticles to increase the Seebeck coefficient by filtering out low energy electrons [15], but a net increase in ZT from this method has not been confirmed yet.

Following the procedure described in Chapter 2 for 3D bulk materials, a detailed derivation of in-plane thermoelectric transport properties (S, σ, and κ_{c}) of 2D quantum well structures will be presented using the Boltzmann equation with relaxation time approximation. Furthermore, as seen in all kinds of low-dimensional systems, quantum well structures provide additional defect-related phonon scattering mechanisms: interface mass-mixing scattering and interface dislocation scattering. Therefore, the phonon thermal conductivity (κ_{ph}) of quantum well systems will be explained in detail by taking into account of these additional interface scattering mechanisms.

Theoretical Modelling of 2D Thermoelectric Transport Coefficients

Due to the constraints imposed by carrier confinement in low-dimensional structures and the need for optimization of the carrier density for achieving a maximum value of ZT, theoretical modelling has played a significant role in the development of the field of low-dimensional thermoelectricity.

In this Chapter, the modelling is made by considering a composite system grown in z-direction of B/A/B layers of material A (comprised of n_A atomic layers of thickness a each, and total thickness d_A) and material B (comprised of n_B atomic layers of thickness b each, and total thickness d_B), with A forming a two-dimensional quantum well. For the theoretical modelling of the system we assume simple parabolic energy bands for electrons (holes) in the conduction (valence) bands. We further assume that electrons and holes occupy only the lowest j sub-bands in the quantum well. Accordingly, for quantum confinement in z direction (i.e. normal to the layer planes), the electronic dispersion relation is considered as [11]

$$E_{2\mathrm{D}}(k_x, k_y) = \frac{\hbar^2 k_x^2}{2m_x^*} + \frac{\hbar^2 k_y^2}{2m_y^*} + E_j, \tag{3.1}$$

where k_x and k_y are the propagation vector components along the axes x and y, the effective mass tensor components of the constant energy surfaces for the material are denoted as m_x^*, m_y^*, and m_z^*, and E_j is the j^{th} quantum sublevel given by

$$E_j = \frac{\hbar^2 \pi^2}{2m_z^* d_A^2} j. \tag{3.2}$$

Following the work of Lin-Chung *et al.* [16], for such a system with current flow perpendicular to the growth direction (with no loss of generality, we may take it

along x-axis) the thermoelectric transport coefficients can be written as

$$\begin{aligned} S &= \frac{d_A\sigma_A S_A + d_B\sigma_B S_B}{d_A\sigma_A + d_B\sigma_B}, \\ \sigma &= \frac{d_A\sigma_A + d_B\sigma_B}{d_A + d_B}, \\ \kappa_{\rm c} &= \frac{d_A\kappa_A + d_B\kappa_B}{d_A + d_B}, \end{aligned} \tag{3.3}$$

where the subscripts A and B label quantities in materials A and B, respectively. As discussed by Lin-Chung *et al.* [16], negligible barrier widths ($d_B \simeq 0$) in quantum wells cause a dramatic increase in ZT. Having finite barrier thicknesses, on the other hand, results in considerably reduced ZT values compared with quantum wells with $d_B \simeq 0$. The reason is that thermal and electrical currents flow along the wells as well as the barriers, and thermal current through the barriers generates a kind of parasitic channel resulting in a reduced value of ZT. By following this suggestion, we consider the limiting case of $d_B \simeq 0$ and express the thermoelectric transport coefficients as

$$S = S_A, \qquad \sigma = \sigma_A, \qquad \kappa_{\rm c} = \kappa_A. \tag{3.4}$$

3.1 Electronic Transport Properties

3.1.1 Fermi Level

To make a quantitative assessment of ZT for quantum well systems the first essential requirement is to determine the temperature as well as the quantum well width dependent Fermi level ($E_{\rm f}$).

In quantum well structures, the temperature dependence of $E_{\rm f}$ in the extrinsic regime can be calculated using the same expression given in Chapter 2 as for bulk systems [17, 18, 19], except that the confinement term $\frac{\hbar^2\pi^2}{2m_z^* d_A^2}$ should be sub-

stracted. Thus, E_{f} -T in the extrinsic regime is found as

for n-type :

$$E_{\mathrm{f}}^{\mathrm{ext,n}} = \frac{1}{2}(E_{\mathrm{c}} + E_{\mathrm{d}}) + \frac{k_{\mathrm{B}}T}{2}\ln\frac{N_{\mathrm{d}}}{2U_{\mathrm{c}}} - k_{\mathrm{B}}T\sinh^{-1}\Big[\sqrt{\frac{U_{\mathrm{c}}}{8N_{\mathrm{d}}}}\exp\Big(\frac{-\Delta E_{\mathrm{i}}^{(\mathrm{n})}}{2k_{\mathrm{B}}T}\Big)\Big] - \frac{\hbar^2\pi^2}{2m_z^* d_A^2}j,$$

for p-type :

$$E_{\mathrm{f}}^{\mathrm{ext,p}} = \frac{1}{2}(E_{\mathrm{a}} + E_{\mathrm{v}}) + \frac{k_{\mathrm{B}}T}{2}\ln\frac{N_{\mathrm{a}}}{2U_{\mathrm{v}}} - k_{\mathrm{B}}T\sinh^{-1}\Big[\sqrt{\frac{U_{\mathrm{v}}}{8N_{\mathrm{a}}}}\exp\Big(\frac{-\Delta E_{\mathrm{i}}^{(\mathrm{p})}}{2k_{\mathrm{B}}T}\Big)\Big] - \frac{\hbar^2\pi^2}{2m_z^* d_A^2}j, \tag{3.5}$$

where E_{c} is the conduction band edge, E_{v} is the valence band edge, E_{d} is the donor energy level and E_{a} is the acceptor energy level [17]. The donor and acceptor ionisation energies are determined respectively as $\Delta E_{\mathrm{i}}^{(\mathrm{n})} = E_{\mathrm{c}} - E_{\mathrm{d}}$ and $\Delta E_{\mathrm{i}}^{(\mathrm{p})} = E_{\mathrm{a}} - E_{\mathrm{v}}$ [17]. The parameters given as U_{c}=$2((m_{\mathrm{n}}^* k_{\mathrm{B}}T)/(2\pi\hbar^2))^{3/2}$ and U_{v}=$2((m_{\mathrm{p}}^* k_{\mathrm{B}}T)/(2\pi\hbar^2))^{3/2}$ where k_{B} is the Boltzmann constant [17]. N_{d} and N_{a} are the concentrations of donor impurity and acceptor impurity atoms, respectively [17]. The effective masses are represented by m_{n}^* for the electron mass and m_{p}^* for the hole mass [17].

In a doped semiconductor, beyond a sufficiently high temperature, donors at the E_{d} level (or acceptors at E_{a}) become fully ionized and the material behaves like intrinsic semiconductor [17]. In this regime the temperature dependences of E_{f} for both n- and p-type doped semiconductor quantum well structures can be expressed by subtracting the confined energy term to the bulk expression as

$$E_{\mathrm{f}}^{\mathrm{int}} = \frac{E_{\mathrm{v}} + E_{\mathrm{c}}}{2} + \frac{3}{4}k_{\mathrm{B}}T\ln\Big(\frac{m_{\mathrm{p}}^*}{m_{\mathrm{n}}^*}\Big) - \frac{\hbar^2\pi^2}{2m_z^* d_A^2}. \tag{3.6}$$

In this thesis, this presented theory is applied for n-type 0.1 wt.% CuBr doped $Bi_2Se_3/Bi_2Te_3/Bi_2Se_3$ and p-type 3 wt.% Te doped $Sb_2Te_3/Bi_2Te_3/Sb_2Te_3$ quantum well systems and neither of these systems reach the intrinsic regime in the

temperature range studied here. Therefore, all the following discussions and expressions giving in this thesis will be based on the use of the extrinsic regime only.

3.1.2 Seebeck Coefficient

As applied for 3D bulk systems in Chapter 2, thermoelectric transport coefficients in 2D quantum well structures are derived when an electric field and a temperature gradient is applied. Conditions have been taken appropriate to an isotropic solid with the diagonal components all equal and the non-diagonal components zero and assumed that all flows (flow of charge and heat current) are in the x direction. To extend the transport theory into two dimensional case the 3D density of states formula used in Chapter 2 should be replaced by an appropriate expression given for 2D dimensional systems as [11]

$$g_{\mathrm{2D}}(E) = \frac{1}{\hbar^2 \pi d_A} \sqrt{m_x^* m_y^*}. \tag{3.7}$$

Similar with 3D bulk systems, the electric current and heat flow expressions can be found by solving the Boltzmann equation as

$$\begin{aligned} i &= \mp \int_0^\infty ev f(E) g(E) dE, \\ w &= \int_0^\infty v(E - E_{\mathrm{f}}) f(E) g(E) dE, \end{aligned} \tag{3.8}$$

where $-$ sign refers to electrons and $+$ sign to holes, $-e$ is the electronic charge, v is the velocity of charge carriers in the x direction, $f(E)$ is the Fermi distribution and $E - E_{\mathrm{f}}$ represents the total energy transported by a carrier [20, 21, 22].

Using the same procedure as applied in Chaper 2, within the single-band nearly-free-electron(hole) consideration in the $x - y$ plane the in-plane electronic transport properties (S, σ, and κ_{c}) of a 2D quantum well system can be determined

in terms of the Fermi level by using Fermi-Dirac statistics. The in-plane Seebeck coefficient for 2D quantum well systems can be found by solving the linearized Boltzmann equation taking the condition as $i = 0$,

$$S = -\frac{1}{eT}\Big[\Big(\int_0^\infty Ev^2\tau g(E)\frac{\partial f_o}{\partial E}dE\Big/\int_0^\infty v^2\tau g(E)\frac{\partial f_0}{\partial E}dE\Big) - E_{\rm f}\Big], \tag{3.9}$$

where the carrier velocity and mobility for 2D systems are assumed to be $v^2 = E/\sqrt{m_x^* m_y^*}$ and $\tau = \mu_x\sqrt{m_x^* m_y^*}/e$. After some algebra, the final expression for the (in-plane) Seebeck coefficient of quantum well structures can be found as [2]

$$S = \pm\frac{k_{\rm B}}{e}\Big[\frac{2F_1}{F_o} - \frac{E_{\rm f}}{k_{\rm B}T}\Big], \tag{3.10}$$

where the plus and minus signs are for p- and n-type semiconductor quantum well systems and the Fermi integral is given as [2]

$$F_i = \int_0^\infty \frac{x^i dx}{e^{(x-\zeta^*)}+1}. \tag{3.11}$$

3.1.3 Electrical Conductivity

As reported for 3D bulk systems, the same $\frac{\partial T}{\partial x} = 0$ condition can be used to find the in-plane electrical conductivity expression for 2D quantum well structures together with the carrier velocity and mobility expressions given in previous section. Therefore, for 2D quantum well systems the electrical conductivity can be found as

$$\sigma = \frac{i}{\mathcal{E}} = -e^2\int_0^\infty v^2\tau g(E)\frac{\partial f_0}{\partial E}dE. \tag{3.12}$$

After substituding the required v^2 and μ expressions, the final electrical conductivity expression for quantum well systems in the extrinsic regime can be found in terms of the Fermi integral as [2]

$$\sigma = e\mu_x\frac{1}{\hbar^2\pi d_A}\sqrt{m_x^* m_y^*}(k_{\rm B}T)F_0. \tag{3.13}$$

3.2 Thermal Transport Coefficients

3.2.1 Electronic Thermal Conductivity

Using the same condition as for the Seebeck coefficient ($i = 0$) the in-plane electronic thermal conductivity of quantum well structures can be described as

$$\begin{aligned}\kappa_{\mathrm{c}} &= -\frac{w}{\partial T/\partial x} \\ &= -\int_0^\infty v^2 E g(E)\tau \frac{\partial f_0}{\partial E} \underbrace{\frac{\partial E_{\mathrm{f}}/\partial x}{\partial T/\partial x}}_{=eS} dE - \int_0^\infty v^2 \frac{E^2}{T} g(E)\tau \frac{\partial f_0}{\partial E} dE \\ &+ \int_0^\infty v^2 E \frac{E_{\mathrm{f}}}{T} g(E)\tau \frac{\partial f_0}{\partial E} dE.\end{aligned} \tag{3.14}$$

By doing some substitutions, the final expression of electronic thermal conductivity can be written in terms of the Fermi integral as [2]

$$\kappa_{\mathrm{c}} = \frac{\mu_x}{e} \frac{1}{\hbar^2 \pi d_A} \sqrt{m_x^* m_y^*} (k_{\mathrm{B}} T)^2 k_{\mathrm{B}} \Big[3F_2 - 4\frac{F_1^2}{F_0} \Big]. \tag{3.15}$$

3.2.2 Bipolar Thermal Conductivity

The electron-hole pair contribution (κ_{bp}) to the total thermal conductivity becomes a significant thermal conductivity contribution above room temperature for small band gap semiconductors. As discussed in Chapter 2, this contribution can be expressed as [18, 19]

$$\kappa_{\mathrm{bp}} = F_{\mathrm{bp}} T^p \exp(-E_{\mathrm{g}}/2k_{\mathrm{B}}T), \tag{3.16}$$

with F_{bp} and p regarded as adjustable parameters. The only difference in the κ_{bp} expression between bulk and quantum well structures originates from the definition of the band gap E_{g} due to the confinement effects on electron and hole energy levels in the latter structure. For a given value of quantum well thickness

d_A, the band gap of the system can be expressed as

$$E_{\rm g}({\rm QW}) = E_{\rm c} - E_{\rm v} + \frac{\hbar^2\pi^2}{2d_A^2}\Big(\frac{1}{m^*_{z,e}} + \frac{1}{m^*_{z,h}}\Big), \tag{3.17}$$

where the effective masses of electrons and holes in the growth direction are $m^*_{z,e}$ and $m^*_{z,h}$, respectively.

3.2.3 Phonon Thermal Conductivity

As applied for 3D bulk systems in Chapter 2, Debye's isotropic continuum approximation is used to determine the lattice thermal conductivity of 2D quantum well systems within the single-mode relaxation time scheme. Therefore, $\kappa_{\rm ph}$ for quantum wells is expressed with the same expression given as [23]

$$\kappa_{\rm ph} = \frac{\hbar^2 q_D^5}{6\pi^2 k_{\rm B} T^2} \sum_s c_s^4 \int_0^1 dx x^4 \tau \bar{n}(\bar{n}+1), \tag{3.18}$$

where q_D is the Debye radius, $x = q/q_D$ is a reduced wavenumber, s is phonon polarisation index, $\bar{n}$ is the Bose-Einstein distribution function, c_s is the velocity of phonons defined for polarisation branch s. The phonon relaxation time in Eq. (3.18) is contributed by several scattering mechanisms: boundary (bs), carriers (carr), mass defects (md), interface mass-mixing (ims), interface dislocation (ids) and anharmonicity (anh). The total phonon relaxation rate is defined by using Matthiessen's rule as τ^{-1}=$\sum_i \tau_i^{-1}$ with τ_i^{-1} representing contribution from $i^{\rm th}$ scattering mechanism.

In Chapter 2, phonon scattering rates orginated from sample boundaries, carriers and mass defects (both from isotopes and alloying effect) have already been discusssed in detail for 3D bulk systems and the same expressions will be used for 2D quantum well structures studied here. Additional to these scattering mechanisms low dimensional solids (quantum wells for this thesis) provide extra defect-related phonon scattering mechanisms: interface mass-mixing scattering (ims)

due to diffusion or mixing of atoms across interfaces, and interface dislocation scattering (ids) which results from dislocations or missing bonds present at interfaces. Finally, anharmonic scattering mechanism for quantum well structures should be re-expressed by taking into account of the confinement effect.

(*i*) ***Mass-mixing Scattering (ims)***:

Several different considerations have been made to calculate the probability and amount of mass-interdiffusion between layers. For instance, in the work of Landry *et al.* [24], they randomly chose hyperbolic tangent form for the variance of mass-mixing across the interface. Hepplestone and Srivastava [25, 26] presented another scheme in which the total mass-mixing decreases as the inverse square distance from an interface. In this thesis, the basic theory adopted by Hepplestone and Srivastava [25, 26] will be followed, but the probability of layer mixing will be choosen to decrease exponentially from an interface. Thus, the interface mass-mixing scattering rate is expressed as

$$\tau_{qs}^{-1}(\mathrm{ims}) = \frac{\Gamma_{\mathrm{ims}}\Omega}{4\pi\bar{c}^3}\omega^4(qs), \tag{3.19}$$

with the mass-mixing parameter for a quantum well system given as

$$\Gamma_{\mathrm{ims}} = \frac{2\beta_0}{(n+m)}\sum_i \exp\Big(-\Big|\frac{l_i - l_0}{d}\Big|\Big)\Big(\frac{\Delta M_i}{\bar{M}}\Big)^2\Big[\Big(1-\frac{e_A^2}{e_B^2}\Big)^2 + \Big(1-\frac{e_B^2}{e_A^2}\Big)^2\Big], \tag{3.20}$$

where d is the interlayer distance (a in the well and b in the barrier), l_i is the layer distance from interface, l_0 is the z coordinate of the interface, β_0 is the mass-mixing fraction at distance nd or md from the interface, and e_B/e_A is the ratio of the amplitudes of eigenvectors in materials B and A.

(*ii*) ***Interface Dislocation Scattering***:

In quantum well structures there may also be broken bonds, especially lines of broken bonds, close to the interface. Phonon scattering rate by such dislocations cannot adequately be described by the traditional theory for bulk solids. While the phonon scattering rate by dislocations in bulk has traditionally been derived by treating solids as elastic continuum [27], an atomic scale theory is required when dealing with scattering from interface dislocations. Following the same procedure as outlined by Hepplestone and Srivastava [25, 26], the phonon relaxation rate due to interface dislocation scattering is exppressed as

$$\tau_{qs}^{-1}(\text{ids}) = \frac{\Gamma_{\text{ids}}\Omega}{8\pi\bar{c}^3}\omega_0^4, \tag{3.21}$$

where ω_0 can be approximated as the highest zone-centre frequency ($\omega_0 = \omega_D = \bar{c}.q_D$) and the interface dislocation parameter is written as

$$\Gamma_{\text{ids}} = \frac{2\beta_0^{'}}{(n+m)}\sum_i \exp\Big(-\Big|\frac{l_i - l_0}{d}\Big|\Big)\Big(\frac{\Delta M_i}{\bar{M}}\Big)^2\Big[1 + \Big(\frac{e_A^2}{e_B^2}\Big)^2 + 1 + \Big(\frac{e_B^2}{e_A^2}\Big)^2\Big], \tag{3.22}$$

with $\beta_0^{'}$ being the fraction of broken bonds in the interface region.

The amplitude ratio e_B/e_A required for both interface mass-mixing and dislocation scattering mechanisms is approximated using the diatomic linear chain model along the growth direction and expressed as [23]

$$\frac{e_B}{e_A} = \frac{\Big[\frac{1}{M_0} - \Delta\Big(\frac{1}{M}\Big)\Big]\cos(l_z q_z)}{\Big\{\Big(\frac{1}{M_0}\Big)^2\cos^2(l_z q_z) + \Big[\Delta\Big(\frac{1}{M}\Big)\Big]^2\sin^2(l_z q_z)\Big\}^{1/2} - \Delta\Big(\frac{1}{M}\Big)}, \tag{3.23}$$

with $1/M_0 = \frac{1}{2}(1/M_A + 1/M_B)$, $\Delta(1/M) = \frac{1}{2}(1/M_A - 1/M_B)$ and $l_z = d_A + d_B$ is the period along the growth direction. The ratio of amplitudes increases in magnitude with increasing wave vector, q_z. This leads to the expected result that the interface will weakly scatter long wavelength modes. When the ratio of amplitudes is very large, then the two layers in each quantum well and barrier unit cell

act out of phase and hence traveling phonons are scattered more strongly by the presence of the interfaces.

(*iii*) ***Anharmonic Phonon Scattering***:

In this thesis, the consideration of the anharmonic phonon scattering mechanism in quantum well systems is based on Srivastava's scheme for bulk systems by restricting ourselves to only three-phonon interaction. This scattering rate is expressed as [23]

$$\tau_{qs}^{-1}(\text{anh, bulk}) = \frac{\hbar q_D^5 \gamma^2}{4\pi\rho\bar{c}^2} \sum_{s's''\varepsilon} \Bigg[\int dx' x'^2 x''_+ [1 - \varepsilon + \varepsilon(Cx + Dx')] \frac{\bar{n}_{q's'}(\bar{n}''_+ + 1)}{(\bar{n}_{qs} + 1)} + \frac{1}{2} \int dx' x'^2 x''_- [1 - \varepsilon + \varepsilon(Cx - Dx')] \frac{\bar{n}_{q's'}\bar{n}''_-}{\bar{n}_{qs}} \Bigg], \tag{3.24}$$

where γ is the Grüneisen constant, $x' = q'/q_D$, x''_+=$Cx \pm Dx'$, $\bar{n}''_\pm = \bar{n}(x''_\pm)$, $C = c_s/c_{s''}$, $D = c_{s'}/c_{s''}$. $\varepsilon = 1$ for momentum-conserving Normal processes, and ε=-1 for momentum-nonconserving Umklapp processes. The first and second terms in equation (3.24) are controlled by class 1 events $\mathbf{q}s + \mathbf{q}'s' \rightarrow \mathbf{q}''s''$ and class 2 events $\mathbf{q}s \rightarrow \mathbf{q}'s' + \mathbf{q}''s''$, respectively. The integration limits on the variables x and x', derived from a detailed consideration of the energy and momentum conservation requirements, have been presented in Ref. [23] elaborately.

Equation (3.24) is only valid for the materials containing only one atom per primitive unit cell, namely for bulk systems. When the number of atoms increases in a unit cell, Eq. (3.24) should be re-written owing to increased amount of anharmonic scattering strength.

In a temperature range where only phonon phonon interactions (via Umklapp processes) are important the lattice thermal conductivity of a solid in this temper-

ature regime have been discussed by Slack [28] and Berman [29] and expressed as

$$\kappa_{\rm ph} = Y\frac{M_a\theta_a^3\Omega^{1/3}}{\gamma^2 T}, \tag{3.25}$$

where M_a is the atomic mass of the atom, θ_a is a Debye temperature for an acoustic phonon branch ($\theta_a = \frac{\hbar\omega_D}{k_{\rm B}}$) and Y is a constant. This expression is valid for structures containing only one atom per primitive unit cell. Using a simple counting scheme, Slack [28] extended the model to crystals with n atoms per unit cell as

$$\kappa_{\rm ph} = Y\frac{\bar{M}_a\theta_a^3\Omega^{1/3}n^{1/3}}{\gamma^2 T}. \tag{3.26}$$

In many circumstances, especially in considering new materials and crystal structures, the phonon dispersion relations used to calculate θ_a are not available either experimentally or theoretically. In these cases, the acoustic mode Debye temperature can be determined from the "traditional" definition of the Debye temperature θ_D by using [30]

$$\theta_a = \theta_{\rm D} n^{-1/3}. \tag{3.27}$$

By increasing the atomic layers (n) for the materials, the size of the unit cell in real space increases which means that the Brillouin zone boundary moves inward, thus cutting off phonon frequencies at smaller values as n increases [30, 31]. The "traditional" Debye temperature $\theta_{\rm D}$ depends on the atomic mass and the bond strength but is independent of n. Thus, Eq. (3.26) can be rewritten to display the explicit n-dependence of the thermal conductivity as [30, 31]

$$\kappa_{\rm ph} = Y\frac{\bar{M}_a\theta_D^3\Omega^{1/3}}{\gamma^2 T n^{2/3}}. \tag{3.28}$$

On the basis of Eq. (3.28) we may now model the anharmonic phonon scattering rate for quantum well systems as [30, 31]

$$\tau_{qs}^{-1}({\rm anh,QW}) = \tau_{qs}^{-1}({\rm anh,bulk})(n_A + n_B)^{2/3}, \tag{3.29}$$

including the atomic layers n_A and n_B of material A and B, respectively.

Bibliography

[1] D. M. Rowe, Thermoelectrics Handbook Macro to Nano (Taylor and Francis Group, London, 2006).

[2] L. D. Hicks and M. S. Dresselhaus, Phys. Rev. B **47**, 12727 (1993).

[3] L. D. Hicks and M. S. Dresselhaus, Phys. Rev. B **47**, 16631 (1993).

[4] L. D. Hicks, The Effect of Quantum Well Superlattices on the Thermoelectric figure of Merit, Ph.D. Thesis, Massachusetts Institute of Technology, department of Physics (1996).

[5] R. Venkatasubramanian, E. Siivola, T. Colpitts, and B. O'Quinn, Nature **413**, 597 (2001).

[6] N. V. Simkin and G. D. Mahan, Phys. Rev. Lett. **84**, 927 (2000).

[7] C. Dames, M. S. Dresselhaus, and G. Chen, in Thermoelectric Materials 2003 - Research and Applications: MRS Symposium Proceedings, Boston, December 2003, G. S. Nolas, J. Yang, T. P. Hogan, D. C. Johnson, Materials Research Society Press, Pittsburgh, 15 (2004).

[8] D. Vashaee and A. Shakouri, Phys. Rev. Lett. **92**, 106103 (2004).

[9] J. P. Heremans, C. M. Thrush, and D. T. Morelli, Phys. Rev. B **70**, 115334 (2004).

[10] L. D. Hicks, T. C. Harman, and M. S. Dresselhaus, Appl. Phys. Lett. **63**, 3230 (1993).

[11] T. M. Tritt, Recent Trends in Thermoelectric Materials Research III (Academic Press, London, 2001).

[12] T. C. Harman, P. J. Taylor, M. P. Walsh, and B. E. LaForge, Science **297**, 2229 (2002).

[13] A. I. Hochbaum, R. Chen, R. D. Delgado, W. Liang, E. C. Garnett, M. Najarian, A. Majumdar, and P. Yang, Nature **451**, 163 (2008).

[14] A. I. Boukai, Y. Bunimovich, J. Tahir-Kheli, J. -K. Yu, W. A. Goddard Iii, and J. R. Heath, Nature **451**, 168 (2008).

[15] W. Kim, J. Zide, A. Gossard, D. Klenov, S. Stemmer, A. Shakouri, and A. Majumdar, Phys. Rev. Lett. **96**, 045901 (2006).

[16] P. J. Lin-Chung and T. L. Reinecke, Phys. Rev. B **51**, 13244 (1995).

[17] J. P. McKelvey, Solid State and Semiconductor Physics (Harper and Row Publishers, New York, 1966).

[18] Ö. C. Yelgel and G. P. Srivastava, Phys. Rev. B **85**, 125207 (2012).

[19] Ö. C. Yelgel and G. P. Srivastava, J. Appl. Phys. **113**, 073709 (2013).

[20] T. M. Tritt, Thermal Conductivity: Theory, Properties, and Applications (Kluwer Academic/Plenum Publishers, New York, 2004).

[21] P. Y. Yu, Fundamentals of Semiconductors: Physics and Materials Properties (Springer, London, 2010).

[22] Y. Gogotsi, Nanomaterials Handbook: Chapter 27 (Low Dimensional Thermoelectricity) by J. P. Heremans and M. S. Dresselhaus (Taylor and Francis Group, London, 2006).

[23] G. P. Srivastava, The Physics of Phonons (Taylor and Francis Group, New York, 1990).

[24] E. S. Landry and A. J. H. McGaughey, Phys. Rev. B **79**, 075316 (2009).

[25] S. P. Hepplestone and G. P. Srivastava, Phys. Rev. B **82**, 144303 (2010).

[26] S. P. Hepplestone and G. P. Srivastava, Phys. Rev. B **84**, 115326 (2011).

[27] J. M. Ziman, Electrons and Phonons (Oxford, Clarendon, 1960).

[28] G. A. Slack, Solid St. Phys. **34**, 1 (1979); G. A. Slack, J. Phys. Chem. Solids **34**, 321 (1973).

[29] R. Berman, Thermal Conduction in Solids (Clarendon Press, Oxford, 1976).

[30] O. L. Anderson, J. Phys. Chem. Solids **12**, 41 (1959).

[31] S. L. Shinde and J. S. Goela, High Thermal Conductivity Materials (Springer, New York, 2006).

Chapter 4

Thermoelectric Properties of n-type $Bi_2(Te_{0.85}Se_{0.15})_3$ Single Crystals Doped with CuBr and SbI_3

4.1 Introduction

As discussed in Chapter 1, to find the best thermoelectric material, it is required to investigate it's thermoelectric efficiency which is assessed in terms of the dimensionless figure of merit ZT as

$$ZT = \frac{\sigma S^2}{\kappa} T, \tag{4.1}$$

where S is the Seebeck coefficient, σ is the electrical conductivity and κ is the total thermal conductivity which has three contributions: carriers (electrons for this chapter) (κ_{el}), lattice (*i.e.* from phonons, κ_{ph}), and bipolar (*i.e.* from electron-hole pairs, κ_{bp}).

There are limited choices for finding materials in nature that exhibit high figure

of merit (*i.e.* with $ZT > 1$). Previous researches have concluded that doped semiconductor alloys with high carrier concentration are among the best bulk thermoelectrics [1]. Two examples are the Bi_2Te_3-Bi_2Se_3 or Si-Ge alloys (two isostructural semiconductors), which with strong point defect scattering exhibit low phonon thermal conductivity, and are the best commercially available thermoelectric materials [1].

In this chapter, thermoelectric properties of n-type 85% Bi_2Te_3 - 15% Bi_2Se_3 single crystal doped with 0.1 wt.% CuBr and 0.2 wt.% SbI_3 samples are investigated theoretically and calculated results are compared with the experimental values obtained by Hyun *et al.* [2].

4.2 Theoretical Considerations

In order to make a quantitative assessment of ZT for a given material, and prediction for other materials (such as alloys of two materials with different fractional contents), it is important to develop accurate theoretical models for the thermoelectric transport coefficients (S, σ, $\kappa_{\rm el}$, $\kappa_{\rm bp}$, and $\kappa_{\rm ph}$). A large number of publications have been devoted in this respect and particularly three groups [3, 4, 5] have provided a reasonably complete account of all the transport coefficients governed by carriers in semiconductors and their alloys. Their works, however, do not explicitly discuss cases of extrinsically doped and intrinsic (undoped) semiconductors and do not account for temperature variation of Fermi level. Furthermore, all previous works have treated phonon transport (lattice thermal conductivity $\kappa_{\rm ph}$) in an *ad hoc* manner, using simplified expressions for alloying and anharmonic phonon interactions, utilising several adjustable parameters. The approaches in Refs. [3, 4] do not distinguish between phonon scattering due to point (i.e. iso-

topic) defects and phonon scattering due to alloying effect. The work in Ref. [3] treats the effect of anharmonic phonon interaction in $\kappa_{\rm ph}$ using a combination of adjustable parameters and an interpolative scheme. Vining [4], on the other hand, uses the frequency and temperature dependence of the form $\omega^2 T^3$ for the Umklapp three-phonon scattering rate and expresses the Normal three-phonon scattering rate as a scaled version of the former. These considerations are normally valid in a limited low-temperature range and expressions for both Umklapp and Normal scattering rates must be reformulated for computation of high-temperature $\kappa_{\rm ph}$. As the role of $\kappa_{\rm ph}$ is regarded as much more important than the role of other transport coefficients in enhancing ZT for low-dimensional semiconductors [6, 7, 8, 9, 10], it is very important to use a well-founded theory of $\kappa_{\rm ph}$ that includes anharmonic phonon interactions without the need for many adjustable parameters.

As mentioned in Chapter 2, based on the temperature dependent Fermi level we develop a theory for the thermoelectric properties of 3D bulk materials. The expressions of electronic transport coefficients (S, σ, and $\kappa_{\rm el}$), $\kappa_{\rm bp}$, and $\kappa_{\rm ph}$ is described by following the Hicks-Dresselhaus theory [5], Price's theory [11], and Srivastava's detailed theory [12], respectively.

4.2.1 Electronic Properties

4.2.1.1 Fermi Level

The electronic transport coefficients S, σ and $\kappa_{\rm el}$ required for an evaluation of the thermoelectric figure of merit ZT for a semiconductor depend on the temperature dependence of the Fermi level $E_{\rm f}$. In the extrinsic regime, as described in Chapter 2, the temperature variation of the Fermi level for an n-doped semiconductor is

given by [13]

$$E_{\mathrm{f}}^{\mathrm{ext}} = \frac{1}{2}(E_{\mathrm{c}} + E_{\mathrm{d}}) + \frac{k_{\mathrm{B}}T}{2}\ln\frac{N_d}{2U_c} - k_{\mathrm{B}}T\sinh^{-1}\Big(\sqrt{\frac{U_c}{8N_d}}\exp(\frac{-\Delta E_i}{2k_{\mathrm{B}}T})\Big), \tag{4.2}$$

where E_{c} is the conduction band edge, E_{d} is the donor energy level, N_d is the concentration of donor impurity atoms, $\Delta E_i = E_{\mathrm{c}} - E_{\mathrm{d}}$ is the donor ionisation energy, U_c=2$((m_n^* k_{\mathrm{B}}T)/(2\pi\hbar^2))^{3/2}$, with m_n^* as the electron mass, k_{B} is the Boltzmann constant, and $\hbar$ is the reduced Planck's constant.

Beyond a sufficiently high temperature, donors at the E_{d} level are completely ionised and the material becomes an intrinsic semiconductor, and consequently the temperature variation of the Fermi level is given by [13]

$$E_{\mathrm{f}}^{\mathrm{int}} = \frac{E_{\mathrm{v}} + E_{\mathrm{c}}}{2} + \frac{3}{4}k_{\mathrm{B}}T\ln\Big(\frac{m_p^*}{m_n^*}\Big), \tag{4.3}$$

where E_{v} is the valence band edge and m_p^* is hole effective mass. With conduction band edge set to zero (E_{c}=0), Eq. (4.3) can be written in terms of the energy gap E_{g}. We have attempted a simple expression [14] of the form $E_{\mathrm{g}}(T) = E_{\mathrm{g}}(0) - \alpha T$, with α considered as an adjustable parameter, to obtain the best fit for the temperature variation of E_{f} , S and σ in the intrinsic regime. With this choice, the Fermi level in the intrinsic regime can be re-expressed as

$$E_{\mathrm{f}}^{\mathrm{int}} = -\frac{1}{2}(E_{\mathrm{g}}(0) - \alpha T) + \frac{3}{4}k_{\mathrm{B}}T\ln\Big(\frac{m_p^*}{m_n^*}\Big). \tag{4.4}$$

4.2.1.2 Seebeck Coefficient

As given in Chapter 2, within a single-band nearly-free-electron consideration, the Seebeck coefficient (S) and the electrical conductivity (σ) can be defined in terms of Fermi energy by using Fermi-Dirac statistics. Accordingly, Seebeck coefficient of n-type materials is written as [14, 15]

$$S = -\frac{k_{\mathrm{B}}}{e}(\delta - \zeta^*), \tag{4.5}$$

where $\zeta^* = E_f/k_B T$ is the reduced chemical potential, and δ is given by [14, 15]

$$\delta = \frac{(r+\frac{5}{2})F_{r+\frac{3}{2}}(\zeta^*)}{(r+\frac{3}{2})F_{r+\frac{1}{2}}(\zeta^*)}, \tag{4.6}$$

by considering that charge carriers (electrons for present work) are scattered in such a way that their relaxation time (τ) may be expressed in terms of the energy (E) with the relation of $\tau = \tau_0 E^r$ where τ_0 and r are constants. In particular, r is called the scattering parameter which is taken as 0.1 from the work of Hyun *et al.* [2]. The Fermi integral required for the above equation is given as [5]

$$F_i = \int_0^\infty \frac{x^i dx}{e^{(x-\zeta^*)}+1}. \tag{4.7}$$

4.2.1.3 Electrical Conductivity

Similarly, within the single-band nearly-free-electron model, the electrical conductivity in the extrinsic regime of a semiconductor can be expressed as [14, 16]

$$\sigma = Ne\mu_c = n\frac{e^2}{m_c^*}\langle\tau\rangle, \tag{4.8}$$

where μ_c is the conductivity mobility, m_c^* is the conductivity effective mass (taken as m_n^*), $\langle\tau\rangle$ is an average relaxation time for carriers, and N is the carrier concentration defined as [16, 15],

$$N = \int_0^\infty g(E)f_0(E)dE = \frac{4}{\sqrt{\pi}}\Big(\frac{m_D^* k_B T}{2\pi\hbar^2}\Big)^{3/2} F_{1/2}(\zeta^*), \tag{4.9}$$

with $g(E)$ representing the density of states for nearly free electron gas, $f_0(E)$ representing the Fermi-Dirac distribution function, and m_D^* as the density of states effective mass.

In n-type doped single crystals electrons mostly interact with the long wavelength phonons (which have low energy). The scattering rate for the dominant scattering involving acoustic phonons can be written as [15, 17]

$$\tau_{ac}^{-1}(E,T) = \frac{\sqrt{2}}{\pi}\frac{E_D^2 {m_D^*}^{3/2} k_B T}{\hbar^4 \rho c_L^2}\sqrt{E}, \tag{4.10}$$

where c_L is the velocity of longitudinal phonons, ρ is the mass density, and E_D is the deformation potential. Using this, we express the average relaxation time as [16],

$$\langle \tau \rangle = \frac{\int \tau(W) W^{3/2} \exp(-W) \mathrm{d}W}{\int W^{3/2} \exp(-W) \mathrm{d}W} = \frac{4}{3}\sqrt{\frac{\pi}{2}} \frac{\hbar^4 \rho c_L^2}{E_D^2 {m_D^*}^{3/2} (k_\mathrm{B}T)^{3/2}}, \tag{4.11}$$

with $W = E/k_\mathrm{B}T$.

Thus, from Eqs. (4.8, 4.9), and (4.11) the electrical conductivity in the extrinsic regime can be written as

$$\sigma_\mathrm{extrinsic} = \frac{4}{3\pi\sqrt{\pi}} \frac{e^2}{m_c^*} \frac{\hbar \rho c_L^2}{E_D^2} F_{1/2}, \tag{4.12}$$

when only acoustic phonon scattering is considered.

As mentioned in Chapter 2 previously, the electrical conductivity expression in the intrinsic regime can be expressed as [13, 18],

$$\sigma_\mathrm{intrinsic} = A^{'} e^{-E_g/2k_\mathrm{B}T}, \tag{4.13}$$

where $A^{'}$ as a parameter that does not strongly depend on temperature.

4.2.2 Thermal Properties

In this chapter, the total thermal conductivity (κ) has three contributions: electronic (κ_el), lattice (*i.e.* from phonons, κ_ph), and bipolar (*i.e.* from electron-hole pairs, κ_bp).

4.2.2.1 Electronic Thermal Conductivity

The electronic part of the thermal conductivity can be described by the Wiedemann-Franz law as [14]

$$\kappa_{\mathrm{el}} = \sigma \mathcal{L} T = \left(\frac{k_{\mathrm{B}}}{e}\right)^2 \sigma T \mathcal{L}_0, \tag{4.14}$$

where $\mathcal{L}$ is the Lorenz number and $\mathcal{L}_0$ can be written in terms of the scattering parameter (r) and the Fermi integral as [14, 15, 2]

$$\mathcal{L}_0 = \frac{\left(r+\frac{7}{2}\right)F_{r+\frac{5}{2}}(\zeta^*)}{\left(r+\frac{3}{2}\right)F_{r+\frac{1}{2}}(\zeta^*)} - \left[\frac{\left(r+\frac{5}{2}\right)F_{r+\frac{3}{2}}(\zeta^*)}{\left(r+\frac{3}{2}\right)F_{r+\frac{1}{2}}(\zeta^*)}\right]^2. \tag{4.15}$$

4.2.2.2 Bipolar Thermal Conductivity

In small band gap semiconductors such as Bi_2Te_3, the bipolar (electron-hole pair) thermal conductivity (κ_{bp}) becomes a dominant contribution above 300 K. As derived in Chapter 2, this contribution can be expressed in terms of the energy band gap as

$$\kappa_{\mathrm{bp}} = F_{\mathrm{bp}} T^p \exp(-E_g/2k_B T), \tag{4.16}$$

regarding F_{bp} and p as adjustable parameters changing with doping type.

4.2.2.3 Lattice Thermal Conductivity

As described in Chapter 2, within the single-mode relaxation time approximation, and adopting Debye's isotropic continuum scheme, the lattice thermal conductivity of 3D bulk materials is expressed as [12]

$$\kappa_{\mathrm{ph}} = \frac{\hbar^2 q_D^5}{6\pi^2 k_B T^2} \sum_s c_s^4 \int_0^1 dx x^4 \tau \bar{n}(\bar{n}+1), \tag{4.17}$$

where q_D is the Debye radius, $x = q/q_D$ is a reduced wavenumber, s is phonon polarisation index (*i.e.* indicates longitudinal and transverse branches), $\bar{n}$ is the

Bose-Einstein distribution function, and c_s is the velocity of phonons in polarisation s.

In Eq. (4.17), the phonon relaxation time (τ) is governed by different scattering mechanisms and within Matthiessen's rule the total phonon scattering rate is obtained as $\tau^{-1} = \sum_i \tau_i^{-1}$ where τ_i^{-1} represents contributions from ith scattering mechanism. Required phonon scattering rates for this chapter are: boundary scattering, mass-difference scattering (sourced from both isotopic point defects and mass difference due to alloying), donor electrons and phonons scattering, and phonon-phonon scattering. All these scattering mechanisms have been described in Chapter 2 and the same expressions given in that chapter will be used for this present chapter.

4.3 Results of Calculations and Discussion

To investigate the effect of doping and dopant type on thermoelectric figure of merit, results for $Bi_2(Te_{0.85}Se_{0.15})_3$ single crystal have been compared with 0.1 wt.% CuBr and 0.2 wt.% SbI_3 dopants.

Relevant parameters used in this chapter have been compiled in Tab. 4.1. All integrals were evaluated numerically by employing Simpson's rule.

4.3.1 Electronic Properties

Fermi Level:

The theoretical calculation of Fermi level-temperature curves for 0.1 wt.% CuBr and 0.2 wt.% SbI_3 doped $Bi_2(Te_{0.85}Se_{0.15})_3$ single crystals are presented in Fig. 4.1. For comparison, the Fermi level values extracted by Hyun *et al.* [2] from their experimental measurements of the Seebeck coefficient is also shown. Based upon an analysis of the Seebeck coefficient and electrical resistivity, Hyun *et al.* find these two samples to exhibit the extrinsic behaviour for the entire temperature range studied here. However, using the parameters listed in Tab. 4.1, and as seen in Fig. 4.1, it is found that the extrinsic regime ceases at around 500 K and 450 K for the CuBr- and SbI_3-doped samples, respectively. The inset in Fig. 4.1 shows the temperature variation of E_{f} by considering both samples as extrinsic.

In the extrinsic regime following Eq. (4.2), below 450 K for SbI_3 doped sample and below 500 K for CuBr doped sample, the Fermi level gently increases with temperature. At a given temperature, the Fermi level is closer to the valence band edge for CuBr-doped sample than for the SbI_3-doped sample. This is because CuBr is a more efficient dopant and, despite a lower doping level, provides a higher concentration (N_d) of halogen donor atoms. For both samples, the weak temperature variation of E_{f} in the extrinsic regime is due to the opposite signs of terms 2 and 3 in Eq. (4.2).

In the intrinsic regime, E_{f} rises faster with temperature. It is found that the parameter α, determining the temperature variation of the band gap, is the decisive factor to match theory with experimentally deduced results. The difference in the extrinsic-intrinsic turn-over temperatures for the two samples is due to the joint effect of N_d in extrinsic regime and the $E_{\mathrm{g}} - T$ variation in intrinsic regime.

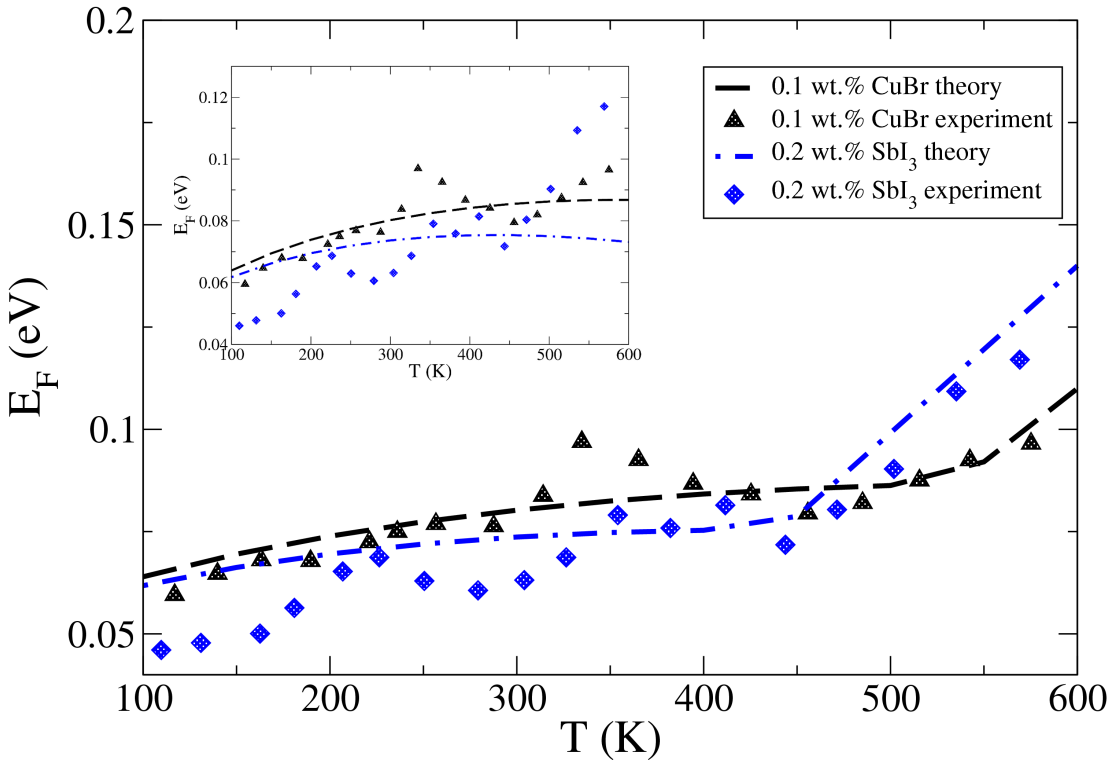

Figure 4.1: Temperature variation of Fermi level for $Bi_2(Te_{0.85}Se_{0.15})_3$ single crystal doped with 0.1 wt.% CuBr (dashed curve) and 0.2 wt.% SbI_3 (dash-dotted curve). The symbols represent the results obtained from experimental measurements of Seebeck coefficient by Hyun *et al.* [2]. The inset shows the results by treating the samples as extrinsically doped throughout the entire temperature range. The bottom of the conduction band is taken as the zero along the energy axis (i.e. $E_c = 0$).

Seebeck Coefficient:

Theoretical results for the Seebeck coefficient, shown in Fig. 4.2, are in reasonably good agreement with the experimentally measured values in the work of Hyun *et al.* [2]. It was expected that the temperature variation of the Seebeck coefficient of the CuBr and SbI_3 doped $Bi_2(Te_{0.85}Se_{0.15})_3$ single crystals to directly reflect the extrinsic-intrinsic turn-over obtained for the corresponding $E_{\rm f}$. This is indeed what is found, as shown in Fig. 4.2. In the temperature region 100 - 450 K (*viz.* the extrinsic regime), the Seebeck coefficient depends on the Fermi level directly (the second term in Eq. (4.5)) and via the Fermi integrals $F_{1/2}$ and $F_{3/2}$ (the first term in Eq. (4.5)). Throughout this temperature range an asymptotic expansion of the Fermi integrals can be made [19]. As $\zeta^* > 1$, using the appropriate asymptotic expansion it can shown that δ, the first term in Eq. (4.5), also varies linearly with the Fermi level. Two points can be made from this simple analysis. Firstly, the temperature variation of S seen in Fig. 4.2, thus, is nearly similar to that of the Fermi level. Secondly, following the variation of $E_{\rm f}$, the difference in S increases with temperature.

In accordance with the $E_{\rm f} - T$, in the intrinsic regime the temperature variation of the Seebeck coefficient is much sharper for the SbI_3 doped sample. While the values of the S are similar for the two samples up to 450 K, results for the SbI_3 doped sample become progressively lower as temperature increases inside the intrinsic regime. At 600 K, the computed value for the SbI_3 doped sample is 12.4% lower than that for the CuBr doped sample.

The inset in Fig. 4.2 shows the S results by treating the samples to exhibit the extrinsic behaviour throughout the temperature range. While the CuBr-doped sample may reasonably well be treated as being extrinsic, the SbI_3-doped sample must be treated as intrinsic above 450 K.

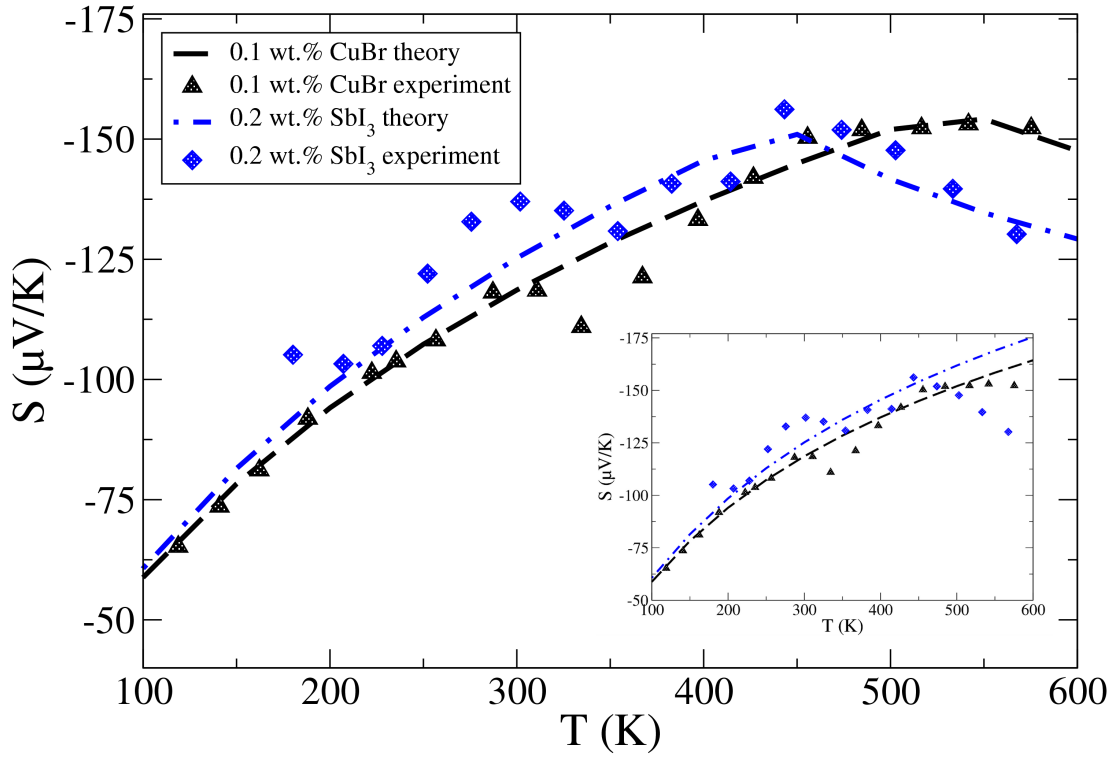

Figure 4.2: Temperature variation of Seebeck coefficient for $Bi_2(Te_{0.85}Se_{0.15})_3$ single crystal doped with 0.1 wt.% CuBr (dashed curve) and 0.2 wt.% SbI_3 (dash-dotted curve). The symbols represent the experimental results from Ref. [2]. The inset shows the results by treating the samples as extrinsically doped throughout the entire temperature range.

Electrical Resistivity:

The electrical resistivity results of CuBr and SbI_3 doped alloys are shown in Fig. 4.3 with their reported experimental results by Hyun *et al.* [2].

To calculate the electrical resistivity in the extrinsic regime a number of different scattering mechanisms, arising from phonons (acoustic and optical phonon scatterings) and imperfections (neutral impurities, ionised impurities, and alloying effects), and carrier-carrier scatterings, need to be considered [15]. For our samples, the acoustic phonon scattering was found the most dominant scattering mechanism in the 100 - 600 K temperature range. Although the acoustic phonon scattering is taken as the main effective mechanism to express the electrical conductivity as in Eq. (4.12), the effect of other scattering mechanisms alters the magnitude as well as temperature dependence. Indeed, as noted before [13], usually experimental electrical conductivity results are at variance with the prediction of Eq. (4.12), and it becomes necessary to scale both the magnitude and temperature dependence of $\sigma_{\text{extrinsic}}$. Therefore the following modified form is used

$$\sigma^{'}_{\text{extrinsic}} = \sigma_{\text{extrinsic}} A T^{\varsigma}, \tag{4.18}$$

where A and ς are adjustable parameters.

In the temperature region 100 - 450 K (*viz.* the extrinsic regime), the electrical conductivity depends on the Fermi level via the Fermi integral $F_{1/2}$. In this temperature range $\zeta^* > 1$, and using the appropriate asymptotic expansion [19] it can be noted that the Fermi integral $F_{1/2}$ is proportional to $\zeta^{*3/2}$. Thus, at a given temperature, the higher Fermi level for the CuBr-doped sample assures that its resistivity is lower than that of the SbI_3-doped sample. In the intrinsic regime, the higher resistivity of the SbI_3-doped sample is achieved by the choice of the parameters $A^{'}$ and ς as presented in Tab. 4.1.

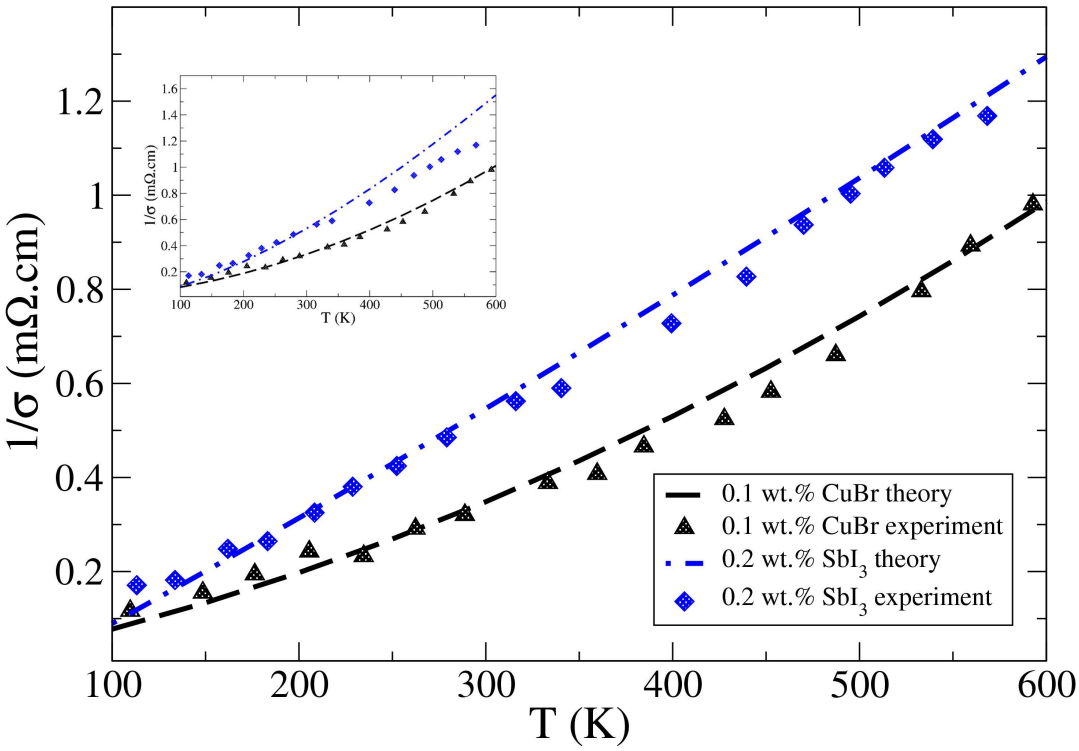

Figure 4.3: Temperature variation of electrical resistivity for $Bi_2(Te_{0.85}Se_{0.15})_3$ single crystal doped with 0.1 wt.% CuBr (dashed curve) and 0.2 wt.% SbI_3 (dash-dotted curve). The symbols represent the experimental results from Ref. [2]. The inset shows the results by treating the samples as extrinsically doped throughout the entire temperature range.

In the intrinsic regime, the temperature dependence of the mobility usually cancels with the temperature dependence of the equilibrium carrier density. So, with a suitable choice of $A^{'}$ the electrical conductivity in the intrinsic regime is defined as in Eq. (4.13). In order to fully reproduce the experimental results in the intrinsic regime, we found it useful to add the free carrier-phonon scattering contribution. At these temperatures such scattering can be treated using metal physics, leading to $\rho_{\mathrm{intrinsic}} = 1/\sigma_{\mathrm{intrinsic}} + BT$ [20]. The fitted value of the parameter B is listed in Tab. 4.1.

We also managed to reproduce the results for the CuBr-doped sample beyond 500 K by treating it as extrinsic only and adding a contribution from carrier-optical phonon scattering. Optical phonons can be expected to be populated at these high temperatures [15]. Such scattering rate can be expressed as $\rho_{(\mathrm{full-extrinsic})} = 1/\sigma^{'}_{\mathrm{extrinsic}} + B'\sqrt{T}$. The parameter B' is listed in Tab. 4.1. Such an attempt, however, did not prove successful for the SbI_3-doped sample. The attempted results are shown in the inset of Fig. 4.3.

4.3.2 Thermal Properties

Electronic Thermal Conductivity:

The theoretical calculation of the electronic thermal conductivities of both CuBr and SbI_3 doped samples are shown in Fig. 4.4. In accordance with the Wiedemann-Franz law, due to its lower resistivity, the CuBr doped sample has bigger κ_{el} than the SbI_3 doped sample. The electronic thermal conductivities of both samples decrease with temperature and the difference between κ_{el} results become progressively smaller as temperature increases. Our theoretical calculations suggest that the value of κ_{el} is (3.0, 2.58) $\mathrm{Wm^{-1}K^{-1}}$ at 100 K and (1.26, 0.98) $\mathrm{Wm^{-1}K^{-1}}$

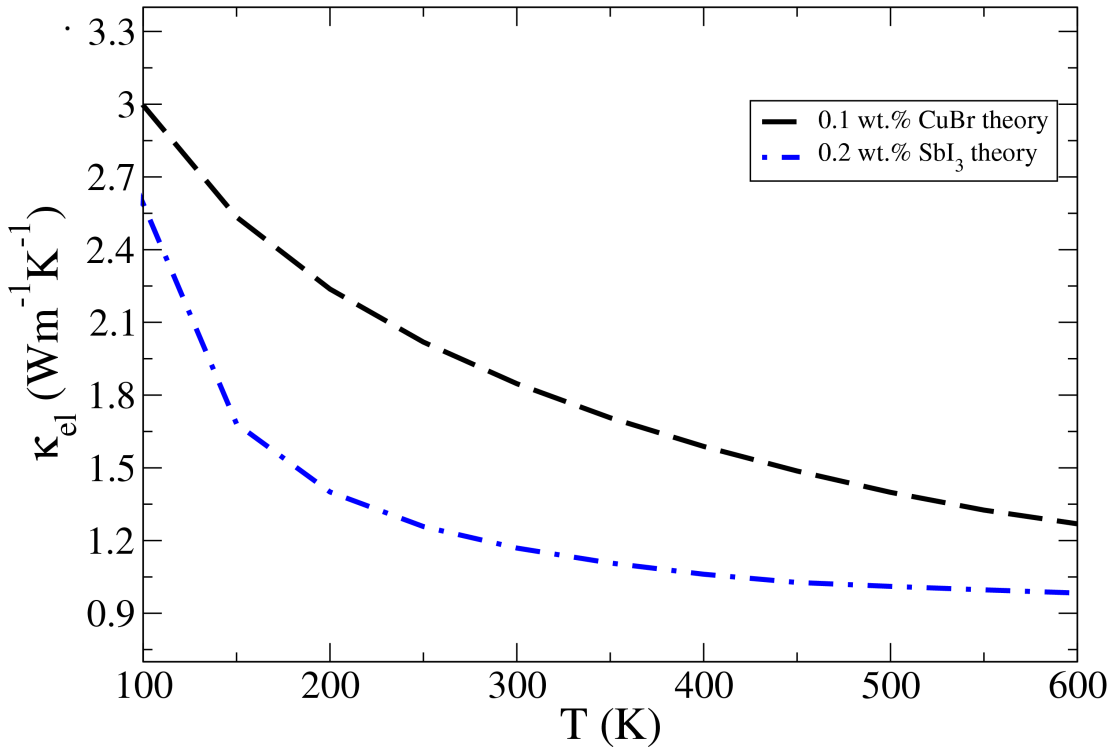

Figure 4.4: Theoretical calculation of electronic thermal conductivity as a function of temperature for $Bi_2(Te_{0.85}Se_{0.15})_3$ single crystal doped with 0.1 wt.% CuBr (dashed curve) and 0.2 wt.% SbI_3 (dash-dotted curve).

at 600 K for (CuBr, SbI_3) doped samples. It is interesting to note that it was not found any significant difference in the results whether the samples were regarded as extrinsic only or with the consideration of the extrinsic-intrinsic turn-over.

Bipolar Thermal Conductivity:

The theoretical calculation of bipolar thermal conductivities of both samples are presented in Fig. 4.5. This contribution is significant only at high temperatures (typically above 150 K). According to Eq. (4.16) it increases at least linearly with temperature. For temperature change from 200 K and 600 K the rise in $\kappa_{\rm bp}$ is 1.95 $\mathrm{Wm^{-1}K^{-1}}$ for SbI_3 and 1.54 $\mathrm{Wm^{-1}K^{-1}}$ for CuBr doped samples, which we believe is mainly due to different energy band gap variation with temperature. Up to 300 K, the bipolar thermal conductivity is insignificant compared to the electronic thermal conductivity, and $\kappa_{\rm el}$ is lower for SbI_3-dopes sample. At 600 K, on the other hand, $\kappa_{\rm bp}$ is larger than $\kappa_{\rm el}$, but the sum $\kappa_{\rm bp} + \kappa_{\rm el}$ is nearly the same for both samples.

Phonon Thermal Conductivity:

The lattice (phonon) plus bipolar thermal conductivity results are shown in Fig. 4.6 and compared with the $\kappa_{\rm total} - \kappa_{\rm el}$ values from Hyun *et al.* [2]. The present calculations for $\kappa_{\rm ph}$ involve the use of a single semi-adjustable parameter defined as $F_{\rm 3ph} = (\frac{\gamma}{\bar{c}})^2$.

For both samples, at low temperatures (below 100 K) boundary and electron-phonon scatterings are dominant. Mass defect scatterings (with the source of isotopic and alloy effects) are important both at low and high temperatures.

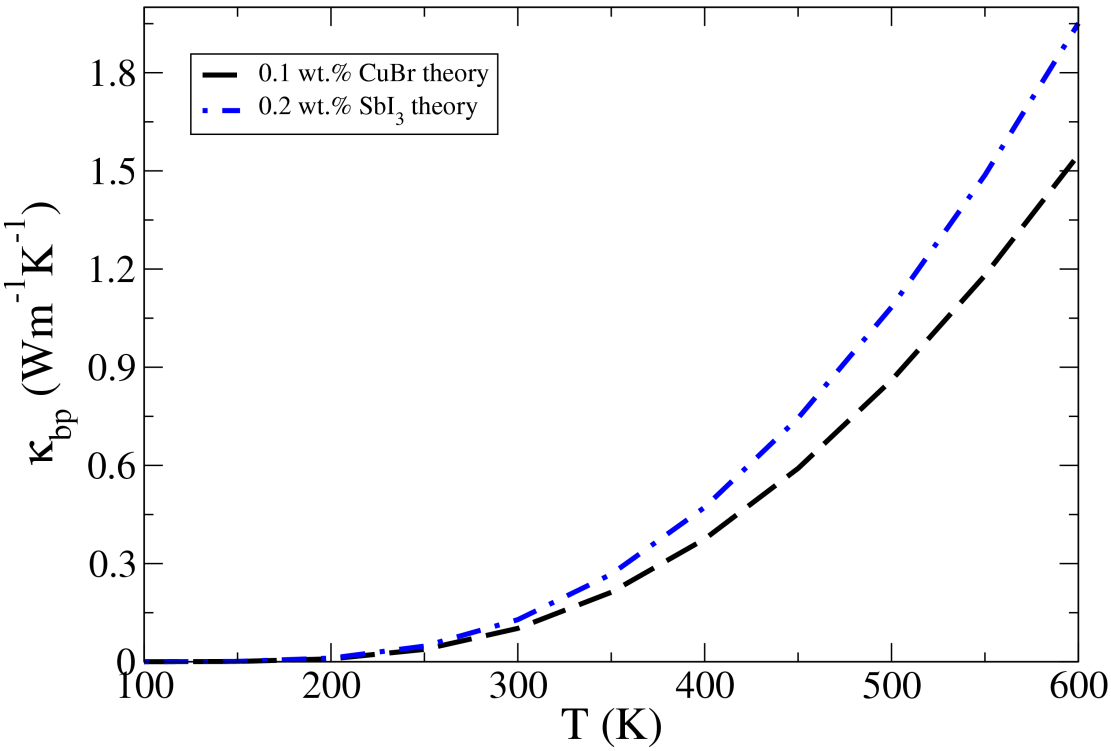

Figure 4.5: Theoretical calculation of bipolar thermal conductivity as a function of temperature for $Bi_2(Te_{0.85}Se_{0.15})_3$ single crystal doped with 0.1 wt.% CuBr (dashed curve) and 0.2 wt.% SbI_3 (dash-dotted curve).

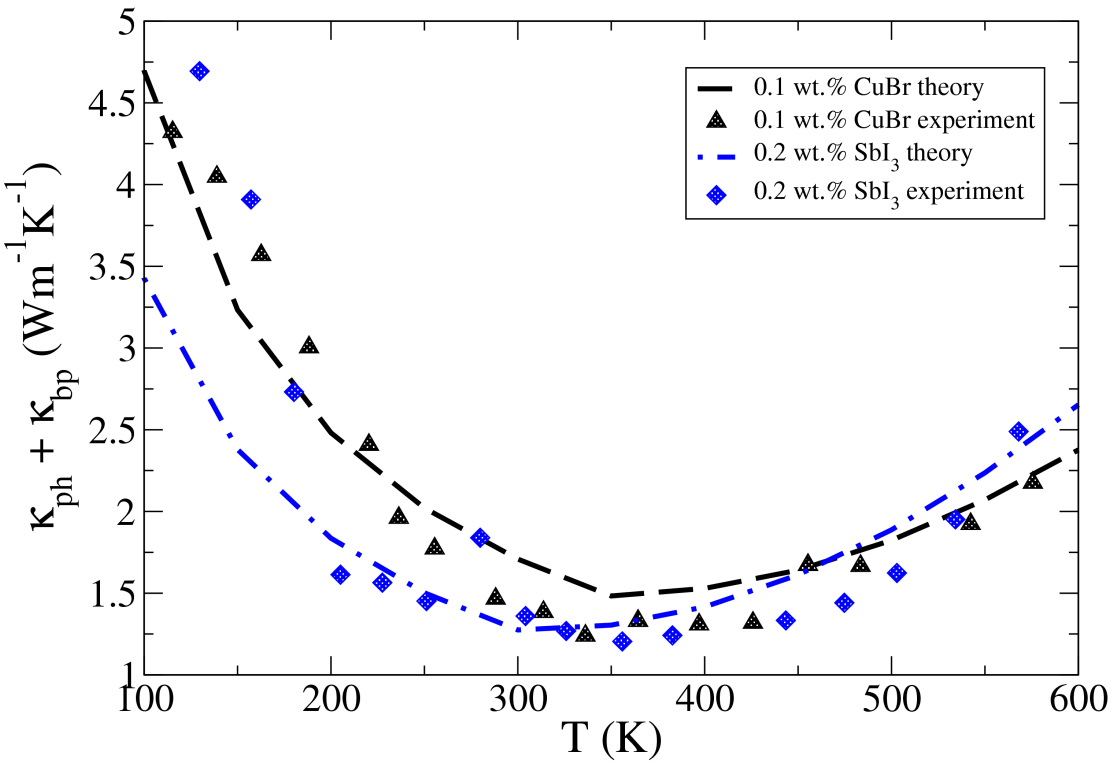

Figure 4.6: Sum of lattice and bipolar contributions of thermal conductivities for $Bi_2(Te_{0.85}Se_{0.15})_3$ single crystal doped with 0.1 wt.% CuBr (dashed curve) and 0.2 wt.% SbI_3 (dash-dotted curve). The symbols represent the extracted values of $\kappa_{\text{total}} - \kappa_{\text{el}}$ by Hyun *et al.* [2].

Phonon-phonon interactions become particularly important at high temperatures (above 100 K) for both materials. Although not shown in a separate graph, in the high temperature regime (i.e. above the Debye temperature of 155 K for bulk Bi_2Te_3) the phonon conductivity decreases linearly with temperature.

Frequency Dependence of Phonon Thermal Conductivity:

In Fig. 4.7, the spectral analysis of conductivity in frequency space for the 0.2 wt.% SbI_3-doped $Bi_2(Te_{0.85}Se_{0.15})_3$ single crystal is presented at several temperatures. We make a few important observations. At low temperatures, most heat is conducted by phonons of low frequencies. At high temperatures, phonons over a very large frequency range provide significant contribution to the conductivity. For example, at 50 K and 500 K up to 80% contribution comes from phonons in the frequency range 1.9 THz $\leqslant \omega \leqslant$ 13.6 THz, and 6.4 THz $\leqslant \omega \leqslant$ 17.8 THz, respectively. The peak of the $\kappa - \omega$ spectrum shifts to the higher values of frequency with increase in temperature. This is consistent with the theoretical result presented by Garg *et al.* [21] for the study of the phonon conductivity in a SiGe alloy. It is also found that while the spectrum peaks at the frequency $\omega_D/3$ at 50 K (where ω_D is the Debye frequency), it becomes $\omega_D/1.25$ at around 600 K. The shift in the peak of the $\kappa - \omega$ spectrum towards higher frequency with increase in temperature is consistent with the concept of dominant phonon approximation, which following the prescription by Ziman [22] can be defined as $\hbar\omega_{dom} \simeq 1.6k_BT$.

Recently, Koh and Cahill [23] have studied the frequency dependence of lattice thermal conductivity of semiconductor alloys by employing the time-domain thermoreflectance technique over a low frequency range and a reasonably large temperature range. Such measurements are considered to provide a convenient

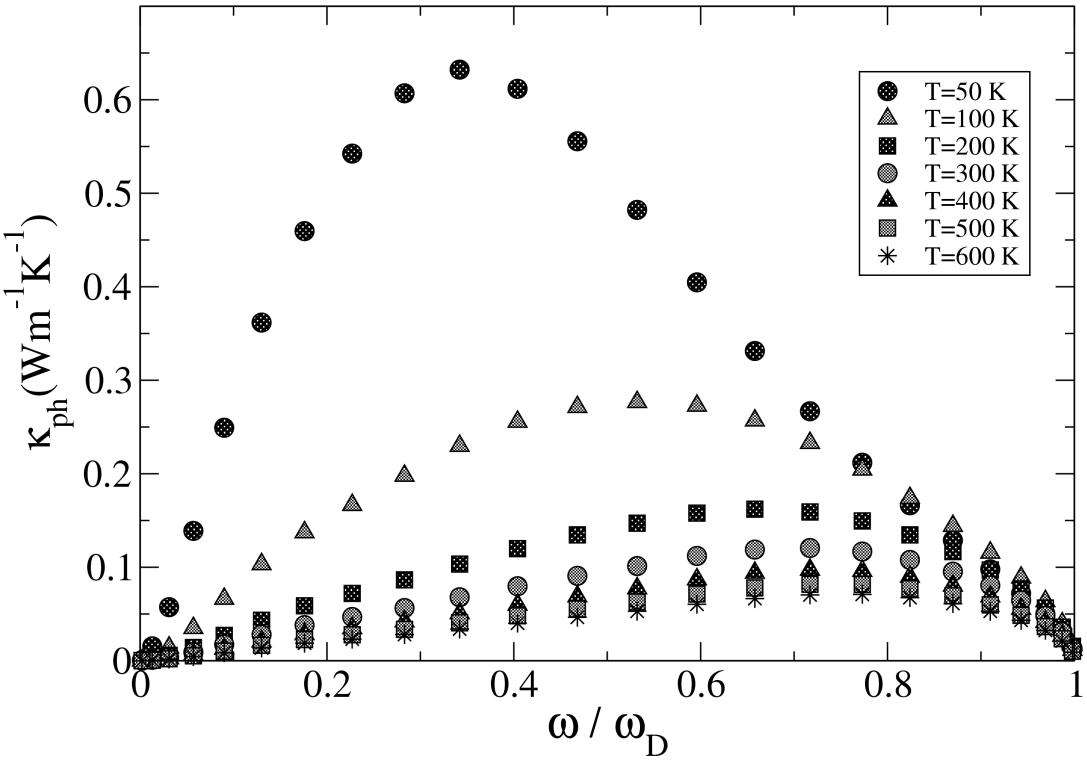

Figure 4.7: Frequency dependence of phonon thermal conductivity for different temperatures for 0.2 wt.% SbI_3 doped $Bi_2(Te_{0.85}Se_{0.15})_3$ single crystal where the Debye frequency is taken as ω_D=18.92 THz.

method for probing the phonon distribution of materials. Their results clearly show that $\kappa(\lambda)$ increases with decrease in the mean free path λ. Noting the general relationship between the phonon mean free path and frequency as $\lambda \propto \omega^{-n}$ [22], our results presented in Fig. 4.7, in the frequency range from zero up to the maximum in the $\kappa(\omega)$ spectrum at any temperature, provide support for the measurements made by Koh and Cahill.

Total Thermal Conductivity:

As seen in Fig. 4.8, there is an overall good agreement between our results for the total thermal conductivity and the experimental data presented by Hyun *et al.* [2]. As stated earlier, in the high temperature range the phonon conductivity decreases linearly and the bipolar contribution rises at least linearly with temperature. Thus the sum of the phonon and bipolar thermal conductivity contributions, $\kappa_{\rm ph}$+ $\kappa_{\rm bp}$, shows a dip at around 350 K for both samples. The experimental measurements by Hyun *et al.* suggest that there is a switch over in the temperature variation of $\kappa_{\rm ph}$+ $\kappa_{\rm bp}$ for the two alloys at around 450 K: the sum of these two contributions is lower for the SbI_3 doped sample below 450 K and for the CuBr doped sample above 450 K. This switch-over is successfully reproduced with the choice of parameters listed in Tab. 4.1.

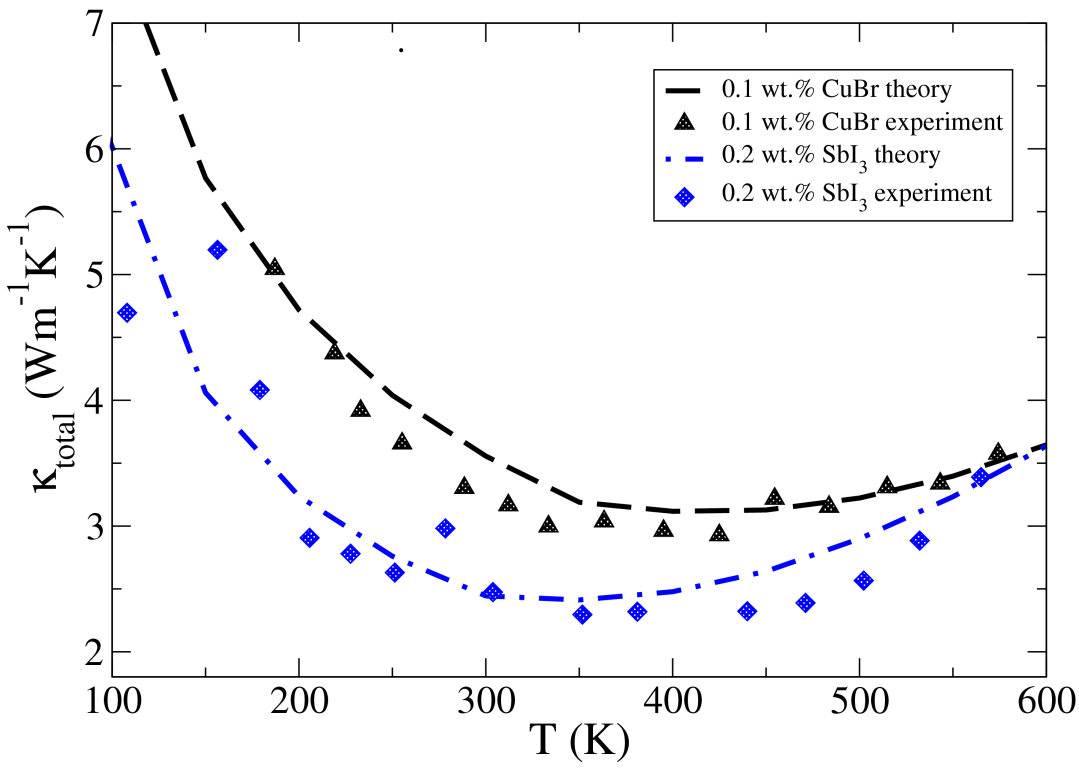

Figure 4.8: Temperature dependence of the total thermal conductivity for $Bi_2(Te_{0.85}Se_{0.15})_3$ single crystal doped with 0.1 wt.% CuBr (dashed curve) and 0.2 wt.% SbI_3 (dash-dotted curve). The symbols represent the experimental results from Ref. [2].

4.3.3 Figure of Merit

The thermoelectric efficiencies of both 0.1 wt.% CuBr and 0.2 wt.% SbI_3 doped $Bi_2(Te_{0.85}Se_{0.15})_3$ single crystals are reported in Fig. 4.9. There is a reasonably good level of agreement between our theoretical results, obtained by considering both extrinsic and intrinsic characteristics of the two samples, and the experimental measurements by Hyun *et al.* [2]. Calculations based on only extrinsic consideration produce worse agreement with experimental data at the higher temperature end, with more disagreement for the SbI_3-doped sample. These disagreements originate from the disagreements noted earlier for the Seebeck coefficient.

In the extrinsic regime the SbI_3 doped alloy sample has only a slightly larger ZT than the CuBr doped sample. This is because both the ratio of the power factor ($S^2\sigma$) and the $\kappa_{\rm total}$ between the samples are nearly equal to each other. At high temperatures (in the intrinsic regime) the CuBr doped alloy sample has larger efficiency due to its higher value of the power factor.

4.3.4 Effect of Alloying on Figure of Merit

As stated earlier, phonon-alloy scattering results in lowering of thermal conductivity and enhancement in thermoelectric efficiency. To investigate the effect of alloying on the 0.1 wt.% CuBr doped sample, different amounts of Te/Se content in the $(Bi_2Te_3)_x(Bi_2Se_3)_{(1-x)}$ single crystal is used. The parameters to calculate $\kappa_{\rm ph} + \kappa_{\rm bp}$ for $x = 0.75$ and $x = 0.90$ are taken as $E_{\rm g}(0)$ =(0.19, 0.15) eV, q_D =(0.715, 0.71) Å^{-1}, lattice constant a_{lat} =(4.321, 4.358) Å, ρ =(7.67, 7.7) g/cm^3 and Ω=(162.2, 166.3) Å^3, respectively. The parameters for $x = 0.85$ has already been given in Tab. 4.1. The temperature dependence of $\kappa_{\rm ph} + \kappa_{\rm bp}$ for all three different x values is presented in Fig. 4.10.

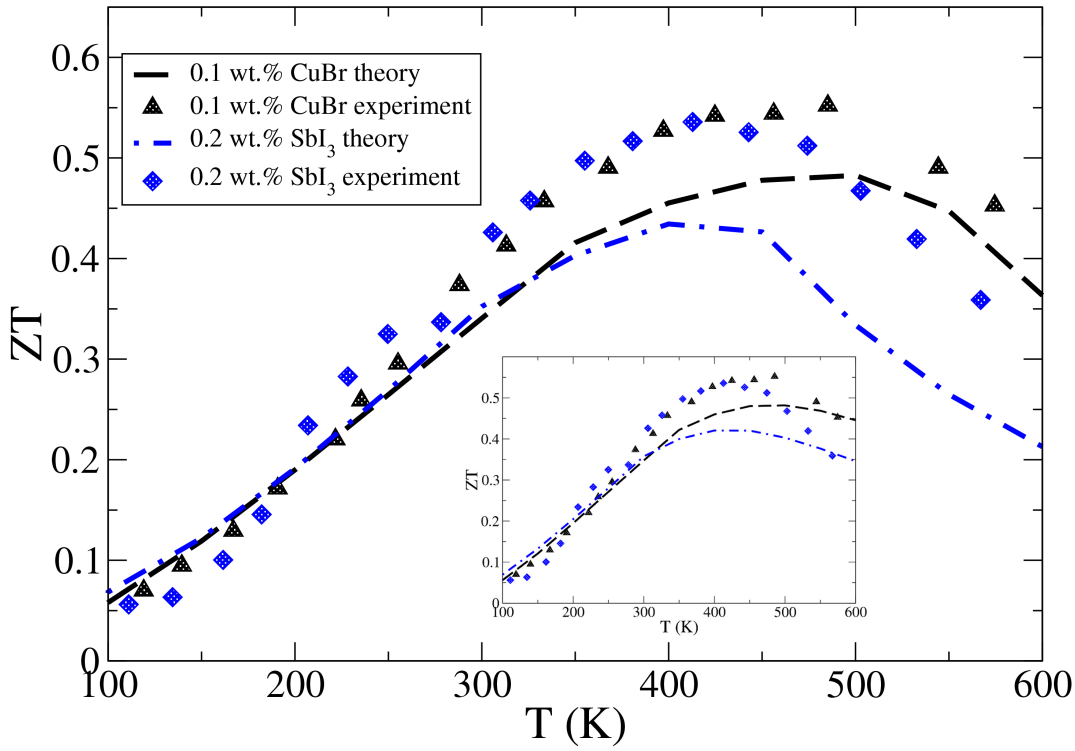

Figure 4.9: Temperature variation of figure of merit for $Bi_2(Te_{0.85}Se_{0.15})_3$ single crystal doped with 0.1 wt.% CuBr (dashed curve) and 0.2 wt.% SbI_3 (dash-dotted curve). The symbols are experimentally expected values from the work by Hyun *et al.* [2]. The inset shows the results by treating the samples as extrinsically doped throughout the entire temperature range.

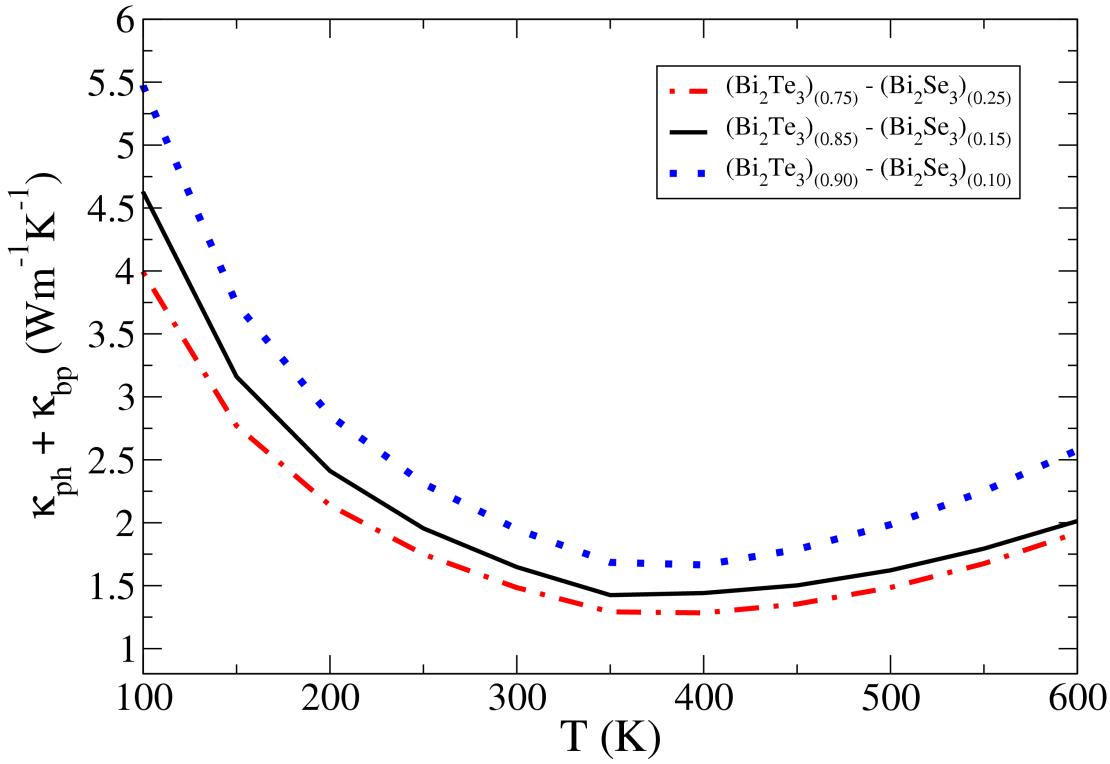

Figure 4.10: Theoretical calculation of sum of lattice and bipolar contributions of thermal conductivities for $(Bi_2Te_3)_x(Bi_2Se_3)_{(1-x)}$ alloys with taking the value of x as 0.75, 0.85, and 0.90, respectively.

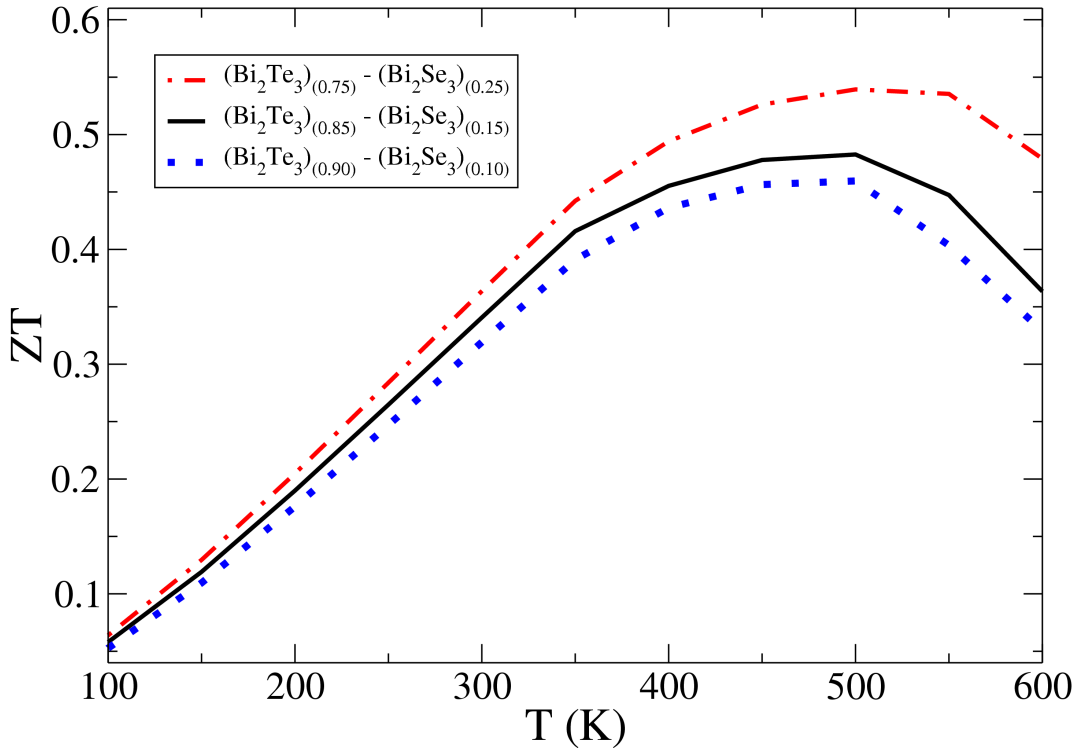

Figure 4.11: Theoretical calculation of the thermoelectric figure of merits for $(Bi_2Te_3)_x(Bi_2Se_3)_{(1-x)}$ alloys with taking the value of x as 0.75, 0.85, and 0.90, respectively.

It is clearly seen that by decreasing the x value (i.e. by increasing Se content) the thermal conductivity becomes lower throughout the entire temperature range due to the increase in the alloy scattering. We predict that by decreasing the x value from 0.90 to 0.75 (i.e. increasing the Se concentration from 10% to 25%) the reduction in $\kappa_{\rm ph} + \kappa_{\rm bp}$ would be 40% at 200 K and 44.5% at 600 K. Consistent with this variation, ZT would be enhanced by 33% and 50% at 200 K and 600 K, respectively (Fig. 4.11).

4.3.5 Effect of Full-scale Thermal Conductivity Calculation on ZT

As discussed earlier in Chapter 1, $\kappa_{\rm ph}$ is the most important parameter to obtain higher values of ZT. Thus, defining and calculating the lattice thermal conductivity of a material correctly has a crucial importance in discussing thermoelectricity. We elaborate on this point by considering two examples. In the first the work of Vining [4] is considered, who assumed the anharmonic phonon scattering as $\tau_{anh}^{-1} \propto C\omega^2 T$ where C is a constant of temperature. It is noted that this assumption is only true in the high temperature regime [12]. Vining further considered a single, polarisation-average phonon branch, expressed $\tau_N^{-1}/\tau_U^{-1} = \beta$, and treated β as a constant of temperature. To make a comparison between our theoretical approach and the Vining model [4], we made a calculation for the temperature dependence of $\kappa_{\rm ph}$ + $\kappa_{\rm bp}$ for the $Bi_2(Te_{0.85}Se_{0.15})_3$ single crystal doped with 0.1 wt.% CuBr. For employing Vining's approach, we fitted the parameter C = 3.25×10^{-7} s/K from our theoretical $\kappa_{\rm ph}$ value at 600 K (the highest temperature in our study). Then with this fixed value of C and $\beta = 2.0$, we calculated $\kappa_{\rm ph}$ and added the temperature dependence of bipolar thermal conductivity for the whole temperature range. As clearly seen in Fig. 4.12, Vining's approach cannot explain the experimental results at low temperatures. For example, at 110 K Vining's approach gives $\kappa_{\rm ph}$ + $\kappa_{\rm bp}$ = 2.1 $\rm Wm^{-1}K^{-1}$, while the experimental result as well as our theoretical result are close to 4.3 $\rm Wm^{-1}K^{-1}$.

From our model we find the following values of $(\beta_{\rm LA}, \beta_{\rm TA})$: (1.8, 0.17) at 100 K and (1.65, 0.18) at 600 K. Thus while β is rather temperature insensitive for TA modes, it does increase with decrease with temperature for LA modes. Our estimate of the temperature-average (over the range considered in our study) value of β is 1.7 for LA modes, 0.18 for TA modes, and 0.7 for polarisation-averaged modes. We thus

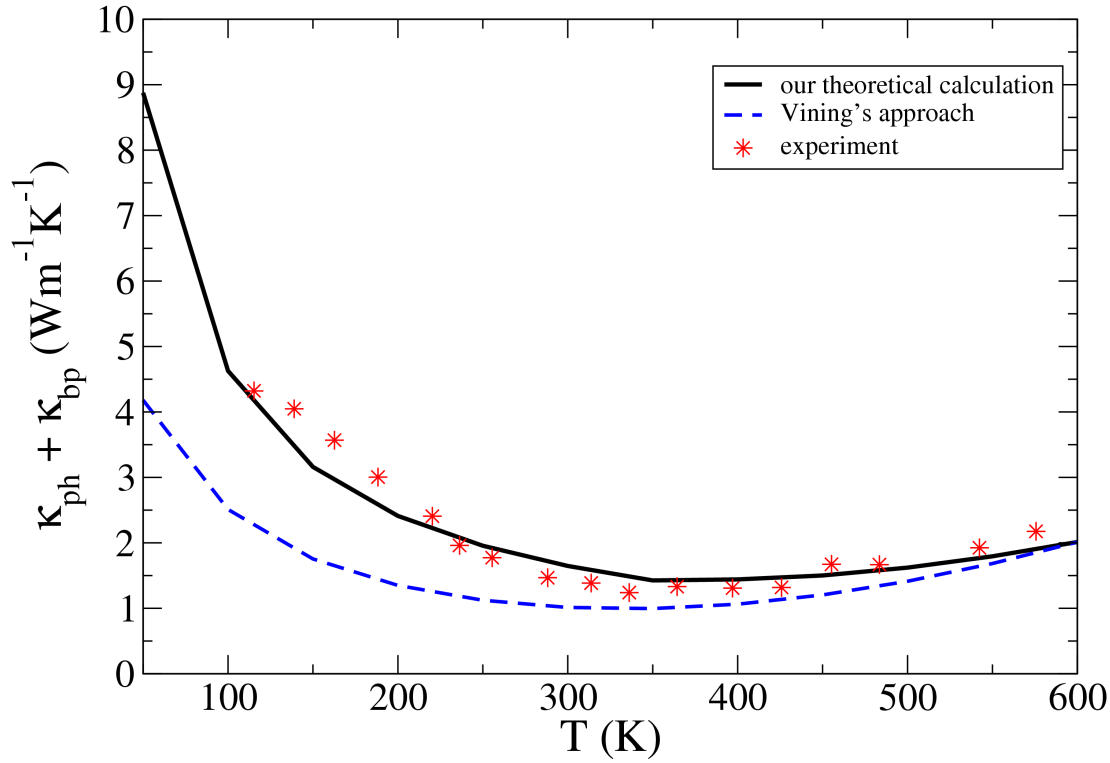

Figure 4.12: Comparison of $\kappa_{\mathrm{ph}} + \kappa_{\mathrm{bp}}$ calculation between our theoretical model and Vining's approach [4] for $Bi_2(Te_{0.85}Se_{0.15})_3$ single crystal doped with 0.1 wt.% CuBr.

find that Vining's choice of β is only reasonable for LA phonons.

As a second example, we consider the work of Hicks and Dresselhaus [5], who treated κ_{ph} as a constant (temperature independent). As shown in Fig. 4.13, to test this approach, we took three different κ_{ph} values at 115 K, 313 K and 575 K by substracted the theoretical values of κ_{bp} from the experimental measurements of κ_{total} - κ_{el} reported by Hyun *et al.* [2]. With any one of these three choices we are unable to fit the experimentally determined magnitude and temperature dependence of ZT at low temperatures (below 300 K). At high temperatures (above 300 K), due to the dominant behaviour of bipolar contribution of thermal conductivity at this temperature regime, the magnitude of ZT comes closer to our theoretical model by taking the values of κ_{ph} at 313 K and 575 K.

From the above two examples, it can be concluded that in order to obtain the correct magnitude and temperature variation of ZT it is important to include the correct magnitude and temperature dependence of κ_{ph} in both low and high temperature regimes. Our model of phonon conductivity is helpful in this respect.

4.4 Summary and Outlook

In this chapter, the thermoelectric properties of the n-type $Bi_2(Te_{0.85}Se_{0.15})_3$ single crystal, containing 0.1 wt.% CuBr and 0.2 wt.% SbI_3 dopants have been studied by considering all the transport coefficients systematically and fully. The present theoretical and computational procedure for the evaluation of the lattice thermal conductivity is much more rigorous than attempted before.

The temperature variation of the Fermi level reveals that the CuBr-doped sample, with dopant concentration of 1.32×10^{25} m^{-3}, is extrinsic up to 500 K and becomes

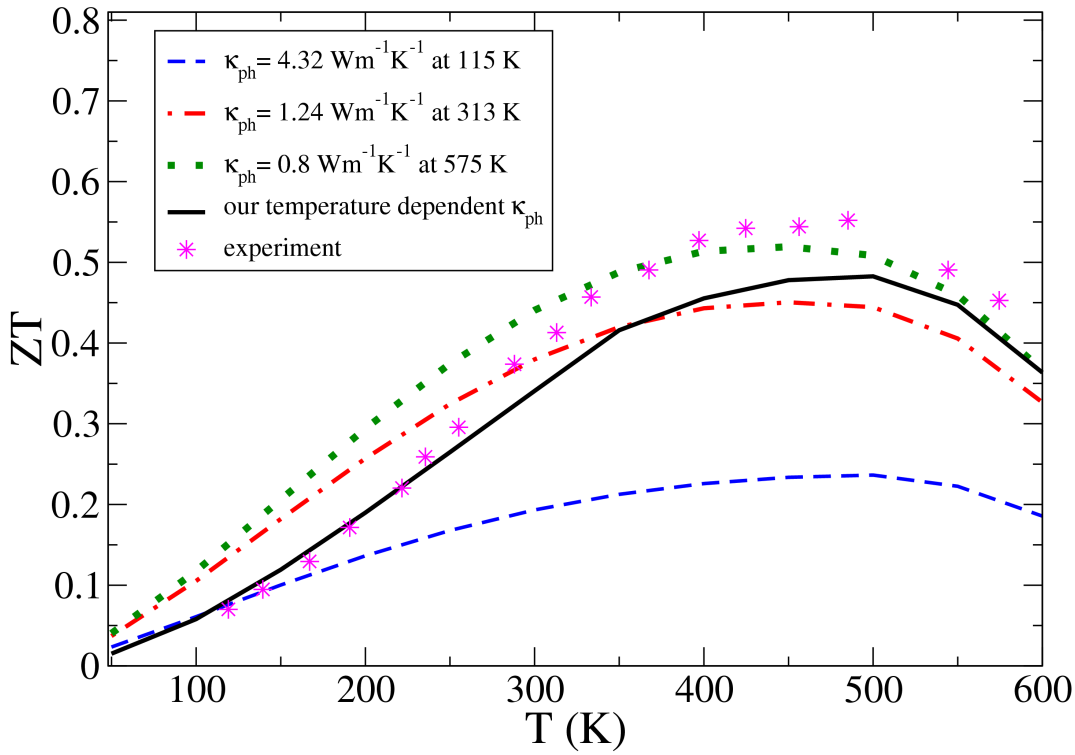

Figure 4.13: Comparison of ZT calculation between our theoretical model and Hicks and Dresselhaus' approach [5] for $Bi_2(Te_{0.85}Se_{0.15})_3$ single crystal doped with 0.1 wt.% CuBr.

intrinsic beyond that temperature. The SbI_3-doped sample, with a lower dopant concentration of 8.0×10^{24} m^{-3}, ceases to be extrinsic beyond 450 K. With these features of the Fermi level, the Seebeck coefficient has almost similar magnitude for both samples up 450 K, but decreases more sharply for the SbI_3-doped sample beyond that temperature. Both the electrical conductivity and the electronic thermal conductivity of the CuBr-doped sample are found to be higher throughout the temperature range from 100 K to 600 K. The electron-hole bipolar contribution to the thermal conductivity is similar for the two samples up to 300 K, beyond which it is found to be lower for the CuBr-doped sample.

The total thermal conductivity (sum of electronic, bipolar, and lattice contributions) is higher for the CuBr-doped sample throughout the temperature range of our investigations. An analysis of the frequency spectrum of the thermal conductivity suggests that while at low temperatures most heat is conducted by phonons of low frequencies, at high temperatures phonons over a very large frequency range provide significant contribution to the conductivity. The peak of the $\kappa(\omega)$ spectrum shifts to higher frequencies as temperature increases.

The magnitude and temperature variation of the figure-of-merit ZT is similar for both samples up to 400 K, and decreases faster for the SbI_3-doped sample beyond that temperature. The calculated maximum value of ZT is 0.43 and 0.49 for the SbI_3- and CuBr-doped samples, respectively. Our results for each of the thermoelectric transport coefficients (S, σ, κ) and ZT are in reasonable agreement with the experimental measurements reported by Hyun *et al.* [2].

The effect of alloying on thermoelectric efficiency is investigated. It is found that due to the reduction in phonon thermal conductivity, a reasonable increase in the Se content in $(Bi_2Te_3)_x(Bi_2Se_3)_{(1-x)}$ single crystals can increase ZT significantly both at low and high temperatures.

Table 4.1: Constants and parameters used in the calculations of thermoelectric properties of $Bi_2(Te_{0.85}Se_{0.15})_3$ single crystal doped with 0.1 wt.% CuBr and 0.2 wt.%SbI_3.

Property/Parameter	85% Bi_2Te_3 - 15% Bi_2Se_3 Single Crystal	
	0.1 wt.% CuBr doped	0.2 wt.% SbI_3 doped
$E_g(0)$ (eV)	0.16	0.16
E_d (eV)	0.09	0.09
α (eV/K)	0.000613	0.0007
N_d (m^{-3})	1.32×10^{25}	8.0×10^{24}
m_n^*/m_e [2]	0.056	0.056
m_p^*/m_e [2]	0.065	0.065
ρ (kg/m^3) [24]	7.74×10^3	7.74×10^3
c_L (m/s) [25]	4.76×10^3	4.76×10^3
c_T (m/s) [25]	2.325×10^3	2.325×10^3
a_{lat} (Å) [26]	4.346	4.346
E_D (eV)	32	32
ς	-0.3	-0.5
A	10.87 $K^{0.3}$	25 $K^{0.5}$
$A^{'}$ ($ohm^{-1}m^{-1}$)	3.03×10^8	1.35×10^8
B ($ohm.m.K^{-1}$)	1.6×10^{-8}	2.1×10^{-8}
$B^{'}$ ($ohm.m.K^{-1/2}$)	7.0×10^{-8}	1.0×10^{-9}
p	1.0	1.0
F_{bp} (Watt m^{-1} K^{-2})	3.4×10^{-4}	2.4×10^{-4}
q_D ($Å^{-1}$)	0.7113	0.7113
L (mm)	5.0	5.0
Ω ($Å^3$)	164.94	164.94
Γ_{isotopes}	0.000112	0.00561
Γ_{alloy}	0.00447	0.00447
F_{3ph} (s^2/m^2) [LT: low temp., HT: high temp.]	0.2×10^{-5} (LT) 0.4×10^{-5} (HT)	0.2×10^{-5} (LT) 0.4×10^{-5} (HT)

Bibliography

[1] A. F. Ioffe, Semiconductor Thermoelements and Thermoelectric Cooling (Infosearch Ltd., London, 1957).

[2] D. B. Hyun, J. S. Hwang, B. C. You, T. S. Oh, and C. W. Hwang, J. Mat.Sci. **33**, 5595 (1998).

[3] H. R. Meddins and J. E. Parrott, J. Phys. C: Solid State Phys. **9**, 1263 (1976).

[4] C. B. Vining, J. Appl. Phys. **69**, 331 (1991).

[5] L. D. Hicks and M. S. Dresselhaus, Phys. Rev. B **47**, 12727 (1993).

[6] Y. Lan, A. J. Minnich, G. Chen, and Z. Ren, Adv. Funct. Mater **20**, 357 (2010).

[7] B. Poudel, Q. Hao, Y. Ma, Y. Lan, A. Minnich, B. Yu, X. Yan, D. Wang, A. Muto, D. Vashaee, X. Chen, J. Liu, M. S. Dresselhaus, G. Chen, and Z. Ren, Science **320**, 634 (2008).

[8] R. Venkatasubramanian, E. Siivola, T. Colpitts, and B. O'Quinn, Nature **413**, 597 (2001).

[9] V. Goyal, D. Teweldebrhan, and A. A. Balandin, App. Phys. Lett. **97**, 133117 (2010).

[10] F. Zahid and R. Lake, App. Phys. Lett. **97**, 212102 (2010).

[11] P. J. Price, Phil. Mag. **46**, 1252 (1955).

[12] G. P. Srivastava, The Physics of Phonons (Taylor and Francis Group, New York, 1990).

[13] J. P. McKelvey, Solid State and Semiconductor Physics (Harper and Row Publishers, New York, 1966).

[14] D. M. Rowe and C. M. Bhandari, Modern Thermoelectrics (Reston Publishing Company, Virginia, 1983).

[15] R. R. Heikes and R. W. Ure, Thermoelectricity, Science and Engineering (Interscience Publishers, New York - London, 1961).

[16] B. R. Nag, Theory of Electrical Transport in Semiconductors (Pergamon Press, Oxford, 1972).

[17] T. M. Tritt, Thermal Conductivity Theory , Properties and Applications (Kluwer Academic/Plenum Publishers, London, 2004).

[18] A. H. Wilson, The Theory of Metals (Cambridge University Press, London, 1953).

[19] J. S. Blakemore, Solid State Physics (W. B. Saunders Company, London, 1970).

[20] C. Kittel, Introduction to Solid State Physics (John Wiley and Sons Inc, Eighth Edition, USA, 2005).

[21] J. Garg, N. Bonini, B. Kozinsky, and N. Marzari, Phys. Rev. Lett. **106**, 045901 (2011).

[22] J. M. Ziman, Electrons and Phonons (Clarendon Press, Oxford, 1960).

[23] Y. K. Koh and D. G. Cahill, Phys. Rev. B **76**, 075207 (2007).

[24] D. R. Lide, CRC Handbook of Chemistry and Physics (Taylor and Francis Group LLC, 87th Edition, 2007).

[25] L. W. Silva and M. Kaviany, Int. J. Heat and Mass **47**, 2417 (2004).

[26] W. Zhang, R. Yu, H. Zhang, X. Dai, and Z. Fang, New J. of Phys. **12**, 065013 (2010).

Chapter 5

Thermoelectric Properties of p-type $(Bi_2Te_3)_x(Sb_2Te_3)_{1-x}$ Single Crystals Doped with 3 wt% Te

5.1 Introduction

Among various TE materials, Bi_2Te_3 based alloys (both n-type and p-type) are the most widely used materials due to their usefulness in the room temperature range and capability to enhance their ZT values ($ZT > 1$) by diverse methods [1, 2, 3]. There are so many experimental studies on thermoelectric properties of Bi_2Te_3 based materials, for instance crystals [4, 5], thin-films [6, 7], and nanowires [8]. These materials have rhombohedral structure with the space group $R\bar{3}m$ and for Bi_2Te_3 five atomic layers stack along the *c* axis by van der Waals interactions in the sequence Te^1-Bi-Te^2-Bi-Te^1.

In this chapter, a detailed theoretical investigation of the thermoelectric coeffi-

cients (E_{f}, S, σ, κ_{total}, ZT) of p-type $(Bi_2Te_3)_x(Sb_2Te_3)_{1-x}$ single crystals in the composition range of $0.18 \leq x \leq 0.26$ is reported and compared with the experimental results obtained by Li *et al.*, whose samples were prepared by the fusion method together with spark plasma sintering [9]. Moreover, a theoretical discussion is presented to clarify the significant influence of the chemical composition on ZT.

5.2 Theoretical Considerations

5.2.1 Electronic Transport Coefficients

The electronic transport coefficients of thermoelectric semiconductor materials (S, σ, and κ_{c}) strongly depend on temperature dependent Fermi level. As described in Chapter2, the temperature variation of E_{f} in the extrinsic regime is expressed as [10]

$$E_{\mathrm{f}}^{\mathrm{ext}} = \frac{1}{2}(E_{\mathrm{a}} + E_{\mathrm{v}}) + \frac{k_{\mathrm{B}}T}{2}\ln\frac{N_{\mathrm{a}}}{2U_{\mathrm{v}}} - k_{\mathrm{B}}T\sinh^{-1}\Big(\sqrt{\frac{U_{\mathrm{v}}}{8N_{\mathrm{a}}}}\exp(\frac{-\Delta E_{\mathrm{i}}}{2k_{\mathrm{B}}T})\Big), \qquad (5.1)$$

for the p-type semiconductors. In Eq. (5.1), E_{v} is the valence band edge, E_{a} is the acceptor energy level, N_{a} is the concentration of acceptor impurity atoms, $\Delta E_{\mathrm{i}} = E_{\mathrm{a}} - E_{\mathrm{v}}$ is the acceptor ionisation energy, and U_{v}=$2((m_{\mathrm{p}}^{*}k_{\mathrm{B}}T)/(2\pi\hbar^2))^{3/2}$ with m_{p}^{*} as the hole effective mass, k_{B} is the Boltzmann constant, and $\hbar$ is the reduced Planck's constant. As the temperature increases, the Fermi level first decreases slowly and then increases up until it reaches the value where the acceptor level becomes fully ionized [10]. Thus, from this point the material behaves like an intrinsic semiconductor and the temperature dependence of E_{f} is expressed as [10]

$$E_{\mathrm{f}}^{\mathrm{int}} = \frac{E_{\mathrm{v}} + E_{\mathrm{c}}}{2} + \frac{3}{4}k_{\mathrm{B}}T\ln\Big(\frac{m_{\mathrm{p}}^{*}}{m_{\mathrm{n}}^{*}}\Big), \qquad (5.2)$$

where E_{c} is the conduction band edge and m_{n}^{*} is the electron effective mass.

In p-type semiconductors, the Seebeck coefficient S is expressed within a single-band nearly-free-hole model as [11]

$$S = \frac{k_{\mathrm{B}}}{e}(\delta - \zeta^{*}), \tag{5.3}$$

where $\zeta^{*} = E_{\mathrm{f}}/k_B T$ is the reduced chemical potential and as discussed in Chapter 4, the δ function is described as [12, 13]

$$\delta = \frac{(r+\frac{5}{2})F_{r+\frac{3}{2}}(\zeta^{*})}{(r+\frac{3}{2})F_{r+\frac{1}{2}}(\zeta^{*})}, \tag{5.4}$$

where r is a scattering parameter.

In the extrinsic regime, the electrical conductivity for the p-type semiconductors is expressed as [14]

$$\sigma_{\mathrm{ext}} = \frac{4}{3\pi\sqrt{\pi}}\frac{e^2}{m_{\mathrm{c}}^{*}}\frac{\hbar\rho c_L^2}{E_D^2}F_{1/2}, \tag{5.5}$$

with the assumption that the hole-acoustic phonon scattering mechanism is the most dominant mechanism. In Eq. (5.5), c_L is the velocity of longitudinal phonons, ρ is the mass density, and E_D is the deformation potential. By following Wilson's expression [15] the electrical conductivity in the intrinsic regime can be given by

$$\sigma_{\mathrm{int}} = A^{'} e^{-E_{\mathrm{g}}/2k_{\mathrm{B}}T}, \tag{5.6}$$

where $A^{'}$ can be taken as a temperature independent parameter .

5.2.2 Thermal Transport Coefficients

The carrier contribution (namely holes in this chapter) to the thermal conductivity is expressed by following the Wiedemann-Franz law as [13]

$$\kappa_{\mathrm{c}} = \sigma\mathcal{L}T = \left(\frac{k_{\mathrm{B}}}{e}\right)^2 \sigma T\mathcal{L}_0, \tag{5.7}$$

where $\mathcal{L}$ is the Lorenz number and for semiconductors $\mathcal{L}_0$ can be described in terms of the scattering parameter r and the Fermi integral as [12, 13]

$$\mathcal{L}_0 = \frac{\left(r+\frac{7}{2}\right)F_{r+\frac{5}{2}}(\zeta^*)}{\left(r+\frac{3}{2}\right)F_{r+\frac{1}{2}}(\zeta^*)} - \left[\frac{\left(r+\frac{5}{2}\right)F_{r+\frac{3}{2}}(\zeta^*)}{\left(r+\frac{3}{2}\right)F_{r+\frac{1}{2}}(\zeta^*)}\right]^2. \tag{5.8}$$

The bipolar contribution (electron-hole pairs) to the thermal conductivity (κ_{bp}) becomes significant above room temperature in narrow band-gap semiconductors [16, 17]and it can be expressed as

$$\kappa_{\mathrm{bp}} = F_{\mathrm{bp}} T^p \exp(-E_{\mathrm{g}}/2k_{\mathrm{B}}T), \tag{5.9}$$

with F_{bp} and p regarded as adjustable parameters depending on doping type [14].

Similar to Chapter 2, the lattice contribution to the thermal conductivity is investigated by employing Debye's isotropic continuum model within the single-mode relaxation time approximation as [18]

$$\kappa_{\mathrm{ph}} = \frac{\hbar^2 q_D^5}{6\pi^2 k_{\mathrm{B}} T^2} \sum_s c_s^4 \int_0^1 dx x^4 \tau \bar{n}(\bar{n}+1), \tag{5.10}$$

where τ is the phonon relaxation time, q_D is the Debye radius, $x = q/q_D$ is a reduced wavenumber, s represents the polarisation branch of phonon (longitudinal or transverse), $\bar{n}$ is the Bose-Einstein distribution function, and c_s is the velocity of phonons for polarisation branch s.

The phonon relaxation rate τ^{-1} in Eq. (5.10) is contributed by several scattering mechanisms: boundary (bs), mass defects (md), carriers (acceptor holes for this chapter) (hp) and anharmonic (anh). Required expressions for these scattering mechanisms have already been given in Chapter 2. As employed for n-type doped Bi_2Te_3 based alloys in Chapter 4, the phonon-phonon scattering rate will be treated by considering $F_{3\mathrm{ph}} = (\frac{\gamma}{\bar{c}})^2$ as an adjustable parameter [14, 19].

5.3 Results and Discussion

To investigate the thermoelectric properties of p-type $(Bi_2Te_3)_x(Sb_2Te_3)_{1-x}$ single crystals in the range $0.18 \leq x \leq 0.26$ all the integrals are numerically evaluated by using Simpson's rule. All the related parameters for the theoretical calculations are given in Tab. 5.1.

5.3.1 Electronic Transport Coefficients

Fermi Level:

The theoretical result for the Fermi level variation with temperature for p-type $(Bi_2Te_3)_x(Sb_2Te_3)_{1-x}$ single crystals is presented in Fig. 5.1. All samples exhibit a change from the extrinsic to the intrinsic behaviour above room temperature. This behaviour is entirely supported by the experimental Seebeck coefficient measurements reported in Ref. [9]. For all the six compositions, $E_{\rm f}$ first falls smoothly in the extrinsic regime and then rises up linearly in the intrinsic regime. In narrow band gap semiconductors, band gap variation with temperature plays a major role in the intrinsic regime. Thus, by setting the valence band edge as zero ($E_{\rm v}$=0) we can re-express $E_{\rm f}^{\rm int}$ in terms of the energy band gap as

$$E_{\rm f}^{\rm int} = E_{\rm c} - \frac{E_{\rm g}(T)}{2} + \frac{3}{4}k_{\rm B}T\ln\Big(\frac{m_{\rm p}^*}{m_{\rm n}^*}\Big). \tag{5.11}$$

To reproduce the experimental results of thermoelectric transport properties (S, σ, and $\kappa_{\rm c}$) for our p-type samples, it is found to be useful to define the temperature dependence of energy band gap as

$$E_{\rm g}(T) = \Big[E_{\rm g}(0) - \frac{\alpha T^2}{\beta + T}\Big] + \frac{\eta T}{\beta + T}, \tag{5.12}$$

where $E_{\rm g}(0)$ is the value of $E_{\rm g}$ at 0 K, α, β and η are treated as adjustable parameters and given in Tab. 5.1. In Eq. (5.12), the temperature variation of $E_{\rm g}$

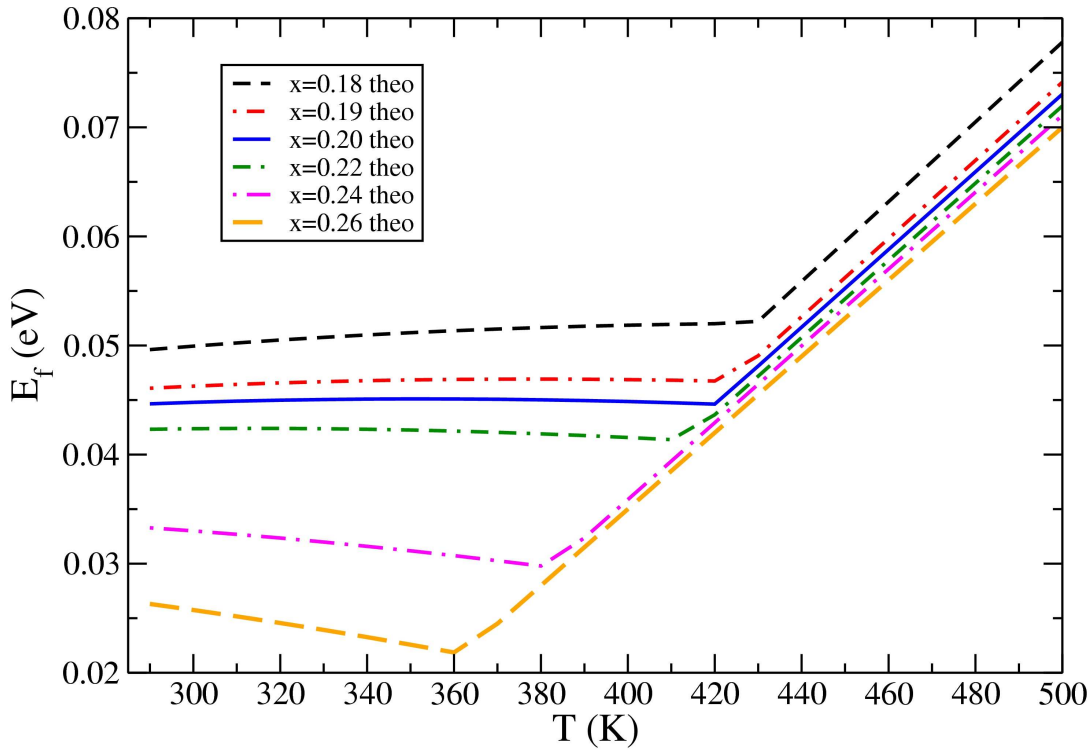

Figure 5.1: Temperature dependence of the Fermi level for p-type $(Bi_2Te_3)_x$ $(Sb_2Te_3)_{1-x}$ single crystals doped with 3 wt% Te.

is slightly different from Varshni's expression [20] with the addition of an extra term. The small value of $E_{\rm g}(0)$, given in Tab. 5.1, is obtained by considering that the band gap of the $(Bi_2Te_3)_x(Sb_2Te_3)_{1-x}$ alloy shows strong bowing with the indirect band gaps of Bi_2Te_3 and Sb_2Te_3 taken as 0.13 eV and 0.15 eV, respectively [21]. Due to the very narrow band gap of our p-type material we consider the same values of $E_{\rm g}(0)$ and $E_{\rm a}$ for all the six samples. To reproduce the experimental measurements of S and σ successfully we found it necessary to include the $E_{\rm g}(T)$ dependence beyond a critical temperature where the material turns from extrinsic to intrinsic for all the samples. From our work the critical turn-over temperatures ($T_{\rm c}$) are: 420 K for x=0.18, 0.19, and 0.20; 410 K for $x = 0.22$; 380 K for $x = 0.24$; and 360 K for $x = 0.26$. As clearly seen in Fig. 5.1, $T_{\rm c}$ shifts to lower temperatures with increasing the Bi_2Te_3 content in our p-type alloy. This is happening mainly because of the reduction in $N_{\rm a}$ (as well as the $m^*_{\rm p}/m^*_{\rm n}$ ratio) while the x value is increasing. As stated in the experimental works already [9, 4], the electronegativity difference between the Bi and Te atoms is bigger than that between the Sb and Te atoms. Therefore, increasing the Bi_2Te_3 content in $(Bi_2Te_3)_x(Sb_2Te_3)_{1-x}$ single crystals causes lower antistructure defects and results in smaller hole concentration.

Seebeck Coefficient:

As expected for p-type semiconductor materials, positive values of the Seebeck coefficient are calculated theoretically for all the compositions in the range 0.18 $\leq x \leq$0.26 and demonstrated in Fig. 5.2. The experimental measurements of S values for all the samples worked by Li *et al.* [9] are successfully reproduced throughout the temperature range studied here. The temperature dependence of the Seebeck coefficient for all the compositions are found to be similar: it first

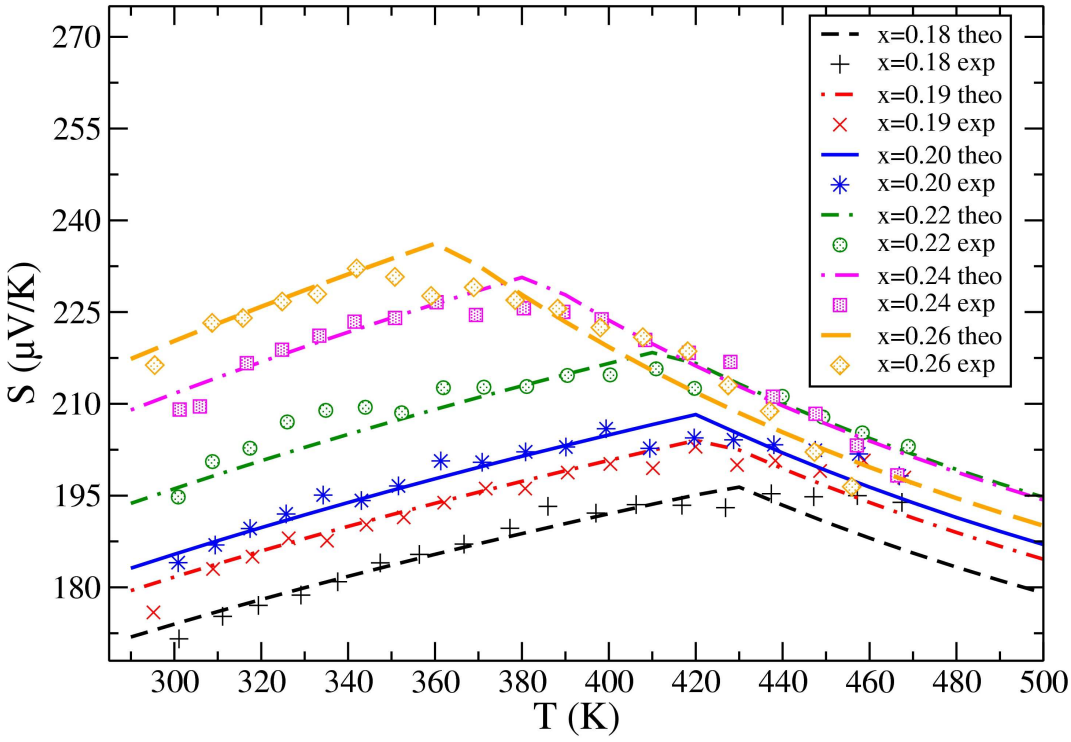

Figure 5.2: Temperature variation of the Seebeck coefficient for p-type $(Bi_2Te_3)_x$ $(Sb_2Te_3)_{1-x}$ single crystals doped with 3 wt% Te. The symbols represent the experimental measurements read from Li *et al.* [9].

increases linearly and after reaching the extrinsic-intrinsic turn-over it decreases with temperature. As can be anticipated from the theoretical calculation of E_{f}, while the value of x becomes higher, the peak value of S moves to lower temperature due to the reduction in N_{a} (or the $m_{\mathrm{p}}^{*}/m_{\mathrm{n}}^{*}$ ratio). Moreover, from Eq. (5.3) it is seen that the Seebeck coefficient (S) directly depends on the Fermi level (E_{f}) and the scattering parameter (r). As illustrated in Fig. 5.2, in the extrinsic regime the magnitude of S becomes larger with increasing the x value. On the other hand, in the intrinsic regime this is not true for the samples with the compositions x=0.22, 0.24, and 0.26 where the effect of inverse proportionality of r with S becomes dominant. Eventually the maximum value of S is gained for x=0.26 as S=236.2 μV/K at 360 K and the minimum value for S is obtained as 175 μV/K at 290 K for x=0.18.

Electrical Resistivity:

The theoretical calculation of the electrical resistivity for various x values is presented in Fig. 5.3 and the experimental results from [9] are included for comparison. In the extrinsic regime we assume theoretically that the most dominant scattering mechanism is caused by the acoustic phonons. In fact, a number of other scattering mechanisms also contribute, e.g. due to optical phonons, impurities and carrier-carrier. To cover these additional scattering mechanisms and to get an accurate explanation of the experimental measurements we scaled the resistivity found from the conductivity given in Eq. (5.5) as

$$\rho_{\mathrm{extrinsic}} = \rho_{\mathrm{ext}} A T^{\varsigma}, \tag{5.13}$$

where A and ς are treated as adjustable parameters as in our previous work [14] and are given in table 5.1.

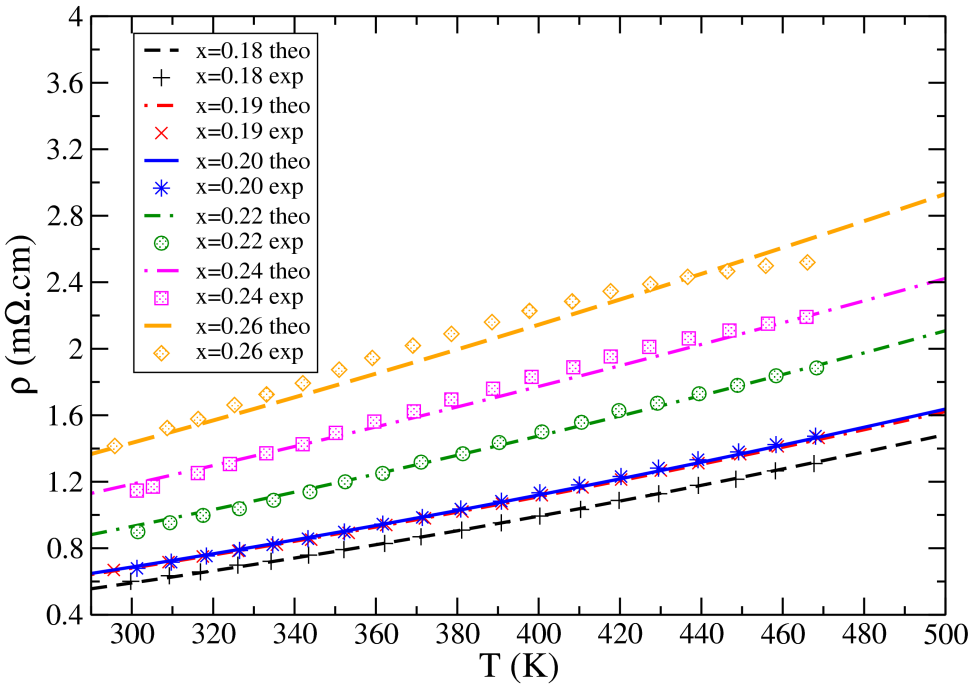

Figure 5.3: Temperature variation of the electrical resistivity for p-type $(Bi_2Te_3)_x$ $(Sb_2Te_3)_{1-x}$ single crystals doped with 3 wt% Te. The symbols represent the experimental measurements read from Li *et al.* [9].

In the intrinsic regime, in addition to the resistivity given by Eq. (5.6) we found that it is necessary to add a temperature dependence of free carrier-phonon scattering to get adequate explanation of the experimental results [14, 22]. Thus, the intrinsic electrical resistivity - T dependence can be written as

$$\rho_{\text{intrinsic}} = \rho_{\text{int}} + BT \tag{5.14}$$

where B is the temperature independent parameter [14, 22] and given in Tab. 5.1.

Using the final expressions for $\rho_{\text{extrinsic}}$ and $\rho_{\text{intrinsic}}$ we successfully explain the experimental measurements of the electrical resistivities for all the compositions as shown in Fig. 5.3. Throughout the temperature range studied here, the magnitude of the electrical resistivity goes up with increasing the value of x. This results from the rising m_{p}^{*} value in the extrinsic regime and increasing the value of B parameter in the intrinsic regime. The lowest value of ρ is attained for the $x = 0.20$ sample for the whole temperature range. It is interesting to note that from the theoretical calculation of the resistivity we did not find any clean signature of the extrinsic-intrinsic turn-over point as in the calculation of E_{f} and S.

Power Factor:

The theoretical calculation of the power factor (PF) - T dependence for all the six compositions is presented in Fig. 5.4. Based on our accurate theoretical calculation of S and ρ, we successfully reproduce the experimentally expected values of PF for all the six samples [9]. Although the sample with x=0.18 has the lowest value of S among all the compositions, it has the largest value of PF=5.21$\times 10^{-3}$ W/(m.K^2) near room temperature both theoretically and experimentally. The reason for this is that the power factor is controlled strongly by σ rather than S. It also should be noted that the largest PF value for an n-type $Bi_2(Te_{0.85}Se_{0.15})_3$ sin-

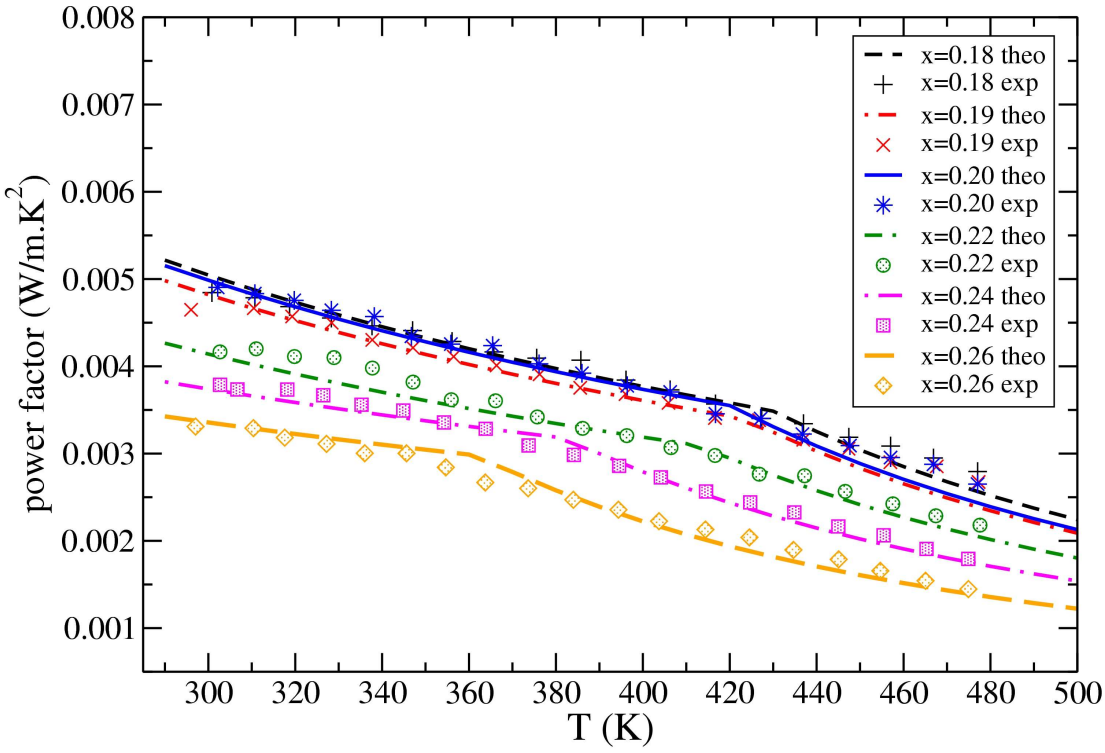

Figure 5.4: Temperature dependence of the power factor for p-type $(Bi_2Te_3)_x(Sb_2Te_3)_{1-x}$ single crystals doped with 3 wt% Te. The symbols represent the experimental results read from Li *et al.* [9].

gle crystal doped with 0.1 wt.% CuBr was obtained as 3.0×10^{-3} W/(m.K^2)at 550 K [14] which is nearly half of that for the p-type x=0.18 sample studied here. Furthermore, it is clearly shown in Fig. 5.4 that the extrinsic-intrinsic turn-over temperatures in PF calculations are the same for all samples as in the E_{f} and S calculations.

5.3.2 Thermal Transport Coefficients

Electronic Thermal Conductivity:

By employing the Wiedemann-Franz law as described in the theory section, the theoretical calculation of the carrier thermal conductivities (arising from holes) of all the samples are shown in Fig. 5.5 along with the experimental results reported in Ref. [9]. As explained in Eqs. (5.7) and (5.8), for our p-type doped Bi_2Te_3 based materials we use the modified and temperature dependent Lorenz number. The value of the $\mathcal{L}$ for the x=0.20 sample is found to be 2.1×10^{-8} W Ω K^{-2}, 2.06×10^{-8} W Ω K^{-2}, and 1.8×10^{-8} W Ω K^{-2} at 300 K, 400 K, and 500 K, respectively. This shows that our modified $\mathcal{L}$ decreases with temperature and it is smaller than the Sommerfeld value 2.44×10^{-8} W Ω K^{-2} for metals [23]. The temperature variation of κ_{c} can be easily understood from the theoretical calculation of ρ. Increasing the Bi_2Te_3 content in our p-type sample leads to smaller values of κ_{c} throughout the temperature range. As seen in Fig. 5.5 we successfully reproduce the experimental results of κ_{c} for all the compositions and find the lowest value of 0.323 WK^{-1}m^{-1} at 500 K for the composition x=0.26.

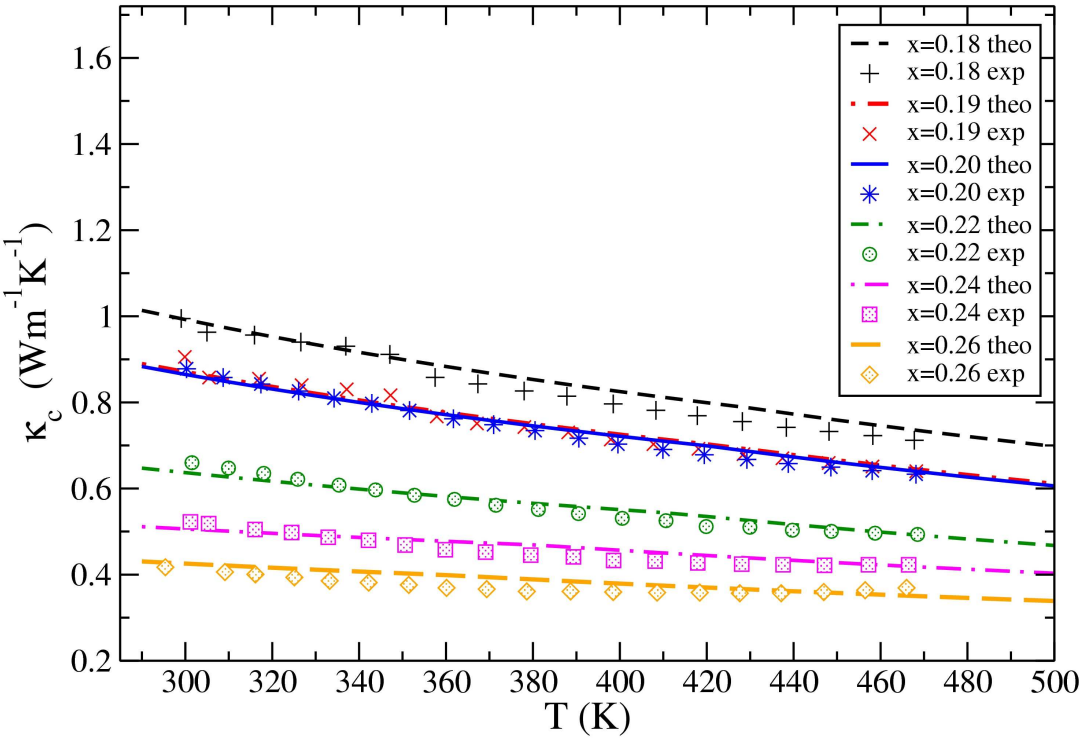

Figure 5.5: Temperature dependence of the electronic thermal conductivity for p-type $(Bi_2Te_3)_x$ $(Sb_2Te_3)_{1-x}$ single crystals doped with 3 wt% Te. The symbols represent the experimental results read from Li *et al.* [9].

Sum of Lattice and Bipolar Contributions of Thermal Conductivity:

The theoretical calculation of the ($\kappa_{\rm ph} + \kappa_{\rm bp}$) - T variation is presented in Fig. 5.6 along with the expected experimental values taken from [9]. Using the related parameters given in Tab. 5.1, the $\kappa_{\rm ph}$ calculation is made in terms of a temperature independent adjustable parameter $F_{\rm 3ph}$= $(\frac{\gamma}{c})^2$. From our theoretical calculations, we note that for all the samples, boundary and hole-phonon scatterings play a major role at low temperatures (below 100 K) and mass-defect scatterings are important at both low and high temperatures (below and above 100 K). Besides this three-phonon interactions become dominant only at high temperatures (above 100 K) for all the six compositions. Additional to these dependences, the bipolar contribution of thermal conductivity ($\kappa_{\rm bp}$) is computed theoretically with $F_{\rm bp}$ and p parameters in the range of 290 K and 500 K. As we pointed out already in our previous works [14, 19], $\kappa_{\rm bp}$ becomes significant when $T > 300$ K for narrow band gap semiconductors. From the parameters $\Gamma_{\rm isotopes}$ and $\Gamma_{\rm alloy}$ given in Tab. 5.1, our theoretical calculations suggest that for all the six samples the mass defect - phonon scattering caused by the alloying effect is larger than the isotopic mass defect scattering. Also these $\Gamma_{\rm isotopes}$ and $\Gamma_{\rm alloy}$ parameters become smaller with increasing the Bi_2Te_3 content in our p-type materials. Moreover, by using more Bi_2Te_3 content, it is seen that the effect of $\kappa_{\rm bp}$ becomes larger. From 290 K to 500 K, $\kappa_{\rm ph} + \kappa_{\rm bp}$ exhibits an almost exponential rise for all the samples, suggesting the electron-hole pair contribution in this temperature range becomes significantly larger compared with other contributions. As seen from the measurements in reference [9] samples with x=0.18 and x=0.20 have the lowest values of $\kappa_{\rm ph} + \kappa_{\rm bp}$ among all the samples throughout the temperature range. Our theoretical calculations also support that with higher values of $\Gamma_{\rm isotopes}$ and $\Gamma_{\rm alloy}$ parameters and lower $F_{\rm bp}$ parameter, smaller $\kappa_{\rm ph} + \kappa_{\rm bp}$ values are found to be 0.375 W m^{-1} K^{-1} for x=0.18 sample and 0.385 W m^{-1} K^{-1} for x=0.20 sample at 330 K.

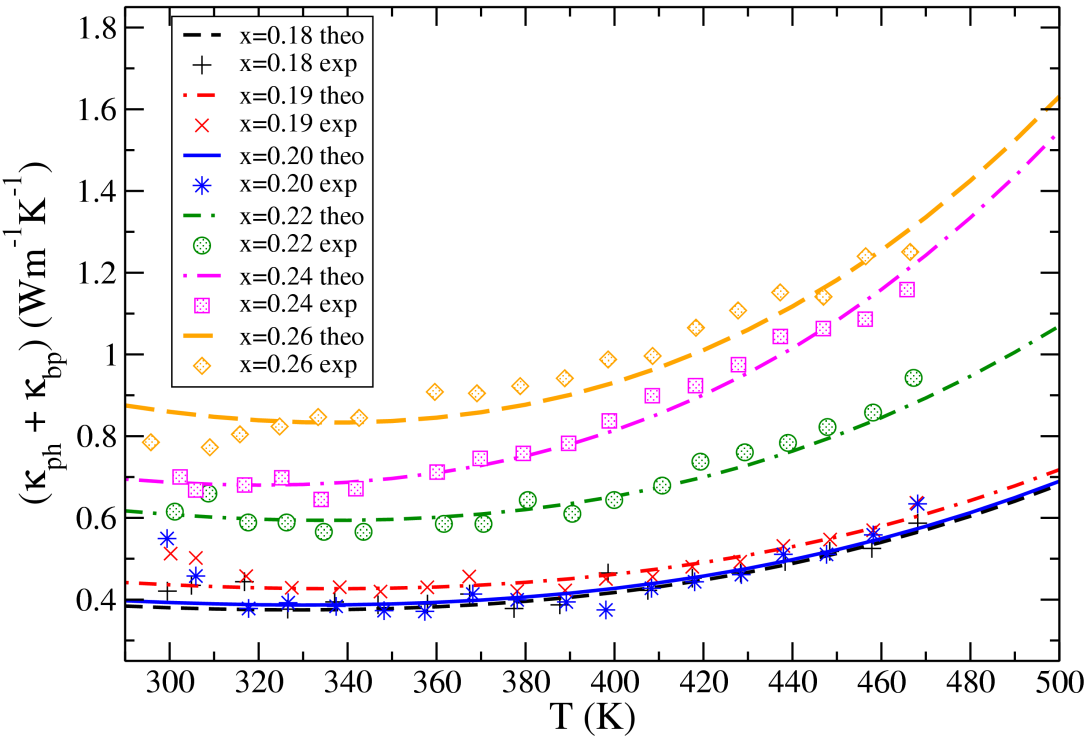

Figure 5.6: Temperature dependence of the sum of the lattice and bipolar contributions of thermal conductivity for p-type $(Bi_2Te_3)_x(Sb_2Te_3)_{1-x}$ single crystals doped with 3 wt% Te. The symbols represent the experimentally expected results read from Li *et al.* [9].

Total Thermal Conductivity:

The total thermal conductivity is calculated by combining all contribution as $\kappa_{\text{total}} = \kappa_{\text{c}} + \kappa_{\text{ph}} + \kappa_{\text{bp}}$ and presented in Fig. 5.7 along with the experimental measurements given by Li *et al.* [9]. As we expect from our κ_{c} and $\kappa_{\text{ph}} + \kappa_{\text{bp}}$ calculations, the magnitude and temperature dependence of κ_{total} for all the samples is analysed accurately.

By having one of the lowest $\kappa_{\text{ph}} + \kappa_{\text{bp}}$ value for the sample with the x=0.20 composition we achieve the smallest κ_{total} value of 1.145 $\text{WK}^{-1}\text{m}^{-1}$ at 400 K theoretically. This small κ_{total} result will have an important effect in achieving the highest value of ZT for this p-type material. For the comparison of n- and p-type materials, we note κ_{total}= 3.15 $\text{WK}^{-1}\text{m}^{-1}$ for n-type $Bi_2(Te_{0.85}Se_{0.15})_3$ single crystal doped with 0.1 wt.% CuBr at 380 K which is three times larger than the result for the x=0.20 p-type material studied here. This comparison clearly suggests that using p-type Bi_2Te_3 based alloys rather than n-type alloys will produce significantly smaller values of κ_{total}.

5.3.3 Thermoelectric Figure of Merit

We theoretically compute the ZT for all compositions in the range of $0.18 \leq x \leq 0.26$ and successfully explain the experimental results shown in Fig. 5.8. For all samples, the temperature dependence of ZT is similar: in the extrinsic regime it increases slightly and after the extrinsic-intrinsic turn-over point it decreases gently. The highest ZT value is experimentally obtained for the 20% Bi_2Te_3 - 80% Sb_2Te_3 sample as 1.33 at 398 K. We theoretically find that the x=0.20 sample has the largest ZT as 1.31 at 390 K which is in very good agreement with the experimental study [9]. The reason that the x=0.20 sample has the biggest value

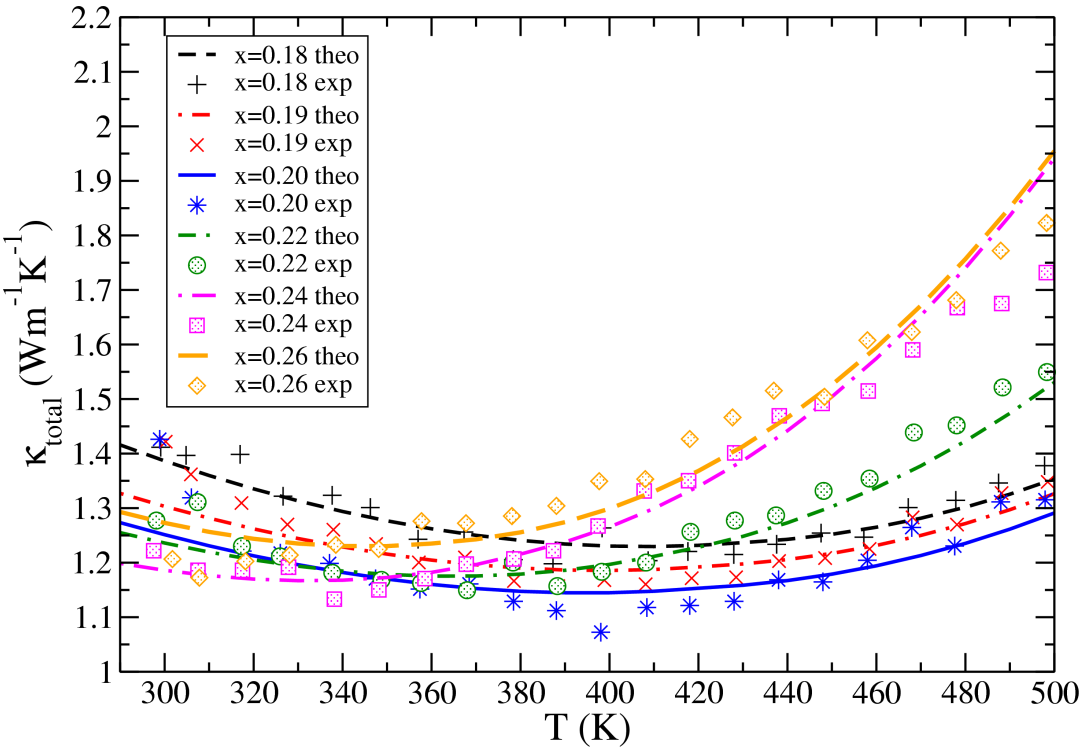

Figure 5.7: Temperature dependence of the total thermal conductivity for p-type $(Bi_2Te_3)_x(Sb_2Te_3)_{1-x}$ single crystals doped with 3 wt% Te. The symbols represent the experimental measurements read from Li *et al.* [9].

of ZT among the six compositions is two-fold: it has the lowest total thermal conductivity and has one of the highest power factor values where the peak value of ZT occurs. Additionally, as seen in Fig. 5.8, when we use less amount of Bi_2Te_3 in our p-type material the effective usage temperature range, with almost a constant ZT value, becomes broader. For instance, while a constant ZT value is obtained for the x=0.26 sample in the temperature range of 300 K $\leq T \leq$ 380 K, for the x=0.20 sample it is in temperature range 320 K $\leq T \leq$ 440 K.

In Fig. 5.9 we compare both theoretical and experimental values of ZT for the p-type $(Bi_2Te_3)_{0.20}(Sb_2Te_3)_{0.80}$ single crystal doped with 3 wt$\%$ Te studied in the present work and the n-type $Bi_2(Te_{0.85}Se_{0.15})_3$ single crystal doped with 0.1 wt.$\%$ CuBr reported in our previous study [14]. As clearly seen ZT can be enhanced up to a factor of 2.6 by choosing the p-type material rather than the n-type material. This is due to the larger value of PF and smaller value of $\kappa_{\rm total}$ for the p-type material. We also note that in the range 300 K $\leq T \leq$ 500 K the temperature variation of ZT is different for n- and p-type alloys: while it monotonously increases for n-type material, after a slight rise it decreases beyond 420 K for p-type material.

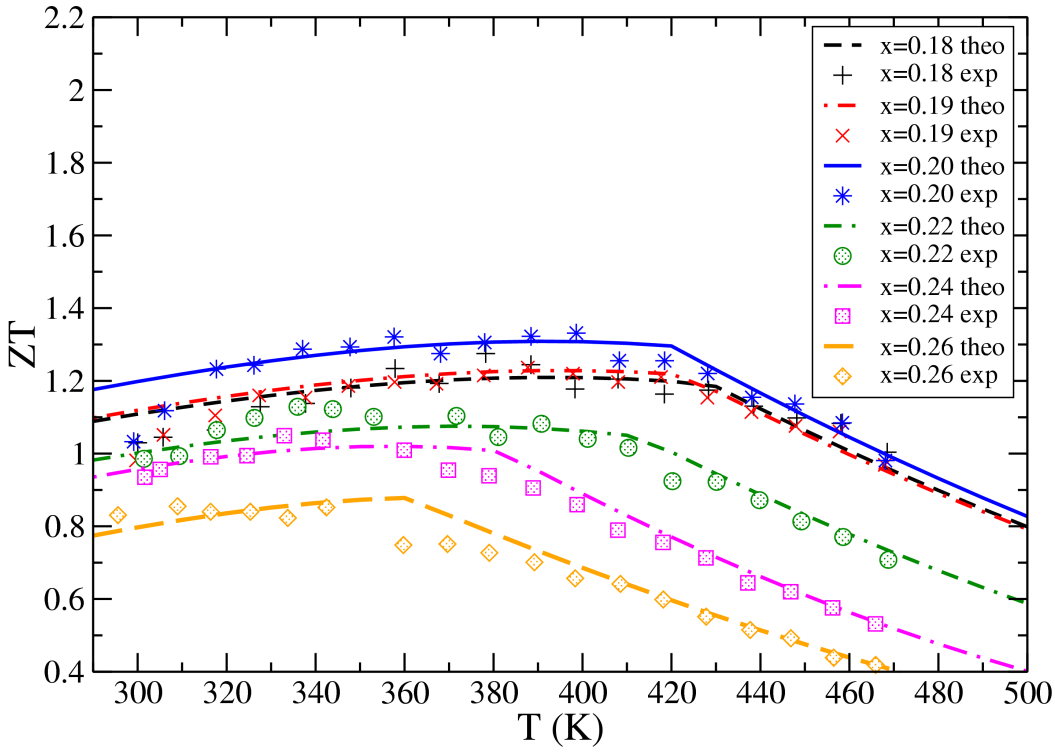

Figure 5.8: Temperature dependence of the thermoelectric figure of merit for p-type $(Bi_2Te_3)_x(Sb_2Te_3)_{1-x}$ single crystals doped with 3 wt% Te. The symbols represent the experimental results read from Li *et al.* [9].

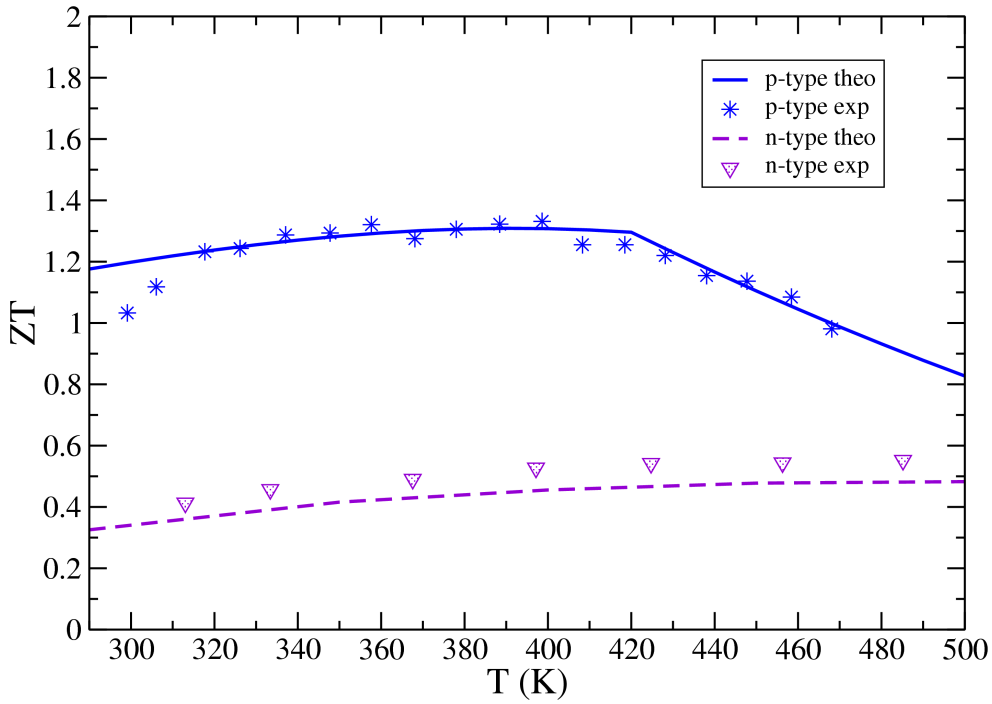

Figure 5.9: Temperature dependence of the thermoelectric figure of merit for p-type $(Bi_2Te_3)_{0.20}(Sb_2Te_3)_{0.80}$ single crystals doped with 3 wt% Te and n-type $Bi_2(Te_{0.85}Se_{0.15})_3$ single crystal doped with 0.1 wt.% CuBr studied in Ref. [14] . Stars represent the experimental results for the p-type material [9] and triangles show the experimental results for the n-type material studied by Hyun *et al.* [24].

5.4 Summary

The purpose of this research was to investigate the thermoelectric properties of p-type $(Bi_2Te_3)_x(Sb_2Te_3)_{1-x}$ single crystal doped with 3 wt% Te in the composition range $0.18 \leq x \leq 0.26$ and to compare the theoretical calculations with the experimental work studied by Li *et al.* [9]. We conclude the following:

(1) For all the compositions, the Fermi level ($E_{\rm f}$) first shows an extrinsic semiconductor behaviour and after an extrinsic-intrinsic turn-over temperature (T_c) it behaves like an intrinsic semiconductor. Also, while the value of x increases, T_c shifts to lower temperatures due to decrement in $N_{\rm a}$, or equivalently the $m_{\rm p}/m_{\rm n}$ ratio.

(2) The Seebeck coefficient of all samples reflects the temperature variation of $E_{\rm f}$. Generally, a larger Bi_2Te_3 content in the p-type material leads to a higher value of S. The largest value of S is found to be 236.2 μV/K for the x=0.26 sample at 360 K.

(3) The electrical resistivity of none of the samples shows the extrinsic-intrinsic turn-over points both theoretically and experimentally. The value of ρ increases while the x values become larger. This is because of bigger $m^*_{\rm p}$ values in the extrinsic regime and the larger B parameter in the intrinsic regime.

(4) The smallest amount of Bi_2Te_3 content (x=0.18 sample) in the p-type alloy produces the highest power factor (PF) of 5.21×10^{-3} W/(m.K^2) near 290 K theoretically, which is almost double of that for the n-type $Bi_2(Te_{0.85}Se_{0.15})_3$ single crystal doped with 0.1 wt.% CuBr studied in our previous work [14].

(5) Higher Bi_2Te_3 content produces lower values of the hole contribution to thermal conductivity ($\kappa_{\rm c}$).

(6) By applying Srivastava's scheme for phonon conductivity ($\kappa_{\rm ph}$) and Price's theory for bipolar contribution ($\kappa_{\rm bp}$), reasonable agreement is achieved with the experimental results for all the samples.

(7) The minimum value of $\kappa_{\rm total}$ is found to be 1.145 $\rm WK^{-1}m^{-1}$ for the x=0.20 sample at 400 K, which is nearly three times smaller than that for the n-type of material reported previously [14].

(8) The experimentally measured ZT - T variation for all the samples [9] has been successfully reproduced. The maximum value of ZT is computed theoretically as 1.31 for the x=0.20 sample at 390 K, which is determined by the lowest total thermal conductivity and one of the highest power factor values among all compositions. The ZT of the p-type x=0.20 sample is 2.6 times larger than that for the n-type sample studied in our previous work [14]. This clearly shows that the influence of the composition range of semiconductor alloys together with its type and amount of dopant plays an important role in enhancing the thermoelectric figure of merit.

Table 5.1: Constants and parameters used in the calculations of thermoelectric properties of p-type $(Bi_2Te_3)_x$ $(Sb_2Te_3)_{1-x}$ single crystals doped with 3 wt% Te.

Property	x=0.18	x=0.19	x=0.20	x=0.22	x=0.24	x=0.26
$E_{\mathrm{g}}(0)$ (eV)	0.09	0.09	0.09	0.09	0.09	0.09
E_{a} (eV)	0.04	0.04	0.04	0.04	0.04	0.04
α (eV/K)	0.0105	0.0105	0.0105	0.0105	0.0105	0.0105
η (eV)	0.32	0.32	0.32	0.32	0.32	0.32
β (K)	14.53	14.53	14.53	14.53	14.53	14.53
N_{a} (m^{-3})	1.0×10^{25}	8.4×10^{24}	8.1×10^{24}	7.7×10^{24}	4.2×10^{24}	2.55×10^{24}
$m^*_{\mathrm{p}}/m^*_{\mathrm{e}}$	1.27	1.13	1.09	1.06	1.03	1.01
r	0.4	0.43	0.45	0.55	0.53	0.43
$\rho(\mathrm{kg/m^3})$[25]	6.67×10^3	6.68×10^3	6.69×10^3	6.72×10^3	6.75×10^3	6.77×10^3
$\bar{c}$ (m/s) [26]	2918.0	2920.3	2922.0	2925.4	2928.8	2932.2
a_{lat} (Å) [27]	4.27	4.27	4.28	4.28	4.28	4.28
E_D (eV)	32.0	32.0	32.0	32.0	32.0	32.0
ς	1.1	1.1	1.1	1.1	1.1	1.1
A ($\mathrm{K}^{-1.1}$)	0.00063	0.00063	0.00058	0.00068	0.00064	0.0007
$A^{'}$ ($\Omega^{-1}\mathrm{m}^{-1}$)	3.03×10^{-9}	3.03×10^{-9}	3.03×10^{-9}	3.03×10^{-9}	3.03×10^{-9}	3.03×10^{-9}
B ($\Omega.\mathrm{m.K}^{-1}$)	2.8×10^{-8}	3.0×10^{-8}	3.1×10^{-8}	4.0×10^{-8}	4.7×10^{-8}	5.6×10^{-8}
p	1.0	1.0	1.0	1.0	1.0	1.0
$F_{\mathrm{bp}}(\mathrm{Wm^{-1}K^{-2}})$	13.0×10^{-4}	13.0×10^{-4}	13.0×10^{-4}	21.0×10^{-4}	35.0×10^{-4}	35.0×10^{-4}
q_D ($\mathrm{Å}^{-1}$)	0.6	0.601	0.603	0.605	0.608	0.61
L (mm)	5.0	5.0	5.0	5.0	5.0	5.0
Ω ($\mathrm{Å}^3$)	160.2	160.3	160.414	160.6	161.0	161.0
$\Gamma_{\mathrm{isotopes}}$	0.028	0.026	0.025	0.0078	0.0054	0.00186
Γ_{alloy}	0.053	0.051	0.05	0.016	0.011	0.004
$F_{3\mathrm{ph}}$ ($\mathrm{s^2/m^2}$)	1.06×10^{-5}	1.058×10^{-5}	1.057×10^{-5}	1.055×10^{-5}	1.052×10^{-5}	1.05×10^{-5}

Figure 5.10: This present work places among the top 25% most downloaded articles published in the Journal of Applied Physics since January 1, 2013.

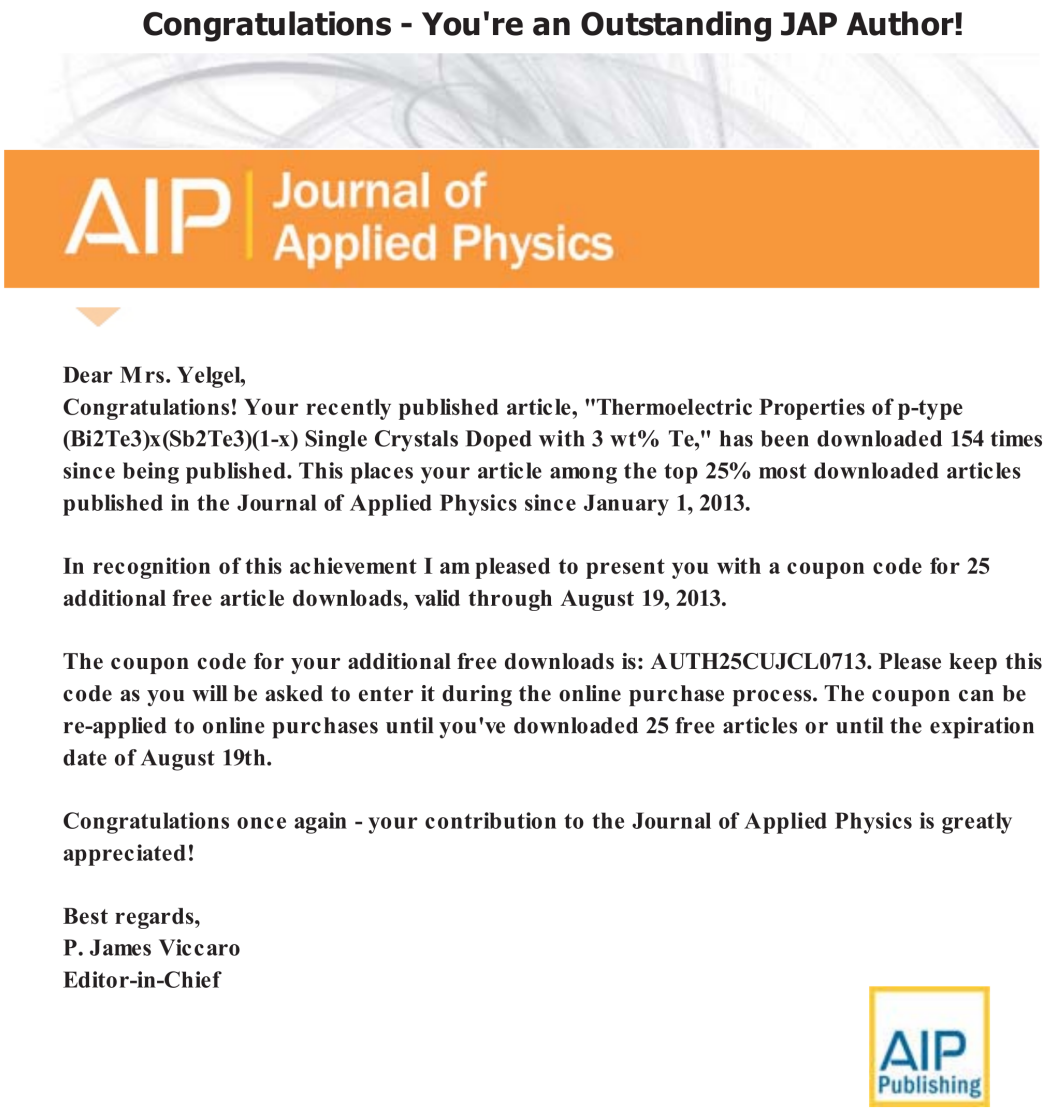

Congratulations - You're an Outstanding JAP Author!

AIP | Journal of Applied Physics

Dear Mrs. Yelgel,
Congratulations! Your recently published article, "Thermoelectric Properties of p-type (Bi2Te3)x(Sb2Te3)(1-x) Single Crystals Doped with 3 wt% Te," has been downloaded 154 times since being published. This places your article among the top 25% most downloaded articles published in the Journal of Applied Physics since January 1, 2013.

In recognition of this achievement I am pleased to present you with a coupon code for 25 additional free article downloads, valid through August 19, 2013.

The coupon code for your additional free downloads is: AUTH25CUJCL0713. Please keep this code as you will be asked to enter it during the online purchase process. The coupon can be re-applied to online purchases until you've downloaded 25 free articles or until the expiration date of August 19th.

Congratulations once again - your contribution to the Journal of Applied Physics is greatly appreciated!

Best regards,
P. James Viccaro
Editor-in-Chief

AIP Publishing

Bibliography

[1] D. M. Rowe, Thermoelectrics Handbook (Taylor and Francis Group, London, 2006).

[2] J. R. Sootsman, D. Y. Chung and M. G. Kanatzidis, Angew. Chem. Int. Ed. **48**, 8616 (2009).

[3] G. J. Snyder and E. S. Toberer, Nature **7**, 105 (2008).

[4] J. Jiang, L. D. Chen, Q. Yao, S. Q. Bai, and Q. Wang, Mater. Chem. Phys. **92**, 39 (2005).

[5] F. Köng, Cryst. Res. Technol. **33**, 219 (1998).

[6] R. Venkatasubramanian, E. Siivola, T. Colpitts and B. O'Quinn, Nature **413**, 597 (2001).

[7] A. Li Bassi, A. Bailini, C. S. Casari, F. Donati, A. Mantegazza, M. Passoni, V. Russo and C. E. Bottani, J. Appl. Phys. **105**, 124307 (2009).

[8] Y. M. Lin, O. Rabin, S. B. Cronin, J. Y. Ying, and M. S. Dresselhaus, Appl. Phys. Lett. **81**, 2403 (2002).

[9] D. Li, R. R. Sun, and X. Y. Qin, Intermet. **19**, 2002 (2011).

[10] J. P. McKelvey, Solid State and Semiconductor Physics (Harper and Row Publishers, New York, 1966).

[11] L. D. Hicks and M. S. Dresselhaus, Phys. Rev. B **47**, 12727 (1993).

[12] R. R. Heikes and R. W. Ure, Thermoelectricity, Science and Engineering (Interscience Publishers, New York, 1961).

[13] D. M. Rowe and C. M. Bhandari, Modern Thermoelectrics (Reston Publishing Company, Virginia, 1983).

[14] Ö. C. Yelgel and G. P. Srivastava, Phys. Rev. B **85**, 125207 (2012).

[15] A. H. Wilson, The Theory of Metals (Cambridge University Press, London, 1953).

[16] P. J. Price, Phil. Mag. **46**, 1252 (1955).

[17] C. J. Glassbrenner and G. A. Slack, Phys. Rev. **134**, A1058 (1964).

[18] G. P. Srivastava, The Physics of Phonons (Taylor and Francis Group, New York, 1990).

[19] Ö. C. Yelgel and G. P. Srivastava, Mater. Res. Soc. Symp. Proc. **1404**, mrsf11-1404-w03-02 doi:10.1557/opl.2012.357 (2012).

[20] Y. P. Varshni, Physica **34**, 149 (1967).

[21] N. F. Hinsche, B. Yu. Yavorsky, M. Gradhand, M. Czerner, M. Winkler, J. König, H. Böttner, I. Mertig, and P. Zahn, Phys. Rev. B **86**, 085323 (2012).

[22] C. Kittel, Introduction to Solid State Physics (John Wiley and Sons Inc, Eighth Edition, USA, 2005).

[23] T. M. Tritt, Thermal Conductivity Theory , Properties and Applications (Kluwer Academic/Plenum Publishers, London, 2004).

[24] D. B. Hyun, J. S. Hwang, B. C. You, T. S. Oh, and C. W. Hwang, J. Mat.Sci. **33**, 5595 (1998).

[25] D. R. Lide, CRC Handbook of Chemistry and Physics (Taylor and Francis Group LLC, 87th Edition, 2007).

[26] L. W. Silva and M. Kaviany, Int. J. Heat and Mass **47**, 2417 (2004).

[27] W. Zhang, R. Yu, H. Zhang, X. Dai and Z. Fang, New J. of Phys. **12**, 065013 (2010).

Chapter 6

A Detailed Theoretical Study of the Thermal Conductivity of Bi_2Te_3 Based Single Crystals

6.1 Introduction

As discussed in Chapter 1, one of the traditional ways to improve ZT is making alloys of single crystals. By this method significant reduction can be gained for the phonon thermal conductivity and larger values of ZT can be attained [1, 2]. Among various thermoelectric materials, Bi_2Te_3-Sb_2Te_3 and Bi_2Te_3-Bi_2Se_3 alloys are characterised with reasonably large ZT values near room temperature and further enhancement can be attempted by using diverse methods [3, 4, 5, 6].

In this Chapter, first of all, a detailed theoretical investigation of the thermal conductivity of $Bi_2(Te_{0.85}Se_{0.15})_3$ single crystals doped with CuBr and SbI_3 (with 0.1 and 0.05 wt.$\%$ doping levels being different studied in Chapter 4) is reported.

Secondly, a detailed comparison for the thermal conductivities of n-type 0.1 wt.% CuBr doped 85% Bi_2Te_3 - 15% Bi_2Se_3 and p-type 3 wt% Te doped 20% Bi_2Te_3 - %80 Sb_2Te_3 single crystals are provided.

6.2 Theory

The total thermal conductivity in semiconductors is expressed as $\kappa_{\text{total}} = \kappa_{\text{c}} + \kappa_{\text{bp}} + \kappa_{\text{ph}}$ where the contributions are from carriers (electrons or holes, κ_{c}), electron-hole pairs (bipolar, κ_{bp}) and phonons (κ_{ph}).

Carrier Thermal Conductivity: As given Chapter 4 and 5, the carrier thermal conductivity is determined by the Wiedemann-Franz law as [1, 2]

$$\kappa_{\text{c}} = \left(\frac{k_B}{e}\right)^2 \sigma T \mathcal{L}_0, \tag{6.1}$$

where $\mathcal{L}_0$ is described in terms of the scattering parameter r as [7]

$$\mathcal{L}_0 = \frac{\left(r+\frac{7}{2}\right)F_{r+\frac{5}{2}}(\zeta^*)}{\left(r+\frac{3}{2}\right)F_{r+\frac{1}{2}}(\zeta^*)} - \left[\frac{\left(r+\frac{5}{2}\right)F_{r+\frac{3}{2}}(\zeta^*)}{\left(r+\frac{3}{2}\right)F_{r+\frac{1}{2}}(\zeta^*)}\right]^2. \tag{6.2}$$

Bipolar Thermal Conductivity: As reported in Chapter 2, bipolar contribution to the total thermal conductivity can be written as [8, 9, 10, 11]

$$\kappa_{\text{bp}} = F_{\text{bp}} T^p \exp(-E_{\text{g}}/2k_{\text{B}}T), \tag{6.3}$$

with F_{bp} and p regarded as adjustable parameters depending on doping type.

Phonon Thermal Conductivity: By following the same procedure reported in Chapter 4 and 5, the phonon thermal conductivity is expressed by applying Debye's isotropic continuum model within the single-mode relaxation time scheme as [12]

$$\kappa_{\rm ph} = \frac{\hbar^2 q_D^5}{6\pi^2 k_B T^2} \sum_s c_s^4 \int_0^1 dx x^4 \tau \bar{n}(\bar{n}+1), \tag{6.4}$$

where q_D is the Debye radius, $\hbar$ is the reduced Planck's constant, c_s is the phonon speed for polarisation branch s, $\bar{n}$ is the Bose-Einstein distribution function and $x = q/q_D$. The phonon relaxation rate τ is contributed from several scattering mechanisms: boundary (bs), mass-defects (md), donor electrons (ep) or acceptor holes (hp), and anharmonic (anh). Expressions for $\tau_{\rm bs}^{-1}$, $\tau_{\rm ep}^{-1}$, $\tau_{\rm hp}^{-1}$, and $\tau_{\rm md}^{-1}$ have already been given in detail in Chapter 2 and the phonon-phonon interaction ($\tau_{\rm 3ph}^{-1}$) Srivastava's scheme [12] is employed in terms of the parameter defined as $F_{\rm 3ph} = (\frac{\gamma}{\bar{c}})^2$.

6.3 Results and Discussion

6.3.1 Thermal Conductivities of $Bi_2(Te_{0.85}\ Se_{0.15})_3$ Single Crystals Doped with CuBr and SbI_3

The thermal conductivity of a doped BiTeSe alloy single crystal can be expressed as $\kappa_{\rm total} = \kappa_{\rm ph} + \kappa_{\rm polar} + \kappa_{\rm bipolar}$, where contributions are from phonons (lattice), carriers, and electron-hole pairs, respectively. The effect of including the CuBr and SbI_3 dopants into $Bi_2(Te_{0.85}Se_{0.15})_3$ single crystals studied by Hyun *et al.* [13] is to provide donor electrons, making the overall doping of the alloys n-type. For this situation we can write $\kappa_{\rm total} = \kappa_{\rm ph} + \kappa_{\rm el} + \kappa_{\rm bipolar}$. The contribution $\kappa_{\rm el}$ is usually estimated via the application of the Wiedemann-Franz law. After subtracting this

contribution, Hyun *et al.* [13] have presented the temperature variation of $\kappa_{\rm total}$ - $\kappa_{\rm el} \equiv \kappa_{\rm ph} + \kappa_{\rm bipolar}$ for samples with different concentrations of CuBr and SbI_3 dopants. We have succeeded in analysing the experimental results for $\kappa_{\rm total} - \kappa_{\rm el}$ by using the parameters listed in Tab. 6.1 and the expressions presented in the theory section above. The calculations for $\kappa_{\rm ph}$ include a single semi-adjustable parameter $F_{\rm 3ph}$ which is given in Tab. 6.1 for low (below 300 K) and high (above 300 K) temperatures.

For all samples, boundary and electron-phonon scatterings are important at low temperatures (below 100 K). Three-phonon interactions become dominant at high temperatures (above 100 K) and the bipolar contribution becomes significant above 300 K. At any temperature throughout the range shown in Fig. 6.1 (a), for the CuBr-doped materials $\kappa_{\rm ph} + \kappa_{\rm bp}$ decreases with reducing the dopant concentration. The behaviour is different for the SbI_3-doped materials: $\kappa_{\rm ph} + \kappa_{\rm bp}$ decreases (increases) with reducing the dopant concentration below (above) 300 K (shown in Fig. 6.1 (b)).

The dopant-dependant behaviour of $\kappa_{\rm ph} + \kappa_{\rm bp}$ at temperatures below above 300 K can be explained by examining the behaviours of $\kappa_{\rm ph}$ and $\kappa_{\rm bp}$ separately. Mass-defect and electron-phonon scatterings increase, resulting in decrease in $\kappa_{\rm ph}$, with increase in dopant level. $\kappa_{\rm bp}$, on the other hand, generally increases with increase in dopant level. Our calculations suggest that typically above 300 K the bipolar contribution is dominant, making $\kappa_{\rm total} - \kappa_{\rm el}$ rise at least linearly with temperature (cf. Eq. (6.3)) for all samples. For the CuBr-doped samples, the $\kappa - T$ curve for the 0.1 wt.% doping level lies above that for the 0.05 wt.% doping level throughout the temperature range 100-600 K. In contrast, for the SbI_3-doped samples the results for the 0.05 wt.% and 0.1 wt.% dopings cross each other at $T = 200$ K: κ for 0.1 wt.% doping lies above(below) that for 0.05 wt.% below(above) 200 K. We found it necessary to use a larger value of the parameter $F_{\rm bp}$ for the smaller

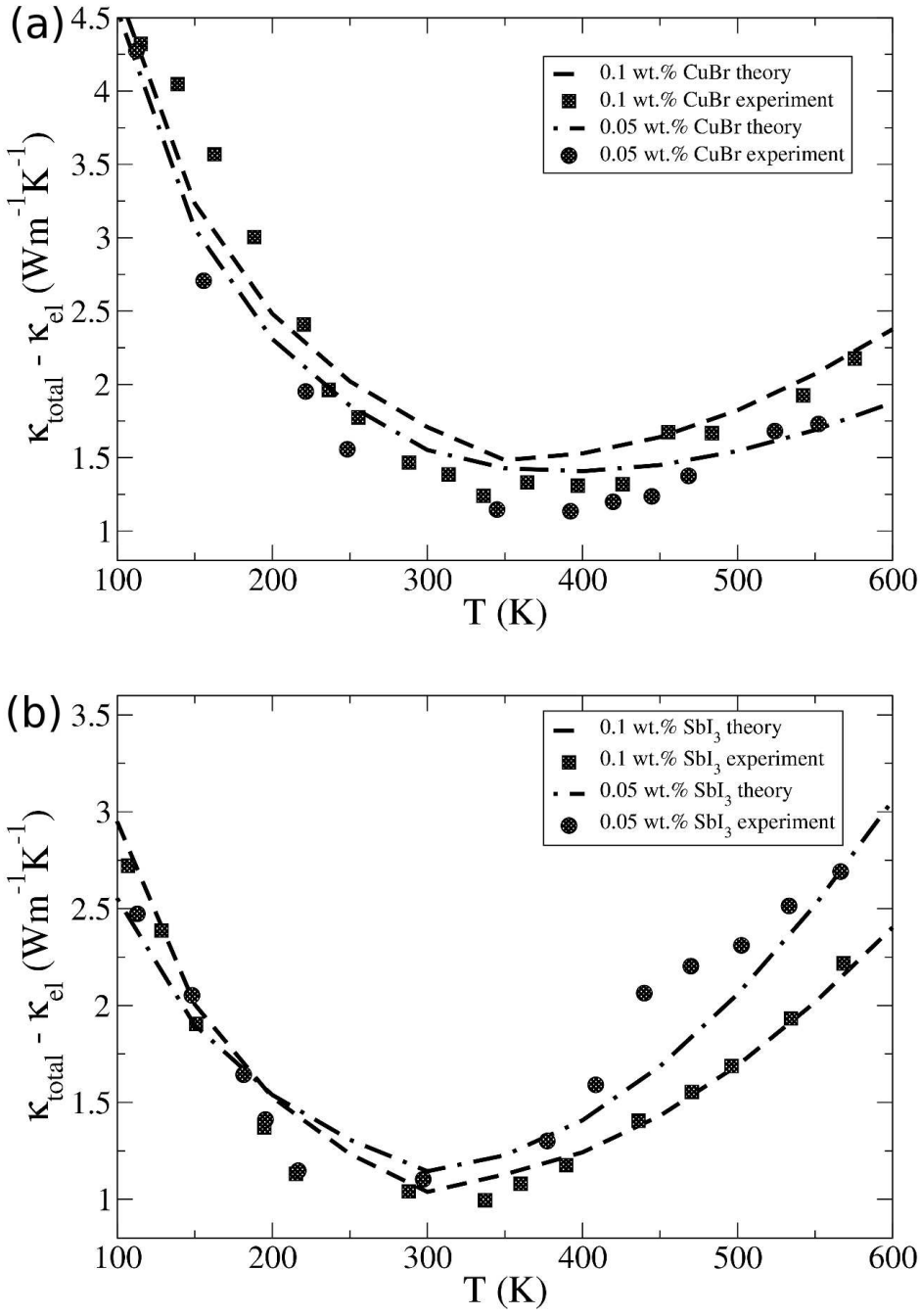

Figure 6.1: Temperature variation of κ_{total} - κ_{el} for $Bi_2(Te_{0.85}Se_{0.15})_3$ single crystals doped with (a) CuBr and (b) SbI_3 with given doping levels. The symbols represent the experimental results from Ref. [13].

concentration of the SbI_3 dopant to explain the results above 200 K.

A detailed lattice thermal conductivity investigations are made for 0.1 wt.% CuBr doped $Bi_2(Te_{0.85}Se_{0.15})_3$ single crystal. As seen in Fig. 6.2, a very high percentage (up to 82%) of the conductivity is carried by transverse phonons in the range of 100-600 K. Figure 6.3 presents frequency-dependant contribution towards the total phonon conductivity at several temperatures. At 50 K the conductivity-frequency spectrum peaks at the frequency $\omega_D/3$ and has the full width at half maxium of $\omega_D/2$, where ω_D is the Debye frequency. The spectrum becomes wider and shifts to higher frequency with increase in temperature. The shift of the maximum value of $\kappa_{\rm ph}$ to higher frequencies with increasing temperature can be understood by employing the concept of dominant phonon approximation, which suggests $\hbar\omega_{dom} \simeq 1.6k_BT$ [14]. Also, noting the general relationship between the phonon mean free path Λ and frequency as $\Lambda \propto \omega^{-n}$, we infer that $\kappa(\Lambda)$ increases with decrease in Λ in the frequency range from zero up to the maximum in $\kappa(\omega)$ for any temperature. This behaviour has been deduced from the experimental measurements of the frequency dependence of the conductivity for semiconductor alloys from Ref. [15].

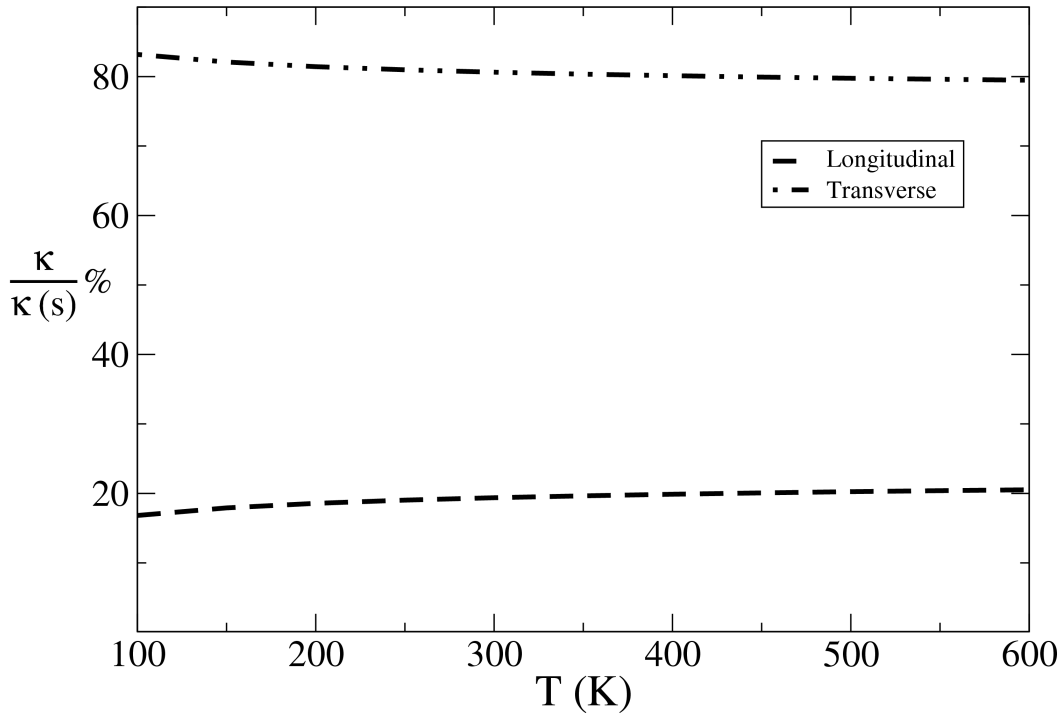

Figure 6.2: Percentage contribution from different polarisations for 0.1 wt.% CuBr doped $Bi_2(Te_{0.85}Se_{0.15})_3$ single crystal.

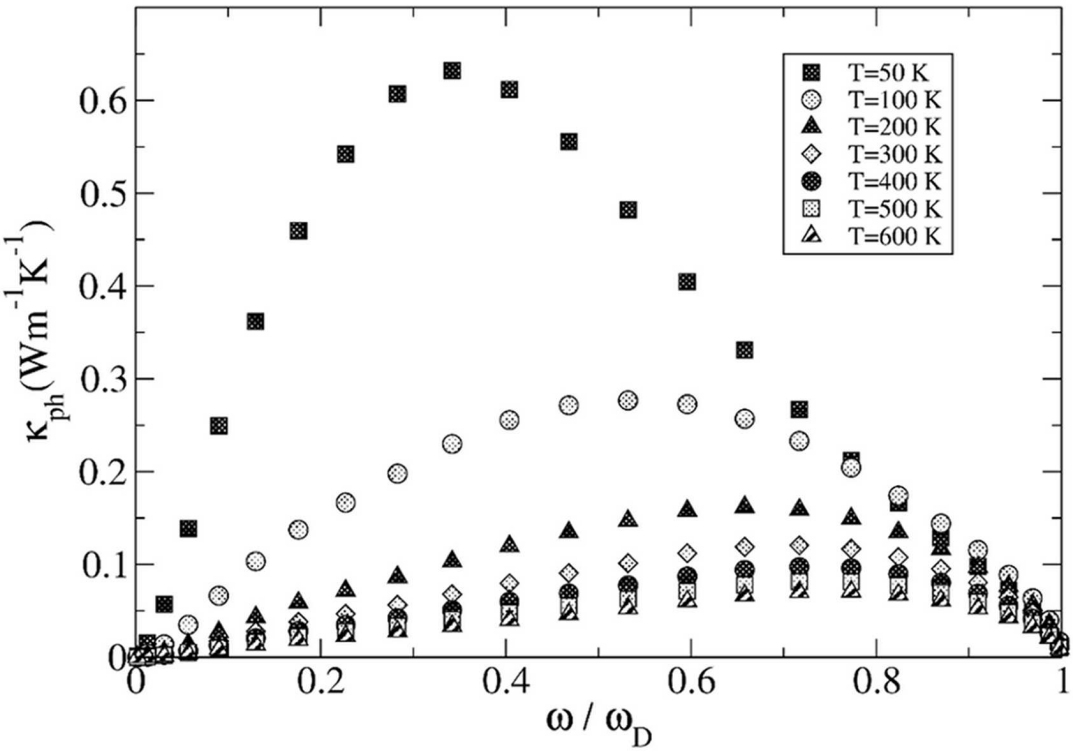

Figure 6.3: Frequency dependence of phonon thermal conductivity for different temperatures for 0.1 wt.% CuBr doped $Bi_2(Te_{0.85}Se_{0.15})_3$ single crystal where the Debye frequency is taken as ω_D=18.92 THz.

6.3.1.1 Summary

In summary, we have made a theoretical investigation of the temperature and frequency dependence of the thermal conductivity of n-type doped $Bi_2(Te_{0.85}Se_{0.15})_3$ single crystals. Experimental measurements by Hyun *et al.* [13] for the contributions from phonons and electron-hole pairs, $\kappa_{\rm total}$ - $\kappa_{\rm el}$, for CuBr- and SbI_3-doped samples have been successfully explained by employing a rigorous theory of phonon conductivity. It is found that, transverse phonons carry much more heat (of the order of 82% for 0.1 wt.% CuBr doped sample) than longitudinal phonons. In agreement with recent experimental observations by Koh and Cahill [15], the conductivity is frequency dependent. The conductivity-frequency spectrum becomes wider and shifts towards higher frequency with increase in temperature.

Table 6.1: Constants and parameters used in the calculations of the thermal conductivity of $Bi_2(Te_{0.85}Se_{0.15})_3$ single crystal doped with CuBr and SbI_3.

Property/Parameter	85% Bi_2Te_3 - 15% Bi_2Se_3 Single Crystal	
	CuBr doped	SbI_3 doped
$E_g(0)$ (eV)	0.16	0.16
α (eV/K)	0.000613	0.0007
n (m^{-3})	1.32×10^{25}	8.0×10^{24}
m_n^*/m_e [16]	0.056	0.056
ρ (kg/m^3) [17]	7.74×10^3	7.74×10^3
c_L (m/s) [18]	4.76×10^3	4.76×10^3
c_T (m/s) [18]	2.325×10^3	2.325×10^3
E_D (eV)	32	32
p	1.0	1.0
q_D ($Å^{-1}$)	0.7113	0.7113
L (mm)	5.0	5.0
Ω ($Å^3$)	164.94	164.94
Γ_{isotopes}	0.000112 (0.05 wt.%)	0.0112 (0.05 wt.%)
	0.00045 (0.1 wt.%)	0.0117 (0.1 wt.%)
Γ_{alloy}	0.00447	0.00447
$F_{3\text{ph}}$ (s^2/m^2)	LT:0.2×10^{-5}	LT:0.2×10^{-5}
	HT:0.4×10^{-5}	HT:0.4×10^{-5}
F_{bp} ($Wm^{-1}K^{-1}$)	2.3×10^{-4} (0.05 wt.%)	3.0×10^{-4} (0.05 wt.%)
	3.4×10^{-4} (0.1 wt.%)	2.2×10^{-4} (0.1 wt.%)

6.3.2 Comparison of the Thermal Conductivities of n- and p-type Bi_2Te_3 Based Single Crystals

Thermal conductivity calculations are performed for n-type 0.1 wt.% CuBr doped 85% Bi_2Te_3 - 15% Bi_2Se_3 and p-type 3 wt% Te doped 20% Bi_2Te_3 - %80 Sb_2Te_3 single crystals at temperatures from 300 K to 500 K and all the related parameters for the theoretical computation are compiled in Tab. 6.2.

By applying the Wiedemann-Franz law the carrier thermal conductivities of both n- and p-type doped Bi_2Te_3 based alloys are theoretically computed in the temperature range 300 K $\leqslant T \leqslant$ 500 K and presented in Fig. 6.4 (a). For comparision, experimental results studied by Hyun *et al.* [13] and Li *et al.* [19] are also presented in that figure. For the calculation of κ_c the required electrical conductivity results are taken from Chapter 4 and 5. In agreement with the experimental measurements, our theoretical results clearly show that κ_c decreases consistently as the temperature increases for both n- and p-type doped alloys. The significantly lower carrier thermal conductivity values for the p-type alloy throughout the temperature range results directly as a consequence of its electrical resistivity being two times bigger than the n-type alloy. With the choice of the parameters presented in Tab. 6.2, we successfully reproduce the experimental measurements for the two different alloys and find the lowest values of 1.4 W K^{-1} m^{-1} and 0.6 W K^{-1} m^{-1}, at 500 K, for the n- and p-type alloy, respectively.

The theoretically computed temperature dependence of the bipolar thermal conductivity is shown in Fig. 6.4 (b) for both the n- and p-type doped alloys. As expected from the Eq. (6.3), for both samples κ_{bp} goes up exponentially as the temperature increases and becomes significantly important above room temperature. The smaller value of κ_{bp} for the p-type alloy results from its narrower energy band gap at a given temperature, as discussed in Chapter 5. The rise in

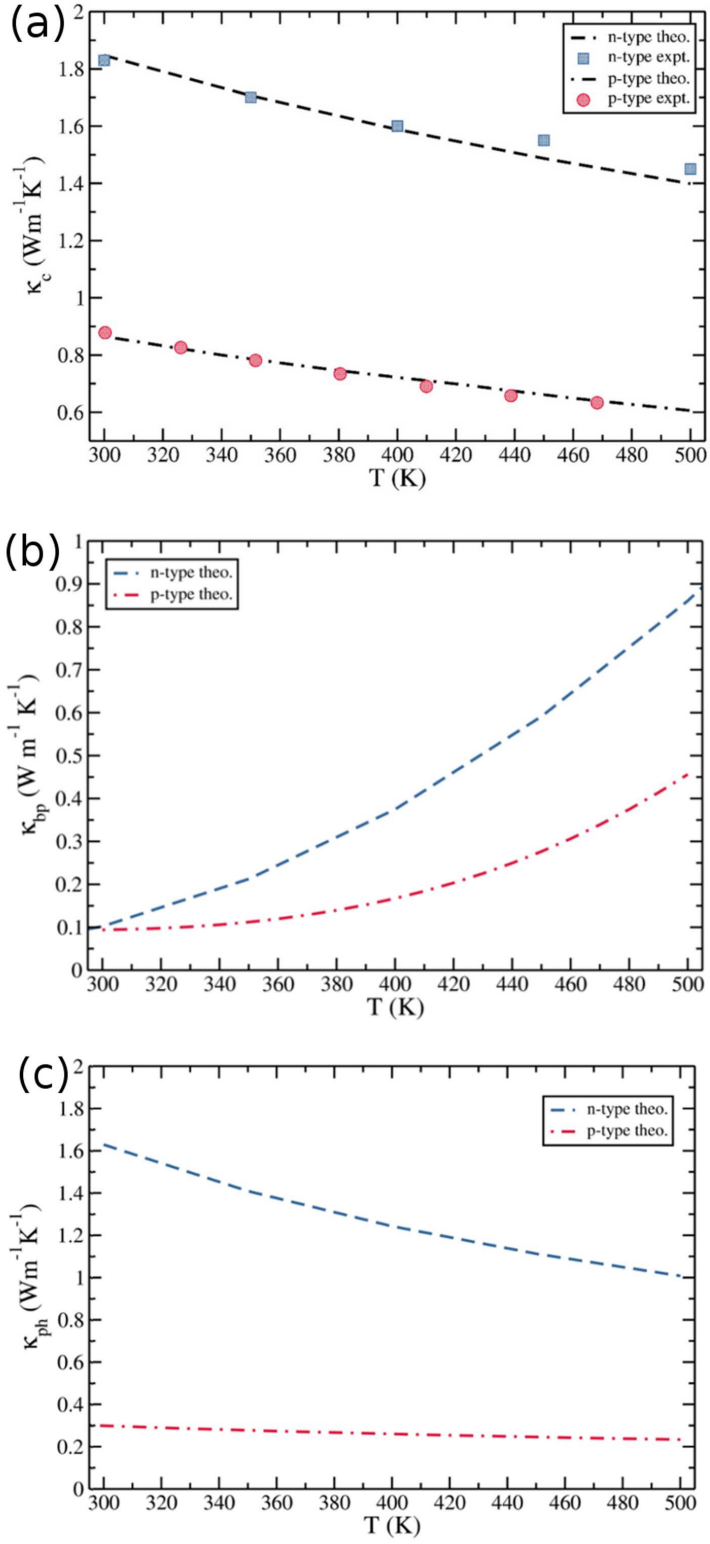

Figure 6.4: Temperature dependence of (a) the carrier thermal conductivity, (b) the bipolar thermal conductivity, (c) the phonon thermal conductivity for n-type 0.1 wt.% CuBr doped $(Bi_2Te_3)_{0.85}(Bi_2Se_3)_{0.15}$ and p-type 3 wt% Te doped $(Bi_2Te_3)_{0.20}(Sb_2Te_3)_{0.80}$ single crystals. The symbols represent the experimental results studied by Hyun *et al.* [13] and Li *et al.* [19].

$\kappa_{\rm bp}$ from 300 K to 500 K is faster for the n-type alloy than for the p-type alloy. At 500 K, the maximum value of the $\kappa_{\rm bp}$ reaches to 0.86 W K^{-1} m^{-1} for the n-type alloy and by 0.456 W K^{-1} m^{-1} for the p-type alloy.

Figure 6.4 (c) shows the temperature dependence of the phonon thermal conductivity for n- and p-type alloys. For both type alloys we theoretically found that boundary and carrier-phonon scatterings are dominant only at low temperatures ($T < 100$ K), the phonon-phonon interaction becomes significant only at high temperatures ($T > 100$ K) and mass-defect scatterings play an important role throughout the temperature range. The p-type doped alloy has notably smaller $\kappa_{\rm ph}$ value than the n-type alloy, with the $\kappa_{\rm ph}({\rm n-type})/\kappa_{\rm ph}({\rm p-type})$ ratio found to be 5.4 at 300 K and 4.34 at 500 K. From our theoretical calculations we find that compared to the n-type doped sample the p-type alloy is characterised by significantly larger mass-defect scatterings determined by $\Gamma_{\rm isotopes}$ and $\Gamma_{\rm alloy}$ parameters. Differences in these parameters upon alloy formation can easily be appreciated by noting that whereas Bi has no stable isotopes, Sb, Se and Te have two, six and eight isotopes, respectively. Also, the n-type alloying results in a much smaller mass difference ($M_{Te} - M_{Se} = 48.6$ amu) compared to the p-type alloying ($M_{Bi} - M_{Sb} = 87.2$ amu).

As demonstrated in Fig. 6.5 the calculated total thermal conductivities of n- and p-type doped alloys successfully explain the experimental results obtained by Hyun *et al.* [13] and Li *et al.* [19]. The lowest value of $\kappa_{\rm total}$ is found to be 3.15 W K^{-1} m^{-1} at 380 K for and 1.145 W K^{-1} m^{-1} at 400 K for the n- and p-type samples, respectively. From the theoretical calculations, we clearly establish that the smaller value of $\kappa_{\rm total}$ for the p-type alloy throughout the temperature range results from its phonon conductivity being nearly five times smaller than that for the n-type alloy. This suggests that using p-type doped Bi_2Te_3 based alloy rather than n-type doped alloy is likely to give rise to a higher value of ZT.

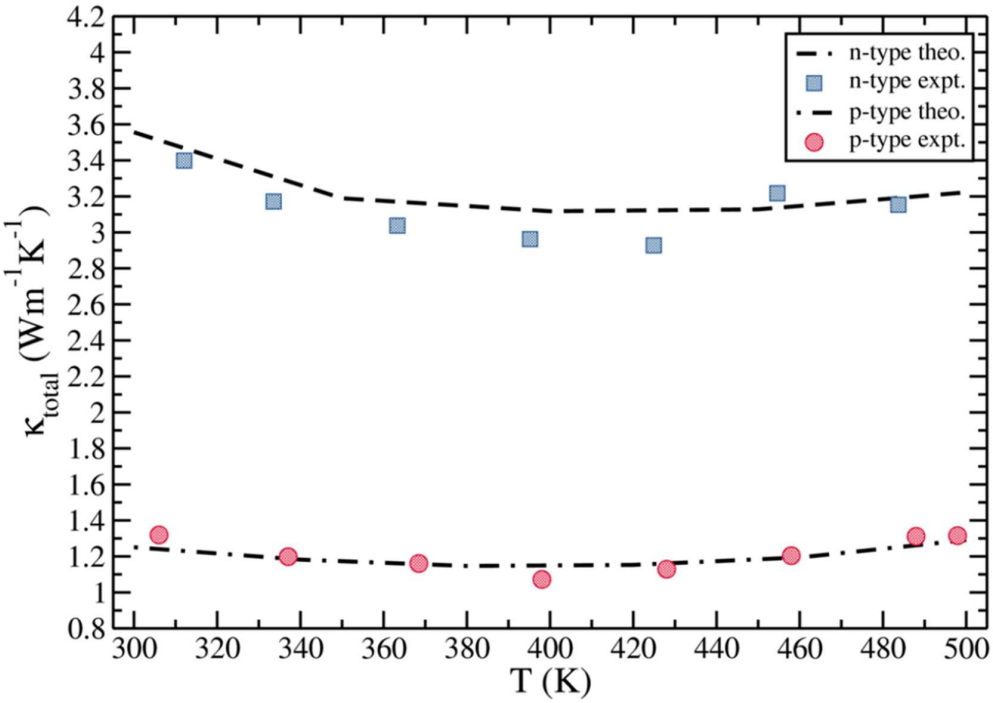

Figure 6.5: Temperature dependence of the total thermal conductivity for n-type 0.1 wt.% CuBr doped $(Bi_2Te_3)_{0.85}(Bi_2Se_3)_{0.15}$ and p-type 3 wt.% Te doped $(Bi_2Te_3)_{0.20}(Sb_2Te_3)_{0.80}$ single crystals. The symbols represent the experimental results studied by Hyun *et al.* [13] and Li *et al.* [19].

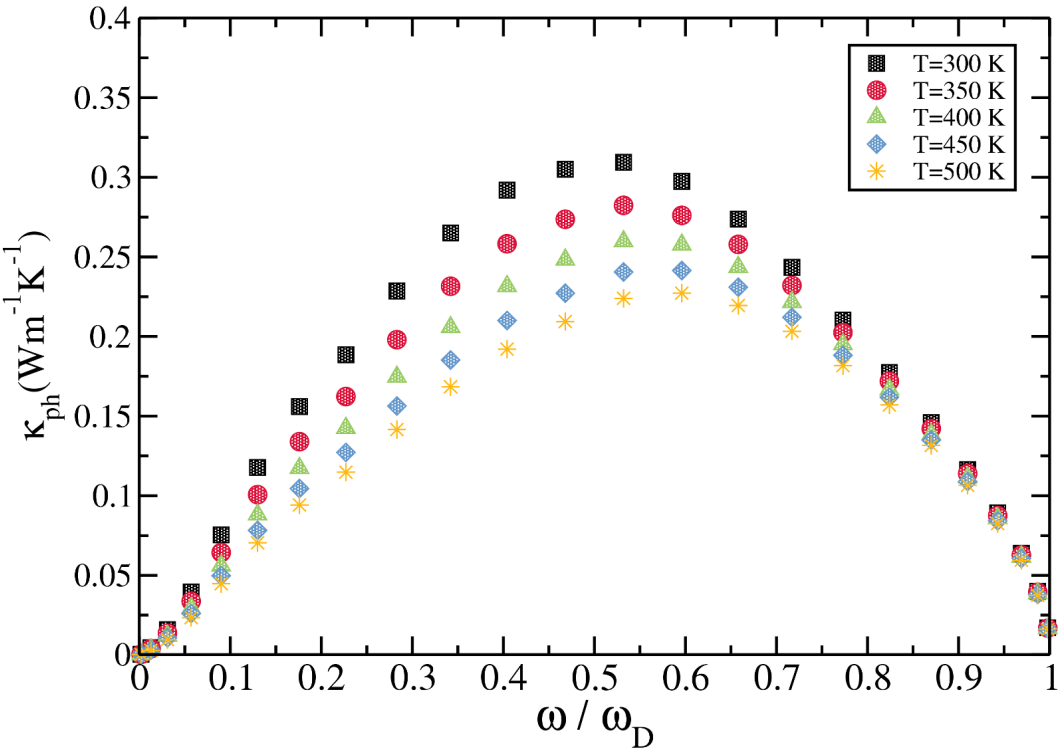

Figure 6.6: Frequency dependence of the phonon thermal conductivity for p-type 3 wt.% Te doped $(Bi_2Te_3)_{0.20}(Sb_2Te_3)_{0.80}$ single crystal at several temperatures where the Debye frequency is taken as ω_D=17.62 THz.

The spectral analysis of the phonon thermal conductivity in the frequency space is represented in Fig. 6.6 for the p-type doped $(Bi_2Te_3)_{0.20}(Sb_2Te_3)_{0.80}$ single crystal at several temperatures. Similar to the n-type doped $(Bi_2Te_3)_{0.85}(Bi_2Se_3)_{0.15}$ single crystal studied in Chapter 4 the spectrum becomes wider and the peak shifts to higher frequency when the temperature increases. This can be easily explained by noting that the energy of the dominant phonon is directly proportional to crystal temperature: $\hbar\omega_{dom} \simeq 1.6k_BT$ [14]. Furthermore, it is theoretically found that the spectrum peaks at the frequency $\omega_D/1.92$ (where ω_D is the Debye frequency) and $\omega_D/1.66$ at 300 K and 500 K, respectively. Compared to the n-type doped alloy presented in Chapter 4 the maximum value of $\kappa_{\rm ph}$ occurs at a considerably lower frequency for the p-type doped alloy. This results from the smaller Debye

frequency of 17.62 THz for the p-type alloy, compared to 18.92 THz for the n-type alloy sample reported in Chapter 4.

6.3.2.1 Summary

The thermal conductivity contributions arising from carriers, electron-hole pairs, and phonons are theoretically studied for n-type 0.1 wt.% CuBr doped $(Bi_2Te_3)_{0.85}$ $(Bi_2Se_3)_{0.15}$ and p-type 3 wt.% Te doped $(Bi_2Te_3)_{0.2}(Sb_2Te_3)_{0.8}$ single crystals and relevant parameters has been fitted to successfully reproduce the experimental measurements obtained by Hyun *et al.* [13] and Li *et al.* [19] in the temperature range 300 K $\leqslant T \leqslant$ 500 K. In this temperature range nearly three times smaller total thermal conductivity is attained for the p-type doped alloy due to its lower $\kappa_{\rm c}$, $\kappa_{\rm bp}$, and $\kappa_{\rm ph}$ results. Comparatively significant reduction in $\kappa_{\rm ph}$ for the p-type sample comes from much stronger isotopic and alloy scattering rates of phonons. Additionally, the phonon thermal conductivity - frequency spectrum is studied for the p-type doped sample and found that the spectrum becomes wider and the peak value shifts to higher frequencies as the temperature increases. Compared to n-type doped alloy, the highest value of $\kappa_{\rm ph}$ takes place at smaller frequency owing to its lower Debye frequency.

Table 6.2: Parameters used in the calculations of the thermal conductivity of 0.1 wt.% CuBr doped $(Bi_2Te_3)_{0.85}(Bi_2Se_3)_{0.15}$ and 3 wt.% Te doped $(Bi_2Te_3)_{0.2}(Sb_2Te_3)_{0.8}$ single crystals.

Property/Parameter	$(Bi_2Te_3)_{0.85}(Bi_2Se_3)_{0.15}$	$(Bi_2Te_3)_{0.2}(Sb_2Te_3)_{0.8}$
$E_g(0)$ (eV)	0.16	0.09
r	0.1	0.45
F_{bp} ($\mathrm{Wm^{-1}K^{-1}}$)	3.4×10^{-4}	13.0×10^{-4}
p	1.0	1.0
q_D ($\mathrm{\AA^{-1}}$)	0.7113	0.603
Ω ($\mathrm{\AA^3}$)	164.94	160.414
$\bar{c}$ (m/s) [18]	2611	2922
$\Gamma_{\mathrm{isotopes}}$	0.000112	0.025
Γ_{alloy}	0.00447	0.05
ρ ($\mathrm{kg/m^3}$) [17]	7.7×10^3	6.69×10^3
$F_{3\mathrm{ph}}$ ($\mathrm{s^2/m^2}$)	LT:0.2×10^{-5}, HT:0.4×10^{-5}	1.057×10^{-5}

Bibliography

[1] D. M. Rowe and C. M. Bhandari, Modern Thermoelectrics (Reston Publishing Company, Virginia, 1983).

[2] D. M. Rowe, Thermoelectrics Handbook (Taylor and Francis Group, London, 2006).

[3] B. Poudel, Q. Hao, Y. Ma, Y. Lan, A. Minnich, B. Yu, X. Yan, D. Wang, A. Muto, D. Vashaee, X. Chen, J. Liu, M. S. Dresselhaus, G. Chen, and Z. Ren, Science **320**, 634 (2008).

[4] R. Venkatasubramanian, E. Siivola, T. Colpitts, and B. O'Quinn, Nature **413**, 597 (2001).

[5] V. Goyal, D. Teweldebrhan, and A. A. Balandin, App. Phys. Lett. **97**, 133117 (2010).

[6] F. Zahid and R. Lake, App. Phys. Lett. **97**, 212102 (2010).

[7] R. R. Heikes and R. W. Ure, Thermoelectricity, Science and Engineering (Interscience Publishers, New York, 1961).

[8] P. J. Price, Phil. Mag. **46**, 1252 (1955).

[9] C. J. Glassbrenner and G. A. Slack, Phys. Rev. **134**, A1058 (1964).

[10] Ö. C. Yelgel and G. P. Srivastava, Phys. Rev. B **85**, 125207 (2012).

[11] Ö. C. Yelgel and G. P. Srivastava, J. Appl. Phys. **113**, 073709 (2013).

[12] G. P. Srivastava, The Physics of Phonons (Taylor and Francis Group, New York, 1990).

[13] D. B. Hyun, J. S. Hwang, B. C. You, T. S. Oh, and C. W. Hwang, J. Mat. Sci. **33**, 5595 (1998).

[14] J. M. Ziman, Electrons and Phonons (Clarendon Press, Oxford, 1960).

[15] Y. K. Koh and D. G. Cahill, Phys. Rev. B **76**, 075207 (2007).

[16] D. B. Hyun, J. S. Hwang, T. S. Oh, J. D. Shim, and N. V. Kolomoets, J. Phys. Chem. Sol. **59**, 1039 (1998).

[17] D. R. Lide, CRC Handbook of Chemistry and Physics (Taylor and Francis Group LLC, 87th Edition, 2007).

[18] L. W. Silva and M. Kaviany, Int. J. Heat and Mass **47**, 2417 (2004).

[19] D. Li, R. R. Sun, and X. Y. Qin, Intermet. **19**, 2002 (2011).

Chapter 7

Thermoelectric Properties of $Bi_2Se_3/Bi_2Te_3/Bi_2Se_3$ and $Sb_2Te_3/Bi_2Te_3/Sb_2Te_3$ Quantum Well Systems

7.1 Introduction

In the early 1990s, Hicks *et al.* [1, 2] theoretically predicted that ZT could be greatly enhanced by using low-dimensional nanostructured thermoelectric materials characterised by quantum confinement of carriers. Their prediction brought an entirely new perspective to the area of thermoelectric research. In addition to the consideration made by Hicks *et al.* [1, 2], it is being realised that by introducing more boundaries or interfaces in nanocomposite materials phonons can be more scattered than in bulk form, resulting in dramatic reduction in phonon thermal conductivity [3, 4]. The advantage of the concept of nanostructuring is

that ZT can be improved by decreasing phonon conductivity without reducing the power factor ($S^2\sigma$) strongly. In fact in some cases increasing power factor is also possible while there is a reduction in $\kappa_{\rm ph}$. In the work of Hicks *et al.* [1], Bi_2Te_3 quantum-well structures are investigated by considering effectively infinite potentials for electron confinement and negligible widths of the barriers for thermal transport. Consequently, it has been theoretically shown that ZT goes up monotonically by reducing the well widths [1, 2]. Lin-Chung *et al.* [5], following the prediction by Hicks *et al.* [1], made a new attempt by considering non-zero barrier widths for realistic $Bi_2Te_3/Pb_{0.75}Sn_{0.25}Te$ superlattice systems. They recovered the results of Hicks *et al.* [1] for zero barrier width and found considerably reduced ZT for finite barrier thicknesses but still higher than the ZT of bulk form. The reduction in ZT results because thermal and electric currents flow along both the barriers and the wells in the non-zero barrier widths case. The theoretical works studied by both Hicks *et al.* [1] and Lin-Chung *et al.* [5] assumed that lattice contribution of the thermal conductivity ($\kappa_{\rm ph}$) could be taken to be the bulk value of Bi_2Te_3 for well widths greater than phonon mean free path and also presumed to be both temperature and well width independent.

Experiments performed by Venkatasubramanian *et al.* [6] also support the nanostructuring approach for finding extraordinarily high ZT value of 1.46 for n-type $Bi_2Te_3/Bi_2Te_{2.83}Se_{0.17}$ superlattices and 2.4 for p-type Bi_2Te_3/Sb_2Te_3 superlattices at 300 K. Very recently, Hinsche *et al.* [7] reported a theoretical work on Bi_2Te_3 / Sb_2Te_3 superlattices of different periods to explain the experimental results obtained by Venkatasubramanian *et al.* [6]. In their theoretical calculations the value of $\kappa_{\rm ph}$ was taken from previous experimental works for superlattices only at room temperature and treated again as temperature and well width independent. However, they did not even discuss different phonon scattering mechanisms and their importance for low-dimensional systems, and indeed could not obtain the

expected ZT values reported by Venkatasubramanian *et al.* [6].

In this chapter, based on temperature and well width dependent Fermi level, a full theory of thermoelectric properties is investigated for n-type 0.1 wt.% CuBr doped $Bi_2Se_3/Bi_2Te_3/Bi_2Se_3$ and p-type 3 wt.% Te doped Sb_2Te_3 / Bi_2Te_3 / Sb_2Te_3 quantum well systems in the temperature region 50 K - 600 K. Different values of well thicknesses are considered for both types of quantum well systems to study the effect of confinement on all thermoelectric transport coefficients. The temperature and well width variations of the electronic transport coefficients S, σ, and $\kappa_{\rm c}$ are calculated by following a slight variation of the theory presented by Hicks *et al.* [1] for quantum well structures. The temperature dependence of the thermal conductivity contributions from electron-hole pairs ($\kappa_{\rm bp}$) and phonons ($\kappa_{\rm ph}$) are computed by employing Price's theory [8] and Srivastava's scheme [9], respectively. Phonon scattering rates including various types of scattering mechanisms are taken into account rigorously. Finally, all the thermoelectric transport properties of both n- and p-type quantum well systems are compared with the corresponding bulk forms as n-type 0.1 wt.% CuBr doped 85% Bi_2Te_3 - 15% Bi_2Se_3 and p-type 3 wt% Te doped 20% Bi_2Te_3 - %80 Sb_2Te_3 single crystals reported in Chapter 4 and 5.

Theoretical Modelling of Thermoelectric Properties in Quantum Well Systems

As given in Chapter 3, a composite system grown in z-direction of B/A/B layers of material A (comprised of n_A atomic layers of thickness a each, and total thickness d_A) and material B (comprised of n_B atomic layers of thickness b each, and total thickness d_B), with A forming a two-dimensional quantum well (2D QW) is considered for the calculation of thermoelectric properties in low dimensional systems. A schematic structure of this quantum well system can be seen in Fig. 7.1. Following the work of Lin-Chung *et al.* [5], for such a system with current

flow perpendicular to the growth direction (with no loss of generality, we may take it along x-axis) and having negligible barrier widths ($d_B \simeq 0$), the thermoelectric transport coefficients can be expressed as [5]

$$S = S_A, \qquad \sigma = \sigma_A, \qquad \kappa_{\rm c} = \kappa_A. \tag{7.1}$$

For both n- and p-type quantum well structures studied here Bi_2Te_3 is the well material (material A) due to its lower band gap.

7.2 Electronic Transport Properties

7.2.1 Fermi Level

As described in Chapter 3, in 2D quantum well structures, the temperature variation of $E_{\rm f}$ in extrinsic regime is given as

for n-type :

$$E_{\rm f}^{\rm ext,n} = \frac{1}{2}(E_{\rm c} + E_{\rm d}) + \frac{k_{\rm B}T}{2}\ln\frac{N_{\rm d}}{2U_{\rm c}} - k_{\rm B}T\sinh^{-1}\Big[\sqrt{\frac{U_{\rm c}}{8N_{\rm d}}}\exp\Big(\frac{-\Delta E_{\rm i}^{\rm (n)}}{2k_{\rm B}T}\Big)\Big] - \frac{\hbar^2\pi^2}{2m_z^* d_A^2}j,$$

for p-type :

$$E_{\rm f}^{\rm ext,p} = \frac{1}{2}(E_{\rm a} + E_{\rm v}) + \frac{k_{\rm B}T}{2}\ln\frac{N_{\rm a}}{2U_{\rm v}} - k_{\rm B}T\sinh^{-1}\Big[\sqrt{\frac{U_{\rm v}}{8N_{\rm a}}}\exp\Big(\frac{-\Delta E_{\rm i}^{\rm (p)}}{2k_{\rm B}T}\Big)\Big] - \frac{\hbar^2\pi^2}{2m_z^* d_A^2}j, \tag{7.2}$$

where j is the number of sub-band, $E_{\rm c}$ is the conduction band edge, $E_{\rm v}$ is the valence band edge, $E_{\rm d}$ is the donor energy level and $E_{\rm a}$ is the acceptor energy level. The donor and acceptor ionisation energies are determined respectively as $\Delta E_{\rm i}^{\rm (n)} = E_{\rm c} - E_{\rm d}$ and $\Delta E_{\rm i}^{\rm (p)} = E_{\rm a} - E_{\rm v}$. The parameters given as $U_{\rm c}$=$2((m_{\rm n}^* k_{\rm B}T)/(2\pi\hbar^2))^{3/2}$ and $U_{\rm v}$=$2((m_{\rm p}^* k_{\rm B}T)/(2\pi\hbar^2))^{3/2}$ where $k_{\rm B}$ is the Boltzmann constant [10]. $N_{\rm d}$ and

$N_{\rm a}$ are the concentrations of donor impurity and acceptor impurity atoms, respectively. The effective masses are represented by $m^*_{\rm n}$ for the electron mass and $m^*_{\rm p}$ for the hole mass.

In a doped semiconductor, beyond a sufficiently high temperature, donors at the $E_{\rm d}$ level (or acceptors at $E_{\rm a}$) become fully ionized and the material behaves like intrinsic semiconductor. In this regime the temperature dependences of $E_{\rm f}$ for both n- and p-type doped semiconductor quantum well structures can be expressed by subtracting the confined energy term to the bulk expression [10]

$$E_{\rm f}^{\rm int} = \frac{E_{\rm v} + E_{\rm c}}{2} + \frac{3}{4} k_{\rm B} T \ln\Big(\frac{m^*_{\rm p}}{m^*_{\rm n}}\Big) - \frac{\hbar^2 \pi^2}{2 m^*_z d_A^2}. \tag{7.3}$$

Neither of n-type 0.1 wt.% CuBr doped $Bi_2Se_3/Bi_2Te_3/Bi_2Se_3$ and p-type 3 wt.% Te doped $Sb_2Te_3/Bi_2Te_3/Sb_2Te_3$ quantum well systems studied here reach the intrinsic regime in the temperature range 50 K $\leq T \leq$ 600 K. Therefore, all the following discussions provided here will be based on the use of the extrinsic regime only.

7.2.2 Seebeck Coefficient

Within the single-band nearly-free-electron(hole) consideration in the $x-y$ plane we determine the in-plane electronic transport properties (S, σ, and $\kappa_{\rm c}$) of a 2D quantum well system in terms of Fermi level and using Fermi-Dirac statistics. Therefore, the Seebeck coefficient can be written as

$$S = \pm \frac{k_{\rm B}}{e} \Big[\frac{(2+r)}{(1+r)} \frac{F_{1+r}}{F_{0+r}} - \zeta^* \Big], \tag{7.4}$$

where the minus sign is for n-type materials, the plus sign is for p-type materials, $\zeta^* = E_{\rm f}/k_{\rm B}T$ is the reduced chemical potential, F_i is the Fermi integral and it is also considered that charge carriers (electrons or holes) are scattered in such way

that their relaxation time (τ) may be expressed in terms of the energy (E) with the relation of $\tau = \tau_0 E^r$ where τ_0 is a constant and r is called the scattering parameter.

7.2.3 Electrical Conductivity

For our quantum well systems studied here it is considered that carriers (electrons or holes) are confined to the $x - y$ plane (parallel to the layers) without suffering scattering at the interface layers. Therefore, the carrier mobility in a direction parallel to the layers is unchanged and will have the same expression as for bulk systems. So the electrical conductiviy in a semiconductor quantum well is given by

$$\sigma = Ne\mu_c = N\frac{e^2}{m_c^*}\langle\tau\rangle, \tag{7.5}$$

where μ_c is the conductivity mobility, m_c^* is the conductivity effective mass, $\langle\tau\rangle$ is an average relaxation time for carriers and N is the carrier concentration and defined as [11, 12, 13],

$$N = \int_0^\infty g(E)f_0(E)dE = \frac{k_{\mathrm{B}}T}{\pi\hbar^2 d_A}\sqrt{m_x^* m_y^*}F_0, \tag{7.6}$$

with $g(E)$ as the density of states for nearly free electron gas for 2D systems and $f_0(E)$ being the Fermi-Dirac distribution function. In our n- and p-type doped Bi_2Te_3 based quantum well systems electrons (or holes) mostly scatter with the long wavelength phonons. The carrier-acoustic phonon scattering rate is given by [11, 14]

$$\tau_{\mathrm{ac}}^{-1}(E,T) = \frac{\sqrt{2}}{\pi}\frac{E_D^2 {m_D^*}^{3/2} k_B T}{\hbar^4 \rho c_L^2}\sqrt{E}, \tag{7.7}$$

where m_D^* is the density of states effective mass, c_L is the velocity of longitudinal phonons, ρ is the mass density, and E_D is the deformation potential. The average

relaxation time is written as [12],

$$\langle\tau\rangle = \frac{\int \tau(W) W^{3/2} \exp(-W) \mathrm{d}W}{\int W^{3/2} \exp(-W) \mathrm{d}W} = \frac{4}{3}\sqrt{\frac{\pi}{2}} \frac{\hbar^4 \rho c_L^2}{E_D^2 {m_D^*}^{3/2} (k_B T)^{3/2}}, \tag{7.8}$$

with $W = E/k_B T$. Thus, the in-plane electrical conductivity of the quantum well systems in the extrinsic regime can be expressed as

$$\sigma = \frac{4}{3d_A} \frac{\hbar^2 \rho c_{\mathrm{L}}^2}{\sqrt{2\pi}} \frac{e^2}{m_x^* \sqrt{m_z^*}} \frac{F_0}{E_{\mathrm{D}}^2 (k_{\mathrm{B}} T)^{1/2}}. \tag{7.9}$$

7.3 Thermal Transport Properties

The total thermal conductivity (κ_{total}) is determined by combining three contributions, arising from carriers (electrons or holes) (κ_{c}), electron-hole pairs (bipolar, or κ_{bp}), and lattice (*i.e.* from phonons, κ_{ph}).

7.3.1 Carrier Thermal Conductivity

The carrier contribution on the total thermal conductivity (κ_{c}) is expressed by the Wiedemann-Franz law as

$$\kappa_{\mathrm{c}} = \sigma \mathcal{L} T = \left(\frac{k_B}{e}\right)^2 \sigma T \mathcal{L}_0, \tag{7.10}$$

where $\mathcal{L}$ is the Lorenz number and including the carrier scattering parameter r for the quantum well systems, and the $\mathcal{L}_0$ parameter can be expressed as

$$\mathcal{L}_0 = \frac{(3+r)F_{2+r}}{(1+r)F_{0+r}} - \left[\frac{2+r}{1+r}\frac{F_{1+r}}{F_{0+r}}\right]^2. \tag{7.11}$$

7.3.2 Bipolar Thermal Conductivity

The electron-hole pair contribution ($\kappa_{\rm bp}$) to the total thermal conductivity can be expressed as [15, 16]

$$\kappa_{\rm bp} = F_{\rm bp} T^p \exp(-E_{\rm g}/2k_{\rm B}T), \tag{7.12}$$

with $F_{\rm bp}$ and p regarded as adjustable parameters. The only difference in the $\kappa_{\rm bp}$ expression between bulk and quantum well structures originates from the definition of the band gap $E_{\rm g}$ due to the confinement effects on electron and hole energy levels in the latter structure given as

$$E_{\rm g}({\rm QW}) = E_{\rm c} - E_{\rm v} + \frac{\hbar^2\pi^2}{2d_A^2}\Big(\frac{1}{m^*_{z,e}} + \frac{1}{m^*_{z,h}}\Big), \tag{7.13}$$

where the effective masses of electrons and holes in the growth direction are $m^*_{z,e}$ and $m^*_{z,h}$, respectively.

7.3.3 Lattice Thermal Conductivity

For the lattice thermal conductivity of quantum well systems we used the same treatment as we made for the bulk systems and applied the Debye's isotropic continuum approximation within the single-mode relaxation time scheme expressed as [9]

$$\kappa_{\rm ph} = \frac{\hbar^2 q_D^5}{6\pi^2 k_B T^2} \sum_s c_s^4 \int_0^1 dx x^4 \tau \bar{n}(\bar{n}+1), \tag{7.14}$$

where q_D is the Debye radius, $x = q/q_D$ is a reduced wavenumber, s is phonon polarisation index, $\bar{n}$ is the Bose-Einstein distribution function, c_s is the velocity of phonons defined for polarisation branch s.

For the quantum well structures, phonon relaxation rate τ^{-1} is contributed by several scattering mechanisms: boundary (bs), carriers (carr), mass defects (md), interface mass-mixing (ims), interface dislocation (ids) and anharmonicity (anh).

The same expressions given in Chapter 2 will be used for the phonon scattering rates sourced from sample boundaries, carriers and mass defects. Additional to these scattering mechanisms, two extra considerations must be made when making a complete assessment of the phonon relaxation time when dealing with quantum well structures: interface mass-mixing scattering (ims) resulting from diffusion or mixing of atoms at the interfaces and interface dislocation scattering (ids) arising from dislocations or missing bonds present at interfaces.

As described in Chapter 3, we express the interface mass-mixing scattering rate as

$$\tau_{qs}^{-1}(\text{ims}) = \frac{\Gamma_{\text{ims}}\Omega}{4\pi\bar{c}^3}\omega^4(qs), \tag{7.15}$$

with the mass-mixing parameter for a quantum well system given as

$$\Gamma_{\text{ims}} = \frac{2\beta_0}{(n+m)}\sum_i \exp\Big(-\Big|\frac{l_i - l_0}{d}\Big|\Big)\Big(\frac{\Delta M_i}{\bar{M}}\Big)^2\Big[\Big(1-\frac{e_A^2}{e_B^2}\Big)^2 + \Big(1-\frac{e_B^2}{e_A^2}\Big)^2\Big], \tag{7.16}$$

where Ω is the volume of a unit cell, d is the interlayer distance (a in the well and b in the barrier), l_i is the layer distance from interface, l_0 is the z coordinate of the interface, β_0 is the mass-mixing fraction at distance nd or md from the interface, and e_B/e_A is the ratio of the amplitudes of eigenvectors in materials B and A.

As reported in Chapter 3 in detail, we express the phonon relaxation rate due to interface dislocation scattering as

$$\tau_{qs}^{-1}(\text{ids}) = \frac{\Gamma_{\text{ids}}\Omega}{8\pi\bar{c}^3}\omega_0^4, \tag{7.17}$$

where ω_0 can be approximated as the highest zone-centre frequency ($\omega_0 = \omega_D = \bar{c}.q_D$) and the interface dislocation parameter is written as

$$\Gamma_{\text{ids}} = \frac{2\beta_0'}{(n+m)}\sum_i \exp\Big(-\Big|\frac{l_i - l_0}{d}\Big|\Big)\Big(\frac{\Delta M_i}{\bar{M}}\Big)^2\Big[1+\Big(\frac{e_A^2}{e_B^2}\Big)^2 + 1 + \Big(\frac{e_B^2}{e_A^2}\Big)^2\Big], \tag{7.18}$$

with β_0' being the fraction of broken bonds in the interface region.

The amplitude ratio e_B/e_A required for both interface mass-mixing and dislocation scattering mechanisms is approximated using the diatomic linear chain model along the growth direction as

$$\frac{e_B}{e_A} = \frac{\left[\frac{1}{M_0} - \Delta\left(\frac{1}{M}\right)\right]\cos(l_z q_z)}{\left\{\left(\frac{1}{M_0}\right)^2 \cos^2(l_z q_z)\left[\Delta\left(\frac{1}{M}\right)\right]^2 \sin^2(l_z q_z)\right\}^{1/2} - \Delta\left(\frac{1}{M}\right)}, \tag{7.19}$$

with $1/M_0 = \frac{1}{2}(1/M_A + 1/M_B)$, $\Delta(1/M) = \frac{1}{2}(1/M_A - 1/M_B)$ and $l_z = d_A + d_B$ is the period along the growth direction.

Finally, our consideration of the anharmonic phonon scattering mechanism in quantum well systems is based on Srivastava's scheme for bulk systems, for which [9]

$$\begin{aligned}\tau_{qs}^{-1}(\text{anh, bulk}) =& \frac{\hbar q_D^5 \gamma^2}{4\pi\rho\vec{c}^2} \sum_{s's''\varepsilon} \Bigg[\int dx' x'^2 x''_+ [1 - \varepsilon + \varepsilon(Cx + Dx')] \frac{\bar{n}_{q's'}(\bar{n}''_+ + 1)}{(\bar{n}_{qs} + 1)} \\ &+ \frac{1}{2} \int dx' x'^2 x''_- [1 - \varepsilon + \varepsilon(Cx - Dx')] \frac{\bar{n}_{q's'}\bar{n}''_-}{\bar{n}_{qs}} \Bigg],\end{aligned} \tag{7.20}$$

where γ is the Grüneisen constant, $x' = q'/q_D$, x''_+=$Cx \pm Dx'$, $\bar{n}''_\pm = \bar{n}(x''_\pm)$, $C = c_s/c_{s''}$, $D = c_{s'}/c_{s''}$. $\varepsilon = 1$ for momentum-conserving Normal processes, and ε=-1 for momentum-nonconserving Umklapp processes. The first and second terms in equation (7.20) are controlled by class 1 events $\mathbf{q}s + \mathbf{q}'s' \rightarrow \mathbf{q}''s''$ and class 2 events $\mathbf{q}s \rightarrow \mathbf{q}'s' + \mathbf{q}''s''$, respectively. The integration limits on the variables x and x', derived from a detailed consideration of the energy and momentum conservation requirements, have been presented in Ref. [9] elaborately. Equation (7.20) is valid for the materials containing only one atom per primitive unit cell, namely for bulk systems. When the number of atoms increases in a unit cell, Eq. (7.20) should be re-written owing to increased amount of anharmonic scattering strength. Following the discussions given in Chapter 3 with Refs. [17, 18] we model the anharmonic phonon scattering rate for QW systems as

$$\tau_{qs}^{-1}(\text{anh, QW}) = \tau_{qs}^{-1}(\text{anh, bulk})(n_A + n_B)^{2/3}. \tag{7.21}$$

7.4 Results and Discussion

In this present work, the thermoelectric properties of n-type 0.1 wt.% CuBr doped Bi_2Te_3/Bi_2Se_3 and p-type 3 wt.% Te doped Bi_2Te_3/Sb_2Te_3 quantum well systems are theoretically investigated for various quantum well widths (7 nm $\leqslant d_A \leqslant$ 20 nm) in the temperature range 50 K - 600 K. All integrals are evaluated numerically by applying Simpson's rule and all other related parameters for the calculations are listed in Tab. 7.1. For the n-type quantum wells we have estimated the values of valence and conduction band off-sets are nearly 0.08 eV and 0.09 eV, respectively. Also, for the p-type quantum wells we have estimated that both band off-sets are nearly equal to 0.01 eV.

7.4.1 Electronic Transport Coefficients

7.4.1.1 Fermi Level

Figure 7.1 represents the Fermi level diagram for both n-type 0.1 wt.% CuBr doped $Bi_2Se_3/Bi_2Te_3/Bi_2Se_3$ and p-type 3 wt.% Te doped $Sb_2Te_3/Bi_2Te_3/Sb_2Te_3$ quantum well systems. Suitable selections for the value of well widths is made by bearing in mind that while the well width decreases the conduction band of the well material increases and at some critical value of the well width d_A this conduction band edge exceeds the conduction band level of the barrier material. We theoretically found that the smallest value of d_A should be taken as 7 nm and 10 nm for the n-type and p-type quantum well systems, respectively.

In Fig. 7.2, the temperature variation of the Fermi level is shown for both n- and p-type doped quantum wells including their theoretical bulk alloy results reported in our previous works [15, 16]. As can be expected from Eq. (7.2), E_{f} of quantum

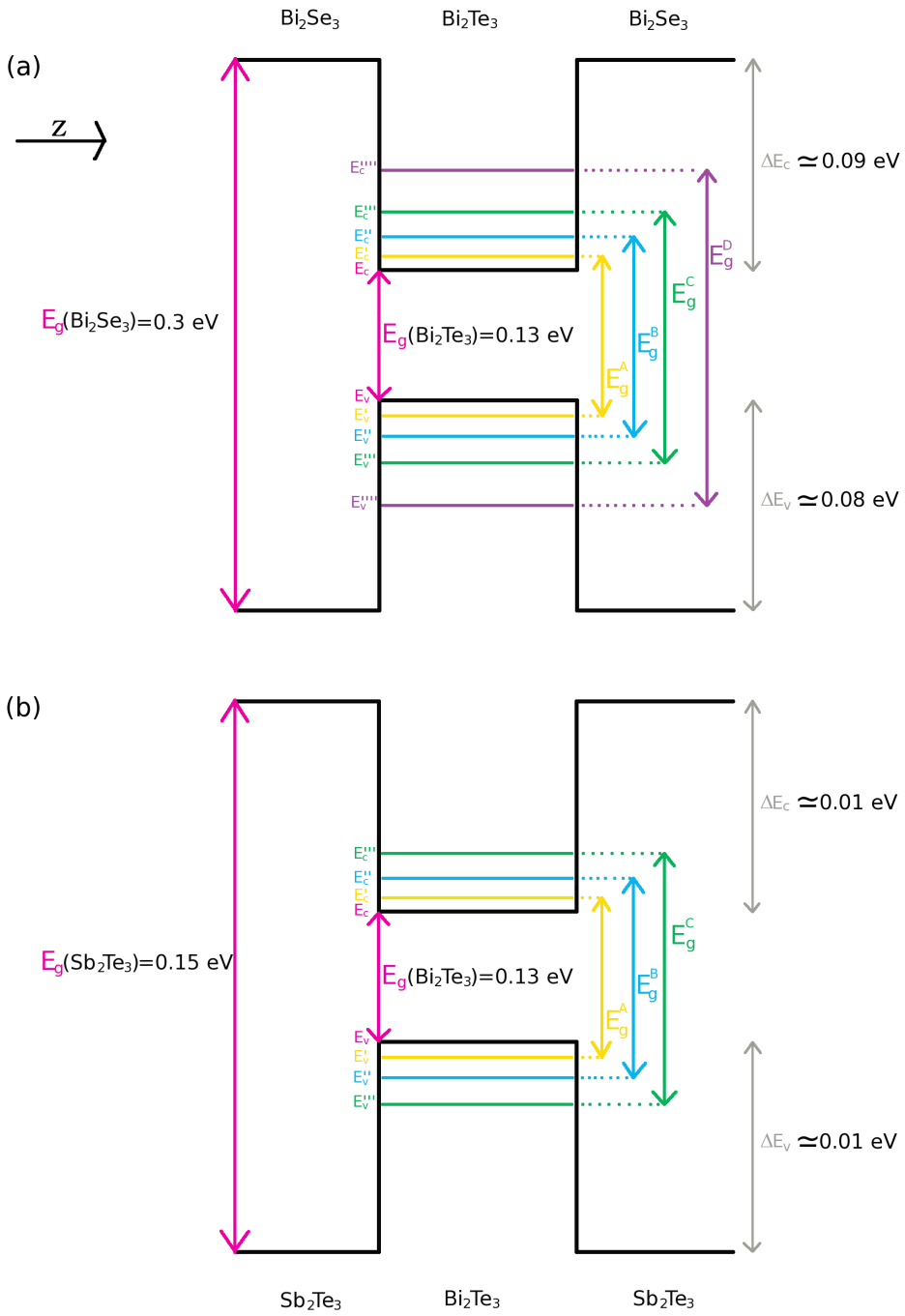

Figure 7.1: Fermi diagram of quantum well systems made with (a) n-type 0.1 wt.% CuBr doped $Bi_2Se_3/Bi_2Te_3/Bi_2Se_3$ and (b) p-type 3 wt.% Te doped $Sb_2Te_3/Bi_2Te_3/Sb_2Te_3$. Indirect band gap values for Bi_2Te_3, Bi_2Se_3, and Sb_2Te_3 are read from Refs. [7] and [19]. Samples with the band gaps of E_g^A, E_g^B, E_g^C, E_g^D are calculated for the values of quantum well widths taken as d_A=20 nm, 15 nm, 10 nm, and 7 nm, respectively.

well systems decreases with reducing the quantum well width d_A. Moreover, as we reported previously [15, 16] both n- and p-type doped bulk alloys show extrinsic behaviour at low temperatures and beyond a certain temperature (T_c=500 K for n-type doped, T_c=425 K for p-type doped sample) they start behaving like an intrinsic material. On the other hand, both the n- and p-type quantum well structures considered here only show extrinsic behaviour and do not reach the intrinsic regime throughout the temperature range studied in this work. Also, for all quantum well systems we studied only a weak temperature variation of E_{f} is found, owing to the opposite signs of term 2 and 3 in Eq. (7.2).

7.4.1.2 Seebeck Coefficient

Figure 7.3 represents the temperature dependence of the in-plane Seebeck coefficient for both n- and p-type doped quantum wells. For comparison the bulk alloy results worked in our earlier studies [15, 16] are also included. As already discussed in the theory section, negative and positive values of the S are gained for the n- and p-type quantum well systems, respectively. The scattering parameters of the n- and p-type quantum wells are taken as the same value for their bulk alloys. For all the quantum well samples the temperature dependence of the S is found to be similar: following Eq. (7.4) it consistently increases with temperature throughout the range studied in this work. This is in contrast to their bulk forms which show a decrement after a certain temperature owing to the onset of the intrinsic behaviour. As shown in Fig. 7.3, for the whole temperature range the magnitude of S for p-type quantum well samples is larger than that for the n-type quantum wells. This suggests that the direct relationship between S and $-\zeta^*$ given in Eq. (7.4) plays a major role for the S - T variation. For all the systems we studied $|S|$ goes up continuously with decreasing the quantum well width, in accordance with Eq. (7.4). This is in an agreement with the work of Lin-Chung *et*

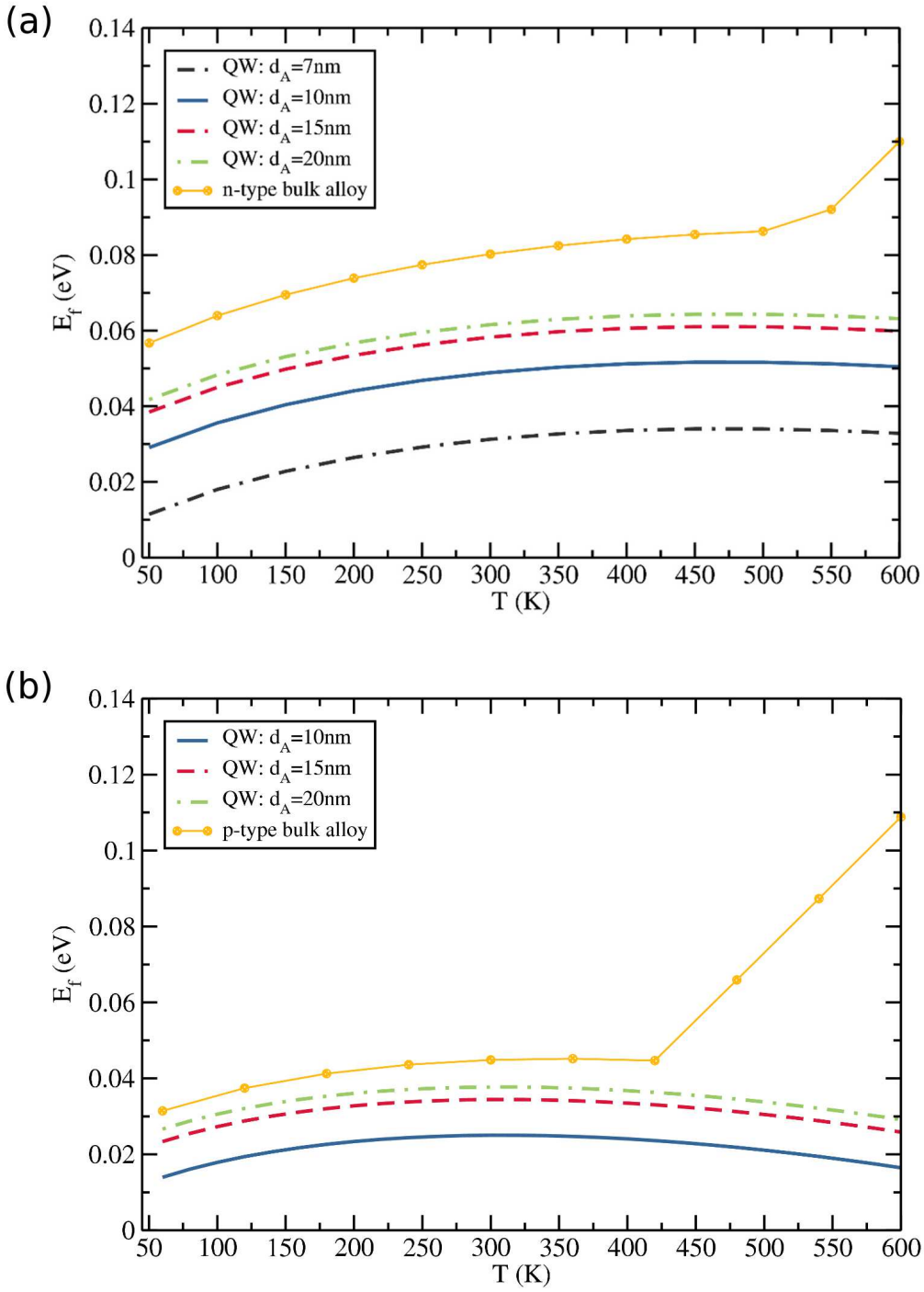

Figure 7.2: Temperature dependence of the Fermi level for (a) n-type 0.1 wt.% CuBr doped $Bi_2Se_3/Bi_2Te_3/Bi_2Se_3$ quantum well where midway between the valence and conduction band edges is set to zero and (b) p-type 3 wt.% Te doped $Sb_2Te_3/Bi_2Te_3/Sb_2Te_3$ quantum well where the valence band edge is set to zero. The symbols represent the theoretical results read from Refs. [15, 16] for n-type 0.1 wt.% CuBr doped 85% Bi_2Te_3 - 15% Bi_2Se_3 and p-type 3 wt% Te doped 20% Bi_2Te_3 - %80 Sb_2Te_3 single crystals.

al. [5] where they have investigated the thermoelectric properties of Bi_2Te_3 quantum wells theoretically. Figures 7.3 (a) and (b) also indicate that magnitudes of S higher than bulk alloys are obtained for the n-type quantum well with d_A=7 nm and p-type quantum well having d_A=10 nm. These results provide a tentative conclusion that use of narrow well widths would be helpful in achieving enhancement in the thermoelectric figure of merit over the corresponding bulk value.

7.4.1.3 Electrical Resistivity

As we did for bulk systems [15, 16], the expression for σ given in Eq. (7.9) is derived by considering that the dominant contribution to the scattering rate comes from the interaction of carriers with acoustic phonons. However, there are additional scattering mechanisms arising from optical phonons, impurities and many-body effects (carrier-carrier). To account for these relatively weak mechanisms, we scaled the electrical resistivity in the following form:

$$\rho = \frac{1}{\sigma} A^{'} T^{\varsigma}, \tag{7.22}$$

where $A^{'}$ and ς are treated as adjustable parameters, with their values given in Tab. 7.1.

Figure 7.4 presents the in-plane electrical resistivity results in the temperature range 50 K - 600 K for both n- and p-type quantum well samples, together with the bulk results studied in our previous works [15, 16] for comparison. The resistivity of all n- and p-type quantum well samples increases with temperature and shows temperature variation similar to the corresponding bulk alloy. For only the n-type quantum well with d_A=7 nm sample we could obtain lower resistivity than its bulk alloy at very high temperatures (above 500 K). In contrast, the calculated electrical resistivities are lower than the corresponding bulk result below

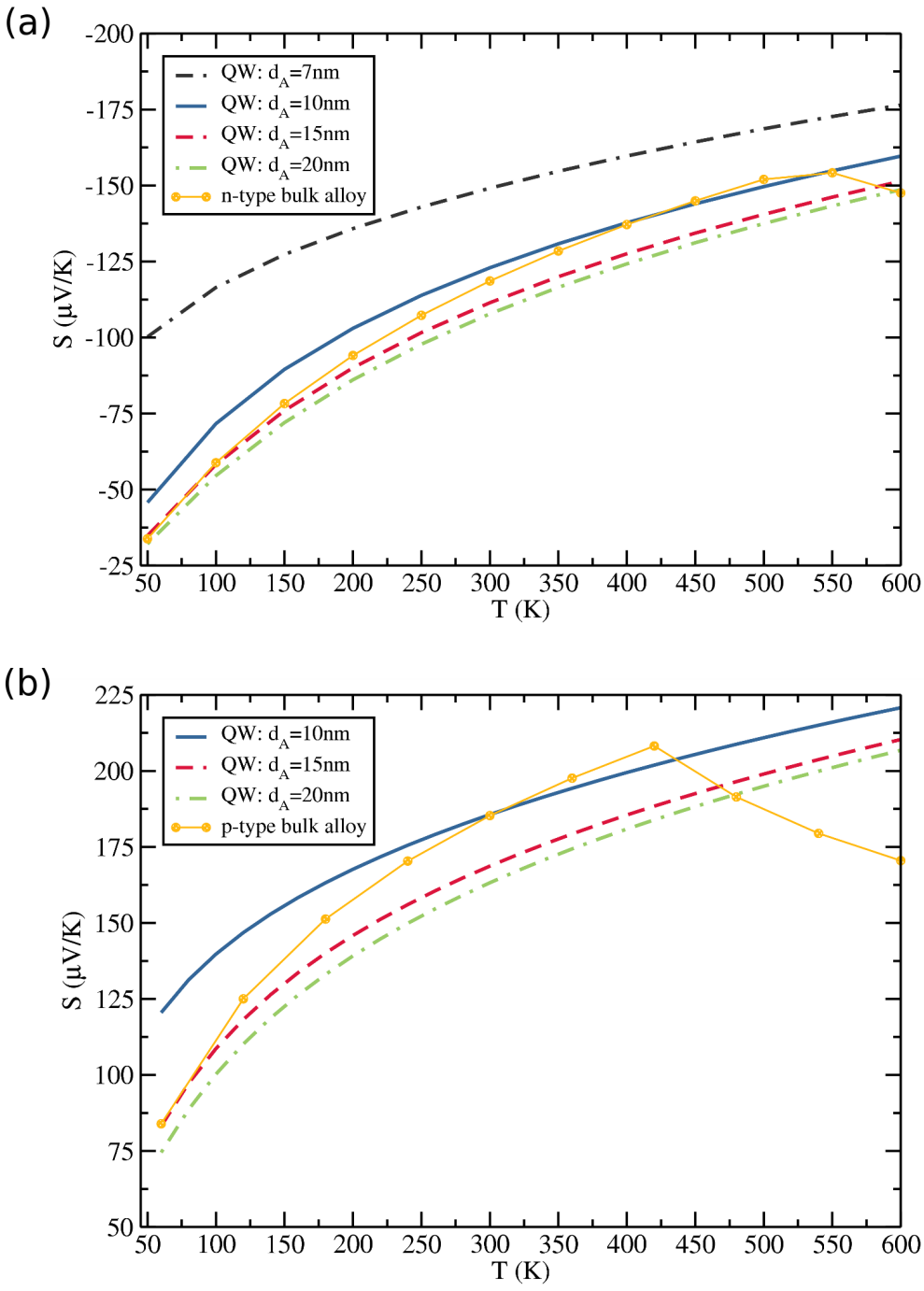

Figure 7.3: Temperature dependence of the Seebeck coefficient for (a) n-type 0.1 wt.% CuBr doped $Bi_2Se_3/Bi_2Te_3/Bi_2Se_3$ and (b) p-type 3 wt.% Te doped $Sb_2Te_3/Bi_2Te_3/Sb_2Te_3$ quantum well systems. The symbols represent the theoretical results read from Refs. [15, 16] for n-type 0.1 wt.% CuBr doped 85% Bi_2Te_3 - 15% Bi_2Se_3 and p-type 3 wt% Te doped 20% Bi_2Te_3 - %80 Sb_2Te_3 single crystals.

350 K, 550 K, and all temperatures for the p-type quantum well with width 20 nm, 15 nm, and 10 nm, respectively. Moreover, for a given d_A the p-type quantum well sample has a larger value of ρ than the n-type quantum well. This can be explained using the appropriate asymptotic expansion of the Fermi integrals. It can be shown that so far as $\eta^* > 1$, the electrical conductivity is proportional to η^* on account of the Fermi integral F_0 in Eq. (7.9). Therefore, at a given temperature higher values of E_{f} lead to lower values for ρ. Additionally, as expected from the Eq. (7.9), the electrical resistivity of our quantum wells increases with increase in the well width d_A. This is also claimed by Lin-Chung *et al.* [5] with similar magnitudes for ρ.

From the above discussion we may conclude that use of narrow p-type quantum wells should help enhance ZT over the corresponding bulk value.

7.4.1.4 Power Factor

For both n- and p-type Bi_2Te_3 based quantum well systems the temperature dependence of the power factor (PF=$S^2\sigma$) is shown in Fig. 7.5 and compared to the previously reported bulk values given in Refs. [15, 16]. In agreement with both the theoretical and experimental work by Dresselhaus *et al.* [20] for the n-type PbTe quantum wells, we found that the PF of both type quantum wells studied here consistently decreases with increase in temperature. Moreover, larger PF values are obtained for narrow quantum well samples (i.e., n-type with d_A=7 nm, and p-type with d_A=10 nm and 15 nm) than their bulk values. The maximum value of the PF occurs at 50 K for both type quantum wells and is found to be 0.055 W m^{-1} K^{-2} for the n-type quantum well with d_A= 7 nm and 0.11 W m^{-1} K^{-2} for the p-type quantum well with d_A=10 nm. This results from the dominant effect of S for the calculation of power factor and higher S^2 values for p-type

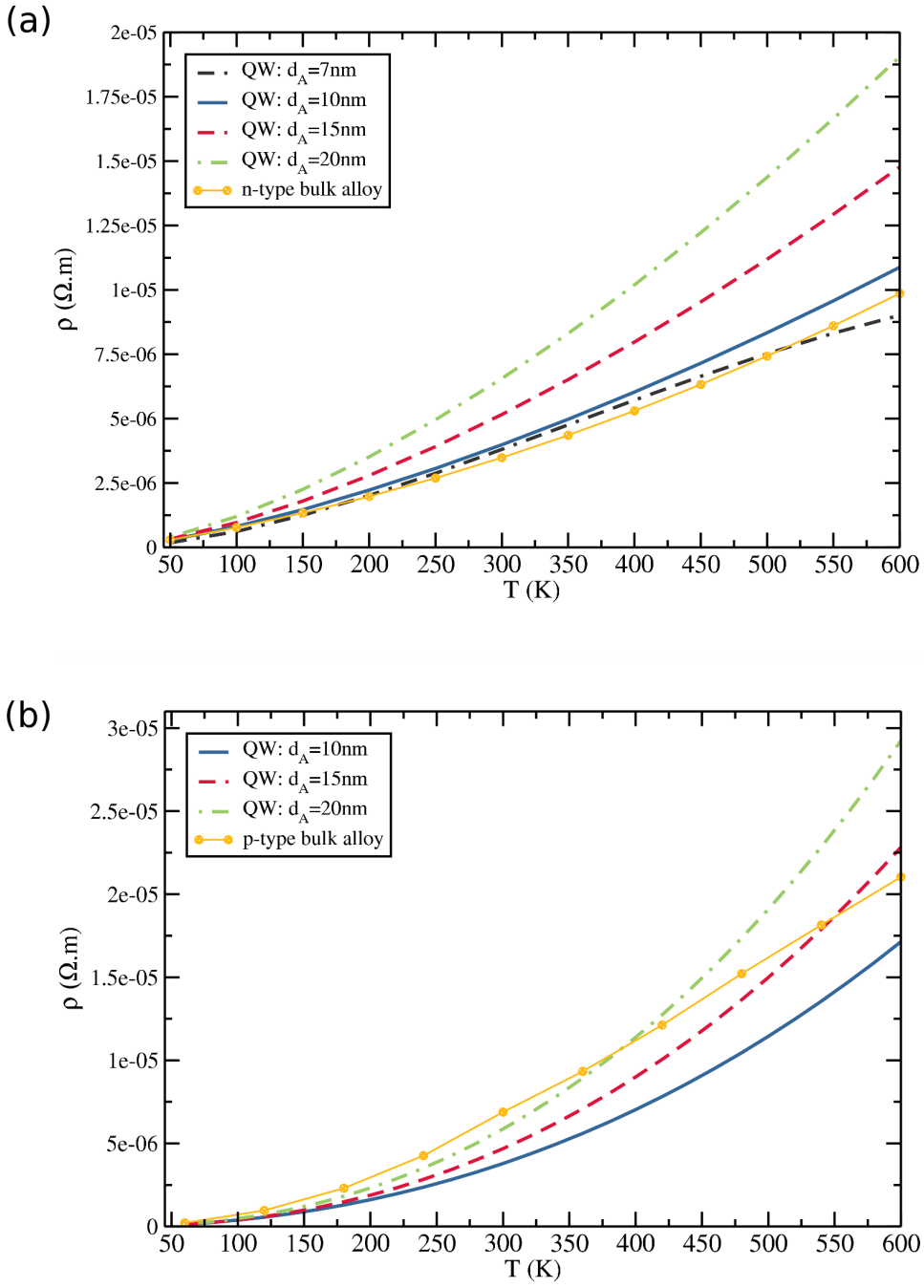

Figure 7.4: Temperature dependence of the electrical resistivity for (a) n-type 0.1 wt.% CuBr doped $Bi_2Se_3/Bi_2Te_3/Bi_2Se_3$ and (b) p-type 3 wt.% Te doped $Sb_2Te_3/Bi_2Te_3/Sb_2Te_3$ quantum well systems. The symbols represent the theoretical results read from Refs. [15, 16] for n-type 0.1 wt.% CuBr doped 85% Bi_2Te_3 - 15% Bi_2Se_3 and p-type 3 wt% Te doped 20% Bi_2Te_3 - %80 Sb_2Te_3 single crystals.

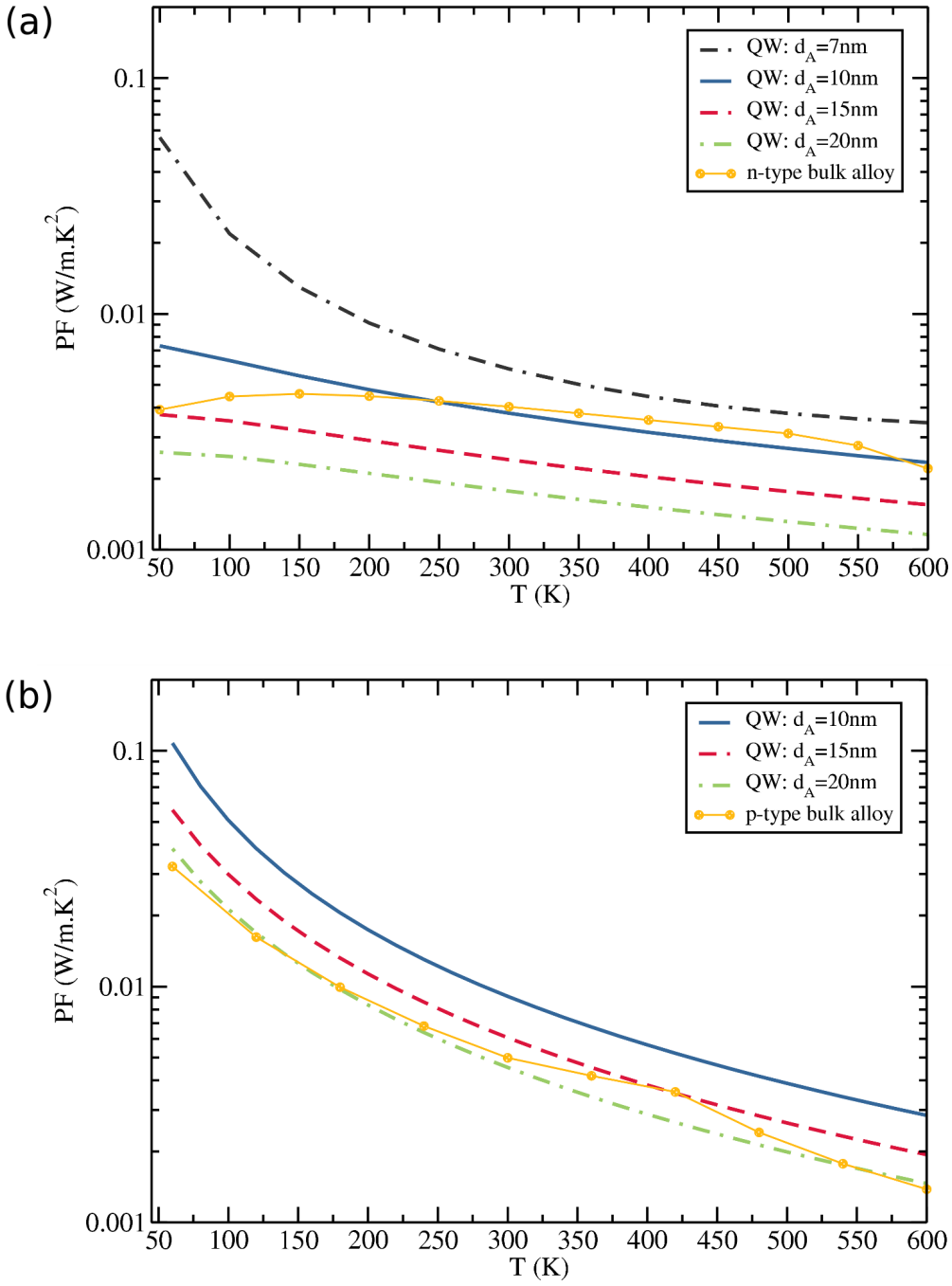

Figure 7.5: Temperature dependence of the power factor for (a) n-type 0.1 wt.% CuBr doped $Bi_2Se_3/Bi_2Te_3/Bi_2Se_3$ and (b) p-type 3 wt.% Te doped $Sb_2Te_3/Bi_2Te_3/Sb_2Te_3$ quantum well systems. The symbols represent the theoretical results read from Refs. [15, 16] for n-type 0.1 wt.% CuBr doped 85% Bi_2Te_3 - 15% Bi_2Se_3 and p-type 3 wt% Te doped 20% Bi_2Te_3 - %80 Sb_2Te_3 single crystals.

quantum wells relative to the n-type quantum well samples. Furthermore, PF droffs off progressively with increase in the quantum well thickness, in agreement with the discussion presented in Ref. [20].

7.4.2 Thermal Transport Coefficients

7.4.2.1 Carrier Thermal Conductivity

The in-plane carrier thermal conductivity for the quantum well systems is determined by employing the Wiedemann-Franz law with the temperature dependent Lorenz number taken as

$$\mathcal{L} = \mathcal{L}_0\Big(\frac{k_{\rm B}}{e}\Big), \tag{7.23}$$

where $\mathcal{L}_0$ is already given in Eq. (7.11) including the scattering parameter r. Thus, $\mathcal{L}$ depends on the Fermi level via the Fermi integrals. As seen in Fig. 7.6, both n- and p-type quantum wells have lower values of $\mathcal{L}$ compared to their bulk samples due to the confinement term in Eqs. (7.2) and (7.3). For a similar reason, while the well thickness decreases $\mathcal{L}$ becomes smaller.

The variation of the carrier thermal conductivity with temperature is shown in Fig. 7.7 for both n- and p-type quantum wells and the theoretical results for their bulk alloys are also added from Refs. [15, 16]. As in the work done by Lin-Chung *et al.* [5], $\kappa_{\rm c}$ for quantum well structures decreases progressively both with temperature and well width. In Fig. 7.7 (a), it is seen that almost all n-type quantum wells (except for some parts of the d_A=7 nm sample) have lower $\kappa_{\rm c}$ throughout the temperature range compared to the value for the bulk alloy.

In contrast, as shown in Fig. 7.7 (b), in the temperature range 50 K - 400 K of the present study, higher values of $\kappa_{\rm c}$ are obtained for all p-type quantum wells

compared the value for the bulk alloy. The difference is much larger at low end of the temperature range. Beyond 400 K, the conductivities of p-type quantum wells approach the bulk value. Our calculation even reveal that for the samples with d_A=15 nm and 20 nm the carrier thermal conductivities become smaller than bulk values beyond 400 K.

7.4.2.2 Bipolar Thermal Conductivity

The theoretical calculation of the in-plane bipolar thermal conductivities of both n- and p-type quantum wells are presented in Fig. 7.8 including their bulk alloys reported in our previous works [15, 16]. For the theoretical calculation of the bipolar thermal conductivities of 2D quantum wells both the adjustable parameters $F_{\rm bp}$ and p, and the temperature dependences of the energy band gaps are taken as the bulk values [15, 16]. For both n- and p-type quantum well materials $\kappa_{\rm bp}$ continuously increases with the quantum well width. This can be easily understood from Eqs. (7.13) and (7.12). While n-type quantum wells have larger $\kappa_{\rm bp}$ compared to n-type bulk alloy, the opposite situation is found for the p-type materials. This is mainly because of the significant difference in the temperature variation of the energy band gaps and the difference in the $F_{\rm bp}$ parameter. Moreover, it is clearly seen that $\kappa_{\rm bp}$ for the n-type quantum wells is nearly five times bigger than the p-type quantum wells. Finally, up to 250 K for both type quantum well systems, the $\kappa_{\rm bp}$ values are insignificant compared to $\kappa_{\rm c}$ results. On the other hand, at 600 K the $\kappa_{\rm bp}$ results are larger than $\kappa_{\rm c}$ for the n-type quantum well samples whereas these values become nearly similar for the p-type quantum well samples.

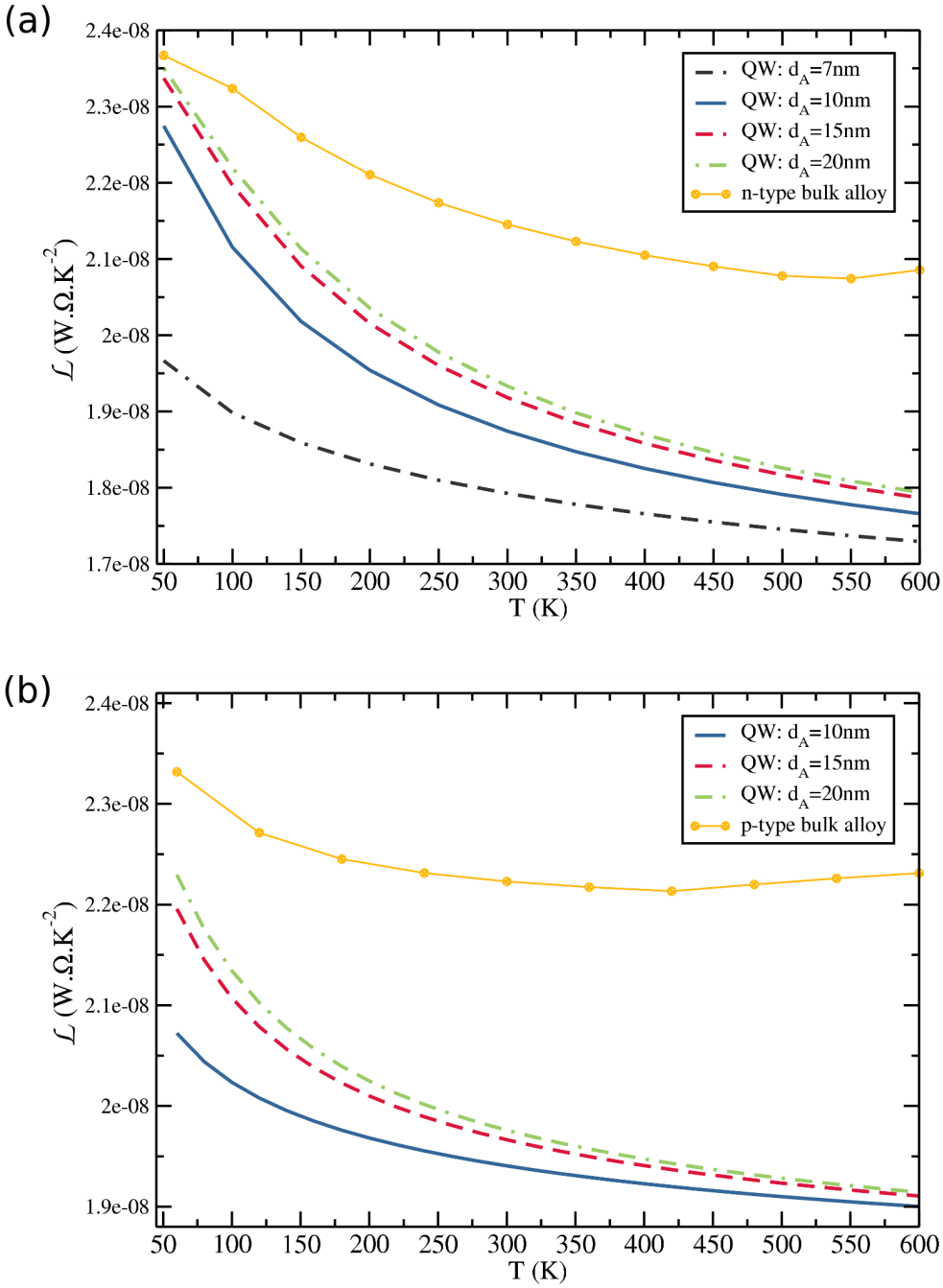

Figure 7.6: Temperature dependence of the Lorenz number for (a) n-type 0.1 wt.% CuBr doped $Bi_2Se_3/Bi_2Te_3/Bi_2Se_3$ and (b) p-type 3 wt.% Te doped $Sb_2Te_3/Bi_2Te_3/Sb_2Te_3$ quantum well systems. The symbols represent the theoretical results read from Refs. [15, 16] for n-type 0.1 wt.% CuBr doped 85% Bi_2Te_3 - 15% Bi_2Se_3 and p-type 3 wt% Te doped 20% Bi_2Te_3 - %80 Sb_2Te_3 single crystals.

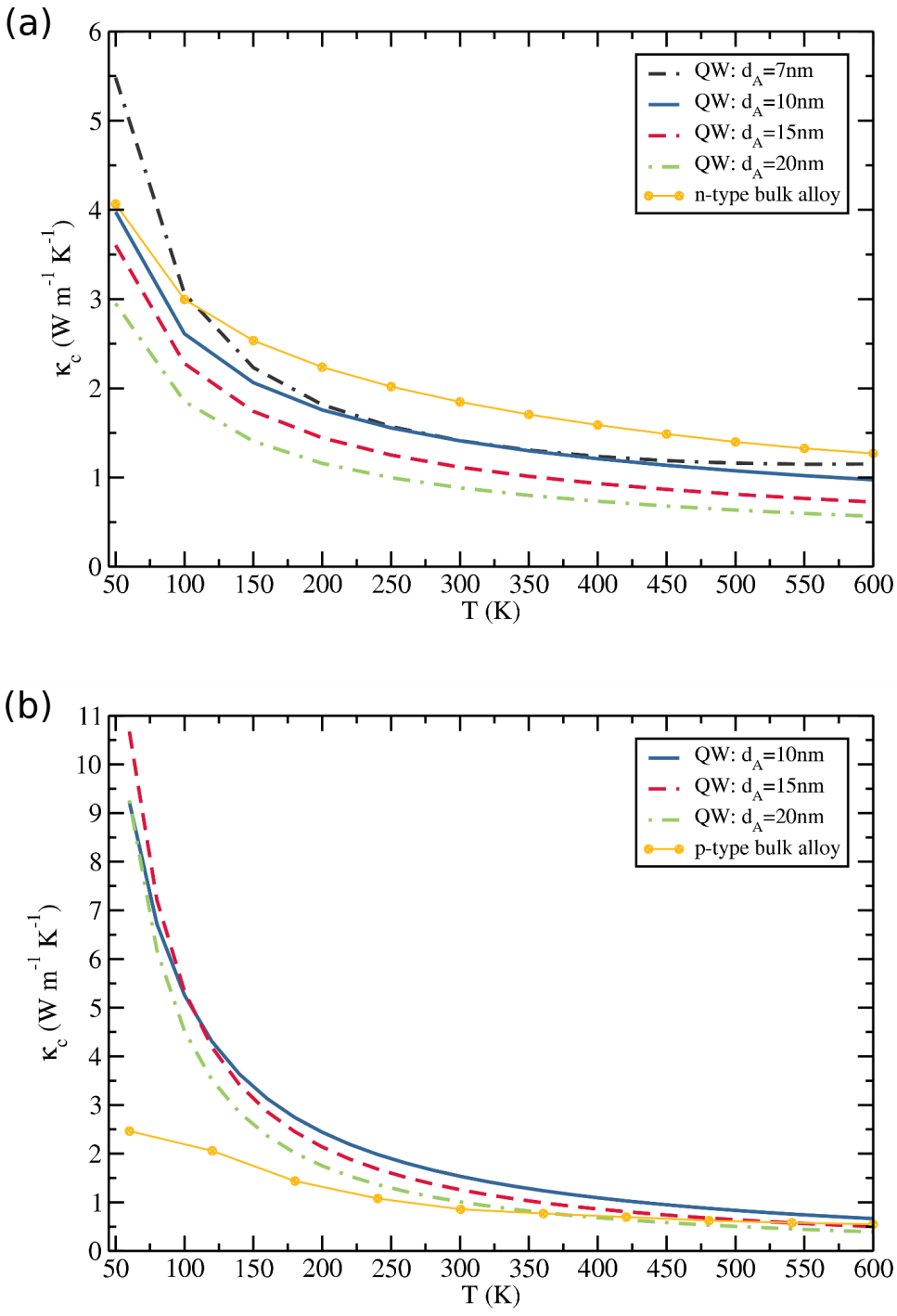

Figure 7.7: Temperature dependence of the carrier thermal conductivity for (a) n-type 0.1 wt.% CuBr doped $Bi_2Se_3/Bi_2Te_3/Bi_2Se_3$ and (b) p-type 3 wt.% Te doped $Sb_2Te_3/Bi_2Te_3/Sb_2Te_3$ quantum well systems. The symbols represent the theoretical results read from Refs. [15, 16] for n-type 0.1 wt.% CuBr doped 85% Bi_2Te_3 - 15% Bi_2Se_3 and p-type 3 wt% Te doped 20% Bi_2Te_3 - %80 Sb_2Te_3 single crystals.

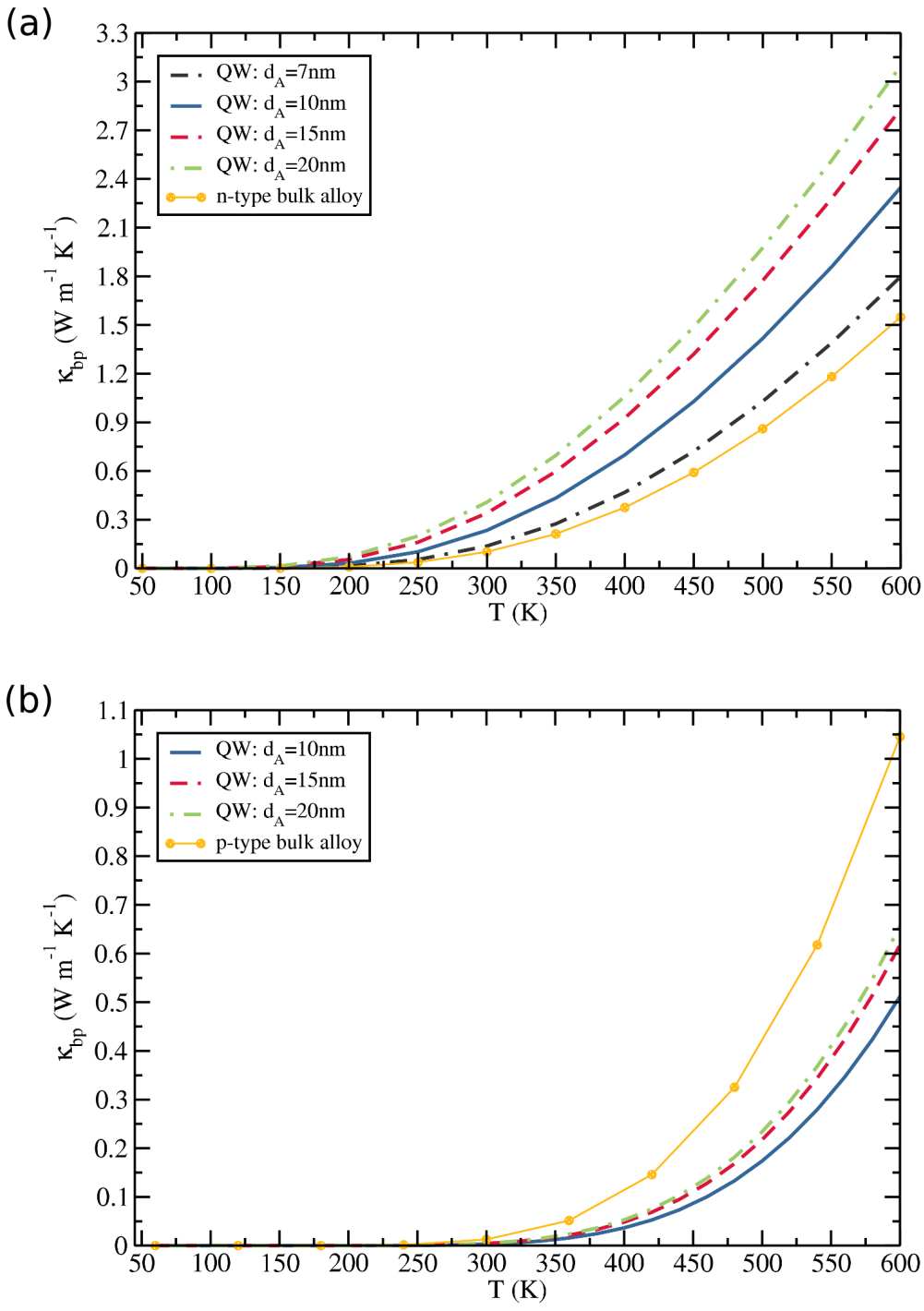

Figure 7.8: Temperature dependence of the bipolar thermal conductivity for (a) n-type 0.1 wt.% CuBr doped $Bi_2Se_3/Bi_2Te_3/Bi_2Se_3$ and (b) p-type 3 wt.% Te doped $Sb_2Te_3/Bi_2Te_3/Sb_2Te_3$ quantum well systems. The symbols represent the theoretical results read from Refs. [15, 16] for n-type 0.1 wt.% CuBr doped 85% Bi_2Te_3 - 15% Bi_2Se_3 and p-type 3 wt% Te doped 20% Bi_2Te_3 - %80 Sb_2Te_3 single crystals.

7.4.2.3 Phonon Thermal Conductivity

As described in the theory section, the temperature variation of the phonon thermal conductivity for the quantum well systems is calculated by including several scattering mechanisms rigorously. The phonon-phonon interactions are computed by employing Srivastava's scheme for bulk systems and incorporating the well width dependence of $\kappa_{\rm ph}$ as described in Refs. [17, 18]. Phonon scattering due to mass mixing and broken bonds or dislocations at interfaces are taken into account with a re-expressed version of the works reported in Refs. [21, 22]. Using the parameters listed in Tab. 7.1 the $\kappa_{\rm ph}$ - T calculations for the 2D quantum wells are made in terms of a temperature independent adjustable parameter $F_{\rm 3ph} = \left(\frac{\gamma}{\bar{c}}\right)^2$.

Similar to both n- and p-type doped bulk alloys studied in our previous works [15, 16], for all the quantum well samples we note that: boundary and carrier-phonon scattering rates play a major role for the $\kappa_{\rm ph}$ - T relationship at low temperatures (below 100 K), mass-defect scattering is important at both low and high temperatures (below and above 100 K) and three-phonon interactions become dominant only at high temperatures (above 100 K). Besides these factors, in Fig. 7.9 (a) and (b) the importance of the interface mass-mixing and interface dislocation scattering rates on the $\kappa_{\rm ph}$ - T for both n- and p-type quantum wells of well width 10 nm is shown clearly. For both quantum n- and p-type quantum well samples the interface dislocation scattering has a very little effect on the $\kappa_{\rm ph}$ for temperatures below 100 K. On the other hand, at high temperatures (above 100 K), the interface mass-mixing scattering has a significant effect on $\kappa_{\rm ph}$ for both types of quantum well systems.

In Fig. 7.10, the temperature dependence of the lattice thermal conductivity is represented for both n- and p-type quantum well systems and their bulk results

[15, 16] are also included for comparison. Due to the additional interface scattering mechanisms and scaled phonon-phonon interactions, all quantum well samples have smaller $\kappa_{\rm ph}$ than their bulk forms. The reduction is about an order of magnitude for all n- and p-type quantum well samples. This is the most desired condition to have for an enhanced value of ZT. Moreover, $\kappa_{\rm ph}$ decreases with increasing the quantum well thickness. This suggests that the most dominant effect on the $\kappa_{\rm ph}$ - d_A relation is coming from the anharmonic interaction since $\tau_{qs}^{-1}({\rm anh})({\rm QW})$ rises with d_A whereas $\tau_{qs}^{-1}({\rm ims})$ and $\tau_{qs}^{-1}({\rm ids})$ scattering rates drop off with d_A.

7.4.2.4 Total Thermal Conductivity

The total thermal conductivity of quantum well systems, computed by combining all contributions as $\kappa_{\rm total} = \kappa_{\rm c} + \kappa_{\rm bp} + \kappa_{\rm ph}$, is represented in Fig. 7.11.

As seen in panel (a), there is a huge difference in $\kappa_{\rm total}$ results between the n-type quantum wells and the n-type doped bulk alloy. This occurs because of the significant decrease in $\kappa_{\rm ph}$ for quantum well systems. Owing to the effect of $\kappa_{\rm bp}$, for the temperatures above 250 K, there is a clear increase in the total thermal conductivity results for the quantum wells. At around 600 K, the total conductivity result for the n-types QWs is found to be very close to the bulk value. The minimum value of $\kappa_{\rm total}$ is obtained for the d_A=20 nm quantum well sample at 1.37 W m^{-1} K^{-1} at 250 K whereas the minimum bulk value is 3.18 W m^{-1} K^{-1} at 400 K [15, 16].

As seen in panel (b), at lower temperatures ($T < 100$ K) $\kappa_{\rm total}$ of the p-type quantum wells is dramatically larger than the p-type bulk sample. This is due to the sudden increase in the carrier thermal conductivity in this temperature regime. At high temperatures ($T > 100$ K) the total thermal conductivities of the quantum

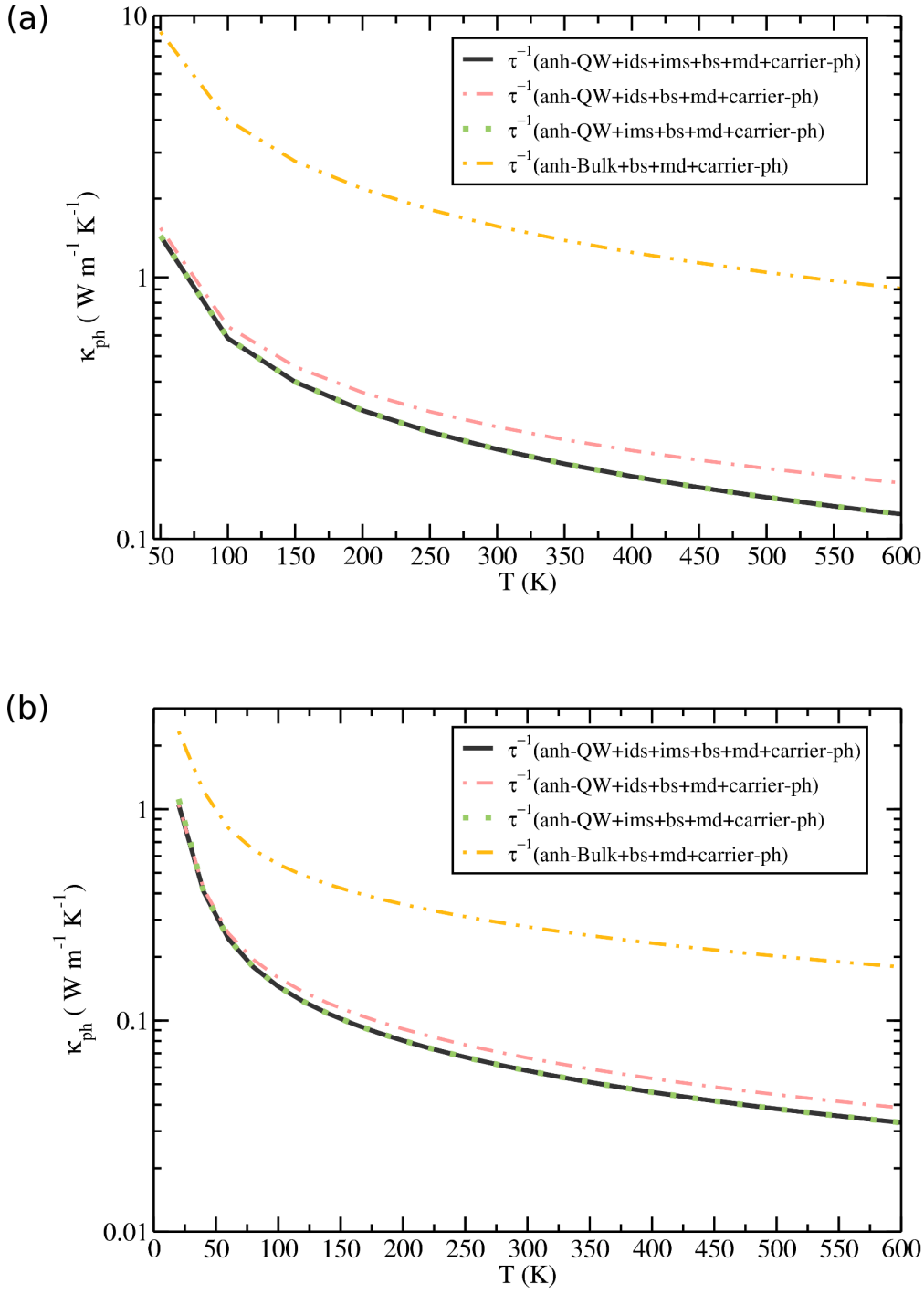

Figure 7.9: The effect of the interface mass-mixing and interface dislocation scattering mechanisms on the temperature variation of the phonon thermal conductivity for (a) n-type 0.1 wt.% CuBr doped Bi_2Se_3 / Bi_2Te_3 / Bi_2Se_3 and (b) p-type 3 wt.% Te doped Sb_2Te_3/Bi_2Te_3/Sb_2Te_3 quantum well systems taking d_A=10 nm.

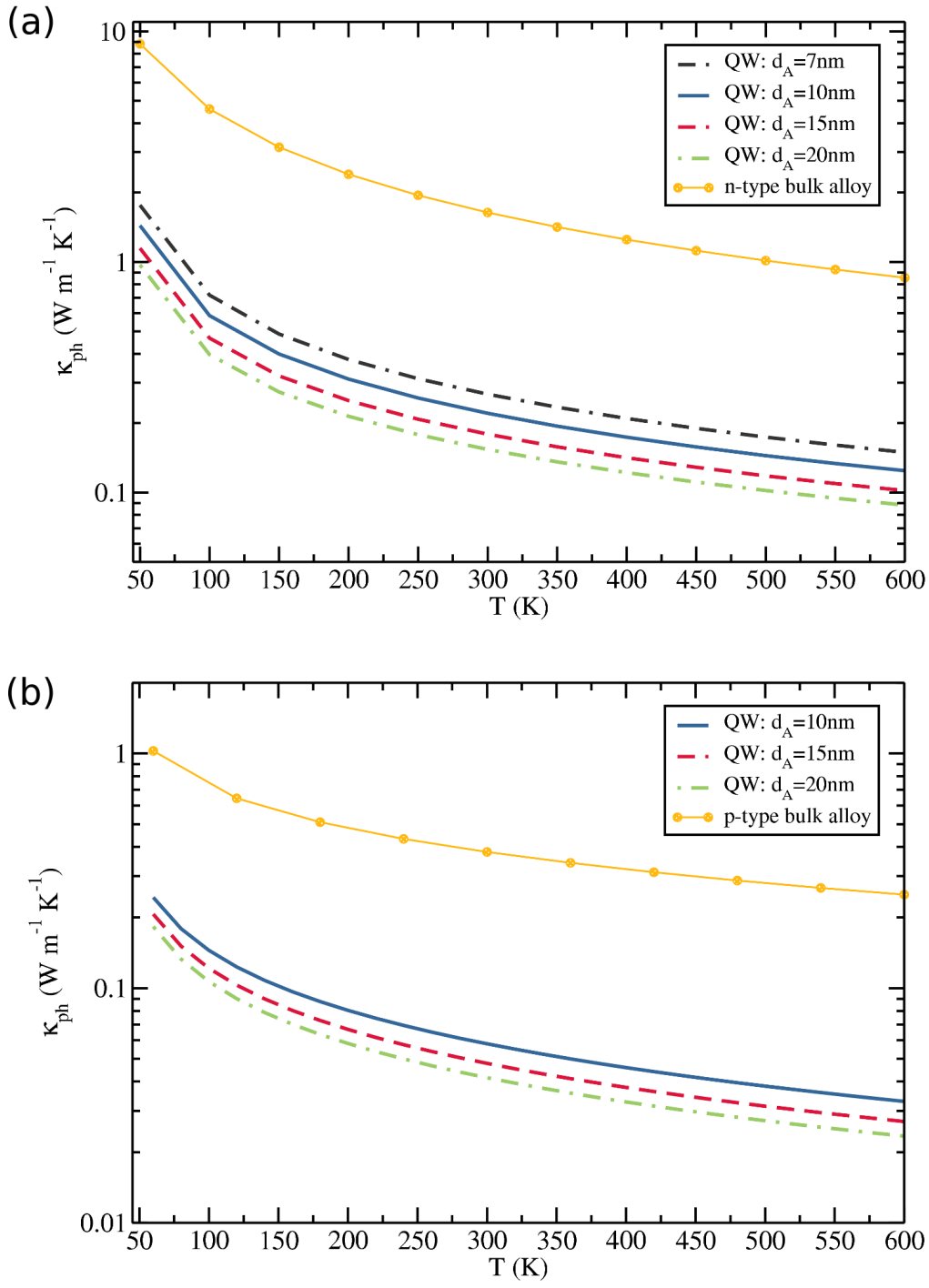

Figure 7.10: Temperature dependence of the phonon thermal conductivity for (a) n-type 0.1 wt.% CuBr doped $Bi_2Se_3/Bi_2Te_3/Bi_2Se_3$ and (b) p-type 3 wt.% Te doped $Sb_2Te_3/Bi_2Te_3/Sb_2Te_3$ quantum well systems. The symbols represent the theoretical results read from Refs. [15, 16] for n-type 0.1 wt.% CuBr doped 85% Bi_2Te_3 - 15% Bi_2Se_3 and p-type 3 wt% Te doped 20% Bi_2Te_3 - %80 Sb_2Te_3 single crystals.

wells lessen continuously, resulting from the reduced $\kappa_{\rm ph}$ value, and approach the bulk value of the $\kappa_{\rm total}$. Unlike the n-type quantum wells, there is a very slight increase in $\kappa_{\rm total}$ for the p-type quantum wells. This is because the p-type quantum wells have lower $\kappa_{\rm bp}$ values than the p-type bulk alloy. Furthermore, whereas the minimum $\kappa_{\rm total}$ of the p-type bulk alloy is 1.15 W m^{-1} K^{-1} at 420 K [15, 16], it is 0.73 W m^{-1} K^{-1} at 460 K for its quantum well with d_A=20 nm.

Thus, for both n- and p-type quantum well systems the d_A=20 nm samples have the lowest value of $\kappa_{\rm total}$ arising from their smallest value of $\kappa_{\rm ph}$ and $\kappa_{\rm c}$ among all other quantum well samples studied in this work.

7.4.3 Thermoelectric Figure of Merit

The theoretical calculation of the thermoelectric figure of merit (ZT) for the quantum well systems is performed by using $ZT = S^2\sigma/\kappa_{\rm total}$. The temperature variation of ZT for both n- and p-type quantum wells is presented in Fig. 7.12, where the theoretical bulk results reported in our previous works [15, 16] also reproduced for comparison.

Panel (a) shows that throughout the temperature range studied in this work significantly higher values of the ZT are gained for the n-type quantum wells with d_A=7 nm and d_A=10 nm compared to n-type bulk alloy. This is because both these two samples have larger power factors and lower total thermal conductivities than the bulk sample. Although the d_A=15 nm and 20 nm samples have smaller $\kappa_{\rm total}$ than the d_A=7 nm and 10 nm samples, their PF results are lower than the n-type bulk alloy, disallowing higher values of ZT for these QWs. As shown in panel (a), the peak values of ZT for the QWs are shifted to lower temperatures with increasing the well thickness. While the peak value of ZT for the n-type bulk

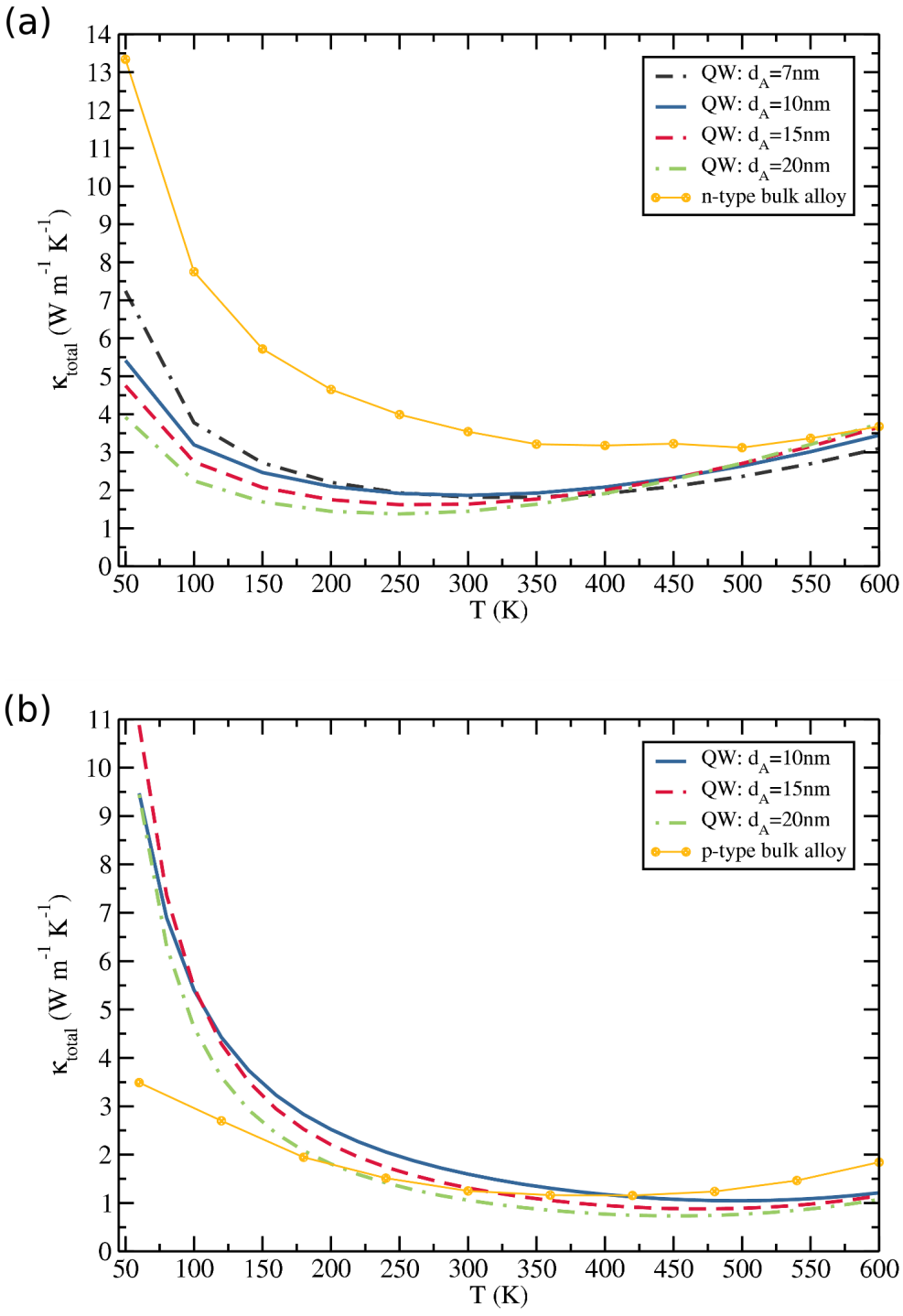

Figure 7.11: Temperature dependence of the total thermal conductivity for (a) n-type 0.1 wt.% CuBr doped $Bi_2Se_3/Bi_2Te_3/Bi_2Se_3$ and (b) p-type 3 wt.% Te doped $Sb_2Te_3/Bi_2Te_3/Sb_2Te_3$ quantum well systems. The symbols represent the theoretical results read from Refs. [15, 16] for n-type 0.1 wt.% CuBr doped 85% Bi_2Te_3 - 15% Bi_2Se_3 and p-type 3 wt% Te doped 20% Bi_2Te_3 - %80 Sb_2Te_3 single crystals.

alloy occurs at nearly 500 K, for n-type quantum wells it appears in the temperature range 275 K - 350 K. This suggests that when n-type quantum wells are used for the thermoelectric applications, the temperature range where the maximum thermoelectric efficiency is gained will move to lower temperatures in contrast to n-type bulk samples. The highest ZT value of 0.97 at 350 K for the n-type QW of width 7 nm is twice that of the n-type bulk alloy (0.482 at 500 K).

In Fig. 7.12 (b), the results of our theoretical calculation for the ZT - T variation are presented for the p-type quantum well samples. For all the p-type quantum wells studied in this work we find that ZT values of larger than 1.0 can be achieved over a large temperature range (typically 250 - 600 K). In particular, we find that for the well width 10 nm ZT is larger than 1.0 for all the temperatures studied above 100 K. Compared to the bulk system, for the d_A=10 nm quantum well sample PF is higher in the entire temperature range but κ_{total} is lower only at high temperatures (above 425 K). This indicates that the increment in PF has more dominant effect on the ZT than the decrement in κ_{total}. For the other two p-type quantum wells, with d_A=15 nm and 20 nm, we also obtain larger ZT values than the bulk alloy where the temperature is higher than 175 K and 275 K, respectively. We also note that the peak values of ZT for QW structures occur at slightly higher temperatures than for the p-type bulk sample. We further note that ZT peaks at higher temperatures (above 400 K) for p-type QWs than for n-type QWs (below 350 K). For the p-type quantum well of width d_A=10 nm the maximum value for ZT is obtained as 1.945 at 440 K while it is 1.3 at 420 K for its bulk alloy.

The present theoretical calculations are in agreement with the experimental work of Venkatasubramanian *et al*. [6] who reported an impressive value of the $ZT = 2.4$ at 300 K for the p-type 10Å/50Å Bi_2Te_3/Sb_2Te_3 superlattices and $ZT = 1.46$ at 300 K for the n-type 10Å/50Å $Bi_2Te_3/Bi_2Te_{2.83}Se_{0.17}$ superlattice. An analysis

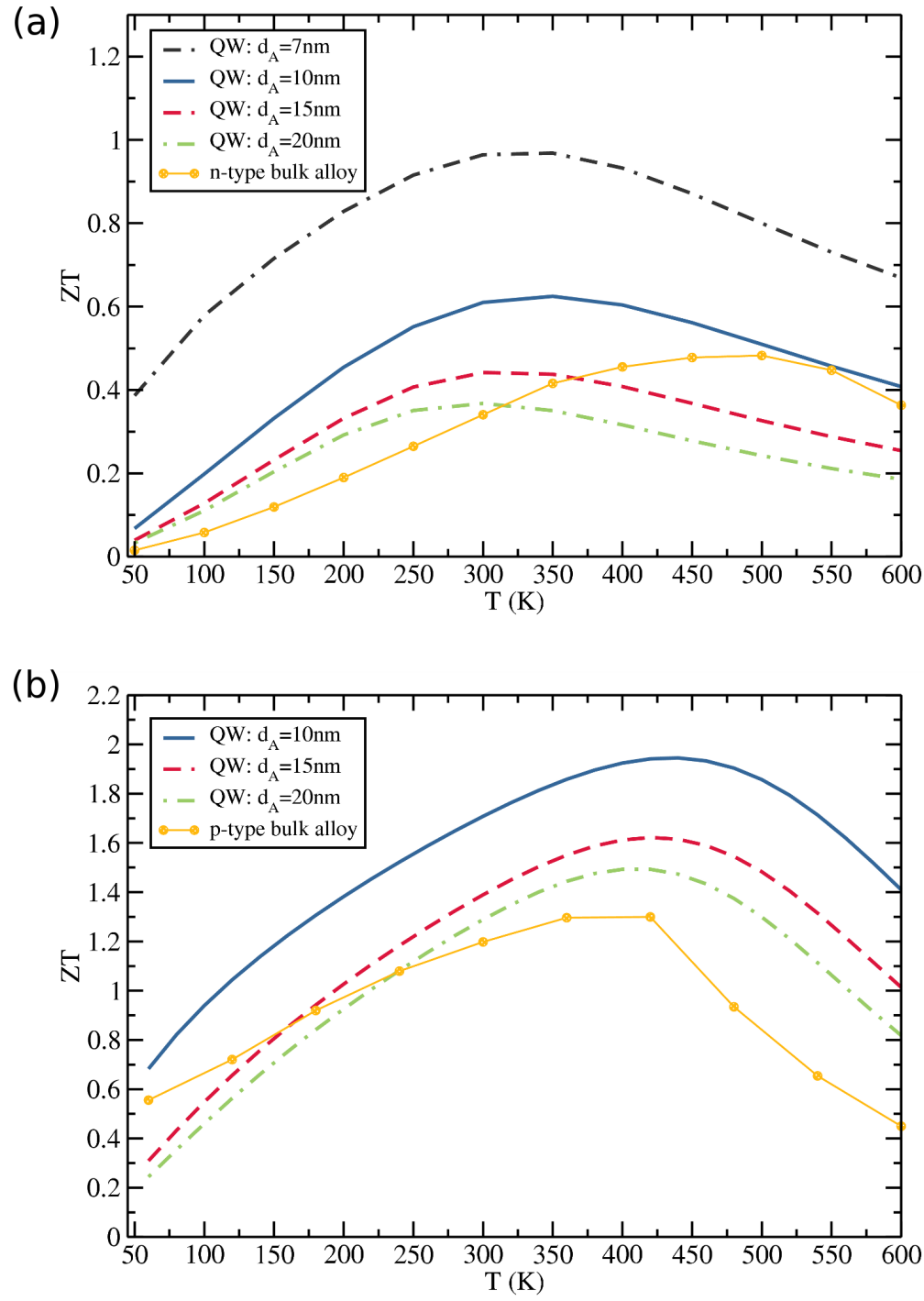

Figure 7.12: Temperature dependence of the thermoelectric figure of merit for (a) n-type 0.1 wt.% CuBr doped $Bi_2Se_3/Bi_2Te_3/Bi_2Se_3$ and (b) p-type 3 wt.% Te doped $Sb_2Te_3/Bi_2Te_3/Sb_2Te_3$ quantum well systems. The symbols represent the theoretical results read from Refs. [15, 16] for n-type 0.1 wt.% CuBr doped 85% Bi_2Te_3 - 15% Bi_2Se_3 and p-type 3 wt% Te doped 20% Bi_2Te_3 - %80 Sb_2Te_3 single crystals.

of the individual contributing factors suggests that just about twice as high ZT values for the p-type quantum wells compared to n-type quantum wells arises mainly from the fact that the thermal conductivity of the former is nearly a third of that for the latter.

In addition to the ZT - T calculation for both n- and p-type Bi_2Te_3 based quantum well systems with a=10 nm we represent the quantum well width dependence of the thermoelectric figure of merit in Fig. 7.13 for several temperatures. In accordance with the theoretical works reported by Hicks *et al.* [1] and Lin-Chung *et al.* [5] we found a smooth lowering of ZT with increase in the quantum well thickness.

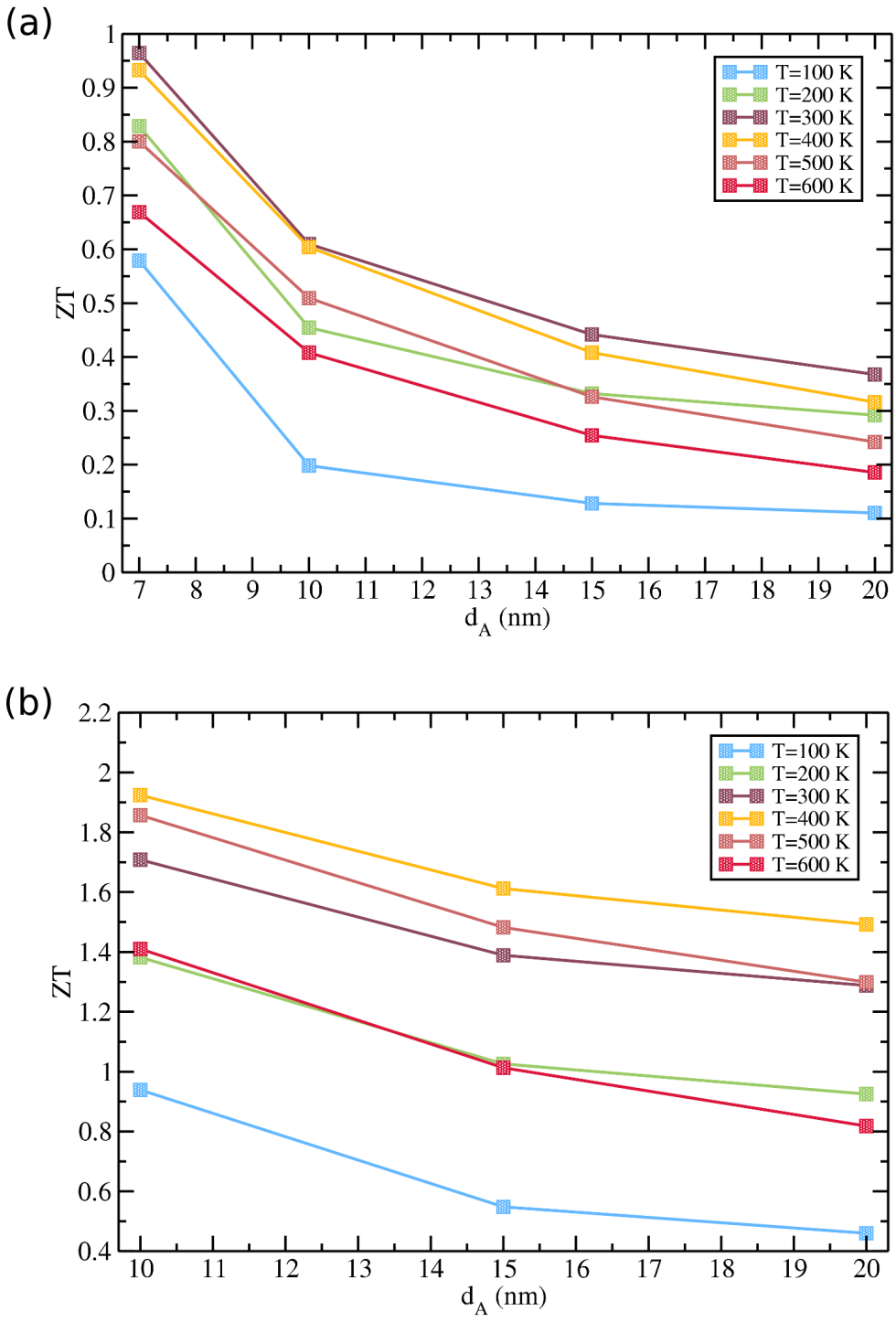

Figure 7.13: Quantum well width dependence of the thermoelectric figure of merit for (a) n-type 0.1 wt.% CuBr doped $Bi_2Se_3/Bi_2Te_3/Bi_2Se_3$ and (b) p-type 3 wt.% Te doped $Sb_2Te_3/Bi_2Te_3/Sb_2Te_3$ quantum well systems at several different temperatures.

7.5 Summary of Results

In this paper, we have investigated the thermoelectric properties of the n-type 0.1 wt.% CuBr doped $Bi_2Se_3/Bi_2Te_3/Bi_2Se_3$ and p-type 3 wt.% Te doped Sb_2Te_3 $/Bi_2Te_3$ $/Sb_2Te_3$ quantum well systems by computing both electrical and thermal transport coefficients systematically. The quantum well widths are taken in the range 7 nm $\leqslant d_A \leqslant$ 20 nm and the barrier width is set to zero.

We conclude the followings:

(*i*) Both n- and p-type quantum well samples show only the extrinsic Fermi level behaviour throughout the temperature range studied in this work.

(*ii*) It is theoretically shown that for the n-type quantum well of width d_A=7 nm the maximum value of the power factor is an order of magnitude larger than its bulk value given in Ref. [15]. The highest value of the power factor for the p-type quantum well sample with d_A=10 nm is nearly four times bigger than its bulk value obtained in Ref. [16].

(*iii*) The carrier thermal conductivities of both n- and p-type quantum well systems progressively decrease with temperature as well as the quantum well width.

(*iv*) The $\kappa_{\rm bp}$ value is generally higher(lower) for the n-type(p-type) quantum wells compared to the bulk value.

(*v*) An order of magnitude smaller values of $\kappa_{\rm ph}$ are predicted for almost all the considered quantum well systems compared to their bulk forms.

(*vi*) The total thermal conductivity $\kappa_{\rm total}$ is the lowest for both n- and p-type quantum wells of width d_A=20 nm.

(*vii*) It is found that reducing the well thickness has a pronounced effect on en-

hancing the thermoelectric figure of merit. For the n-type $Bi_2Se_3/Bi_2Te_3/Bi_2Se_3$ with 7 nm well width the maximum value of ZT is estimated to be 0.97 at 350 K and for the p-type $Sb_2Te_3/Bi_2Te_3/Sb_2Te_3$ with well width 10 nm the highest value of the ZT is found to be 1.945 at 440 K.

Table 7.1: Constants and parameters used in the calculations of thermoelectric properties of n-type 0.1 wt.% CuBr doped $Bi_2Se_3/Bi_2Te_3/Bi_2Se_3$ and p-type 3 wt.% Te doped $Sb_2Te_3/Bi_2Te_3/Sb_2Te_3$ quantum well systems.

Property/Parameter	$Bi_2Se_3/Bi_2Te_3/Bi_2Se_3$ QW	$Sb_2Te_3/Bi_2Te_3/Sb_2Te_3$ QW
$E_{\rm g}$ (eV)	$E_{\rm g}$(7 nm)=0.16 $E_{\rm g}$(10 nm)=0.147 $E_{\rm g}$(15 nm)=0.14 $E_{\rm g}$(20 nm)=0.134	$E_{\rm g}$(10 nm)=0.147 $E_{\rm g}$(15 nm)=0.14 $E_{\rm g}$(20 nm)=0.134
$\Delta E_{\rm i}^{(n,p)}$ (eV)	0.07	0.04
m_x^*/m_e [1]	0.021	0.021
m_y^*/m_e [1]	0.081	0.081
$m_{z,e}^*/m_e$ [1]	0.32	0.32
$m_{z,h}^*/m_e$ [23]	0.730	0.730
$m_{\rm n}^*/m_e$	0.082	0.082
$m_{\rm p}^*/m_e$	0.09	0.09
N ($\rm m^{-3}$)	$N_{\rm d}$=1.32×10^{25}	$N_{\rm a}$=8.1×10^{24}
r	0.1	0.45
ρ ($\rm kg/m^3$)	7.74×10^3	7.74×10^3
c_L (m/s) [24]	4.76×10^3	4.76×10^3
c_T (m/s) [24]	2.325×10^3	2.325×10^3
E_D (eV)	32	32
ς	0.3	1.1
$A^{'}$	0.092 ($\rm K^{-0.3}$)	0.00058 ($\rm K^{-1.1}$)
a_{lat} (Å) [25]	4.383	4.383
Ω ($\rm Å^3$)	169.07	169.07
L (mm)	0.5	0.5
q_D ($\rm Å^{-1}$)	0.705	0.705
p	1.0	1.0
F_{bp} ($\rm W\ m^{-1}\ K^{-2}$)	3.4×10^{-4}	13×10^{-4}
$\Gamma_{\rm isotopes}$	0.0011	0.0648
F_{3ph} ($\rm s^2/m^2$)	0.45×10^{-5}	0.96×10^{-5}
β_0	0.5	0.5
$\beta_0^{'}$	0.0001	0.0001

Bibliography

[1] L. D. Hicks and M. S. Dresselhaus, Phys. Rev. B **47**, 12727 (1993).

[2] L. D. Hicks and M. S. Dresselhaus, Phys. Rev. B **47**, 16631 (1993).

[3] B. Yang and G. Chen, Thermal Conductivity: Theory, Properties and applications (Ed: T. M. Tritt, Kluwer Academic/Plenum Publishers, London, 2004).

[4] L. D. Hicks, T. C. Harman, and M. S. Dresselhaus, Appl. Phys. Lett. **63**, 3230 (1993).

[5] P. J. Lin-Chung and T. L. Reinecke, Phys. Rev. B **51**, 13244 (1995).

[6] R. Venkatasubramanian, E. Siivola, T. Colpitts, and B. O'Quinn, Nature **413**, 597 (2001).

[7] N. F. Hinsche, B. Y. Yavorsky, M. Grandhand, M. Czener, M. Winkler, J. König, H. Böttner, I. Mertig, and P. Zahn, Phys. Rev. B **86**, 085323 (2012).

[8] P. J. Price, Phil. Mag. **46**, 1252 (1955).

[9] G. P. Srivastava, The Physics of Phonons (Taylor and Francis Group, New York, 1990).

[10] J. P. McKelvey, Solid State and Semiconductor Physics (Harper and Row Publishers, New York, 1966).

[11] R. R. Heikes and R. W. Ure, Thermoelectricity, Science and Engineering (Interscience Publishers, New York - London, 1961).

[12] B. R. Nag, Theory of Electrical Transport in Semiconductors (Pergamon Press, Oxford, 1972).

[13] Y. Gogotsi, Nanomaterials Handbook (Taylor and Francis Group, London, 2006).

[14] T. M. Tritt, Thermal Conductivity Theory, Properties and Applications (Kluwer Academic/Plenum Publishers, London, 2004).

[15] Ö. C. Yelgel and G. P. Srivastava, Phys. Rev. B **85**, 125207 (2012).

[16] Ö. C. Yelgel and G. P. Srivastava, J. Appl. Phys. **113**, 073709 (2013).

[17] O. L. Anderson, J. Phys. Chem. Solids **12**, 41 (1959).

[18] S. L. Shinde and J. S. Goela, High Thermal Conductivity Materials (Springer, New York, 2006).

[19] V. A. Greanya, W. C. Tonjes, R. Liub, C. G. Olson, D. -Y. Chung and M. G. Kanatzidis, J. Appl. Phys. **92**, 6658 (2002).

[20] M. S. Dresselhaus, X. Sun, S. B. Cronin, T. Koga, and G. Dresselhaus, K. L. Wang, Mat. Res. Soc. Symp. Proc. **478**, 55 (1997).

[21] S. P. Hepplestone and G. P. Srivastava, Phys. Rev. B **82**, 144303 (2010).

[22] S. P. Hepplestone and G. P. Srivastava, Phys. Rev. B **84**, 115326 (2011).

[23] D. R. Lide, CRC Handbook of Chemistry and Physics (Taylor and Francis Group LLC, 87th Edition, 2007).

[24] L. W. Silva and M. Kaviany, Int. J. Heat and Mass **47**, 2417 (2004).

[25] W. Zhang, R. Yu, H. Zhang, X. Dai, and Z. Fang, New J. Phys. **12**, 065013 (2010).

Chapter 8

Concluding Remarks

8.1 Summary of the Thesis

In this thesis, a systematic theoretical modelling of the thermoelectric properties (Fermi level, Seebeck coefficient, electrical conductivity, and thermal conductivity) of three dimensional bulk and two dimensional quantum well systems has been presented. Electronic properties (Fermi level, Seebeck coefficient, and electrical resistivity) and thermal conductivity contribution from carriers (donor electrons or acceptor holes) have been derived by using the nearly-free electron approximation and the Fermi-Dirac statistics. Other thermal conductivity contributions originated from electron-hole pairs and phonons have been studied using revised version of previous works and Debye's isotropic continuum scheme, respectively.

Chapter 1 provided a broad range of introduction to thermoelectricity including various thermoelectric effects and their applications. Moreover, the state-of-the-art thermoelectric materials and the optimisation methods to enhance the value

of thermoelectric figure of merit ZT were reviewed.

Detailed descriptions of three- and two-dimensional thermoelectric transport theory for semiconductors were given in Chapter 2 and 3, respectively.

In Chapter 4, the 3D thermoelectric transport theory was performed for n-type $(Bi_2Te_3)_{0.85}(Bi_2Se_3)_{0.15}$ single crystals doped with CuBr and SbI_3. In agreement with available experimental work, it was theoretically found that the maximum value of ZT was to be 0.43 (at 400 K) and 0.49 (at 500 K) for the SbI_3- and CuBr-doped samples, respectively. Additionally, it was concluded that due to the reduction in phonon thermal conductivity, a reasonable increase in the Se content in $(Bi_2Te_3)_x(Bi_2Se_3)_{(1-x)}$ single crystals could increase ZT significantly both at low and high temperatures.

The p-type $(Bi_2Te_3)_x(Sb_2Te_3)_{1-x}$ single crystals doped with 3 wt.$\%$ Te were studied in Chapter 5 in the composition range of $0.18 \leq x \leq 0.26$. In agreement with the experimental study the maximum value of ZT was computed theoretically as 1.31 for the x=0.20 sample at 390 K, which was determined by the lowest total thermal conductivity and one of the highest power factor values among all compositions. Furthermore, the largest value of the ZT of p-type x=0.20 sample is 2.6 times larger than that for the n-type sample studied in Chapter 4. This clearly showed that the influence of the composition range of semiconductor alloys together with its type and amount of dopant plays an important role in enhancing the thermoelectric figure of merit.

In Chapter 6, due to its dominant factor for enhancing the value of ZT a detailed thermal conductivity calculations were presented for both n- and p-type Bi_2Te_3 based single crystals including frequency dependence of the phonon thermal conductivity for different temperatures.

In Chapter 7, 2D thermoelectric transport theory was applied for n-type 0.1 wt.% CuBr doped $Bi_2Se_3/Bi_2Te_3/Bi_2Se_3$ and p-type 3 wt.% Te doped $Sb_2Te_3/Bi_2Te_3/Sb_2Te_3$ quantum well systems. Different values of well thicknesses were considered for both types of quantum well systems to study the effect of confinement on all thermoelectric transport coefficients. It was found that reducing the well thickness has a pronounced effect on enhancing the thermoelectric figure of merit. For the n-type $Bi_2Se_3/Bi_2Te_3/Bi_2Se_3$ with 7 nm well width the maximum value of ZT was estimated to be 0.97 at 350 K and for the p-type $Sb_2Te_3/Bi_2Te_3/Sb_2Te_3$ with well width 10 nm the highest value of the ZT was found to be 1.945 at 440 K.

8.2 Future Work

Although no devices based on low dimensional structures have been close to commercialisation, research on low dimensional thermoelectric materials has been stimulating to recent developments in thermoelectric research area, and many research groups worldwide are now studying to bring new ideas to the field based on nanostructures. As an example of this the in-plane thermoelectric transport properties have been theoretically investigated in this thesis for Bi_2Te_3 based quantum well systems and significantly enhanced values of ZT have been gained. Additional to our presented in-plane theory, the cross-plane thermoelectric transport properties of these quantum well structures can be studied to make our theory more detailed and complete. Some theoretical investigations on this subject would be very useful for thermoelectric research area.

Theoretical considerations suggest that because of their increased quantum confinement effects, 1D quantum wires could have an even larger values of ZT than 2D quantum wells [1, 2]. In 2008, Boukai *et al.* [3] reported efficient thermo-

electric performance from the single-component system of silicon nanowires for cross-sectional areas of 10 nm $\times$ 320 nm and 20 nm $\times$ 320 nm. By varying the nanowire size and impurity doping levels, ZT values representing an approximately 100-fold improvement over bulk Si were achieved over a broad temperature range, including $ZT > 1$ at 200 K. Similar results have been reported by Hochbaum *et al.* [4] in 2008 also. They synthesised electrochemically large-area, wafer-scale arrays of rough Si nanowires that are 20-300 nm in diameter. These nanowires have Seebeck coefficient and electrical resistivity values that are the same as those of doped bulk Si, but those with diameters of about 50 nm exhibit 100-fold reduction in thermal conductivity, yielding ZT = 0.6 at room temperature. For such nanowires, the lattice contribution to thermal conductivity approaches the limit for amorphous Si, which cannot be explained by current theories. Bulk Si is a poor thermoelectric material. However, by greatly reducing thermal conductivity without affecting much the Seebeck coefficient and electrical resistivity, Si nanowire arrays show promise as high-performance, scalable thermoelectric material. Very recently, Zhang *et al.* [5] studied on ultrathin Te-rich (n-type) Bi_2Te_3 ultrathin nanowires with an average diameter of 8 nm. Their thermoelectric properties measurements indicated that the thermal conductivity for this nanowire sample is much lower than that of the bulk materials due to the enhanced phonon scattering at the nanoscale interfaces, which results in a 13% enhancement of the ZT value compared to that of the best commercial n-type $Bi_2Te_{2.7}Se_{0.3}$ bulk crystals [6]. In spite of these promising experimental works on thermoelectric properties of 1D nanowires, there is not enough complete theoretical works discussed all the transport coefficients in these structures. Therefore, it is very desirable to present a full account of theoretical study on this subject.

Since the enhancement in ZT is expected to be more pronounced as the dimensionality decreases, one might expect that 0D structures might possess thermo-

electric properties that are even more promising than those of 2D and 1D systems owing to the highly singular electronic density of states of quantum dots. Unlike 1D or 2D systems, where at least one of the directions is not quantum confined and thus able to provide an electrical conduction pathway, 0D structures, such as quantum dots, are quantum confined in all directions. In order to utilize the unique properties of quantum dots for transport applications, it is therefore necessary to devise some means of electron conduction pathways between individual quantum dots. In this respect, some quasi-zero-dimensional systems, such as segmented nanowires [7], a quantum dot [8] located between two quantum point contacts, and quantum- dot superlattices [9, 10] have been tried to use for thermoelectrics. In this respect, Harman *et al.* [11] have synthesized arrays of quantum dots each only a few nanometers in diameter. The materials were PbSeTe-based quantum dot superlattice structures grown by molecular beam epitaxy. The typical device consists of a substrate-free, bulk-like (typically 0.1 mm in thickness, 10 mm in width, and 5 mm in length) slab of nanostructured PbSeTe/PbTe as the n-type leg and a metal wire as the p-type leg. Eventually, they estimated the value of ZT in the range of 1.3 to 1.6 at room temperature with the major mechanism contributing to the enhancement of ZT is from the reduction of the lattice thermal conductivity through the strong interface scattering of phonons. A detail theoretical investigation of the thermoelectric transport properties in such systems would be very informative to the thermoelectric research area.

Bibliography

[1] L. D. Hicks and M. S. Dresselhaus, Phys. Rev. B **47**, 16631 (1993).

[2] X. Sun, Z. Zhang, and M. S. Dresselhaus, Appl. Phys. Lett. **74**, 4005 (1999).

[3] A. Boukai, Y. Bunimovich, J. Tahir-Kheli, J-K Yu, W. III Goddard, and J. Heath, Nat. Lett. **451**, 168 (2008).

[4] A. Hochbaum, R. Chen, R. Delgado, W. Liang, E. Garnett, M. Najarian, A. Majumdar, and P. Yang, Nat. Lett. **451**, 163 (2008).

[5] G. Zhang, B. Kirk, L. A. Jauregui, H. Yang, X. Xu, Y. P. Chen, and Y. Wu, Nano Lett. **12**, 56 (2012).

[6] A. X. Yan, B. Poudel, Y. Ma, W. S. Liu, G. Joshi, H. Wang, Y. C. Lan, D. Z. Wang, G. Chen, and Z. F. Ren, Nano Lett. **10**, 3373 (2010).

[7] Yu-M. Lin and M. S. Dresselhaus, Phys. Rev. B **68**, 075304 (2003).

[8] A. S. Dzurak, C. G. Smith, C. H. W. Barnes, M. Pepper, L. Martin-Moreno, C. T. Liang, D. A. Ritchie, and G. A. C. Jones, Phys. Rev. B **55**, R10197 (1997).

[9] T. C. Harman, L. D. Spears, and M. P. Walsh, J. Electron. Mater. Lett. **28**, LI (1999).

[10] T. C. Harman, P. J. Taylor, M. P. Walsh, and D. L. Spears, J. Electron. Mater. **29**, L1 (2000).

[11] T. C. Harman, P. Taylor, M. Walsh, and B. LaForge, Sience **297**, 2229 (2002).